Precision Measurement of the Neutron Magnetic Form Factor via the Ratio Method at Jefferson Lab Hall A

Maria Satnik

Altoona, Wisconsin

Master of Science, College of William & Mary, 2020
Bachelor of Science, St. Norbert College, 2018

A Dissertation presented to the Graduate Faculty of The College of William and Mary in Virginia in Candidacy for the Degree of Doctor of Philosophy

Department of Physics

The College of William and Mary in Virginia
August, 2025

APPROVAL PAGE

This Dissertation is submitted in partial fulfillment of
the requirements for the degree of

Doctor of Philosophy

María Satnik

Maria Satnik

Reviewed by the Committee, May 2025

Todd Averett

Committee Chair
Todd Averett, Physics
William & Mary

David Armstrong

David Armstrong, Physics
William & Mary

DocuSigned by:
Justin Stevens
1742FB831744416...

Justin Stevens, Physics
William & Mary

Signed by:
Andrew Jackura
24AD1B61DD54439...

Andrew Jackura, Physics
William & Mary

Douglas Higinbotham, Physics
Thomas Jefferson National Accelerator Facility

ABSTRACT

Protons and neutrons, collectively known as nucleons, are composed of quarks and gluons. The Sachs electromagnetic form factors encode information about the spatial distributions of charge and magnetization in the nucleon, particularly at low momentum transfer. In particular, the neutron magnetic form factor (G_M^n) provides crucial information about the distribution of magnetization inside the neutron and helps constrain theoretical models of nucleon structure.

Quasi-elastic electron scattering from deuterium was measured up to $Q^2 = 13.5$ GeV^2 using the Super BigBite Spectrometer in Hall A at Jefferson Lab. In this work, the neutron magnetic form factor G_M^n was extracted at $Q^2 = 3.0$ GeV^2 and $Q^2 = 4.5$ GeV^2 using the Ratio Method. These results represent a subset of the full dataset collected in this experiment, which extended to significantly higher Q^2.

The extracted G_M^n values agree with the existing global fit within approximately two standard deviations at $Q^2 = 3.0$ and show excellent agreement at $Q^2 = 4.5$. The measurements achieved systematic uncertainties of about 2% and statistical uncertainties below 0.5%, among the most precise determinations of G_M^n at these kinematics. These results demonstrate the robustness of the experimental technique and provide an important validation point for future extractions at higher Q^2, where data remain scarce. In addition, the GRINCH heavy gas Cherenkov detector—a key component of the experimental apparatus—was commissioned and achieved an electron detection efficiency of approximately 97%, supporting reliable particle identification. Together, the analysis presented here advances both our understanding of nucleon structure and the validation of the experimental methods and instrumentation used to access it.

TABLE OF CONTENTS

ACKNOWLEDGMENTS

First and foremost, I would like to thank my advisor, Todd Averett, for his unwavering support and enthusiasm from the very beginning. His guidance, expertise, and positive energy have been invaluable throughout my research journey.

I am also deeply grateful to my committee members for their time, insights, and feedback. In particular, I would like to thank David Armstrong, an exceptional mentor who has generously shared his vast knowledge and experience, helping me refine my physics intuition. A special thank you to Doug Higinbotham, whose presentations at JLab on particle detectors inspired me to pursue experimental nuclear physics.

I would also like to express my gratitude to the faculty at William & Mary, the staff scientists at JLab, and the faculty at St. Norbert College who have mentored and supported me. I am especially thankful to Arun Tadepalli for his kindness and guidance through many challenges and to Carlos Ayerbe, whose support and humor have been a constant since the start of graduate school. I would also like to acknowledge Professors Jeff Nelson, Patricia Vahle, and Chris Monahan, as well as the physics office staff, particularly Ellie Wilkinson and Paula Perry, for their invaluable assistance. Additionally, I am grateful to the many physicists I have worked with at JLab who have guided me, including Eric Fuchey, Scott Barcus, Mark Jones, Nadia Fomin, Dave Gaskell, Brad Sawatzky, Bob Michaels, and Rachel Montgomery. I also extend my appreciation to my undergraduate physics professors at St. Norbert College, Eric Brekke and Michael Olson, for fostering my passion for physics.

I would like to thank my collaborators, especially my fellow GMn graduate students: John Boyd, Provakar Datta, Sean Jeffas, Nathaniel Lashley-Colthirst, Ralph Marinaro, Anu Rathnayake, Sebastian Seeds, and Zeke Wertz. I am also grateful to the graduate students from other SBS experiments with whom I have had the privilege to work alongside, including Sean Jeffas, Kate Evans, and Gary Penman, as well as everyone in the collaboration who has contributed to this work.

I am grateful to the Department of Energy for supporting my research through grant award DE-FG02-96ER41003. I also appreciate the support of Jefferson Science Associates for the graduate fellowship I received from 2022 to 2023.

I would like to thank my many colleagues, friends, and peers who have supported me over the years. In particular, I am incredibly grateful to Tangereen Velveteen Bailey Claringbold and Kate Evans—your encouragement has helped me gain so much confidence both in and beyond my academic pursuits. I am endlessly thankful for my dear friends Alex Gruber and Scarlett Andrew who have been cheering me on since undergrad. I also deeply appreciate Sarah Glossen for mentoring me and supporting me through the thesis writing process.

Next, I want to thank my support system, especially my parents, Barb Satnik and Joe Satnik, who have gone above and beyond in supporting me through my higher education. A special thanks to my mom for helping with editing this thesis. I would also like to thank my partner, Aidan Lucas, for his kindness, support, and help in editing this thesis.

I would like to thank the staff at the William & Mary Health Center for their care and commitment to helping me thrive, as well as the William & Mary staff and broader community for helping me navigate my PhD.

I also want to acknowledge my online friends and virtual communities, who have supported me and brought joy to my life, especially during the first few years of the pandemic. I am deeply thankful for the kindness and community I found in my *World of Warcraft* guild, which helped me through incredibly difficult and isolating times.

I would also like to acknowledge the the AI language model, ChatGPT, for assistance brainstorming, editing, and LaTeX formatting support during the writing process.

Lastly, I want to extend a bit of appreciation to myself. I am thankful for the courage and perseverance I have practiced each day—small acts of bravery that have compounded over time. I am proud of the person, physicist, daughter, community member, friend, and partner I have worked so hard to become.

Writing this thesis has given me an opportunity to reflect on my journey through higher education. I am humbled by the kindness and support in my life and by all the incredible people who have walked alongside me. From the bottom of my heart, thank you all.

I dedicate this dissertation to every physicist who has ever felt like an imposter.
You have worked so hard to be here. Be kind to yourself. You belong.

LIST OF TABLES

LIST OF FIGURES

Chapter 1

Introduction

1.1 Historical Context for Nucleon Structure Experiments

Ernest Rutherford, known as "the father of nuclear physics," and his students demonstrated through bombarding metal foils with alpha particles that atoms have a nucleus which contains all the positive charge and most of the mass [1]. This scattering experiment, now understood to be elastic scattering of charged particles by the nuclear Coulomb potential, marked the beginning of a long legacy of discovering the substructure of atoms and nuclei through scattering experiments.

In 1935, James Chadwick was awarded the Nobel Prize in Physics for his discovery of the neutron—a neutrally charged particle with a mass nearly equal to that of the proton [2]. Ernest Rutherford had previously proposed that neutral particles might exist within the atomic nucleus to explain discrepancies in atomic mass that were not accounted for by protons alone.

Protons and neutrons were initially thought to be elementary particles with no internal structure. However, the rapid discovery of new hadrons in the mid-20th century, often referred to as the "particle zoo," suggested that hadrons were composite particles with rich substructure [3]. In 1969, researchers at SLAC provided experimental evidence that nucleons are composed of smaller, point-like particles now known as quarks [4]. This discovery fundamentally shifted our understanding of matter, giving rise to the quark model [3] and ultimately contributing to the development of the Standard Model.

The Standard Model describes how quarks, which make up hadrons such as protons and neutrons, and leptons, which include electrons, form the fundamental building blocks of matter [5]. The strong interaction between quarks is described by quantum chromodynamics (QCD).

In this work, we will be exploring the magnetic form factor of the neutron. The term "form factor" is widely used across different fields, including the culinary arts, where it refers to the shape, size, and distribution of ingredients in a dish. For example, one could argue that a sushi roll and a poke bowl contain the same basic ingredients, yet their form factors make them distinct dishes and experiences.

In nuclear physics, electromagnetic form factors play a similarly fundamental role, encoding information about the internal structure of the nucleon in terms of its charge and current distributions. By experimentally constraining these form factors, we gain deeper insight into the composition of nucleons—the building blocks of the visible matter in our universe [6].

Despite knowing that nucleons are composed of nearly massless, spin-$\frac{1}{2}$ quarks bound together by gluons, many details of how these constituents give rise to the nucleon's macroscopic properties (such as its mass, spin, size, charge, and magnetization) remain elusive [7]. An important goal of modern nuclear physics experiments is to unravel this complexity by probing the distributions of charge and magnetization inside the nucleon.

To study the electric and magnetic form factors of protons and neutrons, we will utilize electron–nucleon elastic scattering. This will be discussed in the upcoming sections in detail.

1.2 The Standard Model

The Standard Model is the theory that describes three of the four known fundamental forces and classifies the known elementary particles in the universe. Figure 1.1 illustrates the particle content of the Standard Model.

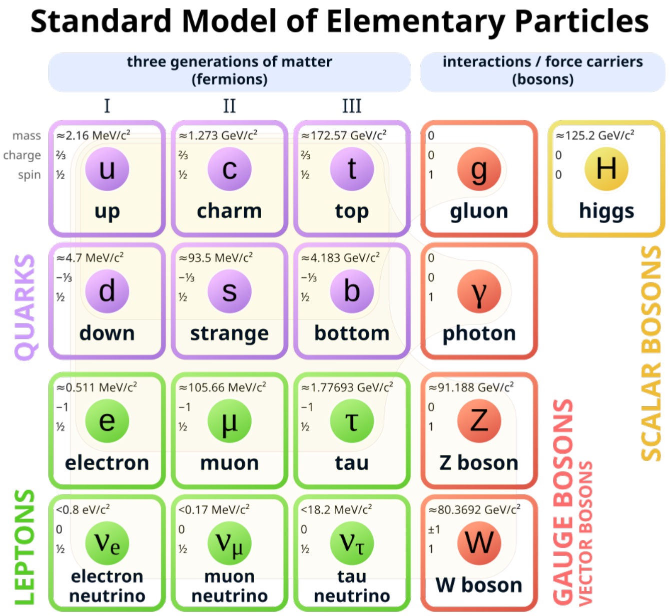

Figure 1.1: Illustration of the Standard Model of particle physics [8].

The Standard Model consists of fermions and bosons. Fermions are spin-$\frac{1}{2}$ particles and are organized into quarks and leptons. Each fermion has a corresponding antiparticle.

Quarks and anti-quarks have color charge and participate in strong and electroweak interactions. They are the constituent particles of hadrons, including protons and neutrons. Leptons and anti-leptons (such as electrons and positrons) do not have color charge and participate in electroweak interactions.

Bosons are the mediators for the fundamental interactions (forces). The Standard Model describes the electromagnetic force, the weak force, and the strong force, but excludes gravity. The photon is the force carrier for the electromagnetic interaction, and the gluon is the force carrier for the strong interaction.

Figure 1.2 illustrates a proton and neutron in a deuterium atom in the Standard Model. Protons consist of two up quarks and one down quark, and neutrons consist of two down quarks and one up quark. The nucleon structure is governed by Quantum Chromodynamics (QCD), which is the theory of the strong force.

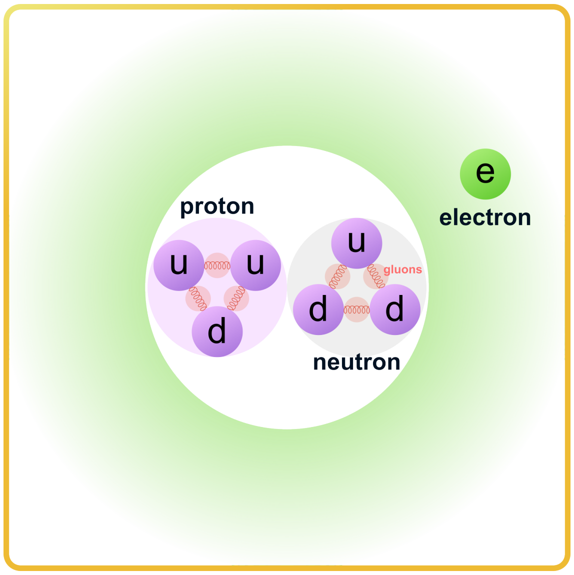

Figure 1.2: Illustration of the valence quark structure of a proton and neutron in deuterium in the standard model [9]. Protons consist of two up quarks and one down quark, and neutrons consist of two down quarks and one up quark. Gluons are the force carrier for the strong force and bind quarks together.

1.3 Quantum Chromodynamics

Quantum Chromodynamics (QCD) is the theory that describes the strong force. QCD governs the behavior of quarks and gluons—the fundamental constituents of hadrons such as protons and neutrons. While Quantum Electrodynamics (QED) describes the electromagnetic interactions between electrically charged particles, QCD uses an analogous charge called *color*. Quarks carry one of three color charges, and gluons (unlike photons) carry color themselves, allowing them to interact with each other as well as quarks.

A defining feature of QCD is *confinement*: quarks and gluons cannot be observed as free particles under normal circumstances. Rather, they are bound into color-neutral hadrons by the exchange of gluons. However, at short distances—corresponding to interactions mediated by a virtual photon with large four-momentum transfer squared (Q^2)—the strong coupling becomes weak. This property is known as *asymptotic freedom*. At sufficiently high Q^2, the quarks inside a nucleon behave as nearly free, point-like particles. This scale dependence makes deep inelastic scattering and high-Q^2 elastic scattering particularly powerful tools for probing the internal structure of the nucleon.

Because quarks are confined inside the nucleon, we cannot directly observe their spacial or momentum distributions. Instead, we must infer information about the internal structure of hadrons through scattering experiments. Elastic electron-nucleon scattering is particularly useful because it involves a well-understood probe (the electron) which interacts predominately via the electromagnetic interaction. By measuring how electrons scatter off nucleons, we can extract the *form factors*. Electromagnetic form factors encode information about distribution of charge and magnetization inside the nucleon—features that emerge from QCD.

1.4 Electron-Nucleon Scattering

In electron-nucleon (eN) scattering, the lowest order approximation is the *one-photon exchange* process, also called the Born term. This involves the exchange of a single virtual photon. This provides a good low-order approximation of elastic electron-neutron scattering, en, and electron-proton scattering, ep [10]. Figure 1.3 shows the lowest-order Feynman diagram[1] for eN scattering in the rest frame of the initial nucleon. We can relate the four-momentum components through conservation of momentum.

In Fig. 1.3, we use the following variables:

- k, (k'): Four-momentum of the incident (scattered) electron.

---

[1] *Feynman diagrams* are standard tools in quantum field theory, named after physicist Richard Feynman. While this terminology remains in widespread use, it is essential to acknowledge that aspects of Feynman's personal behavior—particularly toward women—reflect broader patterns of exclusion in the history of physics. As a community, we must continue working toward a more inclusive and respectful culture in science, one that recognizes and amplifies the voices of women and underrepresented minorities.

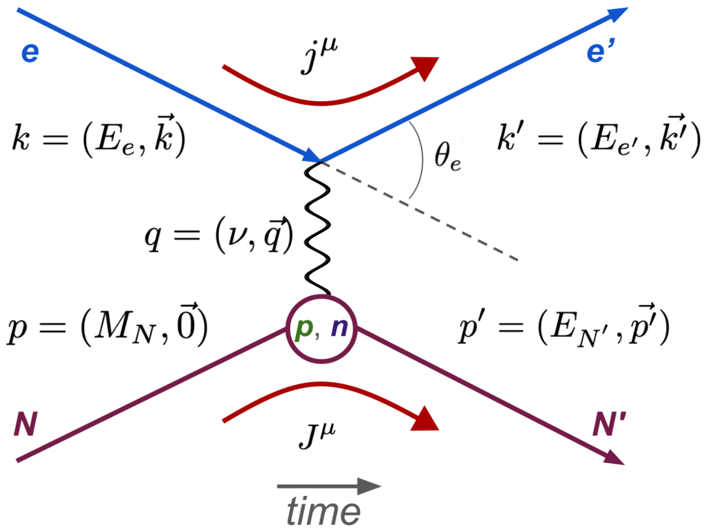

Figure 1.3: Feynman diagram of electron–nucleon (eN) scattering for $N = (p, n)$.

  - ◇ E_e, $E_{e'}$: Energy of the incident (scattered) electron.
  - ◇ $\vec{k}$, $(\vec{k'})$: Three-momentum of the incident (scattered) electron.

- p, (p'): Four-momentum of the incident (scattered) nucleon.
  - ◇ M_N: Energy of the incident nucleon, which in this case is the mass of the nucleon at rest.
  - ◇ $E_{N'}$: Energy of the scattered nucleon.
  - ◇ $\vec{p'}$: Three-momentum of the scattered nucleon.
- $q = k - k'$: Four-momentum of the virtual photon.
  - ◇ $\nu = E_e - E_{e'}$: Energy of the virtual photon.
  - ◇ $\vec{q}$: Three-momentum of the virtual photon.
- θ_e: Polar angle of the scattered electron.
- j^μ: Four-component leptonic current.
- J^μ: Four-component hadronic current.

Since the electron beam energies used in this experiment are in the several-GeV range, we can apply the ultra-relativistic approximation: $E_e \gg M_e$, where M_e is the rest mass of the electron. Under this approximation, the electron's energy and momentum magnitudes are approximately equal, i.e., $|\vec{k}| = E_e$, $|\vec{k'}| = E_{e'}$ and the four-momentum squared of the electron vanishes: $k^2 = k'^2 = 0$.

The conservation of four-momentum in elastic electron-nucleon scattering gives

$$k + p = k' + p' \,. \tag{1.1}$$

We define the four-momentum transfer q as

$$q = k - k' \,, \tag{1.2}$$

which implies

$$p' = p + q \,. \tag{1.3}$$

The squared four-momentum transfer is

$$q^2 = (k - k')^2 = k^2 + k'^2 - 2k \cdot k'$$

or

$$q^2 = -2k \cdot k' \,, \tag{1.4}$$

where we used the fact that $k^2 = k'^2 = 0$ for massless electrons.

The scalar product of the initial and final electron four-momenta is

$$\begin{aligned} k \cdot k' &= E_e E_{e'} - |\vec{k}||\vec{k'}| \cos\theta_e \\ &= E_e E_{e'}(1 - \cos\theta_e) \,. \end{aligned}$$

Substituting Eq. (1.5) into Eq. (1.4), we obtain

$$Q^2 \equiv -q^2 = 2E_e E_{e'}(1 - \cos\theta_e) \,. \tag{1.5}$$

Using the half-angle trigonometric identity, we rewrite this as

$$Q^2 = 4E_e E_{e'} \sin^2\left(\frac{\theta_e}{2}\right) . \tag{1.6}$$

This expression is particularly useful, as it relates the Lorentz-invariant squared momentum transfer Q^2 directly to measurable lab-frame quantities: the incident and scattered electron energies and the scattering angle θ_e.

We now consider the invariant mass W^2 of the final hadronic state. First, note the identity

$$p \cdot q = M_N \nu - \vec{p} \cdot \vec{q} . \tag{1.7}$$

In the lab frame, where the initial nucleon is at rest, $\vec{p} = \vec{0}$, so the dot product simplifies to

$$p \cdot q = M_N \nu . \tag{1.8}$$

The invariant mass of the final hadronic system is defined as

$$\begin{aligned} W^2 &= p'^2 = (p+q)^2 \\ W^2 &= p^2 + q^2 + 2p \cdot q \\ W^2 &= M_N^2 - Q^2 + 2M_N \nu , \end{aligned}$$

where we used $p^2 = M_N^2$, $q^2 = -Q^2$, and Eq. (1.8).

Under the elastic scattering assumption, the final hadronic state is solely the recoil nucleon. Therefore, the invariant mass is $W^2 = p'^2 = M_N^2$.

Substituting into Eq. (1.9), we have

$$\begin{aligned} &M_N^2 = M_N^2 - Q^2 + 2M_N \nu \\ &\Rightarrow \nu = \frac{Q^2}{2M_N} . \end{aligned}$$

This is the expected result for elastic scattering: the energy transfer ν is directly determined by the invariant momentum transfer Q^2 and the nucleon mass.

The scattering amplitude of this process can be expressed in terms of the leptonic current j^μ and the hadronic current J^μ [11], as in the following.

The total scattering amplitude is given by

$$i\mathcal{M} = \frac{-i}{q_\mu^2} j_\mu J^\mu \,. \tag{1.9}$$

The leptonic current is

$$j_\mu = ieg_{\mu\nu}\vec{u}(k')\gamma^\nu u(k) \,. \tag{1.10}$$

The hadronic current, which contains the information about the nucleon structure, is

$$J^\mu = -ie\vec{v}(p')\Gamma^\mu(p', p)v(p) \,. \tag{1.11}$$

Γ^μ encapsulates the electromagnetic structure of the nucleon. The most general form of the hadronic current that includes structure and satisfies relativistic invariance and current conservation is

$$\Gamma^\mu = \left[\gamma^\mu F_1(Q^2) + \frac{i\sigma^{\mu\nu}q_\nu}{2M_N}\kappa_j F_2(Q^2)\right] \,. \tag{1.12}$$

Here, M_N is the nucleon mass, κ_j is the anomalous magnetic moment with $j = p, n$, $\sigma^{\mu\nu} = \frac{i}{2}[\gamma^\mu, \gamma^\nu]$, and $F_1(Q^2)$ and $F_2(Q^2)$ are the Dirac and Pauli form factors, respectively.

Using this expression for the scattering amplitude $i\mathcal{M}$, we can calculate the cross section following a method similar to the derivation of the lepton-lepton scattering cross section, such as for $e^-\mu^- \to e^-\mu^-$ scattering in the lab frame.

The differential cross section is then given by

$$\frac{d\sigma}{d\Omega_e} = \left(\frac{d\sigma}{d\Omega_e}\right)_{\text{Mott}} \frac{E_{e'}}{E_e} \left[F_1^2(Q^2) + \tau\left(F_2^2(Q^2) + 2\left[F_1(Q^2) + F_2(Q^2)\right]^2 \tan^2\frac{\theta_e}{2}\right)\right] . \tag{1.13}$$

Here, τ is defined as

$$\tau = \frac{Q^2}{4M_N^2} . \tag{1.14}$$

The Mott cross section, which describes the cross section for purely leptonic scattering that considers the nucleon to be a point-like, structureless particle with relativistic effects included is defined as

$$\left(\frac{d\sigma}{d\Omega}\right)_{\text{Mott}} = \frac{\alpha^2 \cos^2\frac{\theta_e}{2}}{4E_e^2 \sin^4\frac{\theta_e}{2}} , \tag{1.15}$$

where $\alpha = \frac{e^2}{2\epsilon_0 hc} \approx \frac{1}{137}$ is the fine structure constant, and θ_e is the scattering angle of the electron in the lab frame. It is important to note that the Mott cross section relies on the assumption of elastic scattering, as the nucleon is being treated as a structureless particle [6].

1.5 Electromagnetic Form Factors

It is useful to define an additional set of form factors, G_E and G_M, known as the Sachs electric and magnetic form factors [12]. These are linear combinations of the Dirac and Pauli form factors, F_1 and F_2, and are given by

$$\begin{aligned} G_E^{(p,n)} &= F_1^{(p,n)} - \tau F_2^{(p,n)} \\ G_M^{(p,n)} &= F_1^{(p,n)} + F_2^{(p,n)} . \end{aligned} \tag{1.16}$$

Here, the superscripts (p, n) denote the proton and neutron, respectively.

Using these definitions, the differential cross section for elastic electron-nucleon scattering from Eq. (1.13) can be rewritten in terms of the Sachs form factors as

$$\frac{d\sigma}{d\Omega} = \left(\frac{d\sigma}{d\Omega}\right)_{\text{Mott}} \frac{E_{e'}}{E_e} \frac{1}{1+\tau} \left[(G_E)^2 + \frac{\tau}{\varepsilon}(G_M)^2\right] . \tag{1.17}$$

The virtual photon polarization parameter, ε, is defined as

$$\varepsilon = \left[1 + 2(1+\tau)\tan^2\frac{\theta_e}{2}\right]^{-1} . \tag{1.18}$$

1.6 Quasi-Elastic Scattering

The four-momentum transfer squared, Q^2, characterizes the resolution of electron scattering as a probe ($\lambda \sim \frac{h}{Q}$)—the larger the Q^2, the shorter the distance scale resolved by the virtual photon. The virtual photon is the mediator of the electromagnetic interaction between the incoming electron and the target particle. We can think of Q^2 as a measure of how "hard" or "deep" the scattering is. Higher Q^2 values probe deeper into the structure of the nucleon.

The invariant mass squared, W^2, characterizes the total energy available to the final hadronic system after the scattering interaction. W^2 depends on the energy transferred to the virtual photon, ν, and the four-momentum of virtual photon, Q^2.

In physical terms, W is the mass of the final system produced by the interaction, regardless of reference frame (i.e. invariant). Different ranges of W correspond to different types of scattering processes: elastic, quasi-elastic, and inelastic. These are illustrated in Fig. 1.4 for deuterium.

Elastic scattering occurs when the incident electron interacts with the deuteron as a whole, and the nucleus remains intact after the interaction. In this case, there is no internal excitation or breakup of the nucleus, and the final state contains the same particles as the initial state. This process is characterized by the invariant mass W of the final hadronic system being equal to the rest mass of the deuteron. Elastic scattering provides information about the electromagnetic form factors of the deuteron, which describe its charge and

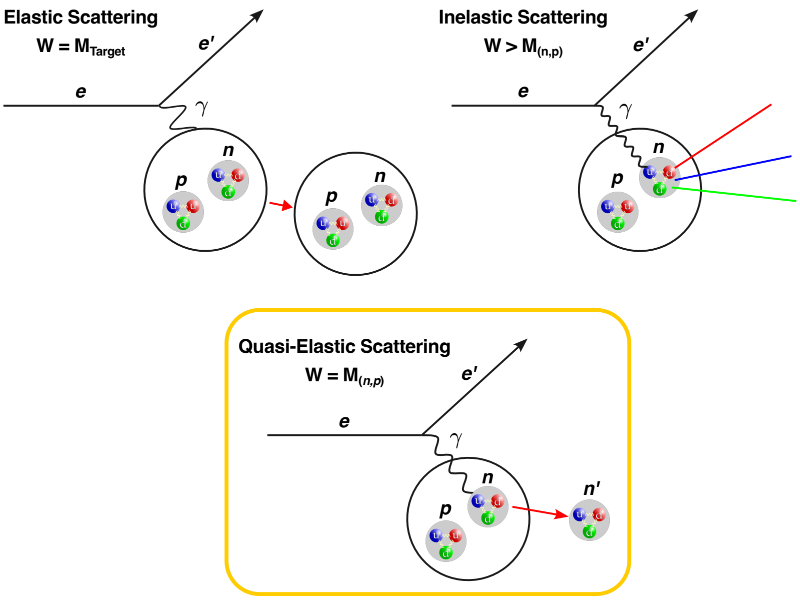

Figure 1.4: Cartoon of elastic, quasi-elastic, and inelastic scattering on deuterium. For elastic scattering, the invariant mass, W, equals the mass of the whole nucleus, and the nucleus stays intact. For quasi-elastic scattering, W equals the mass of an individual nucleon, and the individual nucleon stays intact. For inelastic scattering, W is greater than the mass of an individual nucleon, the nucleon either breaks apart or excites.

current distributions as a composite nuclear system, but it does not reveal much about the internal structure of the individual nucleons.

Quasi-elastic scattering occurs when the electron scatters from an individual nucleon (proton or neutron) inside the deuteron, transferring enough energy to knock it out of the nucleus, but without breaking the nucleon itself. The final state includes the scattered electron and the ejected, intact nucleon. This process typically corresponds to an invariant mass W equal to the nucleon mass. Quasi-elastic scattering is especially useful for probing the momentum distributions of nucleons inside the nucleus, and for studying their electromagnetic properties in the nuclear medium.

Inelastic scattering involves interactions where the energy transferred by the electron is sufficient to excite or break apart the nucleon or nucleus. This results in the production of new particles, such as pions, and/or the excitation of internal degrees of freedom. In this case, the invariant mass W of the final state is greater than the nucleon mass. Inelastic scattering can proceed through nucleon resonance excitation (e.g., N^*, Δ) where the nucleus may remain intact but be left in an excited state, or deep inelastic scattering (DIS), where the electron interacts with the constituent quarks inside a nucleon and the nucleon is broken apart.

To determine the electromagnetic form factors written in Eq. (1.17), we require quasi-elastic scattering from deuterium.

Figure 1.5 shows the relative cross section for scattering from a nucleus as a function of four-momentum transfer squared, Q^2, and the virtual photon energy, ν. The cross section is related to the probability of the interaction occurring.

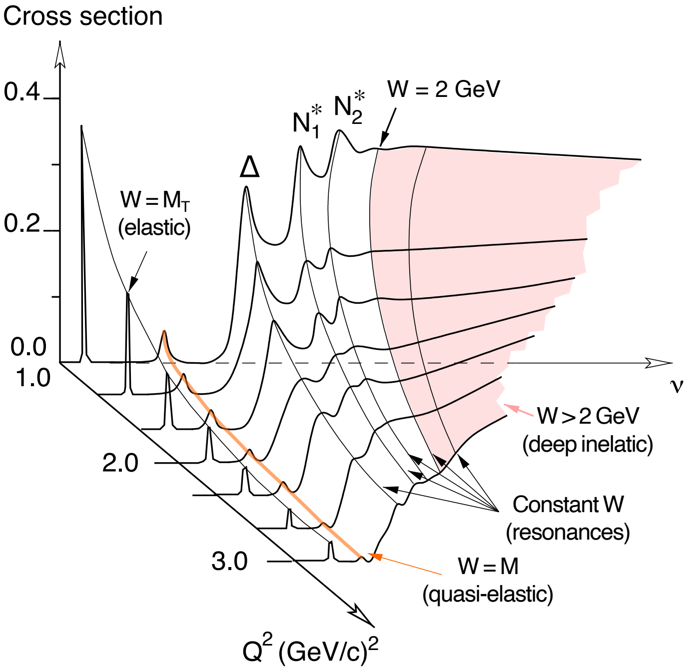

Figure 1.5: Cartoon of the relative cross sections for elastic, quasi-elastic, and inelastic scattering from a nucleus as a function of four-momentum transfer, Q^2, and virtual photon energy, ν. Figure adapted from X. Zheng, with additional annotations [13].

As we can see in illustrated in Fig. 1.5, the cross section for quasi-elastic scattering is smaller than the elastic scattering cross section, and much smaller than the cross sections for various resonances and processes that make up the inelastic regime. This trend continues as Q^2 increases. Since the probability for the quasi-elastic interaction is relatively low compared to inelastic processes, a large number of events must be recorded to collect sufficient quasi-elastic statistics. As Q^2 increases and we probe deeper into the nucleons, even more events need to be taken, and more inelastic events must be carefully rejected to isolate quasi-elastic scattering. Therefore, for this experiment, eliminating inelastic background and accurately identifying quasi-elastic events are crucial.

1.7 Significance of the Form Factors

The Sachs form factors are dependent both on the choice of reference frame as well as the Q^2. To best conceptualize a physical interpretation of the form factors, we can choose the reference frame and Q^2. In the Breit frame, also called the infinite momentum frame or brick wall frame, the final momentum of the nucleon is equal to negative the initial momentum of the nucleon. We have

$$\vec{p} = -\vec{p'} \tag{1.19}$$

and

$$Q^2 = |\vec{q}|^2 = q^2 \,. \tag{1.20}$$

We can then define the Breit frame charge density distribution as

$$4\pi r^2 \rho^{p,n}_{\text{Breit}}(r) = \frac{2}{\pi} \int_0^\infty dq \, qr \sin qr \, G_E^{p,n}(Q^2) \Big|_{\text{Breit}} \,, \tag{1.21}$$

where $\rho(r)$ is the charge distribution inside the nucleon. An analogous expression for the magnetic distribution can be made with G_M in terms of the magnetization instead of the charge density distribution [14].

As the resolution of our probe decreases and we "zoom out" by taking the limit ($Q^2 \to 0$), G_E and G_M reduce to the static properties of the nucleon—the electric charge and magnetic moment. We obtain

$$\text{Proton:} \quad G_E^p(0) = 1, \quad G_M^p(0) = \mu_p \tag{1.22}$$

$$\text{Neutron:} \quad G_E^n(0) = 0, \quad G_M^n(0) = \mu_n \,. \tag{1.23}$$

1.7.1 Proton Radius

The approximate radius of the proton can be extracted in the low-Q^2 limit using Eq. (1.21). For a spherically symmetric charge density $\rho(\vec{r})$, we can expand G_E around small $\vec{q}$ as

$$\begin{aligned}
G_E &= \int \rho(\vec{x}) \left(1 + i\vec{q}\cdot\vec{x} - \frac{(\vec{q}\cdot\vec{x})^2}{2} + \mathcal{O}(\vec{q}^{\,3})\right) d^3x && (1.24)\\
&= \int_0^\infty \rho(r) r^2 dr \int_0^\pi \sin\theta d\theta \left(1 + i|\vec{q}|r\cos\theta - \frac{1}{2}\vec{q}^{\,2} r^2 \cos^2\theta + \mathcal{O}(\vec{q}^{\,3})\right) && (1.25)\\
&= 1 - \frac{1}{6}\vec{q}^{\,2} \int |\vec{x}|^2 \rho(|\vec{x}|) d^3x + \mathcal{O}(\vec{q}^{\,3}) && (1.26)\\
&= 1 - \frac{1}{6}\vec{q}^{\,2} \left\langle r^2 \right\rangle + \mathcal{O}(\vec{q}^{\,3})\,. && (1.27)
\end{aligned}$$

Differentiating the last term with respect to q^2 and then taking the limit $q \to 0$ gives

$$\left\langle r^2 \right\rangle = -6 \left. \frac{dG_E}{d\vec{q}^{\,2}} \right|_{\vec{q}^{\,2}\to 0} . \tag{1.28}$$

This is the RMS charge radius of the nucleon (proton or neutron).

1.7.2 Quark Flavor Decomposition

Assuming isospin symmetry—that is, treating the up and down quarks in the proton and neutron as identical apart from their electric charge—allows us to relate the electromagnetic form factors of protons and neutrons to the underlying up- and down-quark contributions [15]. This is written as

$$F^u_{(1,2)} = 2F^p_{(1,2)} + F^n_{(1,2)} \tag{1.29}$$

$$F^d_{(1,2)} = 2F^n_{(1,2)} + F^p_{(1,2)} \,. \tag{1.30}$$

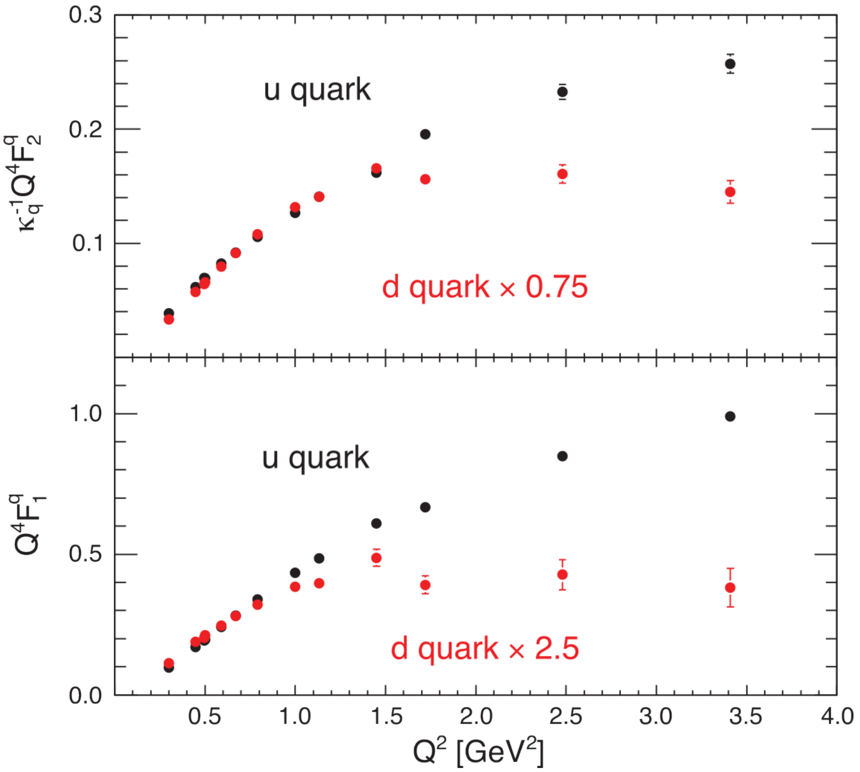

Figure 1.6: Quark flavor decomposition of the nucleon [15].

Constraining ${G_M}^{(p,n)}$ and ${G_E}^{(p,n)}$ constrains $F_1^{(p,n)}$ and $F_2^{(p,n)}$, which in turn constrains $F^u_{(1,2)}$ and $F^d_{(1,2)}$. Figure 1.6 shows the flavor composition for current world data up to $Q^2 = 3.5$ GeV^2. The standard QCD quark-parton model prediction is that the form factors go as Q^4. As form factor experiments produce results at higher Q^2, trends in the flavor decomposition could be resolved. After the SBS experiments are complete, we will be able to extend this decomposition up to $Q^2 = 12$ (GeV)^2. Determining the experimental behavior of the u-quark and d-quark form factors at higher precision and larger Q^2 will help distinguish between various theoretical models [16]. In the context of various models, resolving this behavior may shed light on the importance of diquark correlations and diquark degrees of freedom [17] [18].

1.8 Form Factor World Data

Many experiments have been conducted to measure the electromagnetic form factors. Figure 1.7 shows the current status of the world data with fits, compiled and summarized, along with several theoretical models [19]. The **projections** of the uncertainties for the SBS experiments have been plotted along with the most recently published fit to world data done by Ye *et al.* [20]. This fit will be referred to as the "Ye fit" going forward. The parameters for the Ye fit can be found in Appx. A. These projections do not represent final experimental results.

When plotting the magnetic form factors of the proton and neutron, it is common to normalize the measured form factor by the dipole form factor G_D multiplied by the nucleon magnetic moment μ. This normalization provides a useful reference and allows one to qualitatively assess whether the magnetic distribution of the nucleon resembles a dipole at a given Q^2. The dipole form factor, an empirical parametrization of the data, is defined as

$$G_D(Q^2) = \left(1 + \frac{Q^2\ [\mathrm{GeV}^2]}{0.71\ [\mathrm{GeV}^2]}\right)^{-2}, \tag{1.31}$$

where Q^2 is expressed in units of GeV^2.

Over the course of the SBS program, we conduct experiments to measure G_M^n, G_E^n, and G_E^p at high Q^2. Together, these experiments are expected to increase the precision of the world data fit for the higher Q^2 values. This should help distinguish between different theoretical models for the internal structure of protons and neutrons, and help inform parton distribution functions (PDFs).

Figure 1.8 is an edit of the G_M^n world data graph in Fig. 1.7 to aid in discussion. At low Q^2, the neutron magnetic form factor looks like that of a dipole. Qualitatively, as

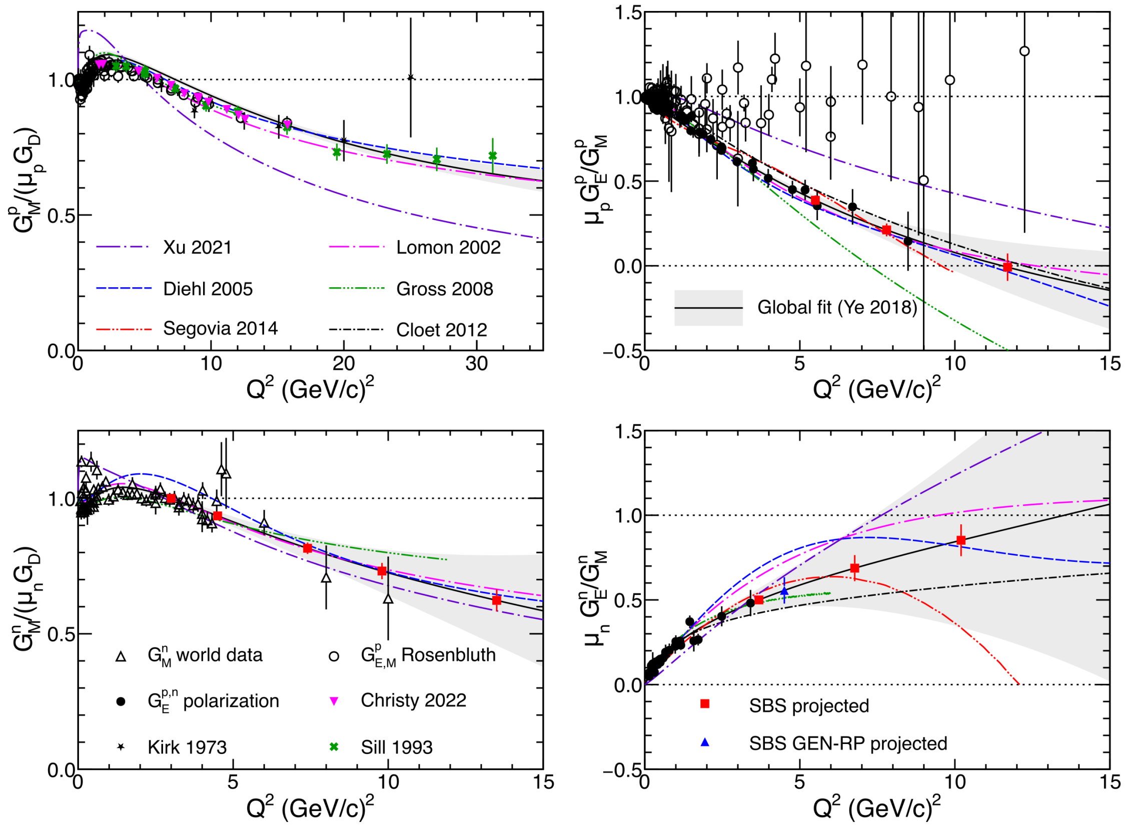

Figure 1.7: SBS **projected** uncertainties plotted over world data and various theoretical predictions as a function of Q^2. (Upper left): The proton magnetic form factor, $G_M^p/(\mu_p G_D)$. The legend for the various theoretical fits is displayed on this subfigure. (Lower left): The neutron magnetic form factor $G_M^n/(\mu_n G_D)$. The legend for the various data points is displayed on this subfigure. (Upper right): The ratio of the proton electric form factor to the proton magnetic form factor $\mu_p G_E^p/G_M^p$. The legend for the Ye Global Fit is found on this subfigure. (Lower Right): The ratio of the neutron electric form factor over the neutron magnetic form factor $\mu_n G_E^n/G_M^n$. The legend for the SBS projected points is found in this subfigure. The gray band is the Ye fit to world data [20]. The red points are the projected SBS uncertainties and **not** experimental results [19]. The green line is the covariant spectator model of Gross *et al.* (2008) [21]. The purple is basis light-front quantization (BLFQ) calculations of (Xu 2021) [22]. The blue line is the GPD-based model of Diehl *et al.* (2005) [23]. The magenta line is the vector meson dominance (VMD) model of Lomon *et al.* (2002) [24]. The red line is the Dyson-Schwinger equations (DSE) based calculations of Segovia *et al.* (2014) [25]. The black line is the quark-diquark model of Cloet *et al.* (2012) [26].

we increase the strength of our probe, Q^2, and look deeper into the neutron, it no longer behaves like that of a dipole. This suggests a more complex distribution than that of a simple dipole for the magnetic distribution of the quarks and gluons as we continue to "zoom in" to the neutron. We can see qualitatively that the GMn experiment should contribute to an increase in the confidence of a new fit to world data at higher Q^2 and help distinguish between various theoretical models at high Q^2.

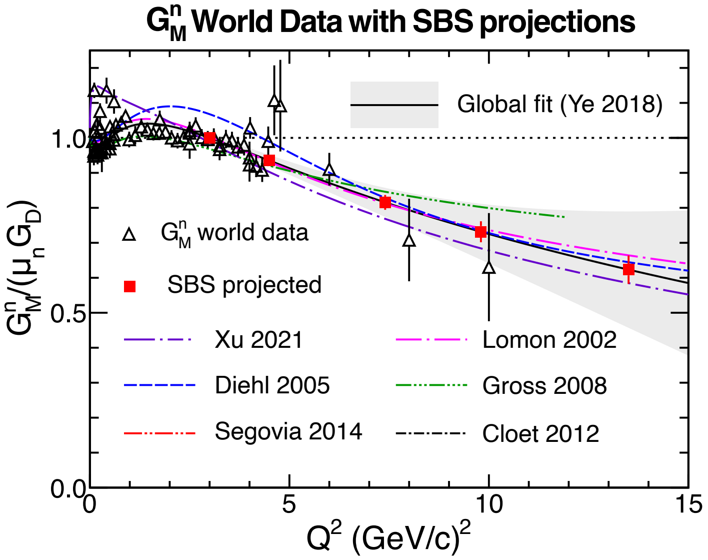

Figure 1.8: $G_M^n/(\mu_n G_D)$ world data with SBS projections. The gray band is the Ye fit to world data [20]. The red points are the SBS GMn experiment's **projected** uncertainties which are drawn on the Ye fit. The red points are **not** experimental results. See the caption of Fig. 1.7 for theoretical model line descriptions. Edited from [19].

The Ye fit to the nucleon electromagnetic form factors, shown as the gray band in Fig. 1.7 and Fig. 1.8, was constructed from world electron scattering data. It incorporated two-photon exchange corrections, constraints on low-Q^2 and high-Q^2 behavior and additional uncertainties. More details on the parameters of this global fit and the fit's error band can be found in Appx. A.

The electromagnetic form factors produced by the various theoretical models are plotted along with the world data in Fig. 1.7 and Fig. 1.8.

If the analysis of our GMn experiment yields values of $G_M^n/(\mu_n G_D)$ near the upper edge of the Ye uncertainty band at high Q^2, this may indicate that the covariant spectator model captures key aspects of the nucleon structure. In this framework, each constituent quark is endowed with its own electromagnetic form factor, and the resulting nucleon is spherically symmetric in both electric charge density and matter distribution. Conversely, if the extracted values fall near the lower edge of the Ye band, the results may favor the BLFQ approach, potentially lending support to the light-front holographic confinement mechanism employed in that model.

Agreement with the central values of the Ye fit could be consistent with either the VMD-based model or the GPD-based model. In the case of the former, this would suggest a significant hadronic component in the photon propagator, consistent with the picture of the photon as a quantum superposition of a point-like photon and intermediate vector meson states. In the case of the latter, it would support a GPD-based description in which the interplay between the longitudinal momentum and transverse spatial structure of valence quarks—reconstructed from fits to the Dirac and Pauli form factors—captures key features of nucleon structure in the intermediate-Q^2 regime.

1.9 This Work

Experiment **E12-09-019**, also know as the **GMn** experiment[2], took place in Hall A at Jefferson Lab from October 2021–February 2022. GMn measures semi-inclusive, quasi-elastic scattering from deuterium [27] [28]. We will discuss the experimental setup in significant detail in Ch. 2, with an overview in Sec. 2.3. The experiment was run on the Super BigBite Spectrometer (SBS), consisting of the electron arm (beam left) and the hadron arm (beam right).

Table 1.1 shows the kinematic points taken in the GMn experiment[3]. The kinematic points SBS-8 and SBS-9 were chosen so that they have the same Q^2 value with different

---

[2] The experiment's name is also sometimes written as G_M^n in other works. To avoid confusion, I will refer to the E12-09-019 experiment as GMn, and the magnetic form factor itself as G_M^n.

[3] The kinematic points are sometimes also written as sbs4, SBS4, or sbs-4.

values of ε. This is so that a Rosenbluth slope may be obtained using L/T separation, where the longitudinal and transverse components of the cross section are isolated [29].

Table 1.1: The kinematic configurations of the GMn experiment. The nTPE experiment consists of SBS-8 and SBS-9. This work evaluates G_M^n for SBS-4, SBS-8, and SBS-9.

SBS Config.	Q^2 (GeV)^2	ε	E_e (GeV)	θ_e°	θ_n°	$E_{e'}$ (GeV)	p_N (GeV)
SBS-4	3.0	0.72	3.73	36.00	31.9	2.12	2.35
SBS-8	4.5	0.80	5.98	26.50	29.9	3.58	3.20
SBS-9	4.5	0.51	4.03	49.00	22.5	1.63	3.20
SBS-14	7.4	0.47	5.97	46.50	17.3	2.00	4.83
SBS-7	9.9	0.50	7.91	40.00	16.1	2.66	6.13
SBS-11	13.6	0.41	9.86	42.00	13.3	2.67	8.11

The SBS magnet on the hadron arm, which is used to separate protons and neutrons, was ran at multiple current strengths (and therefore magnetic field strengths) during several of the Q^2 points. These subsets of runs are categorized by what percent of the maximum current the SBS magnet was run at. The higher the current, the stronger the magnetic field, and the greater the deflection of protons through that field will be. Table 1.2 shows the different magnetic field settings used for each kinematic. Highlighted in yellow are the "production" kinematics—data sets that will be analyzed for the final form factor extractions. Using multiple field settings is extremely useful for calibrations of the hadron calorimeter (HCal). The multiple field settings allow proton events to cover more surface area of the detector, allowing us to calculate quantities such as the proton detection efficiency across as much of the detector as possible. The multiple field settings also serve as cross-checks on the form factors values at the same Q^2. If the value for G_M^n extracted on one field setting is drastically different than other (keeping all other variables including Q^2 the same), there may be a systematic error we are not accounting for. In the GMn experiment, most kinematics have one "production" setting, where most of the beam time and data collection was focused on, with one or two other field settings used for calibrations.

Although this thesis does not calculate the Rosenbluth slope, I have extracted G_M^n

Table 1.2: SBS magnet field settings. Data were taken at various magnetic field settings. Highlighted in yellow are the production kinematics that are used for final physics extractions.

SBS Config.	Data taken at SBS magnetic field setting:					
SBS-4	SBS-4 0%	SBS-4 30%	SBS-4 50%			
SBS-8	SBS-8 0%		SBS-8 50%	SBS-8 70%		SBS-8 100%
SBS-9				SBS-9 70%		
SBS-14	SBS-14 0%			SBS-14 70%		
SBS-7					SBS-7 85%	
SBS-11	SBS-11 0%					SBS-11 100%

values for SBS-8 50%, 70%, and 100% magnetic field settings, and for SBS-9 70%. The GRINCH Cherenkov detector was fully operational only during these two kinematic settings. To make the most efficient use of the data, I chose to extract G_M^n and analyze GRINCH performance using the same datasets (see Sec. 3.2 for details). SBS-4, the lowest Q^2 setting of 3.0 GeV^2, was designated by the collaboration as a benchmark for software development and physics validation due to low expected contamination from inelastic background, and Q^2 overlap with many previous experiments. Several previous experiments have measured G_M^n at this Q^2 (see Sec. 1.8), providing useful points of comparison. Additionally, background contamination from inelastic events is relatively low at SBS-4, making it a strong candidate for baseline studies.

1.10 Ratio Method: Durand's Method

The relevant literature often defines a **reduced cross section**, σ_r, as

$$\sigma_r = \frac{\varepsilon(1+\tau)}{\tau}\frac{E'}{E}\left(\frac{d\sigma}{d\Omega}\right) \Big/ \left(\frac{d\sigma}{d\Omega}\right)_{\text{Mott}} = G_M^2 + \frac{\varepsilon}{\tau}G_E^2 \,. \tag{1.32}$$

At a given Q^2, G_M and G_E can be extracted from a linear fit to the reduced cross section as a function of ε. This is done by varying the beam energy and θ_e (changing ε while keeping Q^2 constant) for two or more points. G_M is the intercept of this fit, and G_E is proportional to the slope. This is called the Rosenbluth separation technique [6].

A measurement of a differential cross section can be an experimental challenge and requires a precise understanding of experimental factors such as solid angles and particle flux. This is particularly challenging with measuring neutron cross sections, as there does not exist a free neutron target.

Writing the *ratio* of reduced cross sections for neutrons and protons, R, we have

$$R = \frac{\sigma_{r,n}}{\sigma_{r,p}} = \frac{\left(G_M^n\right)^2 + \frac{\epsilon_n}{\tau_n}\left(G_E^n\right)^2}{\left(G_M^p\right)^2 + \frac{\epsilon_p}{\tau_p}\left(G_E^p\right)^2}\,. \tag{1.33}$$

If the cross sections for neutrons and protons are *simultaneously* measured on the same apparatus from a target that contains protons and neutrons, such as deuterium, many of the corrections such as beam flux and solid angle cancel. This is the called the Ratio Method or Durand's Technique.

At a high level, this expression then reduces down to a measurement of the yields of the protons and neutrons. Corrections from nuclear and radiative effects must also be put into consideration, as the protons and neutrons are bound together within the target nucleus. Radiative corrections between protons and neutrons will be almost the same and mostly cancel out in the ratio. Two-photon effects are expected to be small and similar between protons and neutrons and also mostly cancel out in the ratio. This allows us to limit ourselves to the first-order Born approximation for these preliminary results. Collaborators are working on incorporating two-photon effects for publication results. For this work, we thus have

$$\frac{\text{Yield}_n}{\text{Yield}_p} \approx \begin{pmatrix}\text{nuclear}\\ \text{corrections}\end{pmatrix}_{p,n} \begin{pmatrix}\text{radiative}\\ \text{corrections}\end{pmatrix}_{p,n} \frac{\left(G_M^n\right)^2 + \frac{\epsilon_n}{\tau_n}\left(G_E^n\right)^2}{\left(G_M^p\right)^2 + \frac{\epsilon_p}{\tau_p}\left(G_E^p\right)^2}\,. \tag{1.34}$$

We estimate G_E^n, G_M^p, and G_E^p by applying values that are functions of Q^2 from the most current fits to global data. We can then solve for G_M^n. Equation (1.34) is an over-simplification of the extraction method of G_M^n in this experiment's analysis. We will be utilizing simulations to account for the nuclear and radiative corrections and not directly counting yields. This method will be discussed in detail in Sec. 4.7.

Chapter 2

Experimental Setup

2.1 CEBAF Electron Accelerator

The Continuous Electron Accelerator Beam Facility (CEBAF) is located at Thomas Jefferson National Accelerator Facility (JLab) in Newport News, Virginia. CEBAF has delivered high-duty-cycle electron beam since beginning operations in 1995. Today, CEBAF includes four experimental halls—Hall A, Hall B, Hall C, and Hall D—where expansive research in nuclear physics is conducted. CEBAF first delivered electron beam to a target in 1994, with an initial energy of up 4 GeV to the three original experimental halls—A, B, and C. Technological improvements increased the delivered beam energy, establishing a level up to 6 GeV beam beginning in 2000, therefore extending physics study into the quark structure of nucleons. This is referred to as "The 6 GeV era". From 2012 to 2017, JLab paused operations in CEBAF to undertake major upgrades: the addition of a new experimental hall (Hall D); upgrades to the existing halls; and many infrastructure upgrades that now enables CEBAF to deliver a maximum beam energy of 12 GeV [30]. This current age is recognized as the "12 GeV upgrade". The technology of CEBAF allows the delivery of simultaneous electron beams to the four halls. These beams consist of 2 ps bunches of electrons at a frequency of 499 MHz. The technology of CEBAF enables simultaneous beam delivery to all four halls, with each beam possessing distinct characteristics to meet the unique experimental requirements of each hall.

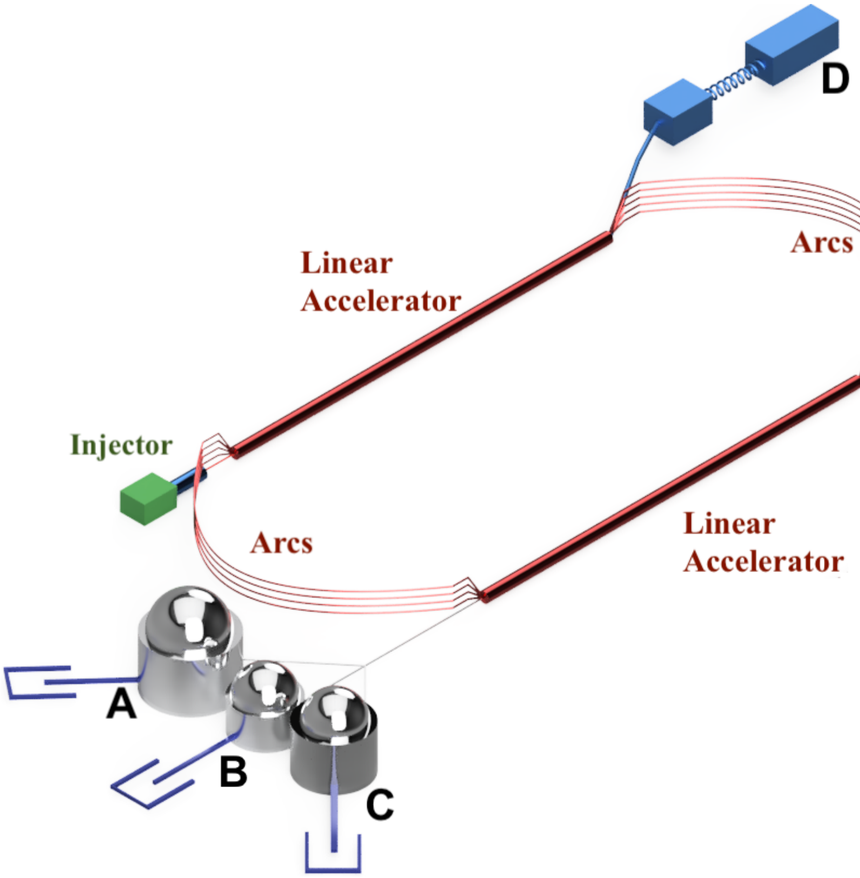

Figure 2.1: CEBAF Accelerator in the 12 GeV upgrade [31].

The complexity of CEBAF's operating process, components, and production of an effective, safe, deliverable electron beam, is extensively reviewed in various works. This work will highlight the main points of the apparatus. Figure 2.1 depicts the large-scale components of CEBAF after the 12 GeV upgrade. CEBAF employs the concept of a recirculating linear accelerator. Bunches of electrons are created at the injector at a frequency of 1497 MHz using lasers on a gallium arsenide (GaAs) photocathode under ultra-high vacuum [1] to create polarized or unpolarized electron beams. Four independent lasers with appropriate frequency and phases allow simultaneous running of all four halls with unique electron beams delivered to each of the four halls, creating the 499 MHz train of electrons. The

---

[1] 10^{-11} to 10^{-12} Torr.

bunches of electrons at the high frequency constitute a "continuous waveform" or "CW" beam. The beam enters the racetrack at the start of the North Linac. The beam gains energy as it passes through the 25 cryomodules, each consisting of 8 superconducting radio frequency cavities. The beam then drifts around the West Arc to the next linac. Quadruples and dipoles are used to focus and steer the beam around the arc. The beam then passes through the South Linac, gaining energy, and is then guided through the West Arc. The beam gains 1.1 GeV with every pass through one of the linacs. After a full "pass" through both linacs, the beam has gained 2.2 GeV. Recirculation of the beam around the racetrack enables beams to be delivered to the experimental halls at various energies. Five passes allows the electron beam delivered to Halls A, B, and C to be up to 11 GeV. One more half-pass through the North linac up to Hall D allows the full 12 GeV to be delivered [32].

2.2 Hall A

The GMn experiment was conducted using the SBS spectrometer located in Hall A at JLab. Hall A, one of four halls at Jefferson Lab, is the largest of the three main experimental halls. Hall A is designed for experiments requiring high-luminosity and high-current electron beam.

The two permanent spectrometer arms historically used in Hall A were decommissioned prior to the onset of the GMn experiment. Hall A utilization is now focused on user-driven, open-floor experiments. The Super BigBite Spectrometer (SBS) and the associated experiments are the first installation in this new chapter of Hall A. The GMn experiment, also written as G_M^n, was the first experiment conducted in the SBS program. GMn served as the commissioning experiment for the detectors. This work explores the GMn experiment, and in particular, the Cherenkov Detector and early physics analysis.

Figure 2.2 shows an aerial photograph of CEBAF labeled with its main components. Halls A, B, C and D, as well as the accelerator itself, are built underground for operational and safety reasons, including radiation shielding. Save for some electronics, monitoring devices, and an external gas system, the main components of the SBS experiments are located in Hall A, including the target, the electron arm, and the hadron arm. Details of each detector will be discussed in the following sections.

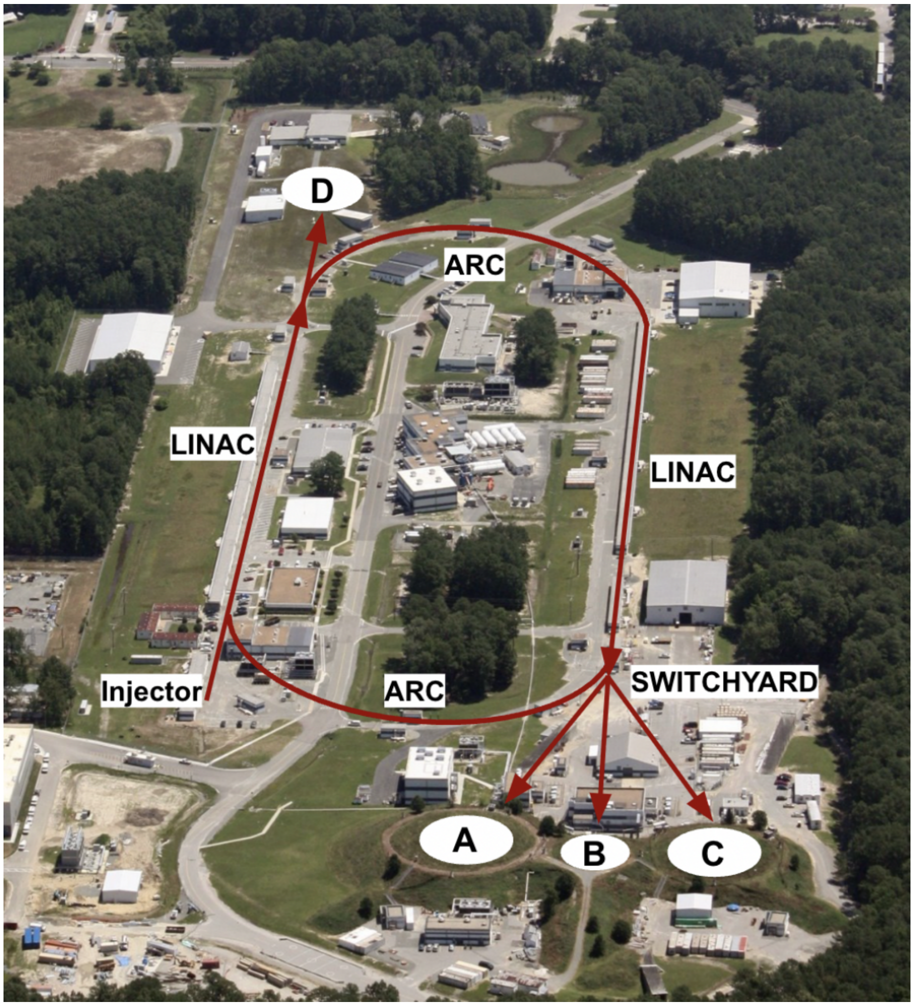

Figure 2.2: Aerial photo of the CEBAF accelerator, annotated to illustrate various main components of CEBAF. The exterior of Hall A can be seen as the leftmost of the main three halls. Photograph: JLab (2012)

2.3 Experimental Configuration

The GMn experiment operated in Hall A from October 2021 to February 2022. Aside from changing the angle of the electron and hadron arms for different measurement points, the layout of the experiment remained consistent.

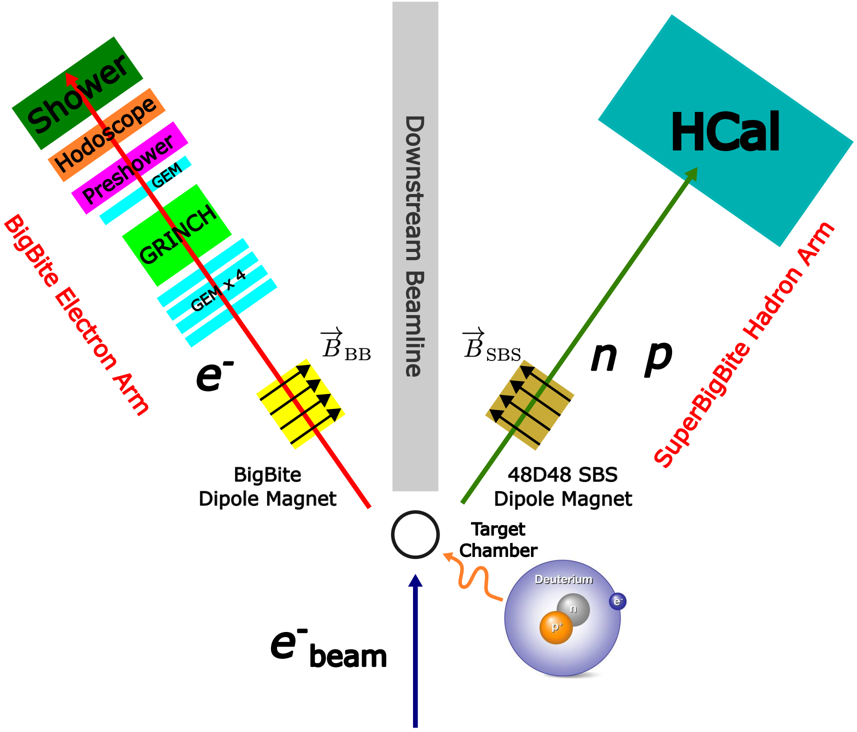

Figure 2.3: Simple block diagram of the Super BigBite Spectrometer. The electron beam is incident on the target inside the target chamber. The scattered electron is measured in the BigBite Electron Arm, also called the BigBite Spectrometer. The scattered proton or neutron is measured in the Super BigBite Hadron Arm, also called the Super BigBite Spectrometer. Deuterium illustration from energy.gov.

An overview of the experimental setup for the GMn experiment is shown in Fig. 2.3. The setup consists of four main components: the beamline, the target, the electron arm, and the hadron arm.

Each major component of the experiment has its own orthogonal, right-handed internal coordinate system. In general, the z-axis is aligned along the nominal trajectory of the detected particle, while the x-axis points vertically downward toward the ground, and the

y-axis completes the right-handed orthogonal system. This convention is illustrated in Fig. 2.4 and will be useful for understanding the GMn experimental layout.

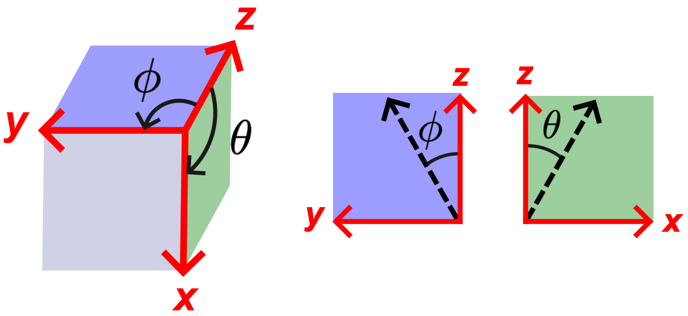

Figure 2.4: Illustration of the SBS right-handed coordinate system conventions. The z-axis follows the nominal particle trajectory (into the page), with x pointing downward and y completing the right-handed orthogonal system. The dispersive angle θ is measured in the xz-plane, and the non-dispersive angle ϕ in the yz-plane.

The dispersive angle, θ, is defined as the angle between the particle's trajectory and the z-x plane (often measured from the z-axis toward the x-axis). The non-dispersive angle, ϕ, is defined as the angle between the trajectory and the z-y plane (measured from the z-axis toward the y-axis).

The electron arm, referred to as the BigBite Spectrometer, consists of the BigBite Dipole Magnet and various detectors to measure the kinematics of the scattered electron.

The BigBite Magnet deflects negatively charged electrons upward into the detectors and deflects positively charged particles downwards. This deflection of positive particles reduces the number of interactions between the detectors and the positively charged particles produced by inelastic collisions. The hadron arm, referred to as the Super BigBite Spectrometer, consists of the SBS Dipole Magnet and the Hadron Calorimeter (HCal). The SBS Magnet bends protons upward while neutrons pass through undeflected, allowing discrimination between protons and neutrons.

The electron beam, which is created by the CEBAF accelerator, is delivered via the the beam pipe to the target. Electrons that do not interact with the target continue along the downstream beam pipe and to the beam dump. The targets used in this experiment consisted of cryogenically cooled liquid hydrogen and liquid deuterium.

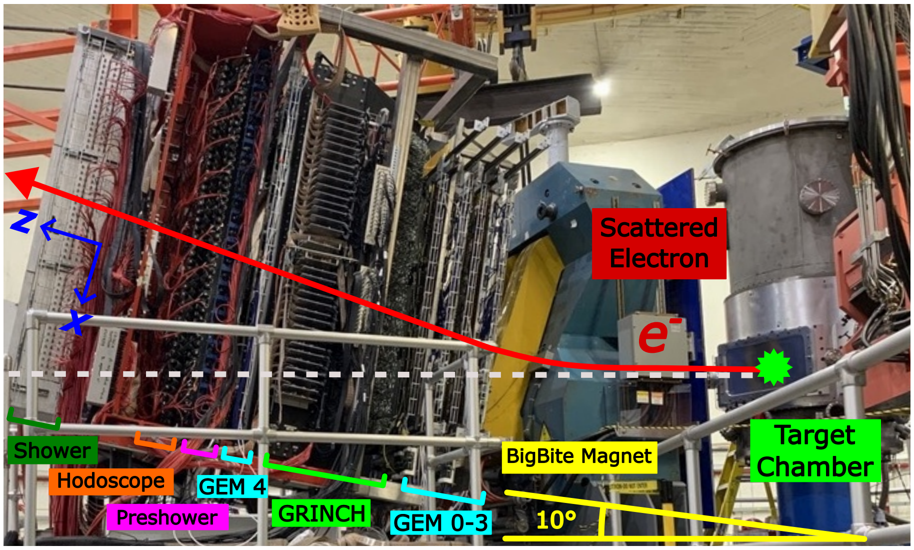

Figure 2.5: Side view of the electron arm. The electron beam arrives from offscreen to the right and is incident with the target in the target chamber. Scattered electrons are bent upward by the BigBite magnet and are measured by the various detectors. Photo credit: E. Z. Wertz.

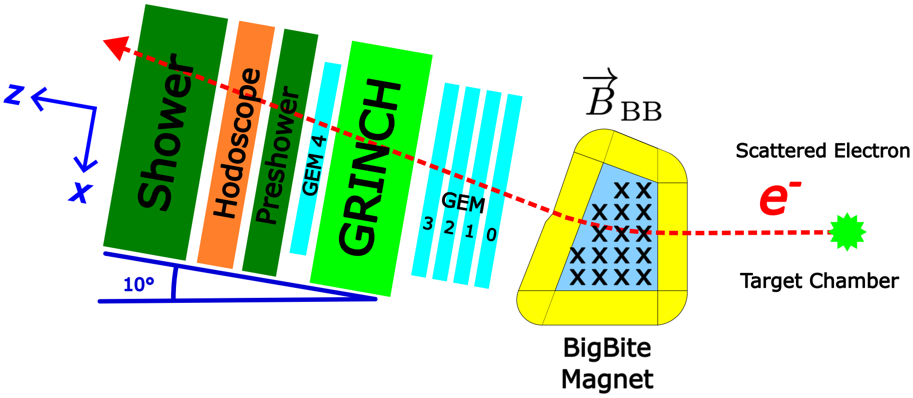

Figure 2.6: Schematic of the BigBite electron arm. This is a simplified block diagram of Fig. 2.5. Scattered electrons originating from the target are bent upward by the BigBite magnet and into the BigBite detector stack. Various detectors record energy deposition and path of the particle.

Figure 2.5 illustrates the configuration of the BigBite Spectrometer. The path of the electron beam and subsequent scattered electron is as follows: the electron beam enters from the right side and is incident on the target in the target chamber. The scattered electron is bent by the BigBite dipole magnet and first encounters four layers of Gas Electron Multiplier (GEM) trackers. These record the path of the charged particle to very high precision. The particle next encounters the GRINCH Heavy Gas Cherenkov Threshold detector. This Cherenkov detector assists with particle identification (PID) to eliminate the pion background. After passing through another GEM layer, the particle encounters the Preshower component of the BigBite Calorimeter (BBCal). The lead glass blocks of the Preshower are arranged perpendicular to the path of the particle. The electrons deposit some of their energy and continue on, while pions typically deposit very little energy, leaving a distinct energy signature in the lower energy range, allowing particle identification between electrons and pions. The particle then encounters the timing hodosope, consisting of an array of plastic scintillators with high timing resolution. The particle last encounters the Shower, consisting of thick lead glass blocks laid parallel to the particle track. The particle deposits its remaining energy and is stopped. The Preshower and the Shower together allow total energy measurement. The reconstruction of the path of the particle through the GEM trackers allow momentum reconstruction.

The Super BigBite Hadron arm consists of the SBS Dipole Magnet and the HCal. The SBS Magnet allows proton-neutron separation by bending the protons upward, while neutrons are unaffected by the magnetic field. HCal consists of alternating layers of iron absorber and scintillator, allowing timing measurement and energy sampling of the hadrons.

The targets for this experiment consisted of 15 cm liquid hydrogen and liquid deuterium. The hydrogen target acted as a proton source and was used for calibrations, while the deuterium target acted as a simultaneous proton and neutron target.

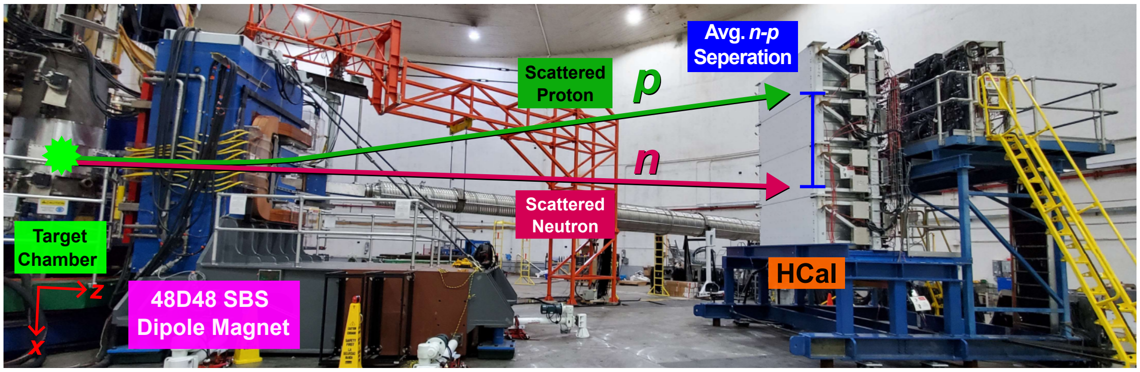

Figure 2.7: The Super BigBite hadron arm in Hall A. The electron beam arrives from off-camera left and interacts with the target. Scattered protons and neutrons pass through the SBS Magnet, where protons are bent upward and neutrons continue straight through to the face of HCal.

2.4 Targets

2.4.1 Cryogenic Targets

This experiment utilized 15 cm long cryogenic liquid hydrogen (H) and liquid deuterium (^{2}H or D) targets to study protons and neutrons. In the context of this experiment, we assigned acronyms “LH2” for the liquid hydrogen target and “LD2” for the liquid deuterium target. The GMn experiment studies the process of elastic scattering of an electron incident on a “free” neutron. The nucleus of a hydrogen atom consists of one proton, whereas deuterium, a stable isotope of hydrogen, consists of one proton and one neutron. Hydrogen provides an excellent target for the study the structure of a “free” proton as well as for the calibration of detectors. On the other hand, an unbound or “free” neutron is not stable and undergoes beta decay, $n \to p + e^- + \bar{\nu}_e$, within approximately 15 minutes [33]. This property makes free neutrons extremely challenging to study and not feasible for use in scattering experiments. Deuterium is often used as a proxy for a neutron target in a scattering experiment.

Nuclear corrections must be included in the final physics extractions to account for the neutron being bound with the proton in the nucleus by the strong nuclear force. Details of the application of nuclear corrections will be discussed in more depth in Sec. 4.6.2.

The existence of both protons and neutrons in the target requires us to have a way to experimentally separate electron–proton and electron–neutron scattering events. The SBS dipole magnet is used to spatially separate the scattered protons and neutrons from the deuterium target. Proton–neutron particle ID techniques will be discussed in much detail in upcoming sections, and particularly in Sec. 4.4. In this experiment, LH2 is primarily used as a proton target for detector calibrations, and LD2 is used as a neutron and proton target for production data and physics extraction.

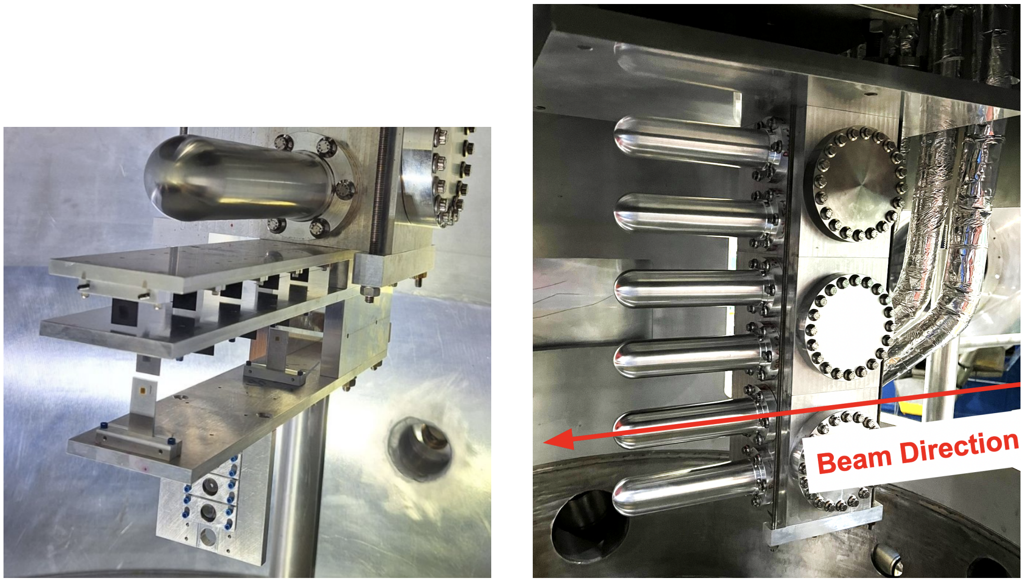

(a) (b)

Figure 2.8: The target ladder for GMn. **(a)** Various targets used for optics such as carbon foils and carbon holes. **(b)** 15 cm cryogenic targets with the direction of the beam. Each rung of the ladder contains a different target, which can be moved in and out of the beam [34].

2.4.2 Optics

In addition to the cryogenic targets, the target ladder houses various “optics” targets used for calibrations. The optics targets are used to calibrate particle transport through the tracking detectors consists of thin foils of carbon lined up along the beam path. Another optics target, referred to as the carbon hole target, is used to determine beam position and consists of a carbon foil with a hole drilled through. The foils and carbon holes can be seen in Fig. 2.8a. Calibrations utilizing these targets will be further discussed with context in Sec. 2.5.5: the BigBite dipole magnet, and Sec. 4.3: Momentum and Optics Calibrations.

2.5 Electron Arm

As already mentioned, the electron arm, also called the BigBite Spectrometer, consists of the BigBite dipole magnet and several particle detectors. The purpose of the electron arm is to identify and reconstruct to high precision electrons from quasi-elastic scattering events in the target to high precision. In this section, we will discuss the various components of the electron arm.

2.5.1 BigBite Calorimeter

The BigBite Calorimeter (BBCal) consists of two lead-glass calorimeters in the electron arm: the Shower (SH) and the Preshower (PS, Pre-Shower). In conjunction, they measure the total energy of the electron as well as generate the trigger signal for the data acquisition system (DAQ). Thus, careful calibration and analysis of data from BBCal are vital to the success of the GMn experiment.

An electron passing through a lead-glass block produces bremsstrahlung radiation as high energy photons (x-rays). Those photons produce an e^+ (positron) and e^- (electron) pair, which in turn produce bremsstrahlung radiation and make more e^+ e^- pairs, and this continues on, creating the shower. The electrons and positrons produced in the electromagnetic shower create Cherenkov light in the lead-glass blocks. Cherenkov light is produced when a charged particle travels faster than the speed of light in the medium. This light is in the optical and ultraviolet spectrum and is measured by a photomultiplier tube (PMT) attached to each block. The PMT converts photons into electric pulses that are recorded by the DAQ. These pulses can then be related back to the energy of the particle that created the shower.

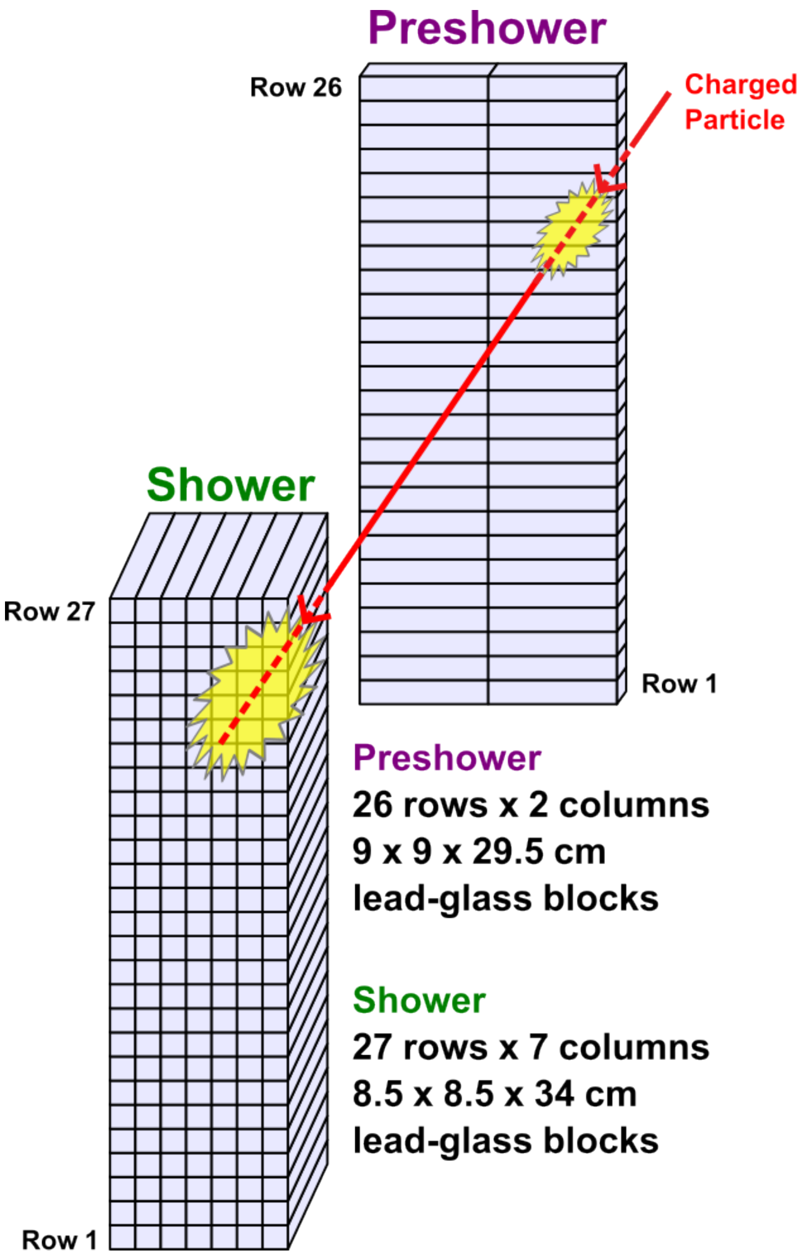

Figure 2.9: Diagram of the Preshower and Shower of BBCal. A charged particle travels through and deposits energy into the Preshower and Shower. The Preshower blocks are perpendicular to the path of the particle, while the Shower blocks are parallel.

The Preshower is located upstream from the Shower and is composed of 52 lead-glass blocks laid perpendicular to the path of the particle (Fig. 2.9). Electrons interact electromagnetically with the lead glass right away and create a shower almost immediately, depositing a large amount of energy in the Preshower. Pions ($\pi^{\pm}$), on the other hand, are minimally ionizing particles (MIP) at these energies and tend to only deposit a small amount of energy via ionization as they pass through the small width of the perpendicularly laid block.

Pions thus create a distinctive low-energy signal PS energy spectrum. Electrons have a broad energy spectrum and create a much wider signal at a higher energy in the PS. This allows particle identification (PID) between electrons and pions in the PS.

The Shower is located downstream of the Preshower and consists of 189 lead-glass blocks laid parallel to the path of the particle. Figure 2.10 depicts a number of shower blocks with PMTs glued on their ends being stacked in the BigBite frame. Due to the longer distance the particle travels through the block, it deposits its remaining energy and is stopped. The total energy of the particle is obtained by adding the energy of the Shower and the Preshower together.

The Shower and Preshower together form the "BBCal overlapping regions trigger" for the DAQ. The signals in each row in the Preshower and each row of the shower are summed. When the sum of the signals from two rows in the Shower plus the corresponding rows in the Preshower is above a threshold, a signal is sent to the DAQ to trigger the DAQ to record data for all the detectors for that event. The threshold was adjusted for each kinematic setting to keep the trigger rates low enough for the DAQ to handle [36].

Furthermore, BBCal is used to help constrain search parameters for tracking reconstruction in the GEM trackers. The vertical and horizontal cluster positions of the event in the Shower are used to constrain a physical search region in each GEM for track reconstruction. This constraint reduces the search area of the GEMs to 2–3% of the total GEM acceptance. This decreases the number of computations needed to find tracks by several orders of magnitude, greatly increasing track reconstruction efficiency [37].

Figure 2.10: Lead-glass blocks stacked in the Shower. PMTs are attached to the lead-glass blocks which are stacked in the Shower housing. [35].

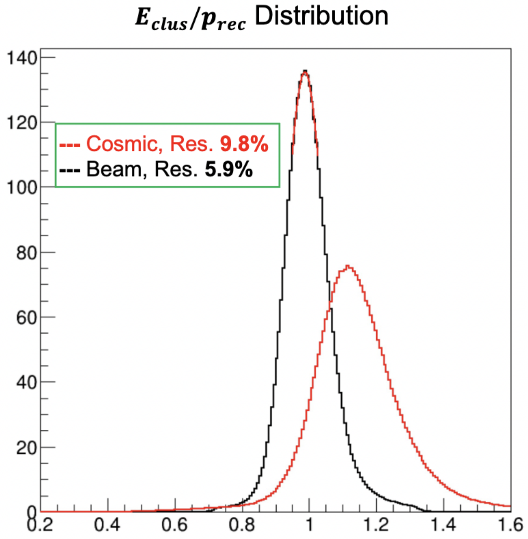

Figure 2.11: E'/p for BBCal with cosmic and beam calibrations [36]. The mass of cosmic muons is not negligible, and thus the E/p using muon calibrations is not centered around 1.

Data from both cosmic particles and ep scattering on hydrogen are used to calibrate BBCal for electrons. The ratio of the total energy of the particle to the particle's momentum is expected to be unity, i.e. $(E'/p) = 1$, due to the electron's small mass. Figure 2.11 shows the total energy (SH + PS) distribution with cosmic calibrations and hydrogen scattering calibrations. BBCal is able to achieve energy resolutions of up to 5.9% in the lower Q^2 kinematics after the implementation of calibrations [36].

2.5.2 Gaseous Electron Multiplier (GEM)

Gaseous Electron Multiplier (GEM) detectors are a type of gaseous ionizing detector that are used for particle tracking in the electron arm. Each GEM detector records a two-dimensional position of an ionizing particle and a three-dimensional trajectory is calculated by placing GEMs at several points in the electron arm. Figure 2.6 in Sec. 2.3 illustrates qualitatively how the GEMs are placed in the electron arm. The path of the particle through the GEMs is calculated using sophisticated track reconstruction. More detail on tracking will be given in Sec. 4.2. In combination with optics calibrations, which will be spoken about more in Sec. 2.5.5 and Sec. 4.3, the momentum of the particle is calculated and the path of the particle is propagated back through the BigBite magnet to the target. Background events from interactions in the target wall can then be removed. In contrast to shielded spectrometers, such as the permanent HRS spectrometers historically used in Hall A, the BigBite apparatus is unshielded. The unshielded nature exposes the detectors to high rates of charged particles. GEMs are designed to work in high rate environments and cover large areas of acceptance, making them ideal for this experiment. In contrast, more traditional tracking detectors such as drift chambers would be overwhelmed by the high rates, and silicon trackers would require orders of magnitude more channels to cover BigBite's acceptance [38]. GEMs can operate at rates up to 500 kHz/cm^2 with a position resolution of 70 μm and large areas of acceptance [39].

A single GEM foil consists of a thin polymer layer, approximately 50 μm thick, typically made of Kapton, with a 5 μm metal coating, usually copper, on both sides. Chemically etched microscopic holes, about 70 μm in diameter, create the characteristic conical shape visible in Fig 2.12a [40]. A potential difference of 350–450 V is applied to the metal layers which induces a strong electric field of about 65 kV/cm inside the perforations [41]. Figure 2.12a illustrates a cross section of the perforations and the shape of the electromagnetic field formed. The precision engineering and manufacturing of a GEM foil can be appreciated in the electron microscope image of Fig. 2.12b.

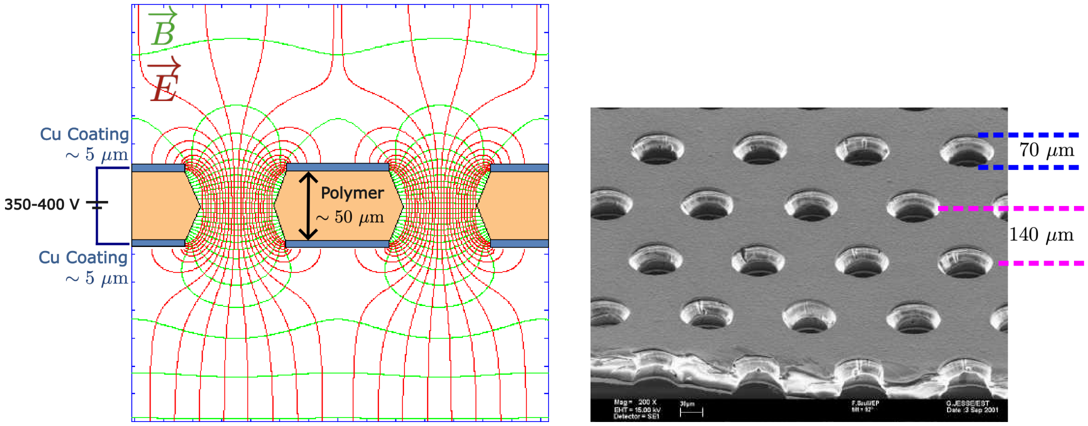

(a) (b)

Figure 2.12: Diagrams of GEM foil design on a microscopic scale. An electromagnetic field is induced in the conical shaped perforations by applying a potential difference between the metal coatings. **(a)** Electric and magnetic fields in the region of the perforations of a GEM foil as modeled in simulation [42]. **(b)** Electron microscope imaging of a GEM foil [40].

A triple-foil GEM utilizes 3 GEM foils separated by 1.5–3 mm, as illustrated in Fig. 2.13. These foils are placed in an air-tight frame and filled with a gas mixture of 75% Argon and 25% CO_2. Our GEM modules are based on the design for COMPASS GEMs at CERN. The majority of our GEM modules were assembled at the University of Virginia (UVA) from GEM foils manufactured at CERN.

Figure 2.13 illustrates an ionizing particle producing a track in a triple-foil GEM. A particle passes into the drift gap and ionizes a few particles in the gas, creating electrons. The electrons drift down to the first GEM foil and encounter the strong electric field in a perforation, causing the electrons to accelerate and ionize the gas, creating up to 20 times

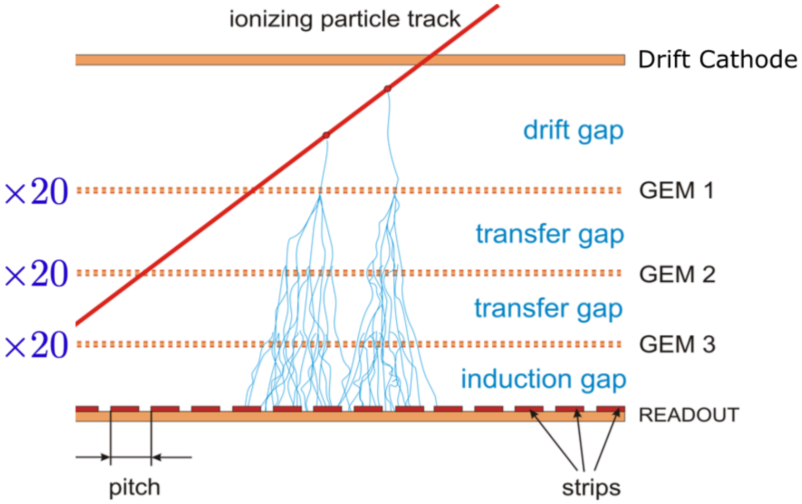

Figure 2.13: Illustration of an electron avalanche created in a triple-foil GEM by an ionizing particle passing through the GEM. The three layers of GEM foils can create $20^3 = 8000$ electrons from a single ionizing particle. The signal is read out by readout strips as an analogue signal [43].

more electrons. This multiplication continues through the second and third foil, allowing up to 8000 electrons to be produced from a single ionizing particle traversing through the detector. The electrons are then converted to a current by readout strips. Placing readout strips perpendicular to each other or in another non-parallel direction allows determination of the two-dimensional position of the event. This experiment utilizes GEMs with two types of readout strip configurations: UV and XY. The XY configuration uses Cartesian coordinates, with the readout strips oriented perpendicular to each other, while the UV configuration features readout strips set at a stereo angle of 60°. The four front trackers, GEMs 0–3, are of the UV configuration, while the back tracker, GEM 4, is of the XY configuration [44].

A single trigger event can produce many thousands of hits in the five GEM trackers. Finding and reconstructing a track from this would require huge computational power that is not feasible for this experiment. Thus, the location of the cluster in the BBCal Shower is used to constrain the search region for reconstructing the track. Figure 2.14 shows a typical trigger event in the GEM single-event display. The pink boxes show where the algorithm is being constrained by the BBCal cluster location. These tracking constraints help make tracking in these high rates possible.

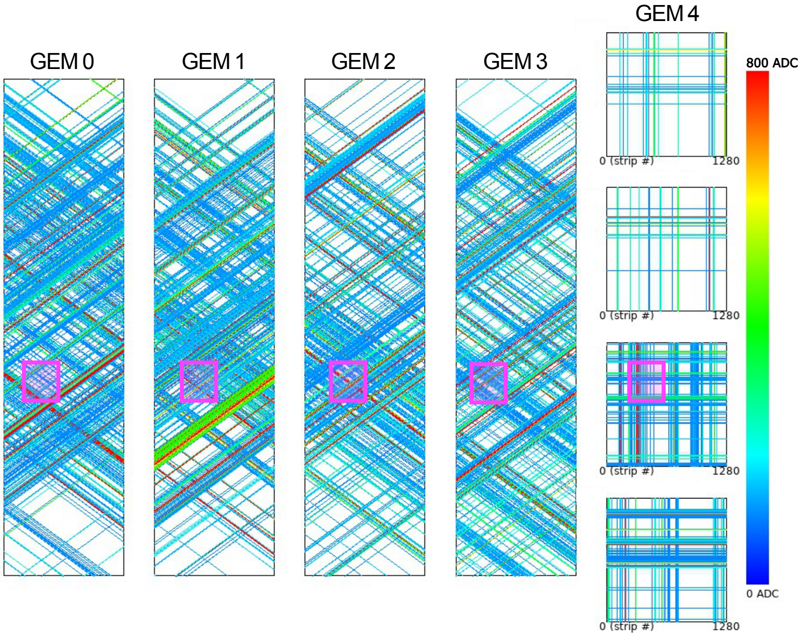

Figure 2.14: An event in the GEM single-event display illustrated with constraints from BBCal. The pink boxes illustrate the constraint of the search region for tracks provided by the cluster locations in BBCal. The readout strips of GEMs 0–3 are of the UV readout strip configuration, while GEM 4 is of the XY perpendicular strip configuration. Figure adapted from A. Puckett, with additional annotations [37].

2.5.3 Timing Hodoscope

The timing hodoscope is located between the Shower and the Preshower in the BigBite electron arm. It consists of 89 stacked plastic scintillator bars with light guides and PMTs on each end for a total of 178 read out channels. During the GMn experiment, it achieved a position resolution of 4–6 cm in the dispersive direction and 1.5–2 cm in the non-dispersive direction, and a timing resolution of 0.5–0.75 ns [45]. Figure 2.15 shows the layout of the timing hodoscope. Alternating curved and straight light guides accommodate for the thickness of the shielding around the PMTs and allow the bars to be stacked directly on each other with no space between [46].

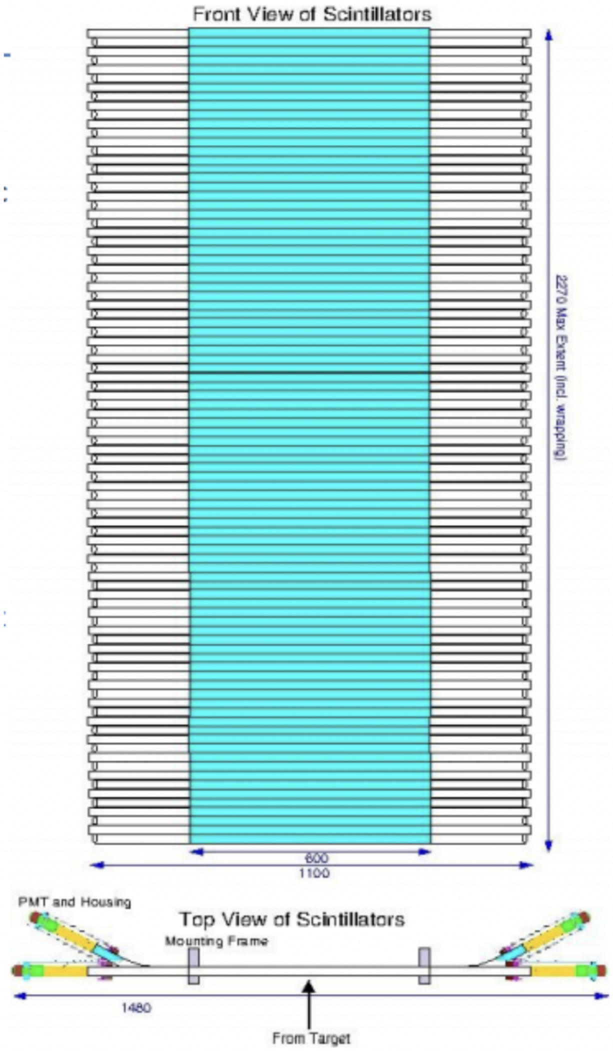

Figure 2.15: Diagram of the timing hodoscope. 89 plastic scintillator bars are stacked on top of each other with light guides and PMTs on each end. Bars have alternating curved and straight light guides to allow space for the PMT shielding [46].

When an ionizing particle passes through the scintillating material, organic molecules in the material are excited and then quickly decay, emitting optical photons, which are measured by the PMTs on each end of the bar. The time difference between the signals in the PMTs on each end of a bar gives the horizontal position where the particle interacted with the bar within 1.5–2 cm. The luminescence process is very rapid in plastic scintillators and on the order of 2–3 ns with high luminosity output [47].

When the hodoscope was first assembled in the BigBite stack in 2019, it was discovered that the setup was very susceptible to damage from impacts or disturbances. Many of the glue joints between the bars and light guides broke. The hodoscope was thus disassembled and a new support structure for the bars was designed. For several months in 2020, I assisted in the disassembly and reassembly of the hodoscope bars, testing them and installing them into the BigBite frame. Figure 2.16 illustrates the metal supports that were installed to take the strain off of the glue joints and onto the bars supports. The connection points between the scintillator bars and light guides were sanded to increase the surface area for the optical glue to adhere to as seen in Fig. 2.17. With these reinforcements, it now takes significantly more force to break the glue joints. During testing, we attempted to break one by securing it with a clamp over the edge of a table and pushing down. There was no noticeable damage of the glue joints.

Figure 2.16: Illustration of straight (top) and curved (bottom) assembled hodoscope paddles. Aluminum bars have been secured to reinforce the paddles and take the strain off the glue joins between the scintillator and light guides [48].

The precision timing resolution of the hodoscope is useful when performing timing

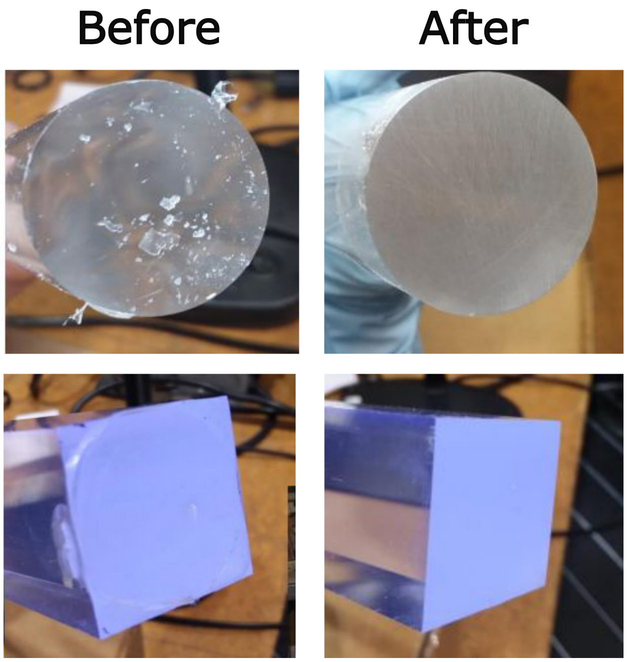

Figure 2.17: Connection points between the Hodoscope light guides (top) and scintillating bars (bottom) before and after sanding. The increased surface area caused by the small scratches from sanding significantly increased the strength of the glue joints.

calibrations for other detectors. The timing calibrations of other detector subsystems, including BBCal and GRINCH, rely on subtracting the hodoscope time. Any delay or time variation that may have happened in the data acquisition is subtracted out when the hodoscope time is subtracted. We will look at how GRINCH utilizes the hodoscope time for calibrations in more detail in Ch. 3.

Figure 2.18 illustrates how subtracting off the hodoscope time event-by-event from another channel eliminates variation caused by the timing difference in the DAQ itself. Even though the signals' leading edge time is different with these two events, the time difference between the signals in this example is the same. This allows us to eliminate the event-by-event time variation due to the DAQ. This method works best when the hodoscope is well calibrated and the timing well aligned.

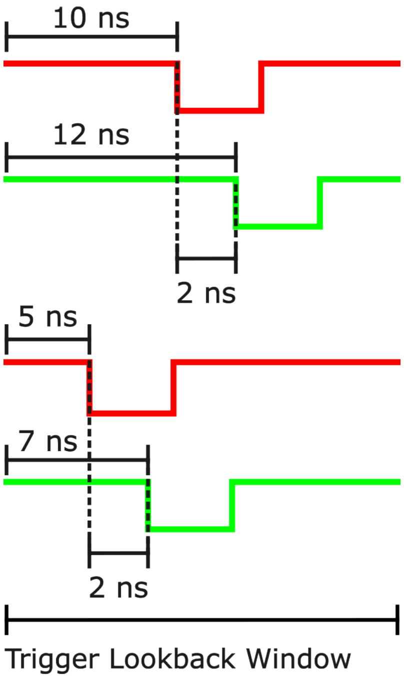

Figure 2.18: Illustration of two channels under two different trigger events. Subtracting the red time from the green time eliminates overall variations caused by the trigger and DAQ. Although the two events come in at different absolute times, 10 ns and 12 ns (top), 5 ns and 7 ns (bottom), the time difference of 2 ns is the same. Typically, a hodoscope time would be the red waveform being subtracted off in this example. The times shown here are arbitrary.

2.5.4 GRINCH Heavy Gas Cherenkov Detector

The Gas Ring Cherenkov detector (GRINCH) is a heavy gas Cherenkov detector designed to help distinguish pions from electrons. Hardware and software work on this detector were large components of my contributions to this experiment. We will describe GRINCH in detail in Ch. 3.

2.5.5 BigBite Dipole Magnet

The BigBite magnet is a room-temperature dipole magnet that sits downstream of the target and left of the beam pipe. It sits directly upstream of the BigBite detector stack and is the first component of the electron arm. As illustrated in Fig. 2.6, scattered electrons that enter the opening at the center of the magnet, also called the yoke, are deflected upward in proportion to their momentum and the strength of the magnetic field. This also has the benefit of bending positively charged particles, such as π^+ produced during inelastic reactions, down and out of the acceptance of the detector, and thus reducing our inelastic background. The BigBite detector stack sits at a 10° incline from level with the beam pipe to maximize the acceptance of quasi-elastic electrons at their expected momentum spectrum.

We can accurately measure the momentum of a scattered electron by relating its momentum and deflection angle to the field strength integral using the deflection formula

$$\theta_e = \frac{0.3 \times \int B \cdot dl\ (\mathrm{T} \cdot \mathrm{m})}{p_e(\mathrm{GeV}/c)}\,, \tag{2.1}$$

where p_e is the momentum and θ_e is the out-of-plane angle of the scattered electron. The factor of 0.3 arises from conversion between units. The field strength integral and thus the right hand side of this equation is known. θ_e is measured by utilizing a sieve in front of the magnet during calibration runs that only allows electrons through at specific positions. This allows us to solve for the momentum of the particle and translate it the back to the interaction point in the target. This is called Magnetic Optics Calibration and will be discussed further in Sec. 4.3.

The maximum mean field integral of the BigBite magnet is approximately $\int B \cdot dl = 0.9$ T·m. The field strength was tuned at the beginning of the experiment by adjusting the current to the magnet (750 A) where it remained at that setting.

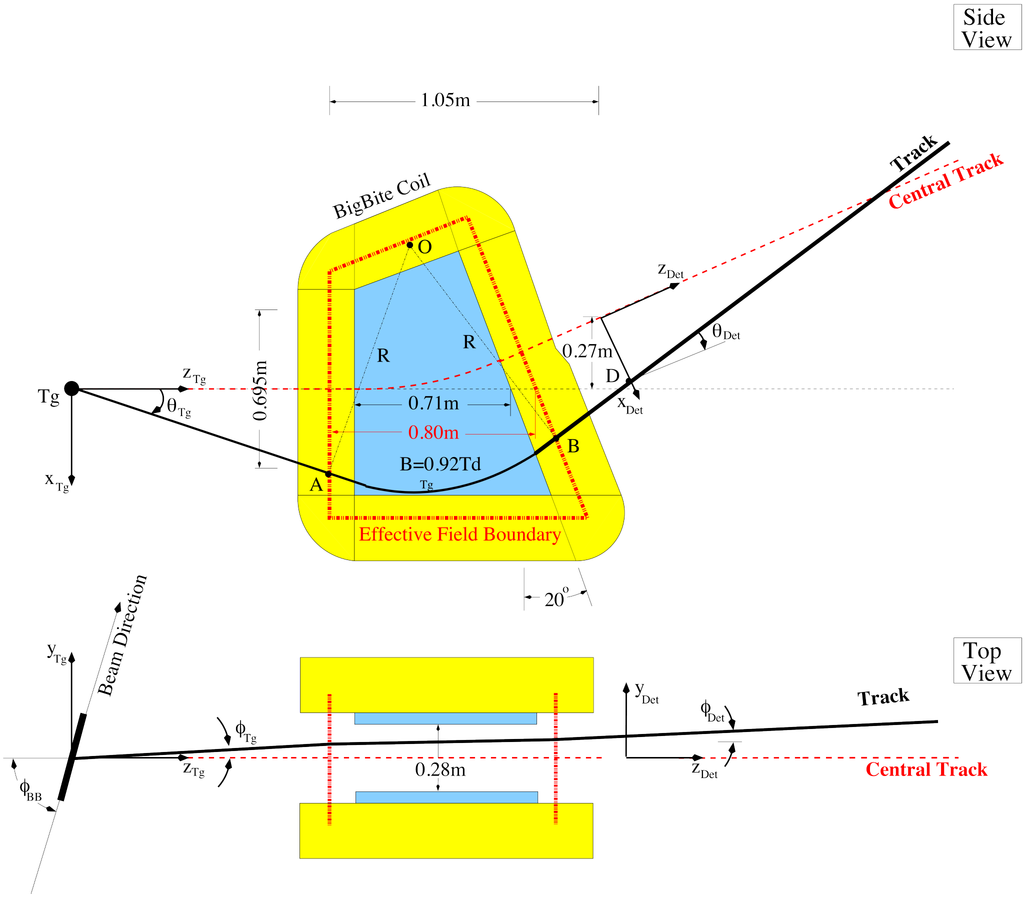

Figure 2.19: Schematic of the dispersive (top) and non-dispersive (bottom) planes of the BigBite dipole magnet [49]. Note: This schematic is adapted from a schematic for a previous experiment in Hall A that utilized BigBite. In this figure, the BigBite magnet is on beam right, whereas in GMn, BigBite was on beam left.

2.6 Hadron Arm

The hadron arm consists of a large-acceptance dipole magnet and the HCal hadron calorimeter. The purpose of the hadron arm is to measure the position and energy of protons and neutrons from quasi-elastic scattering events and separate them in space by charge using the magnetic field.

2.6.1 SBS Dipole Magnet

The SBS Magnet is a large room temperature dipole magnet originally used at Brookhaven National Lab (BNL)[2]. As seen in the photograph in Fig. 2.20, the SBS Magnet sits downstream of the target to the right of the beam pipe as part of the hadron arm.

Figure 2.21 illustrates how the magnetic field bends positively charged scattered particles upward. This results in a separation of scattered protons and neutrons from quasi-elastic events, as protons will be deflected in the magnetic field whereas neutrons will not. The stronger the magnetic field (i.e. larger integral field strength), the larger the separation between protons and neutrons. The integral field strength of the SBS Magnet is 2 T·m, or 2.5 T·m with pole shims [50]. We adjust the field integral strength by adjusting the current through the magnet coils to optimize the separation of protons and neutrons so as to increase the precision for identification between protons and neutrons. This will be discussed in more detail in Sec. 4.4.

One might suggest setting the field strength to its maximum to create a large separation between protons and neutrons, to minimize peak overlap and ensure the most accurate counts. However, complete separation is not always feasible. A significant fraction of protons may be deflected too high to hit the face of HCal, resulting in missed detections.

The reader may have noticed I have yet to define "separation" and "overlap" in the context of proton and neutron identification. For each event, the straight-line projection to the face of HCal is compared to the actual location of the event in HCal. As demonstrated

---

[2] The magnet is of type 48D48. Many such magnets were produced for BNL.

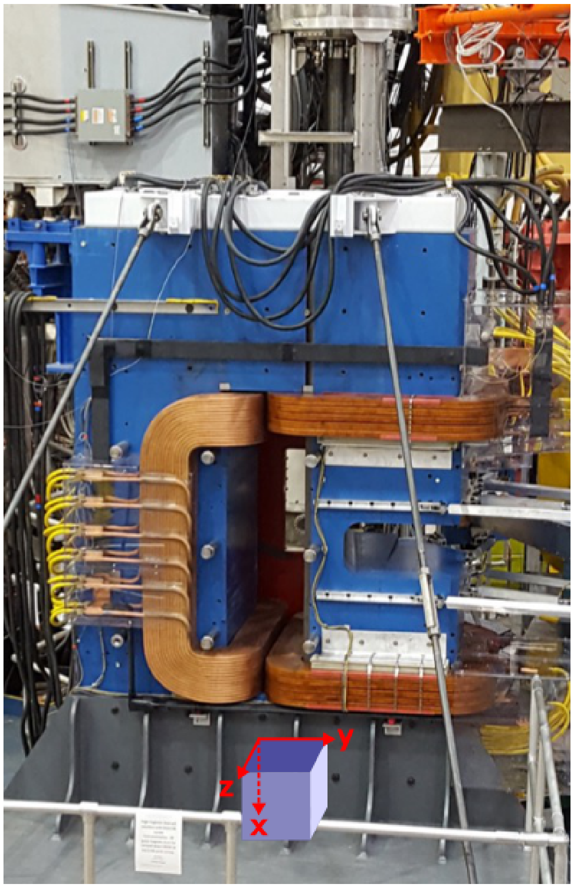

Figure 2.20: The SBS Magnet in Hall A. The SBS Magnet is placed beam-right, downstream of the target and before HCal. The box is to help orientate us in the right-handed orthogonal H-arm coordinate system, with the scattered particle passing through the yoke along the z axis.

in Fig. 2.21, protons are deflected by the magnetic field while neutrons are not. For the neutron, we would expect the actual event location to be near the straight line projection to the face of HCal. For the proton, in contrast, we would expect the actual event location to be deflected some distance from the straight line projection. Section 4.4 discuss in detail this key aspect of this experiment.

2.6.2 Hadron Calorimeter (HCal)

The Hadron Calorimeter (HCal) is a segmented sampling calorimeter designed to detect protons and neutrons up to several GeV in the SBS experiments. Protons are bent upward

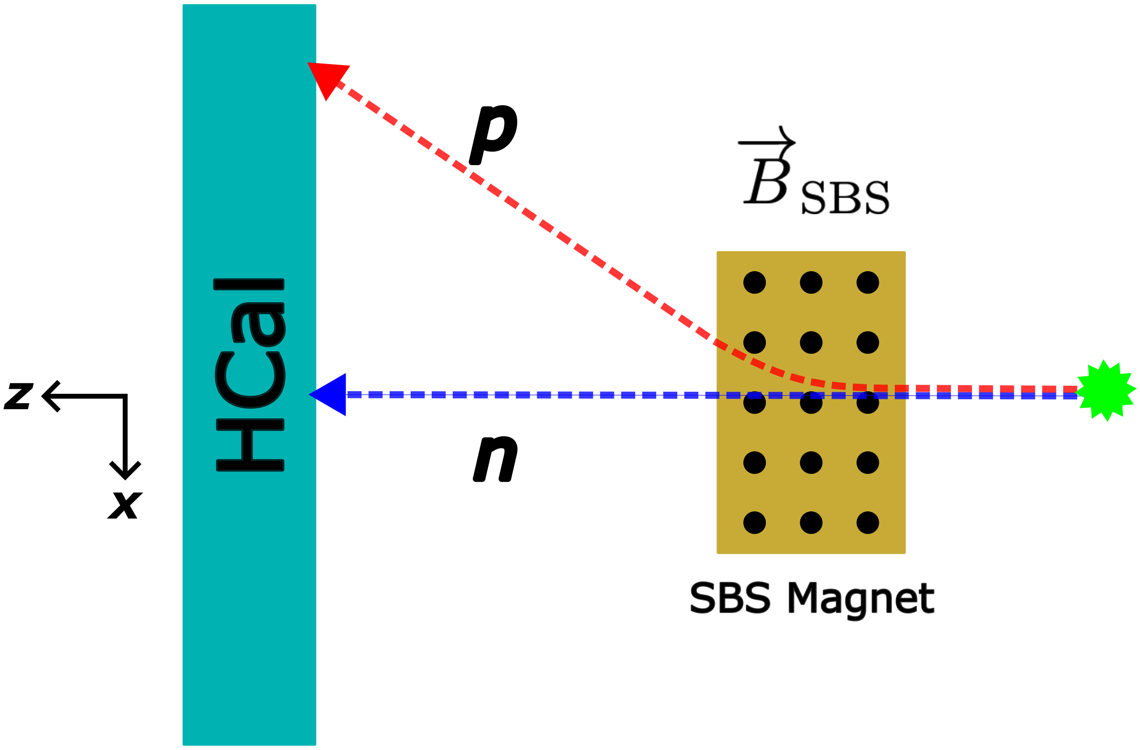

Figure 2.21: Cartoon of neutron and proton separation by the SBS Magnet. Protons are deflected upward in the dispersive direction ($-x$) in the magnetic field. In contrast, the neutron's trajectory is unaffected by the magnetic field. This illustration is not to scale.

towards the top of HCal by the SBS Dipole Magnet, while neutrons continue straight through. HCal was designed to have 30% energy resolution, 0.5 ns timing resolution, and 3-4 cm position resolution [51].

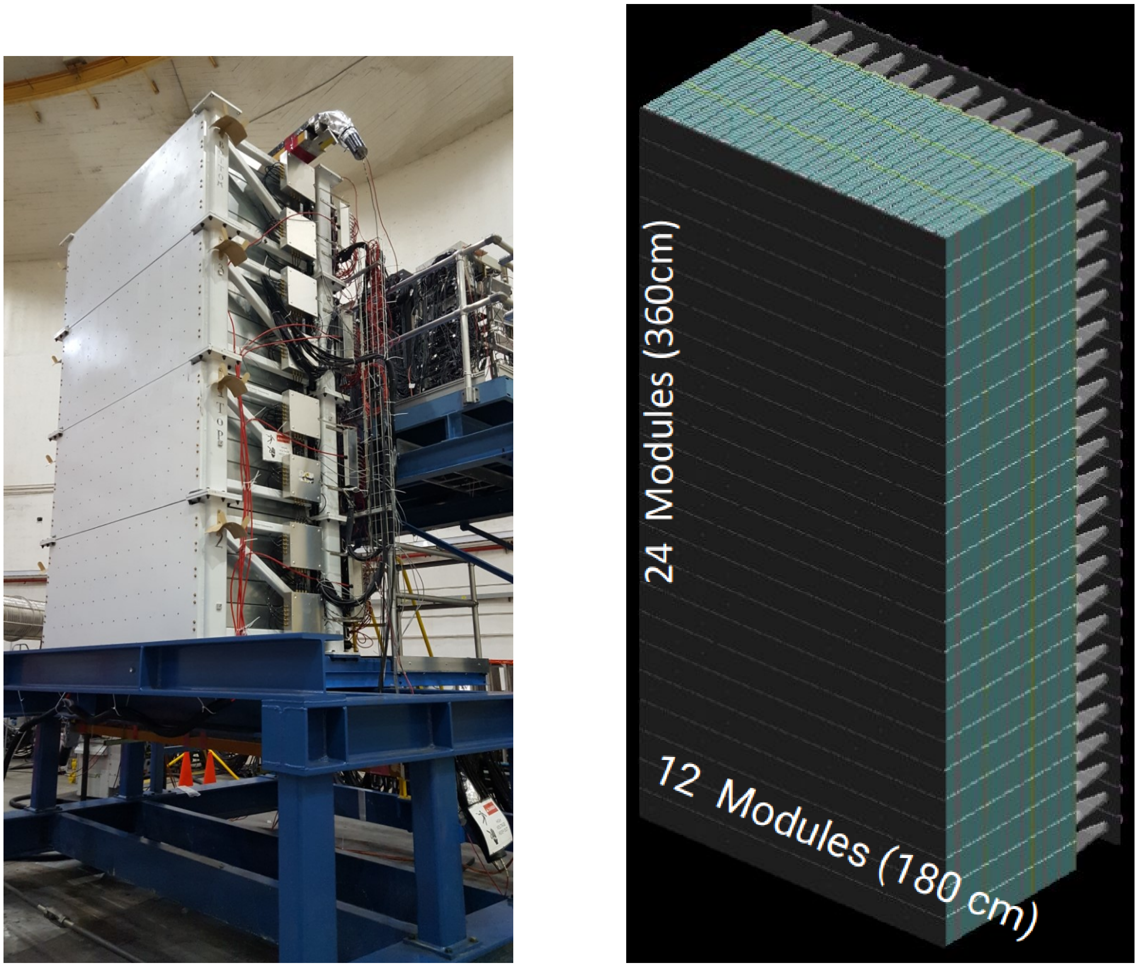

(a) (b)

Figure 2.22: The Hadron Calorimeter (HCal). **(a)** HCal sits beam-right on the platform, downstream of the SBS 48D48 Magnet. **(b)** HCal consists of 288 modules of alternating layers of absorbers and scintillators. See Fig. 2.23.

HCal consists of 288 detector modules in 24 rows by 12 columns. Figure 2.23 illustrates the composition of the HCal modules. Each module consists of alternating layers of 40 iron absorbers and 40 plastic scintillators. The protons and neutrons create a hadronic shower in the iron absorbers. The charged particles created by the hadronic shower interact with the scintillator planes where some of the energy is converted to light. This light is shifted to the wavelength that the PMTs are sensitive to and then is passed through the wave guide to the PMT. One hadron interacting with HCal typically creates a signal in several modules, which creates a "cluster". The signal in the PMTs is proportional to the energy of the original hadron and the energy can be reconstructed from the sum of the signals in the cluster.

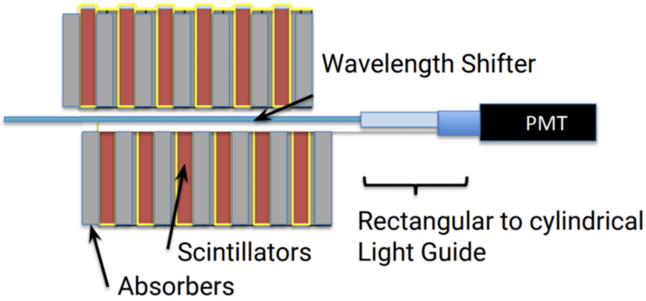

Figure 2.23: Diagram of an HCal Module. One HCal module consists of alternating planes of 40 iron absorbers and 40 plastic scintillators, wavelength shifter, light guide, and PMT. Protons and neutrons create a hadronic shower in the absorbers which produces other ionizing particles that cause fluorescence in the scintillators. The light is then shifted to wavelengths that the PMT can detect and travels down the light guide to the PMT [51].

2.7 Data Acquisition System

With numerous detectors, each with multiple signal channels, a data acquisition system (DAQ) is needed to collect, process, and store detector signals in a coordinated way.

Identification requires the detector to recognize the occurrence of a trigger and subsequent onset to record. Processing involves converting the generated analog signals into meaningful digital signals.

A simple explanation of a trigger is that it is a condition that when it's met, all of the signals are read out from the various detectors. During the GMn experiment, the trigger we used for data collection was the BigBite High (BBHI) trigger, also called the "overlapping regions trigger". This trigger is created when the Preshower and the Shower have regions above threshold that overlap. See Section 3.7 of P. Datta's thesis for more detail on the DAQ and BBCal trigger [36].

Chapter 3

GRINCH Heavy-Gas Cherenkov Detector

The Gas Ring-Imaging Cherenkov Detector (GRINCH) is a heavy-gas threshold Cherenkov detector. It consists of C_4F_8 heavy gas, four cylindrical mirrors, and 510 1-inch photomultiplier tubes. The main purpose of GRINCH is to assist with pion rejection and electron selection in SBS experiments utilizing the BigBite electron arm. The GMn experiment served as the commissioning experiment for GRINCH. GRINCH was fully operational only during the last two kinematic settings of GMn: SBS-8 and SBS-9. GRINCH was not vital for pion rejection in the GMn experiment. The BigBite calorimeter, and particularly the Preshower, is able to distinguish between good electrons and background quite well in the kinematics of GMn. In the experiment following GMn, GEnII, the background is much higher, and GRINCH is needed to aid in particle ID.

3.1 Cherenkov Radiation

Cherenkov radiation occurs when a charged particle travels through a medium faster than the speed of light *in the medium.* An electromagnetic "sonic boom" of light is created along the path of the particle.

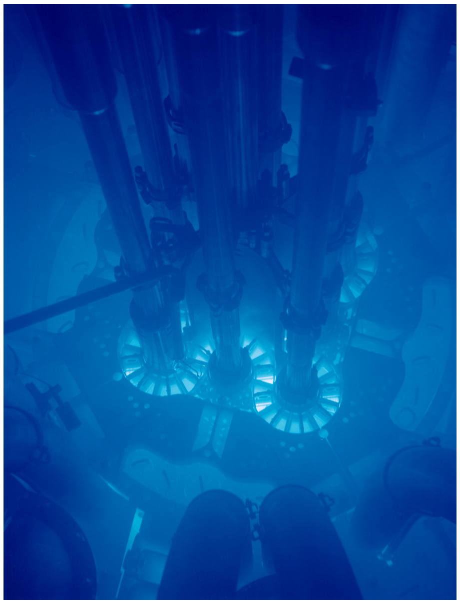

Figure 3.1: Cherenkov radiation in the Advanced Test Reactor at Argonne National Laboratory is observed as a blue glow. Charged particles from nuclear reactions travel through the water faster than the speed of light in the water. Image from Argonne National Laboratory.

The speed of light in a medium is given by

$$v_{\text{light}} = \beta c = \frac{c}{n}\,. \tag{3.1}$$

The index of refraction, n, varies between different media and in a typical gas, is a function of both wavelength and pressure. Materials used as a Cherenkov medium are often reported in terms of $\delta = n - 1$. For these calculations, we will treat n as a constant over the relevant wavelength range (see Sec. 3.2.3).

Figure 3.2 illustrates how a coherent waveform of Cherenkov light is formed geometrically. When the charged particle moves faster than the light propagates, a light cone is formed.

We can write down an expression for the angle of the light propagation,

$$\cos(\theta_c) = \frac{L_{\text{light}}}{L_{\text{particle}}} = \frac{(c/n)\Delta t}{\beta c \Delta t} = \frac{1}{n\beta}\,. \tag{3.2}$$

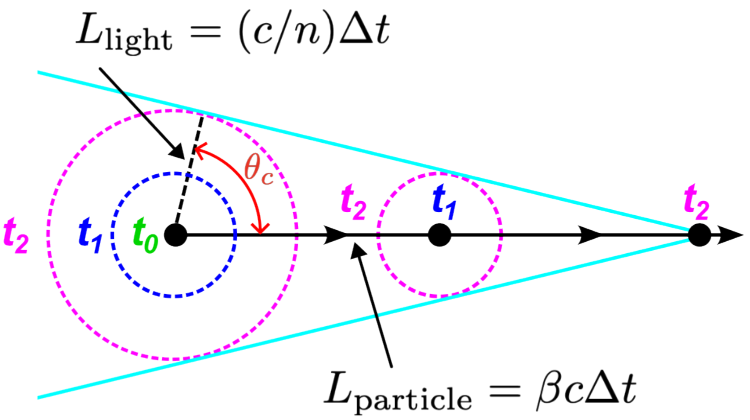

Figure 3.2: Illustration of the propagation of Cherenkov light. At time t_0, the light begins to propagate out. At time t_1, the particle has traveled to the next position, and the light wave that originated at the previous position has propagated out. At time t_2, the particle has traveled to the next position, and light from the particle at the previous positions has propagated out.

The Cherenkov "threshold velocity" is defined when $\theta = 0$ as

$$\theta_c = 0 \Rightarrow \beta_t = \frac{1}{n}. \tag{3.3}$$

Particles above the threshold speed, β_t, are able to produce a coherent light wave and θ_c is greater than 0. In other words, when $\beta > 1/n$, Cherenkov light can be produced. A larger n would lead to a larger momentum threshold.

The Frank-Tamm formula expresses the number of photons emitted per unit length per wavelength interval:

$$\frac{d^2N}{dxd\lambda} = \frac{2\pi\alpha}{\lambda^2}\left(1 - \frac{1}{\beta^2 n^2(\lambda)}\right), \tag{3.4}$$

where N is the number of photons, λ is the wavelength of the emitted light, x is the path length of the particle, and $\alpha \approx 1/137$ is the fine-structure constant.

If we assume that n is reasonably constant over the wavelength range of interest, we integrate Eq. (3.4) over the wavelength range that the PMTs are sensitive to, i.e. where the PMTs have non-zero quantum efficiency. Evaluating the integral over $[\lambda_{\text{min}}, \lambda_{\text{max}}]$, we find

$$\begin{aligned}\frac{dN}{dx} &= \int_{\lambda_{\mathrm{min}}}^{\lambda_{\mathrm{max}}} \frac{2\pi\alpha}{\lambda^2}\left(1-\frac{1}{n^2\beta^2}\right) d\lambda \\ \frac{dN}{dx} &= 2\pi\alpha\left(1-\frac{1}{n^2\beta^2}\right)\left(\frac{1}{\lambda_{\mathrm{min}}}-\frac{1}{\lambda_{\mathrm{max}}}\right).\end{aligned} \tag{3.5}$$

The integral of dx is the path length L, so

$$N = 2\pi\alpha L\left(1-\frac{1}{n^2\beta^2}\right)\left(\frac{1}{\lambda_{\mathrm{min}}}-\frac{1}{\lambda_{\mathrm{max}}}\right). \tag{3.6}$$

Note that N is proportional to $(1-\frac{1}{n^2\beta^2})$. Therefore, a larger index of refraction produces more photons per unit length, so a larger index of refraction is often desirable.

3.1.1 Threshold Detector Principles

Cherenkov detectors can be used for a variety of purposes, and their design and choice of materials depend on the specific experimental goals.

Some Cherenkov detectors aim to measure the radius of the Cherenkov light cone precisely, from which the particle's speed, β, can be inferred via the Cherenkov angle θ_c and momentum from other detectors. These detectors are typically equipped with mirrors and allow the light to propagate over large distances, so that the ring radius can be measured accurately.

Alternatively, Cherenkov detectors can be designed to measure the number of emitted photons, which is related to the particle's velocity through Eq. (3.4). These designs often use large PMTs to collect as many photons as possible, without resolving the Cherenkov ring.

A particularly important application is particle identification using a *threshold Cherenkov detector*. Here, the detector exploits the fact that Cherenkov radiation occurs only when a particle's velocity exceeds the threshold value determined by the refractive index of the medium, $\beta_t = 1/n$ (see Eq. (3.3)). By selecting a medium with an appropriate refractive index n, the detector can distinguish between particles of different masses within the momentum acceptance of the experiment.

We can express β in terms of the particle's momentum p and mass m using relativistic mechanics:

$$\beta = \frac{v}{c} = \frac{p}{E} = \frac{p}{\sqrt{p^2 + m^2}} = \frac{1}{\sqrt{1 + (m/p)^2}} \,. \tag{3.7}$$

(Note: here $c = 1$ in natural units.)

The *threshold momentum* p_t—the minimum momentum required for a particle to produce Cherenkov radiation—follows from Eq. (3.7) with $\beta_t = 1/n$:

$$p_t = \frac{m}{\sqrt{n^2 - 1}} \,. \tag{3.8}$$

Particles with $p > p_t$ emit Cherenkov radiation, while those with $p < p_t$ do not. Since p_t depends on the particle's mass, a threshold Cherenkov detector can suppress signals from heavier particles (e.g., π^-) that fall below threshold while detecting lighter particles (e.g., electrons) in the same momentum range. The GRINCH detector is designed in this way, choosing the medium's refractive index so that pions in the spectrometer's acceptance do not produce Cherenkov light, while electrons do.

3.2 Design

GRINCH was designed specifically to operate in the high-background environment of the SBS experiments. This is achieved using small-diameter PMTs, thin PMT window glass, and by positioning the PMTs away from the beam side of the detector.

Unlike some Cherenkov detector designs, GRINCH employs PMTs that are only ≈ 1 inch in diameter. This minimizes backgrounds from pions and other particles interacting directly with the PMT windows and producing showers in the glass. A single large PMT on one signal channel would experience a high rate of background hits, whereas with many small PMTs, these hits are distributed across multiple channels. Additionally, the glass windows of the GRINCH PMTs are significantly thinner than those of larger PMTs, further reducing the probability of background interactions. The PMTs are also positioned as far as possible from the beam side of the detector to mitigate backgrounds.

Finally, the precise timing of the GRINCH TDCs provides additional background suppression by rejecting out-of-time hits that are not from the scattering event in the target. Figure 3.3 shows a CAD rendering of GRINCH from the outside. Incoming particles enter along the z-axis, and the Cherenkov cone is reflected into the PMT array.

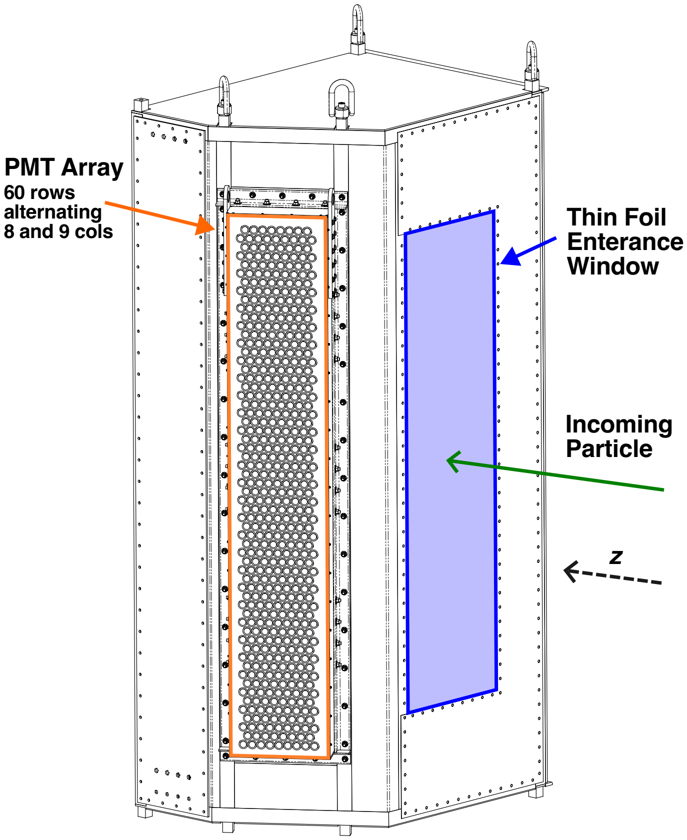

Figure 3.3: GRINCH as seen from the outside. Particles scattered from the target enter the thin foil entrance window of GRINCH along the z-axis. Light from the Cherenkov cone is reflected onto the PMT array.

Together with offline analysis methods, these features enable GRINCH to achieve high electron detection efficiency and reject pion backgrounds in the challenging SBS environment.

3.2.1 Mirrors

The GRINCH mirrors consist of four cylindrical concave mirrors that collect and focus the light onto the PMT array. The mirrors are optical quality with aluminum coating. Tests by the manufacturer found their reflectivity to be $\approx 90\%$ in the light wavelength range of our phototubes. Figure 3.4 shows the layout of the GRINCH mirrors. The middle two mirrors are placed perpendicular to the particle path, and the top mirror and the bottom mirror are angled slightly. The mirrors overlap slightly in the vertical direction in order to capture as much light as possible.

The cylindrical mirrors focus the light in the horizontal direction only. As seen in Fig. 3.4 the top mirror and the bottom mirror are angled slightly to reflect Cherenkov light near the top and bottom of the detector onto the PMT array.

The cylindrical mirrors were adjusted to have a radius of curvature so that the focal length is approximately equal to the distance from the entrance window to the center of the mirror: $f \approx 65$ cm [52]. Figure 3.5 shows the layout of the mirrors in GRINCH as seen from the top. The incoming particle produces a light cone, which is reflected and focused into by the mirrors into the PMT array. We will discuss the calculations that lead to this design in Sec. 3.2.4.

Figure 3.6 shows the positions of the mirror relative to the metal frame the mirrors are mounted to. The mirrors are slightly overlapped in the vertical direction the top and bottom mirrors are angled vertically.

3.2.2 GRINCH Photomultiplier Tubes

The PMTs in GRINCH are refurbished 29 mm diameter PMTs from the BaBar DIRC Cherenkov detector at SLAC, which used ultrapure water as their medium [53]. The PMTs consist of 11 dynodes and are operated at positive high voltage of 900–1300 V. More details about these particular PMTs—ET Enterprises 9125B—can be found in the manufacturer's data sheet [54].

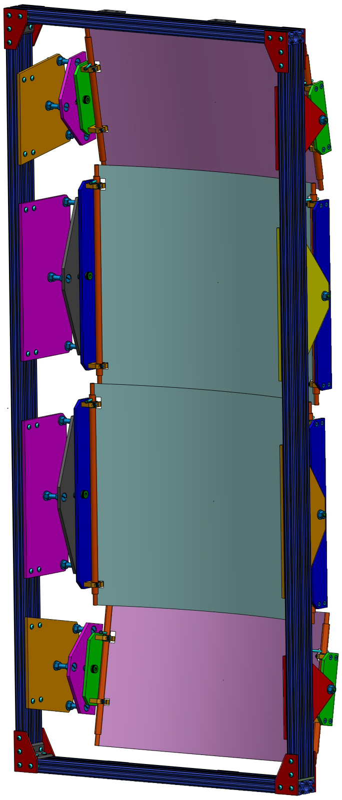

Figure 3.4: The four GRINCH cylindrical mirrors in the mirror frame. The mirrors focus the light in the horizontal direction and reflect it to the PMT array. The top and bottom mirrors are angled slightly in the vertical direction to guide light from the top and bottom of the detector onto the array.

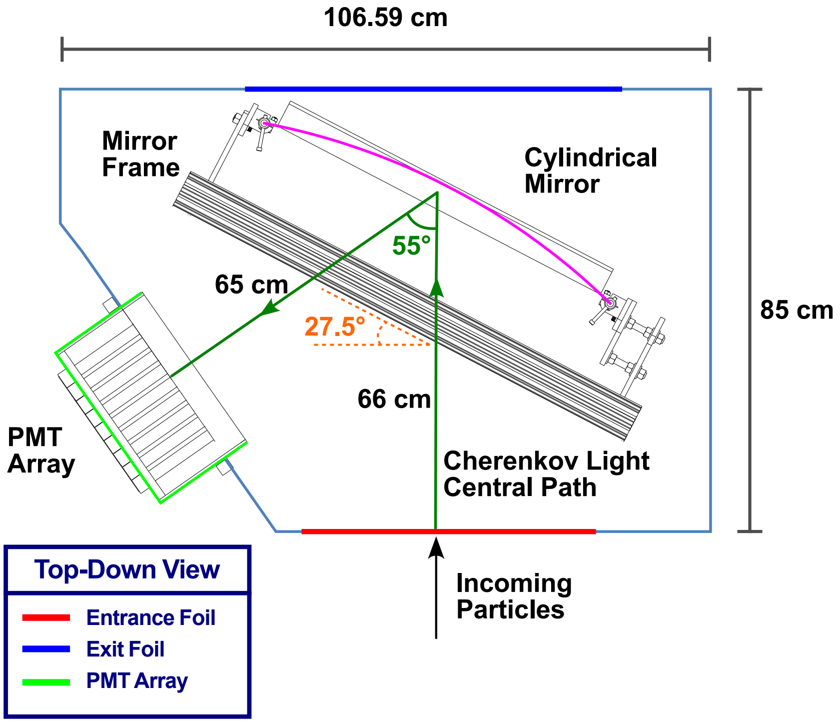

Figure 3.5: GRINCH as seen from above. The Cherenkov light from an incoming particle is reflected by the cylindrical mirrors and onto the PMT array.

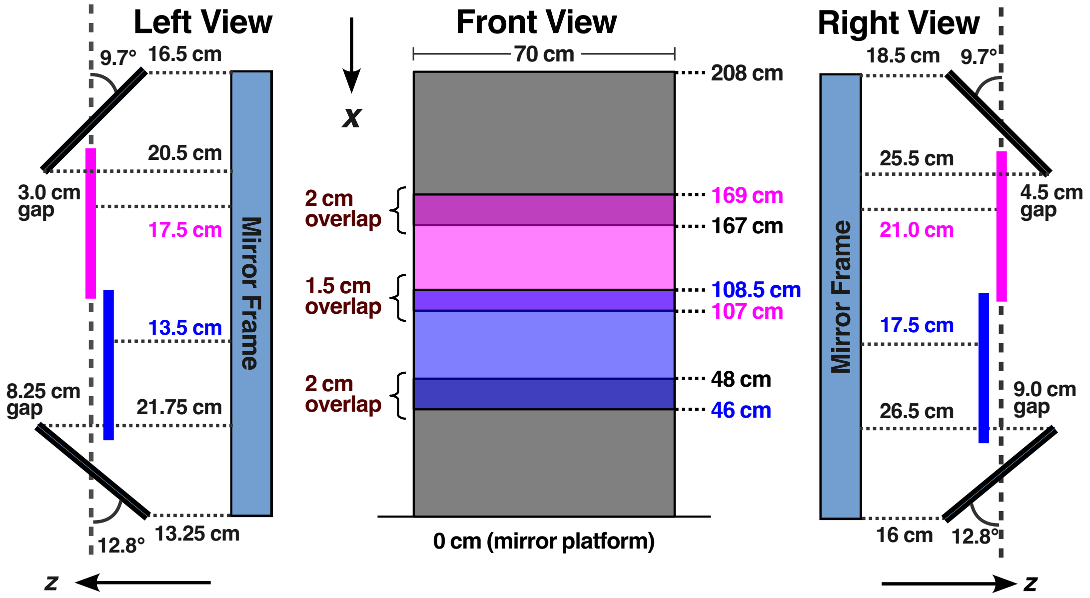

Figure 3.6: GRINCH mirrors as seen from front, left, and right. Not to scale. Figures adapted from B. Yale.

As plotted in Fig. 3.7, the quantum efficiency (QE) of the PMTs was measured to be non-zero between approximately 275 nm and 635 nm, peaking at approximately 375 nm with a quantum efficiency of 27%.

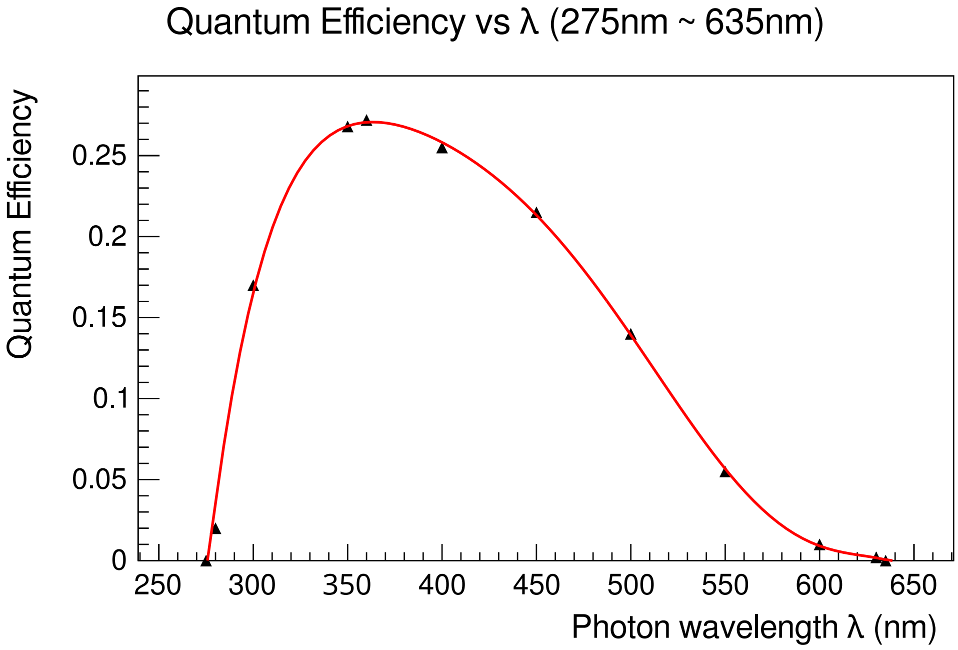

Figure 3.7: The quantum efficiency for GRINCH PMTs. The PMTs are sensitive to light from approximately 275–635 nm.

The 510 PMTs are arranged in a honeycomb configuration inside aluminum-coated light-catchers: 60 rows with alternating columns of 8 and 9 PMTs. Figure 3.8 is a photograph of a section of the GRINCH PMT array as seen from inside the detector. The light-catchers on each PMT focus photons onto the face of the PMT that would land inside the "cell" but outside the PMT face.

Figure 3.9 illustrates the geometry of the PMTs in the PMT array and the distances between neighboring PMTs. The calculated size of a typical Cherenkov cone is also shown, which we will discuss in Sec. 3.2.4. The glass faces of the PMTs were degraded due to long exposure in the ultrapure water [55]. For use in GRINCH, optical quality borosilicate glass disks were glued onto the face of each PMT using optical glue rated for UV wavelengths.

Figure 3.8: Photograph of a section of the GRINCH PMT array as seen from inside the detector. The aluminum-coated light-catchers focus the Cherenkov light onto the face of the PMTs in each cell.

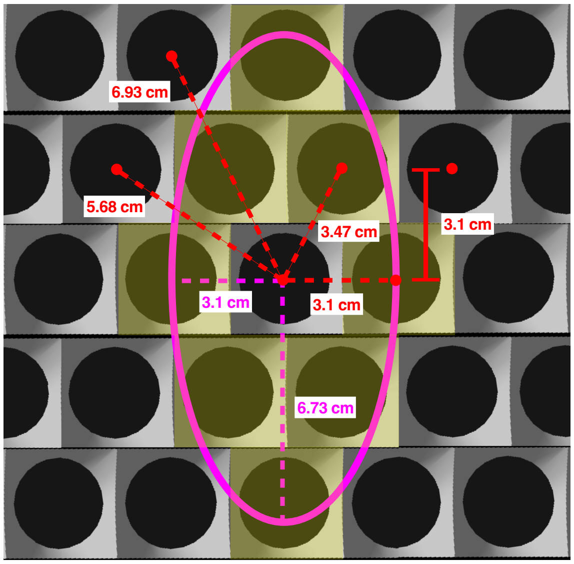

Figure 3.9: Illustration of the PMT configuration of GRINCH. The PMTs and light catchers are arranged in an offset grid, where every other row is offset by one half the width of a light catcher. Distances from the center of a PMT to neighbors and next-neighbors are in red. The light cone from an electron entering GRINCH along the z-axis is drawn in pink (see Sec. 3.2.4). The highlighted PMTs are to illustrate which PMTs may register a signal and what a cluster may look like in this example event. Figure is to scale.

Figure 3.10 illustrates the geometry of a single "cell" in the PMT array. The PMT face is 29 mm, and the active area of the PMT is 25 mm [54]. The area of a cell is 31^2 (mm^2).

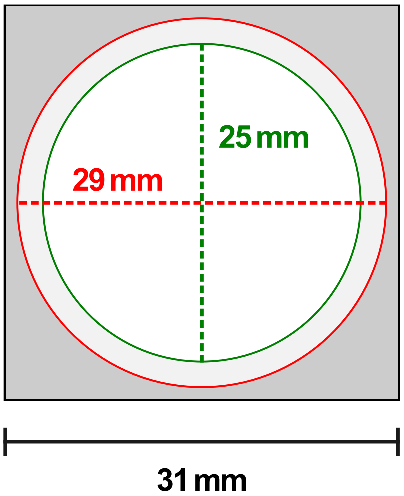

Figure 3.10: Dimensions of a "cell" in the GRINCH PMT array. The area of the aluminum coated light-guides (projected onto the 2-dimensional plane) is in gray. The face of the PMT is in red, and the active area of the PMT face is in green. Figure is to scale.

3.2.3 Heavy Gas

There are several variables to balance when choosing a medium for a Cherenkov detector. For GRINCH, we need to consider the momentum of the particles we wish to detect and reject. Since GRINCH is utilized as a threshold Cherenkov detector, we are particularly interested in the momentum thresholds for pions and electrons. We must also consider practical variables like cost and availability.

The index of refraction of heavy gasses C_4F_8 and C_3F_8 were carefully measured at 405 nm for various gas pressures [56]. Table 3.1 compares these results and useful calculations to CO_2 and air.

For the purposes of our experiment, C_4F_8 was chosen over C_3F_8 due to it's lower cost, high photon output, and still allowing pion rejection up to reasonably high momentum of 2.7 GeV.

3.2.4 Cherenkov Calculations for GMn

Now, we will investigate the design of GRINCH by completing a back-of-the-envelope style calculation of the number of photoelectrons we expect to see in each phototube in a typical

Table 3.1: Cherenkov thresholds for various gasses at 1 atm. The index of refraction for the heavy gasses was measured experimentally [56]. The index of refraction for CO_2 [57] and air [58] in the ultraviolet range were extrapolated from world data using the refractiveindex.info database [59]. Calculated for each gas is the threshold velocity β_t, the number of photons produced per meter of propagation for electrons N/L, the momentum threshold p_t for electrons, and the momentum threshold p_t for charged pions.

Gas	C_4F_8	C_3F_8	CO_2	Air
n ($\lambda = 405$ nm)	1.00132	1.00111	1.00045875	1.0002825
N/L for e^- (photons/m)	254	214	86	54
$\beta_t = v/c$	0.99868	0.99889	0.99954	0.99972
p_t (MeV) for e^-	9.94	10.84	16.86	21.49
p_t (MeV) for π^+	2715	2961	4607	5871

GRINCH cluster, and compare the results to early GRINCH simulations.

In the SBS-8 and SBS-9 kinematic points where the GRINCH was functioning, the average energy of the scattered electron E_e recorded in the electron arm ranges from about 1000 MeV to 4000 MeV as seen in Fig. 3.11.

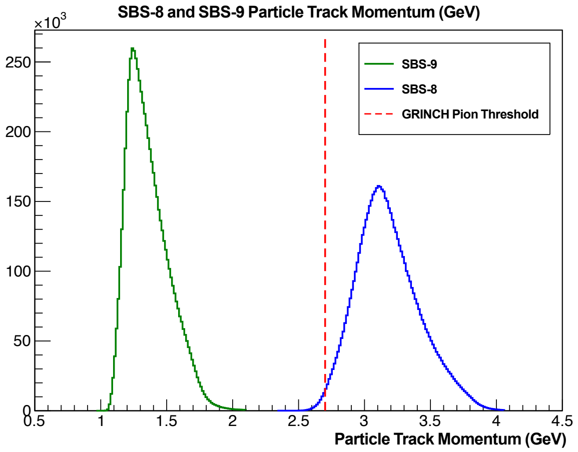

Figure 3.11: Particle track momentum distribution for SBS-8 (blue) and SBS-9 (green) from data, calculated by the GEM tracks. The red line at 2.7 GeV denotes the GRINCH pion threshold. The SBS-8 distribution extends above the threshold, while SBS-9 remains below.

For electrons, once their kinetic energy is much greater than their rest energy ($K \gg 0.511$), their speed is extremely close to c. Since most experimental electrons are in the multi-MeV range or higher, with G_M^n having electrons in the GeV range (Fig 3.11), we approximate $\beta \approx 1$, with errors on the order of 10^{-3} or less—negligible for Cherenkov calculations.

Using $\beta = 1$, $n = 1.00132$ for C_4F_8 gas (see Sec. 3.2.3), we use Eq. (3.2) to solve for the Cherenkov angle θ_c,

$$\begin{aligned} \cos(\theta_c) &= \frac{1}{n\beta} \approx \frac{1}{1.00132} = 0.99868 \\ \theta_c &= 0.051386 \text{ rad} = 2.94^\circ \approx 3^\circ \,. \end{aligned} \tag{3.9}$$

We can also now solve for the number of photons produced in the range the PMTs are sensitive to based on their quantum efficiency from Eq. (3.6). Figure 3.7 shows the active range is $[\lambda_{min} \approx 265 \text{ (nm)}, \lambda_{max} \approx 600 \text{ (nm)}]$, and $L \approx 66$ (cm), yielding

$$\begin{aligned} N &= 2\pi(1/137)(0.66)\left(1 - \frac{1}{1.00132^2 1^2}\right)\left(\frac{1}{265 \times 10^{-9}} - \frac{1}{600 \times 10^{-9}}\right) \\ N &= 168 \text{ photons} \,. \end{aligned} \tag{3.10}$$

Or, expressed as the number of photons per unit length, $N/L = 254.5$ (photons/m) for C_4F_8.

Now, we have all the tools we need to calculate the expected size of the Cherenkov cone as seen by the PMT array. For these simple example calculations, we use an ideal event of an electron coming in parallel to the z-axis in the center of the GRINCH window, incident on either of the two middle mirrors which are perpendicular to the z-axis in the vertical direction.

In the vertical direction, we can treat the cylindrical mirrors as flat and use a point-to-point approximation, where the effective distance the light travels is the 66 cm from the window to the mirrors for our ideal event. In reality, the path length can be longer than this, depending on the incoming angle and location on the detector and the angle of the mirror frame in respect to the z-axis. In our ideal event, the light then travels 65 cm from the mirrors to the PMT array. The total propagation distance is therefore $D_{eff} = 131$ cm, so we have.

$$
\begin{aligned}
R_{\text{vertical}} &= D_{\text{eff}} \tan(\theta_c) \\
R_{\text{vertical}} &= 131 \text{ cm} \times 0.051 = 6.73 \text{ cm}\,.
\end{aligned}
\tag{3.11}
$$

Using the mirror equation, we can calculate the ideal angle of the mirror so that the reflected rays are at 55° relative to the z-axis. We find that $\theta_m = 55°/2 = 27.5°$.

The angle of 55° was chosen due to the physical constraints of the frame that holds the BigBite Spectrometer. All of GRINCH needed to fit into a given space, and this particular design worked well within that space.

In the horizontal direction, the cylindrical mirror acts as an ideal concave mirror. For an ideal concave mirror, light rays coming in parallel to the mirror will converge at the focal point. Therefore, we can reverse the direction of the light and see that for a point source located at the focal length, the rays will reflect off the mirror parallel. Our eyes can't see the image produced, since it is at infinity, but the parallel rays are ideal for propagation over long distances and for detection by PMTs.

Using

- $\theta_{(\text{window – mirror – pmt})} = 55°$
- $\theta_{\text{mirror – horizontal}} = 27.5°$
- $\theta_c = 3°$
- $R = 66$ cm

and then carefully applying trigonometry, we find the radius of the Cherenkov cone in the horizontal direction to be

$$
\begin{aligned}
r_{\text{pmt}} &= 65 \frac{\sin(3°)}{\sin(180° - 27.5° - 3°)} \cos(27.5°) \\
r_{\text{pmt}} &= 3.08 \text{ cm} \approx 3.1 \text{ cm}\,.
\end{aligned}
\tag{3.12}
$$

Figure 3.12 shows a ray trace simulation of a cylindrical mirror in GRINCH and the relevant angles.

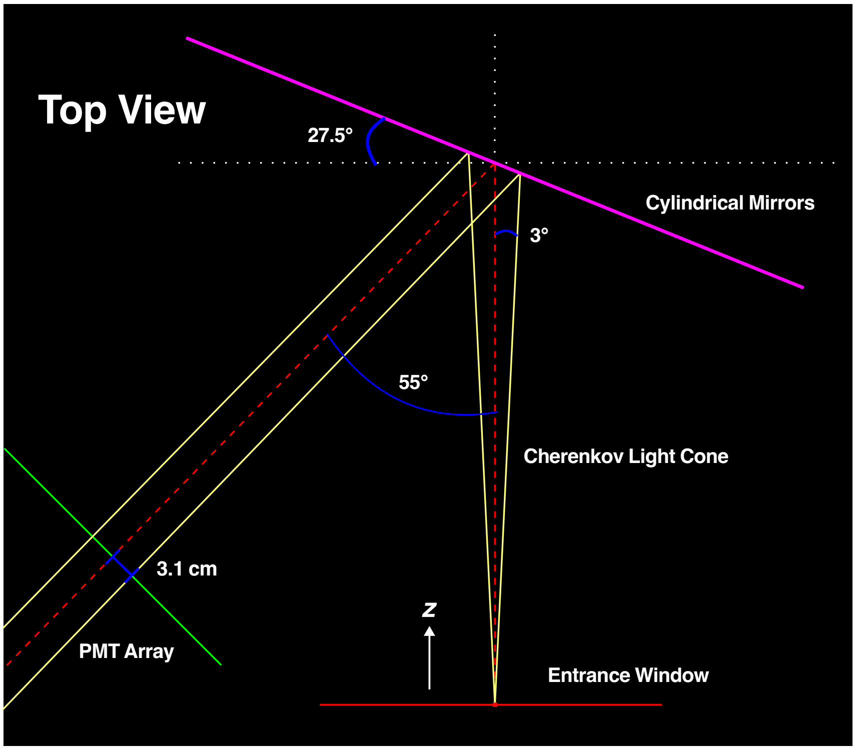

Figure 3.12: A simple ray trace for the GRINCH mirrors in the horizontal direction. An electron enters GRINCH along the z-axis and produces a light cone originating at the entrance window. The cylindrical mirrors have been set to have a focal length approximately equal to the distance from the mirror to the entrance window. For an ideal spherical mirror, the rays originating from the focal length are parallel after reflection and are transported over to the PMT array. This figure was created using the open source *Ray Optics Simulation* application [60].

Therefore, at the GRINCH PMT array, a cluster that comes in along the z-axis will be an ellipse with semi-minor axis = 3.1 cm and semi-major axis = 6.73 cm. This aligns conveniently with the spacing between PMTs, which when placed as close together as possible with room for light guides, was 3.1 cm apart.

This ellipse covers about 8 PMTs on the array. Let's approximate that each light-catcher in the ellipse gets an equal number of photons. To calculate the number of photoelectrons for each tube, we need to take the geometry of the light-catchers and PMTs into account, as well as the reflectivity of the aluminum coatings and the QE of the PMTs. Taking these into account, we have

$$\frac{\text{Photoelectrons}}{\text{PMT}} = \frac{N * R_{\text{M}} * QE}{[\text{Cluster size}]_{\text{avg}}} * \left(A_{\text{PMT}} + A_{\text{L}} * R_{\text{L}} * F\right)/A_{\text{cell}}\,. \tag{3.13}$$

where N is the total number of photoelectrons in the Cherenkov cone, R_{M} is the reflectivity of the mirror, QE is the average quantum efficiency of the PMTs, A_{PMT} (m^2) is the area of the **active area** of a PMT, A_L (m^2) is the area covered by a light-catcher around a PMT, F is the fraction of light reflected from the light-catcher that is successfully directed to the active area of the PMT, and A_{cell} (m^2) is the area of one unit cell of the array, which is equivalent to the distance between PMT centers. Note that this is a simplification of the physics of this system. A more accurate calculation would be to incorporate the quantum efficiency in Eq. (3.5) by integrating the functional fit to the QE of Fig. 3.7.

The reflectivity of a typical Al coating is $\sim 90\%$. The area covered by the light-catcher around a PMT is the area of a cell subtracted by the area of the PMT face. I lack data on the performance of the geometry of the light-catcher, F. However, we can put boundaries on the calculation of the number of photoelectrons per PMT by computing the result at $F = 1$ and at $F = 0$. The computation at $F = 1$ represents the light-catchers perfectly focusing light that is reflected by the light-catchers onto the PMT active area, and $F = 0$ represents the light-catchers directing none of the light. The true solution exists somewhere between these extremes.

Utilizing the geometric values illustrated in Fig. 3.10 as well as the calculation of $N = 168$ from Eq. (3.10), we calculate the best case scenario where $F = 1$ to be

$$\begin{aligned}\left.\frac{\text{Photoelectrons}}{\text{PMT}}\right|_{\text{F=1}} &= \frac{168 * 0.9 * 0.15}{8} * \left[\pi(0.25/2)^2 + (0.31^2 - \pi(0.29/2)^2) * 0.9 * 1\right]/0.31^2 \\ &= 2.25\ \text{photoelectrons/PMT}\,.\end{aligned} \tag{3.14}$$

For the worst case scenario of $F = 0$, we find

$$\begin{aligned} \left.\frac{\text{Photoelectrons}}{\text{PMT}}\right|_{\text{F=0}} &= \frac{168 * 0.9 * 0.15}{8} * \pi(0.25/2)^2/0.31^2 \\ &= 1.45 \text{ photoelectrons/PMT}\,. \end{aligned} \tag{3.15}$$

To conduct a more detailed evaluation of uncertainties, we would need to assign appropriate uncertainties to the variables and propagate them through the calculation. Particularly, the measurements of the QE and the Al coating reflectivities should have associated uncertainties. A measurement of F or a more grounded estimate with uncertainty would also be helpful. As for now, this conservative estimate for the average number of photoelectrons per PMT in an electron event is between 1.5 and 2.25 photoelectrons per tube with the simple average of those two being 1.85 photoelectrons per tube. Since we can't have fractions of photoelectrons, it is reasonable to conclude that this calculation predicts that there will be one, two, or three photoelectrons per tube in a typical event, with the most likely number being two photoelectrons. This does not take into account the elliptical nature of the light-cone at the PMT array that we calculated above and is illustrated in Fig. 3.9. The number of Cherenkov photons incident on each cell likely varies, and thus the number of photoelectrons detected in each PMT in a cluster varies. In this calculation, we did not take into account the 3-dimensional nature of the light-catchers: here we used a projection of the area onto the plane of the PMT face, which may not fully account for the behavior of the light-catchers. A simulation that models the variation in photons per cell and the behavior of the light catchers could be an interesting next step.

Simulations conducted during the design process simulations found an average of 1.7 photoelectrons per PMT in a cluster [61], suggesting that we expected one-to-two photoelectrons per PMT. The above calculations of one-to-three photoelectrons agrees with that result to first order. The original result of one-to-two photoelectrons motivated setting the trigger for the front-end signal amplifier for the GRINCH PMTs very low—we wanted the amplifier to trigger on a single photoelectron, which is the smallest signal that can be produced by single photon incident on the photocathode. The back-of-the-envelope result presented here agrees with this low-threshold approach. However, this causes the individual GRINCH PMTs to frequently trigger on noise, making clustering extremely important for identifying correlated signals in GRINCH that come from Cherenkov events.

This initial result also suggested that there would be very little variation in the signal output for each PMT—leading us to not prioritize studying the shape and amplitude of the signals because they were assumed to be very uniform, and rather focus on studying the timing of the signals. Although more consideration would need to be put into quantifying uncertainty of both the simulation and the calculations presented here before making definitive statements, the result of one-to-three photoelectrons (with an average of 1.7) suggests that there may be slightly more variation in signal amplitude than originally anticipated, although further study of the light catchers would be needed. The signal amplitude directly impacts when the signal crosses over threshold (LE), and without correcting for the variations caused by signal size, called time-walk corrections, there is a limit on how well the LE timing can be aligned. There are both pros and cons to this approach of focusing on the solely timing and rather than signal shape, and given the chance to go back, I may have approached things differently. We will discuss further in the Conclusions Section of this thesis.

3.2.5 DAQ

The small electrical signals in the GRINCH PMTs are collected, amplified, transported and stored by the GRINCH Data Acquisition (DAQ) system. Figure 3.13 shows the layout of the GRINCH DAQ. GRINCH has a Time-to-Digital Converter (TDC) channel on every PMT, and Analogue-to-Digital Converter (ADC) channels on some PMTs that were mainly used for debugging and calibrations. The path the TDC signals take from the PMT to the modular electronics crate containing the TDCs are along the top of the diagram, the ADC path to the modular electronics crate is in the middle, and the high voltage (HV) is on the bottom.

The signals from the PMTs go to 32 ultra-fast front-end amplifier/discriminators called NINO boards located on the side of GRINCH [62] [63]. These NINO boards take 16 channels, have adjustable thresholds, and have LVDS and analogue output. The thresholds for these boards were set low so that single photoelectron signals would be above threshold. Low-voltage power distribution boards power the NINO cards.

The LVDS output from each NINO card travels to the patch panels located on the detector. From the patch panels, the LVDS signals travel 100 m to the LVDS-to-ECL converters. These converters also acts as repeaters, minimizing the signal degradation issues that arise over transporting signals long distances. The ECL signals then travel another 100 m along ribbon cables to a patch panel in the shielded bunker where the back-end DAQ electronics for all the SBS detectors reside. The 16 channel ribbon cables are then combined into the 32-channel input required by the VETROC[1] read-out controller, which we use as a TDC. When the VETROC receives a trigger, the data are recorded.

The analogue signal output from four NINO cards are transported to the detector hut via BNC cables and patch panels. JLab-designed fast analogue to digital converters, fADC-250, read in the analogue signals from GRINCH.

The high voltage system is also shown in this diagram. 64 high voltage channels are used to power all the GRINCH PMTs. For GRINCH, every one HV channel sets the high voltage of 8 PMTs in parallel. PMTs with similar gain were grouped together.

3.2.6 High Voltage and Gain Matching

Starting with approximately 800 PMTs, each PMT was carefully tested for performance and gain characterization. The PMTs were organized into groups of 10 that shared similar gains at a given HV [64]. The HV system for GRINCH has 8 PMTs in parallel for each high voltage channel, meaning all 8 have the same HV value. These groups of 10 PMTs allowed groups of 8 PMTs to be powered by one high voltage channel, plus 2 spare PMTs in each group to be installed if a PMT was damaged. During production running, these

---

[1] "Virginia Tech Read-Out Controller"

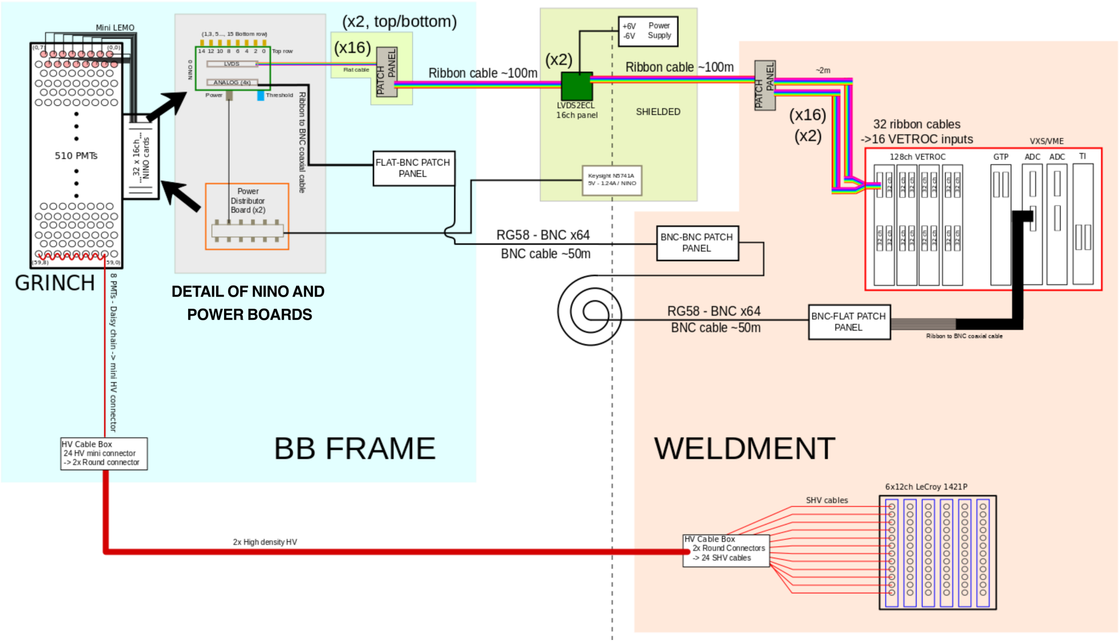

Figure 3.13: GRINCH DAQ layout. The path the TDC signals take from the PMT to the read-out-controller (VETROC) are along the top of the diagram, the ADC path is in the middle, and the high voltage is on the bottom. The hardware components to the right of the dotted line are in the bunker behind concrete shielding.

groups were set to the HV values determined during these groupings[2]. Some adjustments were made during running when the time-over-threshold looked small in certain groups[3].

3.3 Timetable

During GMn running, it took us some time to learn and make adjustments to GRINCH to be able to see signals from electrons during production data taking. Table 3.2 shows which gas was in GRINCH and its status during the various GMn kinematics. The very nature of a Cherenkov detector makes it challenging to calibrate outside of production running. Cosmic ray muons do not have the speed necessary to produce Cherenkov radiation in air, CO_2, or C_4F_8 gas. The only signal we can get from cosmic rays is when a cosmic ray interacts directly with the glass on the face or side of a PMT and creates a small amount of Cherenkov light in the glass itself. To emulate a Cherenkov event generated by an electron, we use a UV LED fed by a pulse generator at a very low voltage and small pulse width. Generating a pulse to produce just a few photons from the LED setup is difficult. And thus it is challenging and an imperfect method for calibrating the HV of the PMTs without the electron beam. Because of this, we had to do a large amount of problem solving and calibrating while we were taking production data.

In this analysis, we will mainly focus on SBS 8 and SBS 9 where the HV for the GRINCH PMTs was high enough and the TDC DAQ was working properly. Some valuable analysis may be able to be recovered for the other kinematics, especially SBS 14 where the HV was high enough and the heavy gas was being used. We would have to account for the large sections of missing channels by perhaps making a cut on the track projection and rejecting events whose light cones would land on empty channels. These missing channels were due to a firmware issue with the new VETROC TDCs, which was found and solved the morning after production data-taking was completed for SBS 14.

---

[2] They were set to the values determined by this study after I realized the HVs were set way too low during production running.

[3] ADC's on every channel in GRINCH would have been helpful with adjusting gains during running, as we would be then be able to look at the signal shape and amplitude.

Table 3.2: The status of GRINCH during the GMn experiment. There were several challenges with the running of GRINCH during GMn. SBS 8 and SBS 9 are the only kinematics where the GRINCH TDC DAQ was working properly, the HV was set high enough, and the heavy gas was being used.

KINE.	START	END	RUNS	GAS	GRINCH NOTES
SBS-4	10/22/2021	10/25/2021	11493 -11622	CO_2	HV too low
SBS-5	10/25/2021	11/12/2021	11624 - 11941	CO_2	HV too low
SBS-7	11/13/2021	11/22/2021	11964 - 11209	CO_2	HV too low
SBS-11	11/23/2021	12/21/2021	12236 - 13064	CO_2	HV too low
SBS-14	01/10/2022	01/20/2022	13168 - 13407	C_4F_8	Various TDC issues Many missing channels
SBS-8	01/21/2022	01/31/2022	13424 - 13620	C_4F_8	HV and TDC Stable
SBS-9	02/01/2022	02/08/2022	13639 - 13799	C_4F_8	HV and TDC Stable

3.4 GRINCH Analysis

3.4.1 Individual Channels

Figure 3.14 illustrates how an electrical signal from a PMT is processed by a discriminator. The PMT output is a negative voltage. When the signal first crosses the discriminator threshold, a digital pulse is generated at the leading edge (LE); when it crosses back above the threshold, a pulse is generated at the trailing edge (TE). The time difference between TE and LE is called the time-over-threshold (ToT), which is proportional to the signal amplitude. The TDC measures the LE, TE, and thus the ToT, relative to the hodoscope mean cluster time.

GRINCH employs time-to-digital converters (TDCs) on all 510 PMTs, and analog-to-digital converters (ADCs) on only 64 channels. TDCs provide fast measurements of timing (LE, TE, ToT), whereas ADCs can capture the full signal shape and amplitude. For production analysis, GRINCH utilizes TDC data, as the LE and ToT is sufficient for its role as a threshold detector.

The GRINCH TDC has a time resolution of 1 ns per bin. To suppress global DAQ timing jitter, the hodoscope cluster mean time is subtracted from the GRINCH LE time on an event-by-event basis. This subtraction improves the apparent resolution of the

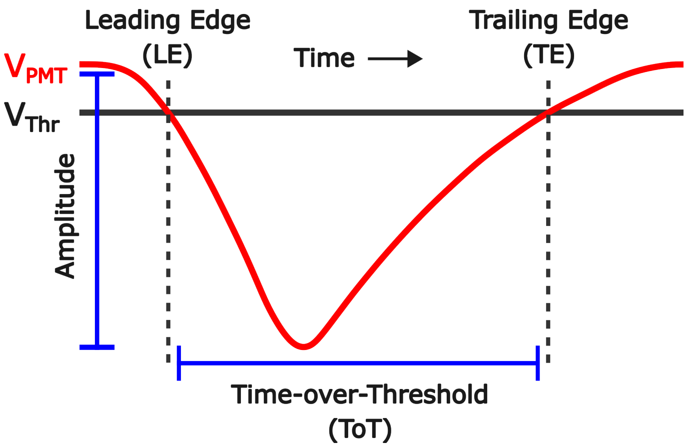

Figure 3.14: Diagram of a PMT signal in a discriminator. The PMT signal voltage is shown in red, and the threshold voltage in black. The leading edge (LE) marks the time the signal crosses the threshold, and the trailing edge (TE) when it rises back above. Time-over-threshold (ToT) is the duration between LE and TE. The amplitude is the peak signal value. Figure adapted from W.R. Leo [65].

GRINCH, since the hodoscope TDC resolution is better than 1 ns. Figure 3.15 shows the LE time distribution of a single PMT after this correction; a Gaussian fit gives $\sigma \approx 4.6$ ns, which can be interpreted as the GRINCH timing resolution for that PMT.

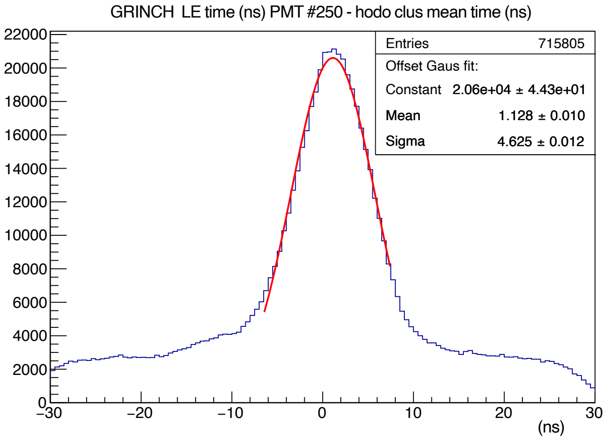

Figure 3.15: LE time distribution of a single GRINCH PMT during production running of SBS-9. The hodoscope cluster mean time is subtracted from the GRINCH TDC time to remove DAQ jitter effects.

For comparison, Fig. 3.16 shows the LE distribution of the same PMT without the hodoscope correction, illustrating the broader distribution of $\sigma \approx 5.1$ ns due to DAQ jitter. This jitter subtraction method is also used in other detectors such as BBCal [36] and assumes precise calibration of the hodoscope timing. Future calibration improvements could further improve GRINCH timing resolution.

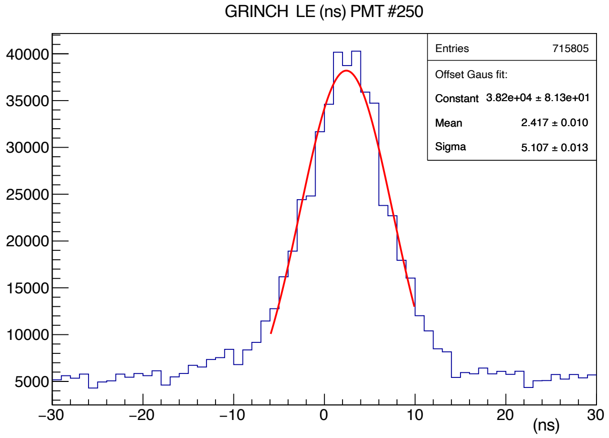

Figure 3.16: LE time distribution of a single GRINCH PMT during SBS-9, without hodoscope time correction. DAQ jitter broadens the distribution compared to Fig. 3.15.

Unless otherwise specified, this analysis includes a “global cut” on the number of tracks, invariant mass, and target vertex, based on the reconstructed GEM track. Details of these cuts are listed in Table B.1.

Figure 3.17 shows the ToT spectrum of a single PMT, which peaks around 11 ns. As the ToT is proportional to signal amplitude, it provides a measure of the signal strength, albeit in TDC time units. A calibration would be required to convert ToT into an integrated charge. The ToT distribution is quite large, likely due to a large range in path-lengths of the light cones, depending on the position and angle of the charged particle passing through GRINCH.

Although GRINCH has 510 PMTs, only 64 channels were equipped with ADCs. In principle, one could correlate ADC-measured pulse amplitudes with TDC ToT values to calibrate the ToT to charge conversion. However, since GRINCH is used as a threshold detector, and only 64 ADC channels were available, this calibration was not performed during production running—ToT was deemed sufficient.

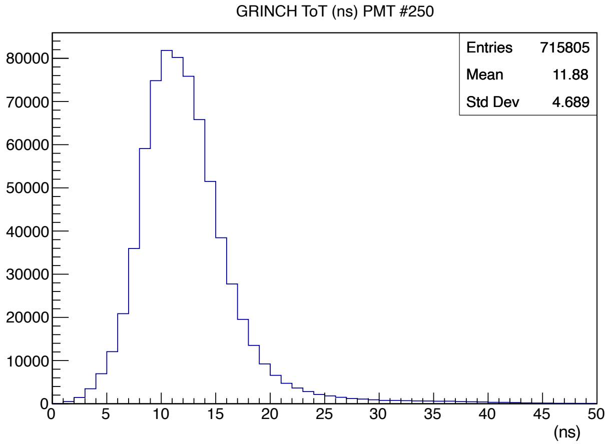

Figure 3.17: ToT distribution of a single GRINCH PMT. The ToT is proportional to the amplitude of the signal. Units are in nanoseconds and would need calibration to relate to integrated charge.

3.4.2 Leading Edge Calibrations

The main calibration applied to GRINCH is the timing alignment of its photomultiplier tubes (PMTs). Ideally, a good electron event should appear at the same time relative to the trigger, regardless of which PMT detects the light. However, each PMT channel can have a slightly different mean time for such events, due to factors such as signal cable lengths, intrinsic electronics delays, variations in optical path length, and the size of the signal pulse. Channel-to-channel differences that add a constant delay—such as differences in cable length—can be corrected by applying offsets individually to each channel.

To eliminate timing jitter from the event trigger, the hodoscope mean cluster time is subtracted from each GRINCH TDC time. See Sec. 2.5.3 for further details on this correction.

The first-order leading edge (LE) calibration consists of shifting each channel's LE distribution so that its mean aligns to zero for good electron events. This is accomplished by fitting the LE distribution in each channel to a Gaussian plus a constant background and then applying an appropriate offset. To reduce background in these calibration data, we apply good electron selection cuts based on other detectors, such as track quality, target vertex, and invariant mass cuts (see Sec. 4.5 and Tab. B.1 for details). We also use GRINCH-specific clustering and track-matching (described in Secs. 3.4.3 and 3.4.4) to further select good electron events. However, applying overly tight cuts reduces the available statistics and can make the calibration challenging.

Figure 3.18 shows the GRINCH leading edge times before and after alignment. After calibration, the LE distribution is narrower and centered closer to zero. Specifically, the Gaussian width decreases from $\sigma = 5.252$ ns before alignment to $\sigma = 4.494$ ns after alignment.[4]

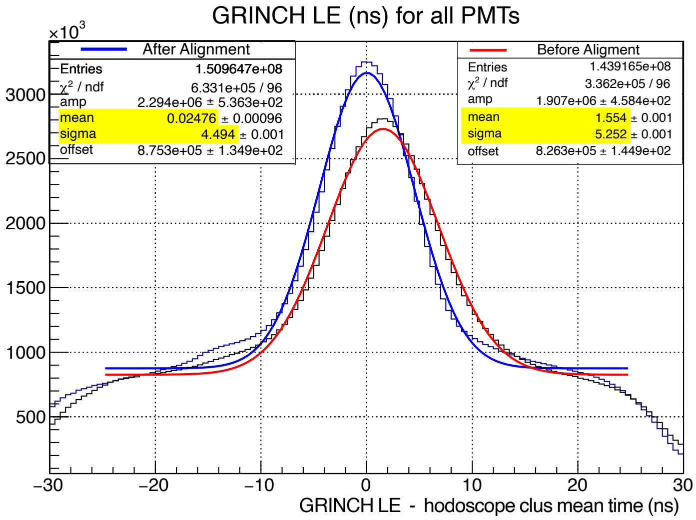

Figure 3.18: GRINCH leading edge alignment. The red fit shows the LE distribution before alignment, and the blue fit shows it after alignment. The Gaussian width decreases after alignment, indicating improved timing resolution.

Improved alignment around zero enables more stringent timing cuts, which enhance electron selection by reducing background contamination.

3.4.3 Clustering

Due to the small distance the light has to propagate in GRINCH, the Cherenkov cones often appear as bunches of PMTs firing near each other, which we call "clusters". Figure 3.19

---

[4] In Fig. 3.18, the red "before" histogram is plotted as (GRINCH LE time −900 ns), since it was centered around 900 ns during SBS-8 and SBS-9 in GMn. This shift is for illustrative purposes.

shows an event in GRINCH in the single-event display. Although the implementation of clustering algorithms is complex, the idea of our clustering is straight-forward. First we cut out any PMTs whose leading edge are outside the time window we expect the electron events to arrive in. We then go through the remaining hits and group hits together that are either adjacent or 1 PMT away from each other in any direction. Then for each cluster, we calculate the center (geometric average of positions of the tubes that fired), the total time-over-threshold, and the index of each PMT which makes up the cluster. Clustering helps eliminate background from dark noise from the PMTs that happen to fire in-time, and well as in-time background events. If there are multiple clusters, track-matching is utilized to choose which cluster is the "best cluster". We will discuss track matching in Sec. 3.4.4.

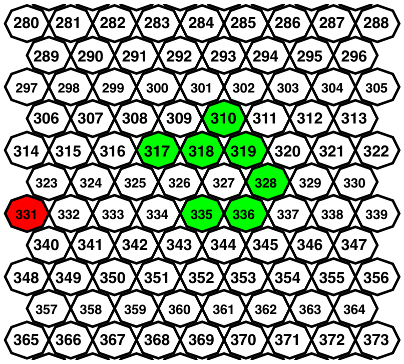

Figure 3.19: GRINCH cluster in the single-event display. All hits pictured are within a 60 ns time window. The PMTs are numbered 0–509. This figure is zoomed-in around a cluster in the 300's. The single PMT firing at position 331, colored red, has been identified as a separate cluster to the 7-PMT event in green, since it is more than 2 PMTs away in the array.

Figure 3.20 and Fig. 3.21 show several examples of real events in GRINCH in the single-event display. The green highlighted events are clusters that have been track-matched and determined to be the "best cluster" in the event.

The utility of clustering is demonstrated in Fig. 3.22. The number of PMTs fired in-time in GRINCH does not give much insight into particle ID. However, cluster size gives us a clearer distinction between good electron events and other events. After applying track

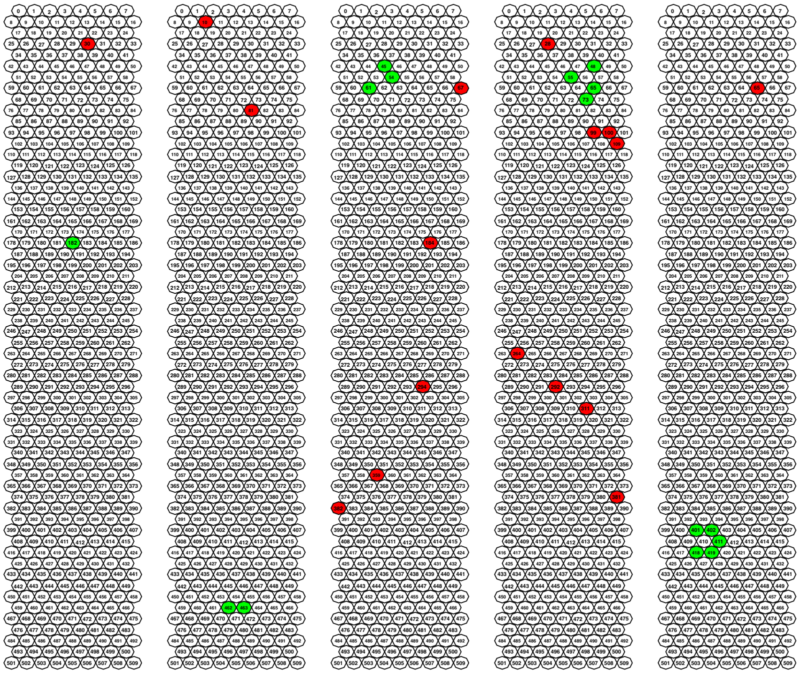

Figure 3.20: Examples of cluster sizes 1 (leftmost) through 5 (rightmost) in the GRINCH single-event display.

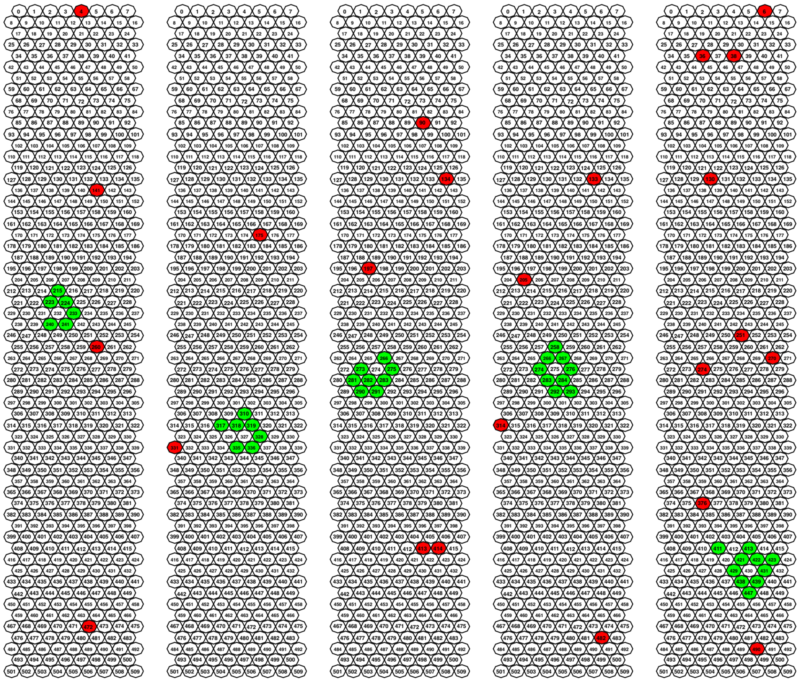

Figure 3.21: Examples of cluster sizes 6 (leftmost) through 10 (rightmost) in the GRINCH single-event display.

matching discussed in Sec. 3.4.4, this distinction becomes clearer, allowing electron detection and background rejection. We will investigate the detection efficiency of GRINCH in relation to the other detectors in BigBite in Sec. 3.4.5.

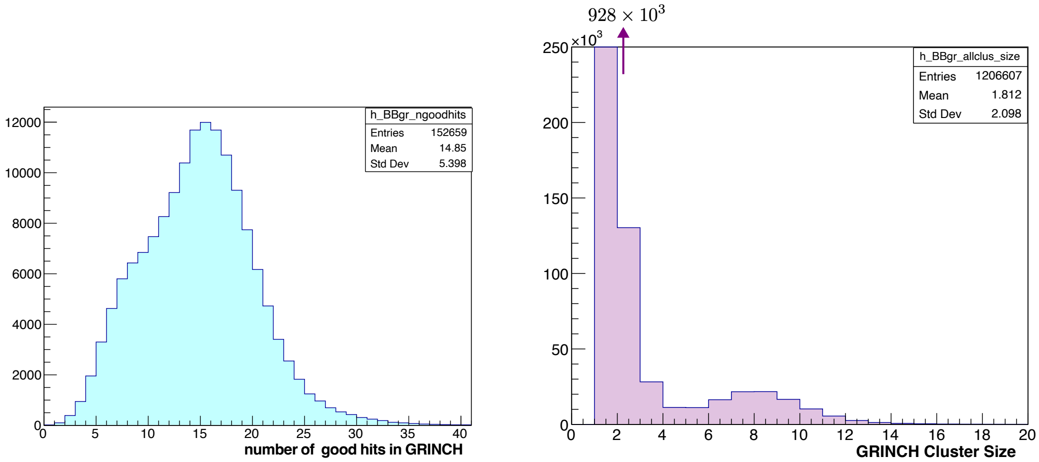

(a) Good hits: no clustering

(b) Cluster size

Figure 3.22: The number of good hits in GRINCH compared to GRINCH cluster size in SBS-9. **(a)** A "good hit" is when the LE is within the 60 ns time window. **(b)** The cluster size for all GRINCH channels fired during trigger events and are within the 60 ns time window. Note that cluster size of 1 extends far beyond the axis range. By using clustering, we can more easily extract what hits may be from good electron events.

3.4.4 Track-Matching

In GRINCH, we observe an approximately linear correlation in the dispersive direction, x, between the location of the track projected to the entrance window of the GRINCH and the cluster location on the PMT array (Fig. 3.23). We exploit this correlation to suppress background and improve electron selection and pion rejection.

The projected location at the GRINCH window is computed with simple trigonometry from the track parameters at the focal plane. Refer to the diagrams of Figs. 2.4 and 2.6 for the coordinate system. Track-θ is defined in the dispersive direction of the electrons.

Using the small-angle approximation, we calculate

$$x_{\text{proj}}^{\text{GRINCH}}\,[\text{m}] = x_{\text{track}}\,[\text{m}] + \theta_{\text{track}}\,[\text{rad}] \times 0.48\,[\text{m}]\,, \tag{3.16}$$

where x_{track} and θ_{track} are defined at the focal plane, a reference plane located upstream of the first GEM detectors and outside the magnetic field of the BigBite magnet. The GRINCH entrance window lies 0.48 m downstream of the focal plane.

Similarly, the projection in the non-dispersive direction y is given by

$$y_{\text{proj}}^{\text{GRINCH}} = y_{\text{track}} + \phi_{\text{track}} \times 0.48\,. \tag{3.17}$$

We note that this approach projects the track to the entrance window rather than to the mirror surfaces, where the reflection of the light cone formation actually occurs. While projecting directly to the mirror faces would be more physically accurate and logically grounded, the analysis was already well underway with the window projection by the time this consideration arose, and redoing the fits was not practical.

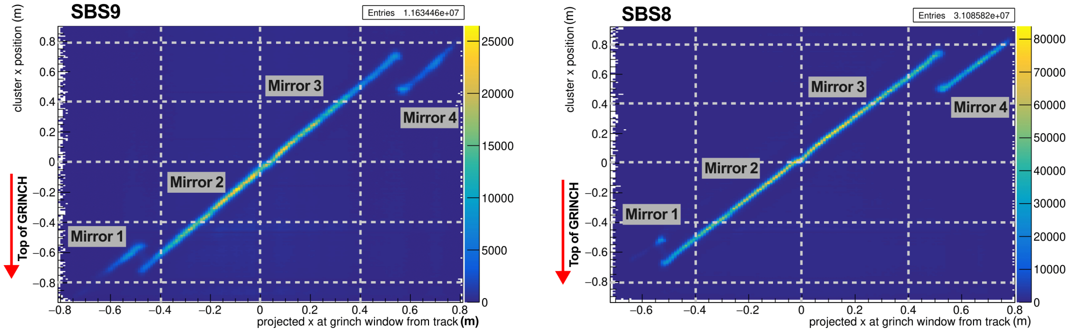

(a) SBS-9

(b) SBS-8

Figure 3.23: GRINCH cluster x position vs. projected x position at GRINCH window from GEM track. The projected x position is calculated using Eq. (3.16). Sub-figure **(a)** shows this relationship for the lower momentum kinematic, SBS-9, and **(b)** shows this for the higher momentum kinematic, SBS-8. Note that the correlation is slightly shifted between kinematics.

Figure 3.23 illustrates the dispersive correlation for two kinematic settings, SBS-8 and

SBS-9. We observe a slight shift between the kinematics, which is expected because higher-momentum electrons experience less bending in the magnetic field, and their light cone intercepts the mirrors at slightly different positions, producing clusters at shifted locations on the PMT array. Nevertheless, the slopes of the correlations remain consistent, suggesting that a single linear functional form can describe each mirror across kinematics.

To quantify the offset between the track projection and the observed GRINCH cluster, we define

$$\begin{aligned} \text{GRINCH } dx &= x_{\text{cluster}} - x_{\text{proj}}^{\text{GRINCH}} \\ \text{GRINCH } dy &= y_{\text{cluster}} - y_{\text{proj}}^{\text{GRINCH}}\,, \end{aligned} \tag{3.18}$$

where $x_{\text{proj}}^{\text{GRINCH}}$ and $y_{\text{proj}}^{\text{GRINCH}}$ are given by Eqs. (3.16) and (3.17).

In Fig. 3.24, we show GRINCH dx versus track-θ for the two kinematics. Four approximately linear trends corresponding to the four mirrors are visible and exhibit consistent slopes across kinematics. This observation justifies constructing one linear fit per mirror, valid for all kinematic settings.

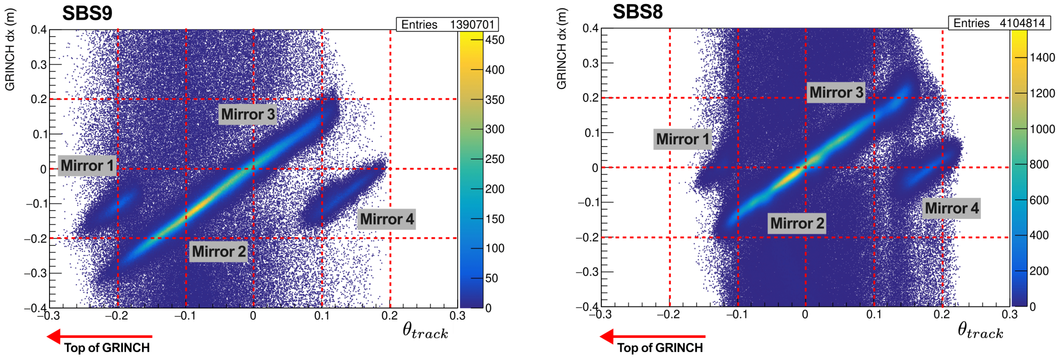

(a) SBS-9

(b) SBS-8

Figure 3.24: GRINCH dx vs. track θ (dispersive direction). Subfigure **(a)** shows this relationship for SBS-9, and Subfigure **(b)** shows this relationship for SBS-8.

For each mirror, events are selected by applying a 1 cm wide cut on the GRINCH cluster x position (x_{cluster}) to isolate hits on that mirror. Each bin in track-θ is then projected onto GRINCH dx, and the distribution is fitted with a Gaussian plus a constant offset to account for background. The Gaussian mean values are then fit linearly as a function of

θ_{track} to obtain a functional description for each mirror (Fig. 3.25).

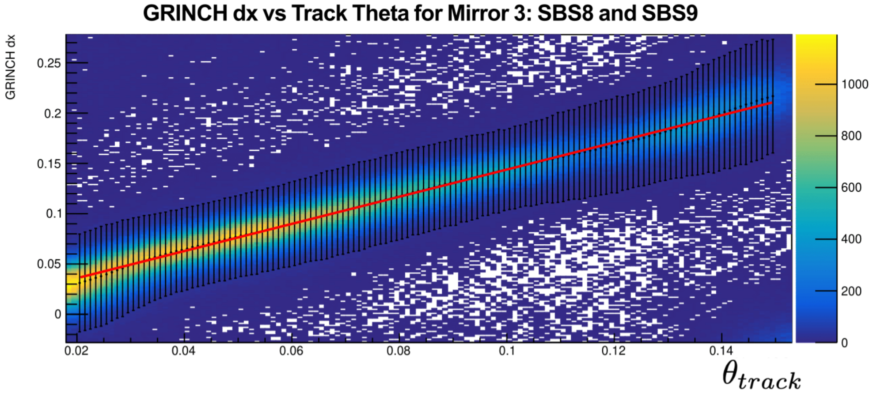

Figure 3.25: Fit to GRINCH dx vs track-θ for mirror 3. This histogram combines data from SBS-8 and SBS-9. Each bin in Track-θ is projected onto GRINCH dx. A Gaussian fit is applied to each histogram. A linear fit is applied to the mean of the Gaussian fits (red). The error bars represent $\pm 3\sigma$, where σ is the width parameter from the Gaussian fit. See Appx. C for more details on Gaussian and linear fits.

In the non-dispersive direction (y), a similar procedure is applied, using GRINCH dy versus track-ϕ. However, as seen in Fig. 3.26, the relationship in y is non-linear and requires a higher-order fit. Because the PMT array is much taller than it is wide, constraints in y are less effective: beyond a few σ, events already fall outside the PMT area.

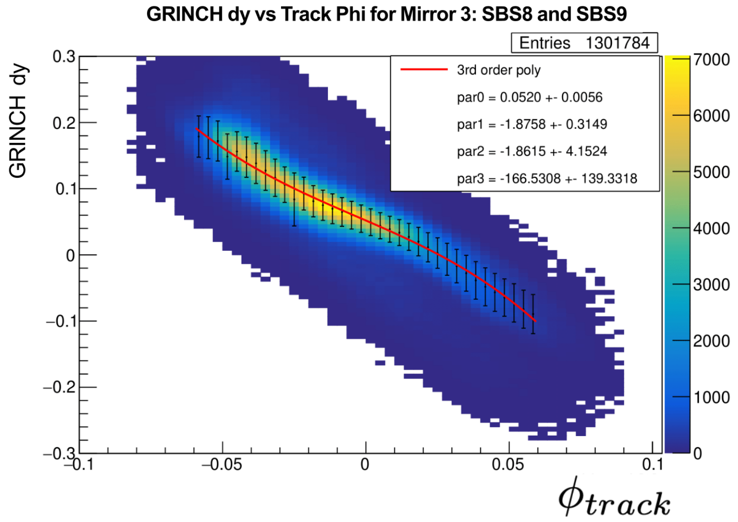

Figure 3.26: Fit to GRINCH dy vs track ϕ mirror 3, illustrated with $\pm 3\sigma$ fits on the error bars.

An event is considered "track-matched" if the deviation from the fitted line in both x and y falls within a specified number of standard deviations (N_σ). Specifically, we compute:

$$\sqrt{\left(\frac{\text{GRINCH } dx}{\sigma_x}\right)^2 + \left(\frac{\text{GRINCH } dy}{\sigma_y}\right)^2} < N_\sigma \,, \tag{3.19}$$

where σ_x and σ_y are the average widths of the Gaussian fits for x and y, respectively. The smallest such N_σ across all mirrors and clusters is used to identify the best track-matched cluster.

Figure 3.27 shows the Preshower energy distribution under different GRINCH track-matching and cluster size cuts. Track-matched events with clusters of at least three PMTs (green) populate the higher-energy peak consistent with electrons, while unmatched events (red) and track-matched clusters with fewer PMTs (blue) tend to populate the lower, MIP-like peak, which is typical of pions or noise. We also note a small bump near 0.1 GeV in the green distribution, suggesting that some noise or MIP-like events still pass the track-matching criteria. Since pions should be below Cherenkov threshold at these kinematics, the origin of this bump remains uncertain and warrants further investigation.

To further explore the relationship between track-matching, cluster size, and PID, Fig. 3.28 shows the GRINCH cluster size distributions for SBS-9 events, separated by whether the cluster was track-matched and whether the Preshower energy exceeds 0.2 GeV, a loose cut intended to identify electrons. This simple cut is not sufficient to fully separate electrons from pions because the two distributions overlap: pions tend to produce a narrow peak around 0.1 GeV in the Preshower, while electrons produce a broader distribution peaking at higher energies. Consequently, some electrons and MIPs are inevitably misclassified with this cut alone. The Preshower thus serves here as an independent PID estimator to cross-check the GRINCH performance, though a more reliable separation requires combining information from the Preshower, Shower, and GRINCH detectors.

Clusters that are track-matched (Fig. 3.28a) exhibit larger cluster sizes when the Preshower energy is consistent with electrons (green), while clusters that are not track-

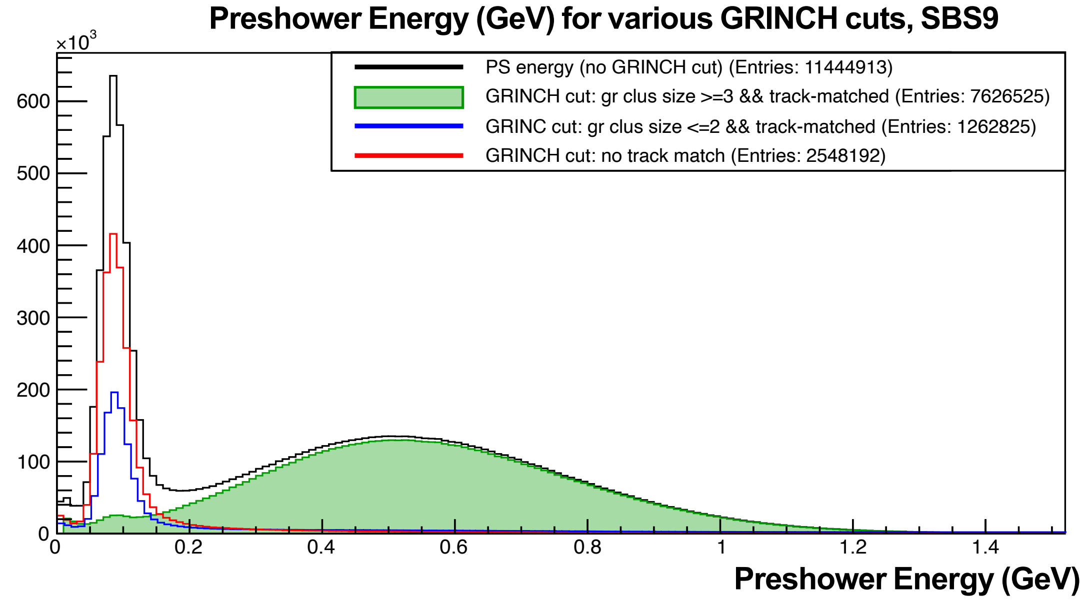

Figure 3.27: Preshower energy for various GRINCH track-matching cuts. (Green): GRINCH cluster >= 3 and track-matched. (Blue): GRINCH cluster <= 2 and track-matched. (Red): No track-match found.

matched (Fig. 3.28b) predominantly populate lower cluster sizes, especially when the Preshower energy is consistent with pions (red). This qualitative behavior supports the interpretation that track-matching effectively suppresses noise and MIP-like events, although additional detectors are necessary for robust PID, which will be explored in the next section.

3.4.5 Pion Rejection Efficiency and Electron Detection Efficiency

As shown earlier in Fig. 3.11, some pions in SBS-8 have momenta above the GRINCH pion threshold and can therefore produce Cherenkov light, albeit with a weaker signal than electrons at the same momentum. In contrast, in SBS-9, the pion momenta lie below the threshold, so pions are not expected to emit Cherenkov light. Consequently, GRINCH should reject pion events more effectively in SBS-9 than in SBS-8.

One method for characterizing GRINCH performance is to compute electron detection efficiency and pion rejection efficiency, relative to the other detectors in the BigBite elec-

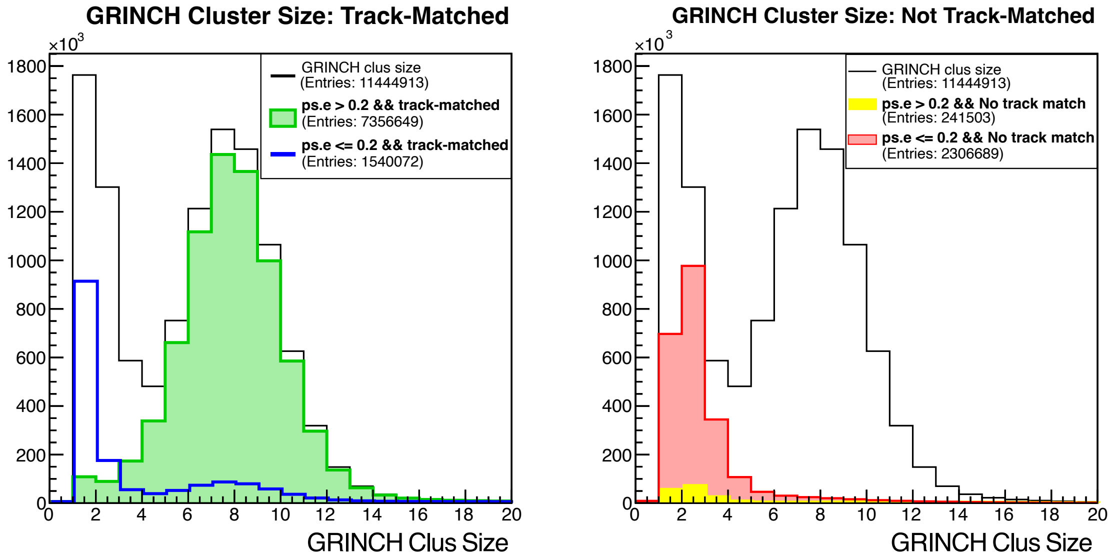

(a) Track-matched clusters.

(b) Unmatched clusters.

Figure 3.28: GRINCH cluster size distributions for SBS-9. **Left (a):** Clusters matched to a track. The green distribution corresponds to events where the Preshower energy $> 0.2\,\text{GeV}$ (electron-like), and the blue distribution corresponds to events where the Preshower energy $\leq, 0.2\,\text{GeV}$ (pion-like). **Right (b):** Clusters not matched to a track. The yellow distribution corresponds to events where the Preshower energy $> 0.2\,\text{GeV}$, and the red distribution corresponds to events where the Preshower energy $\leq 0.2\,\text{GeV}$. The black line in both plots shows the total cluster size distribution.

tron arm. We apply tight electron PID cuts in the other detectors and check whether GRINCH detects a cluster above a given cluster size threshold for those events. This analysis assumes that the other detectors do not produce false positives or miss true electrons—an assumption that should be revisited in future work. A more complete analysis could incorporate the estimated efficiencies of the other detectors, such as the GEMs and BBCal Shower and Preshower.

We examine GRINCH performance as a function of the minimum required cluster size and the presence or absence of track-matching. An event is considered "detected" in GRINCH if it contains a cluster with size greater than or equal to a specified threshold. The electron detection efficiency and pion rejection efficiency are defined as

$$\begin{aligned}&\textbf{Electron Detection Efficiency}(N) = \\ &\frac{\#\text{events passing } e^- \text{ cuts and GRINCH Cluster Size} \geq N}{\#\text{ events passing } e^- \text{ cuts}},\end{aligned} \tag{3.20}$$

$$\begin{aligned}&\textbf{Pion Rejection Efficiency}(N) = \\ &\frac{\#\text{events passing } \pi^- \text{ cuts and GRINCH Cluster Size} < N}{\#\text{ events passing } \pi^- \text{ cuts}}.\end{aligned} \tag{3.21}$$

It is worth noting that in SBS-9 the pion momenta lie below the GRINCH Cherenkov threshold, so true pions should not produce Cherenkov light. Therefore, the events identified by the π^- cuts in SBS-9 that produce GRINCH signals are unlikely to be actual pions; they may instead originate from noise or misidentified electrons. Nevertheless, we retain the term "pion rejection efficiency" for consistency, keeping this caveat in mind.

The e^- and pion cuts used in this analysis are detailed in Table B.1. This study includes only cuts on the electron arm; adding quasi-elastic cuts on the hadron arm could improve PID confidence but would reduce statistics. If the efficiencies varied significantly with tighter hadron-arm cuts, that could contribute to the uncertainty in the GRINCH efficiency.

Figure 3.29 shows that track-matching slightly reduces the electron detection efficiency (from ~ 0.977 without track-matching to ~ 0.967 with track-matching) while improving the pion rejection efficiency. This is consistent with track-matching rejecting some true electrons, but better suppressing background events. Since SBS-9 pions are below threshold, the signals in GRINCH we see in the pion region are unlikely to be pions, and may originate from noise or misidentified electrons.

It is important to note that this analysis starts from events with cluster size ≥ 1, since a cluster must exist to attempt track-matching. Events with no cluster at all are excluded, which could lead to an underestimate of GRINCH's rejection capability. However, in practice such zero-cluster events are rare due to high background rates.

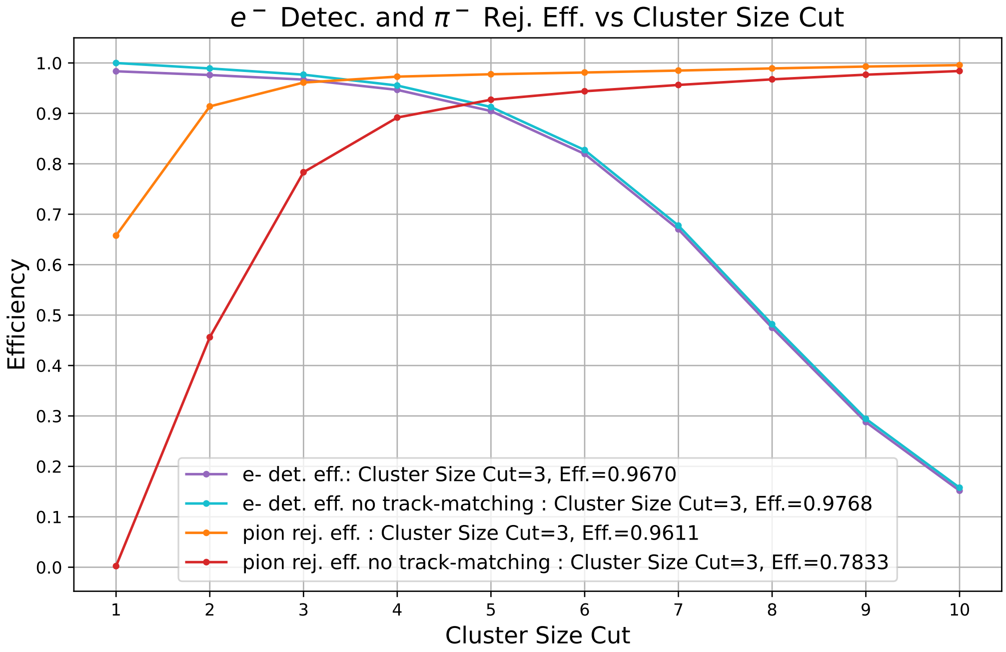

Figure 3.29: GRINCH efficiency as a function of minimum cluster size for SBS-9, comparing track-matching (solid) to no track-matching (dashed). Track-matching improves rejection of pion events while slightly reducing electron detection efficiency.

Figure 3.30 shows the same analysis, focusing only on track-matched events. As the minimum cluster size increases, electron detection efficiency decreases while pion rejection efficiency increases. This trade-off illustrates the balance between maximizing electron purity and maintaining acceptable statistics. For example, a cut at cluster size ≥ 7 yields nearly perfect rejection of pion events but retains only $\sim 70\%$ of electrons. In contrast, a cut at cluster size ≥ 3 achieves high rejection with minimal loss of electrons, making it a reasonable choice for production data. With a cut at cluster size 3, GRINCH achieves an electron detection efficiency of approximately 97%, and a pion rejection efficiency of approximately 96%.

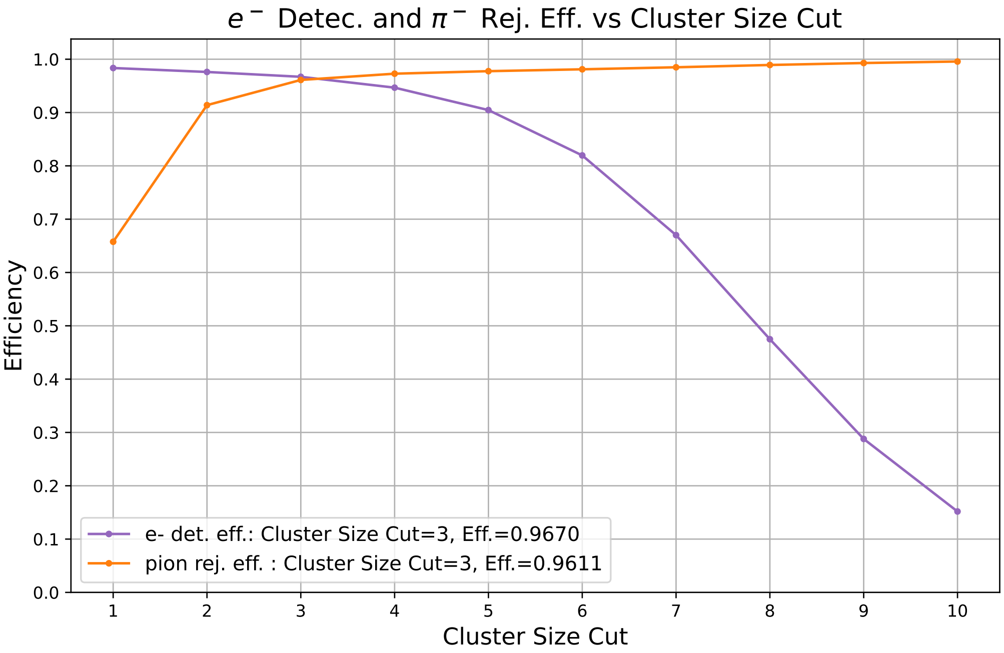

Figure 3.30: GRINCH efficiency as a function of minimum cluster size for SBS-9, with track-matching applied. A cut at cluster size ≥ 3 balances high electron detection efficiency and pion rejection.

Future work should explore the uncertainties associated with these efficiency estimates. In particular, the assumption that the other detectors are 100% efficient could be relaxed, e.g., assuming $99\% \pm 0.9\%$ efficiency and propagating this uncertainty. Similarly, varying the electron and pion cut definitions could quantify systematic uncertainties. Table B.1 includes looser cut configurations that yield noticeably different efficiencies, but these were excluded here to maintain tighter PID selection.

GRINCH demonstrates strong performance in both electron detection and suppression of pion events on the order of 97%, particularly when applying track-matching and an appropriate cluster size cut. While tighter cuts improve purity, they reduce efficiency and statistics. A cluster size cut at ≥ 3 with track-matching represents a practical compromise. The next section discusses possible reasons for the unexpectedly high rates observed in GRINCH during these measurements.

3.5 Event Rates in GRINCH

During in-beam production data for the GMn experiment, GRINCH experienced exceptionally high singles rates, with individual PMTs registering between 600 kHz and 1 MHz. These high rates were expected due to the combination of high luminosity, large spectrometer acceptance, direct line of sight to the target, and the absence of shielding. They were also consistent with predictions from the SBS Monte Carlo simulation. In fact, the GRINCH design—small-diameter PMTs, distributed over many channels, and relying solely on precise timing—was specifically chosen to handle such rates. It is notable that GRINCH successfully operated under these conditions, as such high-rate performance is uncommon among gas Cherenkov detectors.

At a rate of approximately 1 MHz per tube, one can estimate the rate of random coincidences within the typical 60 ns timing window. Given this rate, about three random tubes are expected to fire during the 60 ns window simply from background noise. Therefore, isolated single-tube hits and even some small clusters observed in GRINCH that are in-time with the trigger are entirely consistent with random background, rather than true electron signals. This highlights the importance of clustering and track-matching techniques to distinguish signal from background. It is also worth noting that all PMTs were selected to have dark noise rates below 10 kHz, making the contribution from intrinsic PMT dark noise within a 60 ns window negligible. While δ-electrons (knock-on electrons) can also contribute random hits, their rate is small compared to the dominant background singles rate. In summary, the random tubes firing in the timing window—but not part of a cluster or matched to a track—are expected and consistent with the high background environment. Future studies could investigate whether such randoms contribute to pion misidentification or affect pion rejection efficiencies.

An additional observation was made during beam-off periods, after prolonged running: a residual rate of about 50 kHz per tube was observed, which decayed back to the nominal dark noise rate within 1–2 hours. Since the Cherenkov threshold in the gas corresponds to electron energies of $\sim$10 MeV, these signals were unlikely to be due to ambient electrons producing Cherenkov light. A plausible explanation is that radioactive decay products from activated detector materials, likely β-decays, produced Cherenkov light in the PMT glass windows themselves.

Finally, for context, the NINO discriminator thresholds were set at approximately two-thirds of the maximum single-photoelectron (SPE) signal observed. This accounts for natural fluctuations in SPE signal amplitudes due to Poisson statistics as well as tube-to-tube gain variations, while ensuring efficient detection of SPEs.

These observations underscore the unique challenges of operating a threshold Cherenkov detector in the high-rate SBS environment, and the success of the GRINCH design in addressing them.

Chapter 4

Data Analysis

Extractions of G_M^n for this experiment are accomplished by directly comparing experimental data to Monte Carlo simulated data. For both, we select for quasi-elastic events to minimize background, evaluate the deflection of the scattered nucleon by the magnet for neutron–proton identification, and and make cuts to avoid biasing between protons and neutrons. This chapter will go over the various cuts, calculations, and analysis done on both experimental data and Monte Carlo, as well as discuss the Monte Carlo simulation itself.

4.1 Coordinate Systems

There are several different coordinate systems used to describe the positions of the various components of the SBS spectrometer. The choice of the best coordinate system depends on the context.

Figure 4.1 shows the various coordinate systems of the SBS apparatus. The Hall Coordinate System, detonated with subscript v for "vertex", can be thought of as the perspective of the electron beam being incident on the target. The z_v direction points in the direction of the beam, towards the beam dump, and the origin is located at the center of the target. The x_v direction points toward beam left, and the y_v direction points up. This coordinate system is useful for electron-nucleon scattering calculations.

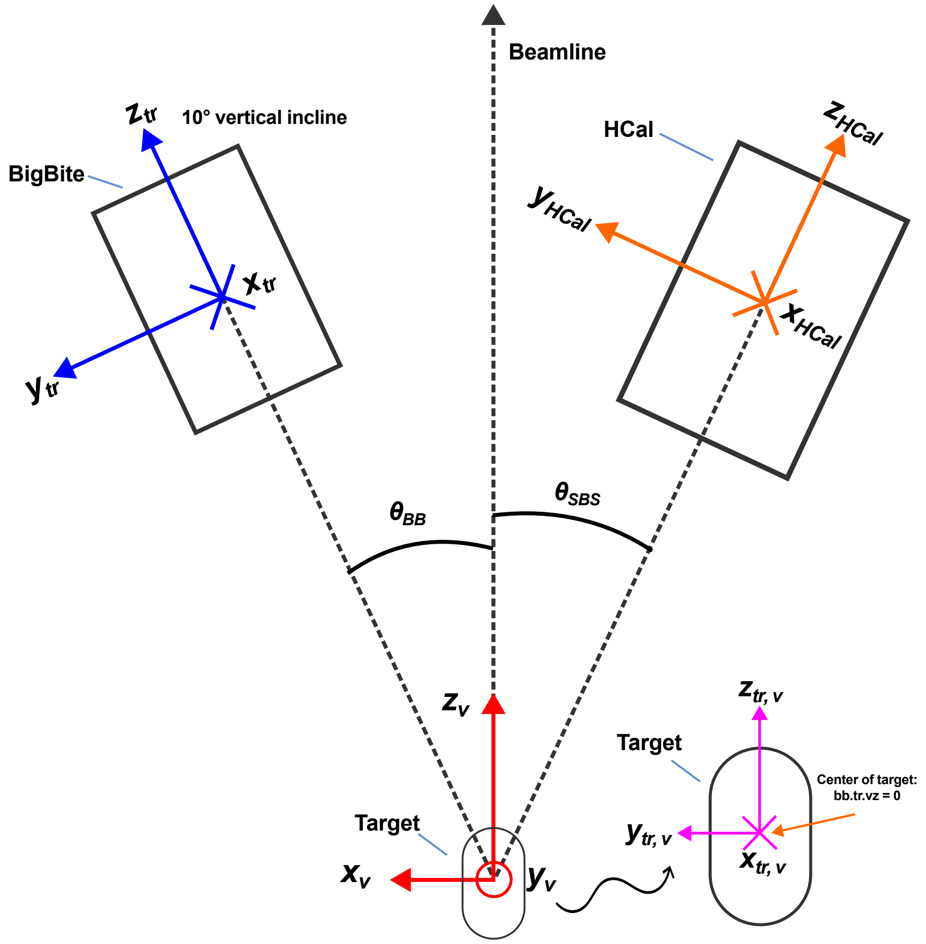

Figure 4.1: Coordinate systems of SBS as seen from above. The "Hall" or "vertex" coordinate system is denoted with subscript v. The electron arm transport coordinate system is denoted with subscript tr. The HCal coordinate system is denoted with subscript $HCal$. The target vertex coordinate system, illustrated on the lower right, is the target vertex relative to the transport coordinate system. See Fig. 2.4 for the illustration of the zx-plane angle θ and the xy-plane angle ϕ.

The electron arm coordinate system or "transport" coordinate system, denoted with subscript tr, can be thought of as the perspective of a scattered electron passing through the BigBite spectrometer. The entire coordinate system has a 10° vertical incline to align with the incline of the BigBite detector stack (see Fig. 2.5). The z_{tr} direction points from the target center to the BigBite detector stack, x_{tr} points towards the ground, and y_{tr} completes the right-handed orthogonal coordinate system. y_{tr} is parallel to the face of the detector stack and points away from the beamline.

The "transport, target vertex" coordinate system, denoted with subscript tr, v, is a representation of the target vertex in the coordinates that are more compatible with the electron arm coordinate system. This system is mainly utilized to project the charged particle track from BigBite back to the target to determine if the scattering event originated from near the center of the target. Since the cryogenic target is 15 cm long, a cut is make a cut on $|z_{tr,v}| < 0.07$ m to ensure the event originated from the target material (see Sec. 4.5.1.4).

The hadron arm/HCal coordinate system can be thought of as coming from the perspective of a scattered neutron passing through the hadron arm. The z_{HCal} direction points towards HCal from the target and is level with the beam pipe and the center of HCal. The x_{HCal} direction points towards the ground, and the y_{HCal} direction completes the right-handed orthogonal system. y_{HCal} points towards the beam pipe and is parallel to the face of HCal.

The "ideal coordinate system" of BigBite (not pictured) is denoted as $tr.r$. This system is ideal for optics validation and will be used for the optics quality cuts (see Sec. 4.5.1.2).

4.2 Particle Tracking and Reconstruction

The GMn experiment relies heavily on particle tracking in the electron arm with the GEM detectors. The GEM detectors and their ability to operate at high rates make tracking in an unshielded experiment like GMn possible. Comprehensive track reconstruction processes the many signals in the GEM detectors to reproduce the path and timing of the ionizing particle through the electron arm. The details of the tracking algorithm are complex. A detailed explanation of GEM tracking is given by S. Jeffas in their PhD thesis in Sec. 4.5.8 and Sec. 4.5.9 [39]. This work will briefly highlight a few key aspects of GEM tracking.

As discussed in Sec. 2.5.2, each GEM module has two-dimensions of readout strips. The GEM modules are each of either of the perpendicular XY configuration or the 60° UV configuration. One-dimensional clustering must first be conducted on each one-dimensional axis: X and Y, or U and V, depending on the GEM module. This one-dimensional clustering process takes into account the magnitude of the individual readout strip ADC channel signals, the timing of the signals, as well as the location of the channels. Two-dimensional clusters are then formed by pairing every possible combination of the one-dimensional clusters. The two-dimensional clusters are referred to as "hits". The coincidence time and position between the two clusters that form a hit are evaluated for every hit and cuts are applied. Hits that pass these cuts will then participate in track finding between the GEM modules. As discussed in Sec. 2.5.2, the Shower cluster location is used to constrain the track search regions in each module. Combinations of hits between the modules are fit to attempt to form a straight line. To select for good tracks, cuts are made on the χ^2 of the fit results, and the track is projected back to its origin to see if it originated from the target. The projection back to the target was described in Sec. 4.3, and the cut on the fit will be spoken about in Sec. 4.5.1.2.

4.3 Optics and Momentum Reconstruction

It is vital for this experiment to be able to accurately reconstruct the path of the scattered electron back to the interaction point of the target, as well as reconstruct the momentum. This requires us to have a detailed understanding of the field inside the BigBite magnet. We achieve this for this experiment by utilizing a "sieve", which is a 4 cm thick lead block with holes drilled through it in a grid-like pattern that is placed upstream of the BigBite magnet. The single-foil carbon target is used as a point-source. Particles pass through the holes at known positions and the lead absorbs the majority of the other particles.

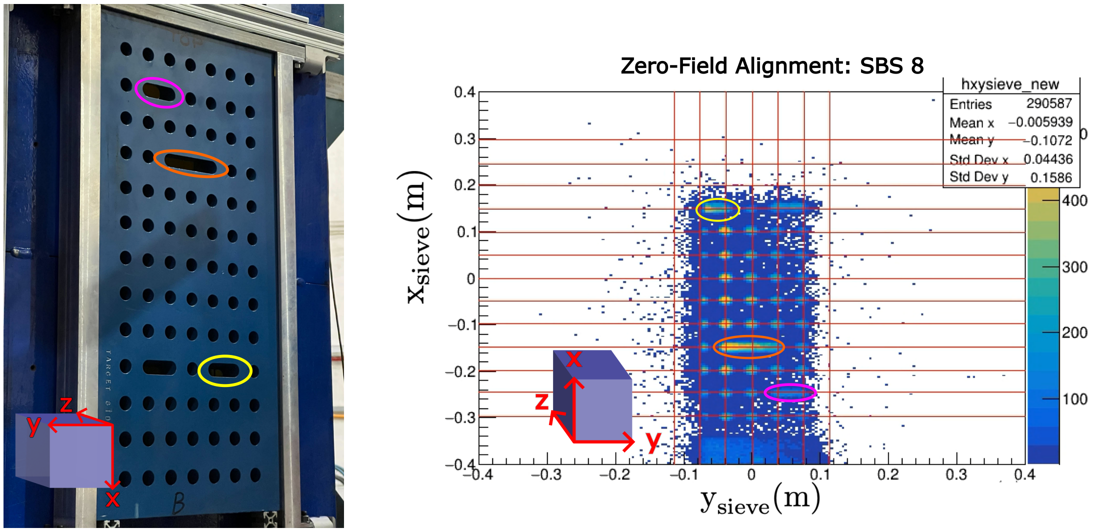

(a) (b)

Figure 4.2: **(a)** The sieve used in Hall A for optics and momentum calibrations. It is placed just upstream of the BigBite magnet. Holes in the sieve allow particles to pass through at only known locations and block the majority of others. **(b)** Reconstructed events with the BigBite magnetic field off. Several matching holes are color-coded and circled for illustration [37]. The right-handed orthogonal coordinate system is drawn on the figures.

The dimensions and positions of the sieve slit in the hall are well known, and the position and size of the GEMs are known in respect to the sieve slits; this enables the absolute positions and orientations of each GEM to be determined relative to the Hall using “zero-field” runs where $\vec{B} = 0$ in the BigBite magnet.

The absolute position of the sieve holes are then used to calculate how the particles are projected back through the magnetic field and to the target. It is important to know where in the target the interaction took place in order to eliminate events that originated from the target walls rather than the target itself.

The Hadron arm does not have a sieve, and therefore we can not do this procedure to determine the projection back through the SBS 48D48 magnet. However, precise reconstruction and resolution of the quasi-elastic electron on the BigBite arm allows precise straight-line elastic projections through the Hadron arm, discussed further in Sec. 4.4. A key aspect of particle identification between protons and neutrons is the deviation from that projection. Further details on these calibrations can be found in the PhD thesis of S. Jeffas [39].

4.4 Straight-Line Projection to HCal

As explained in Sec. 2.6.1, proton-neutron separation is achieved by utilizing a strong magnetic field from the SBS Dipole magnet. The positively charged protons are deflected upward towards the top of HCal while the neutral neutrons are not deflected. A hadron scattered in the target for each scattering event is going to have a different initial angle, momentum, and energy and will cover the entire phase space may hit anywhere on HCal. Therefore, we are not able to simply say that events near the top of HCal are protons and events near the middle or bottom are neutrons. We need to look at the *difference* between the position of the straight line projection to the face of HCal (x_{exp}, y_{exp} etc.), and the actual position of the event in HCal (x_{act}, y_{act} etc.). We call these quantities Δx and Δy, where

$$\begin{aligned} \Delta x &= x_{\text{act}} - x_{\text{exp}} \\ \Delta y &= y_{\text{act}} - y_{\text{exp}} \, . \end{aligned} \tag{4.1}$$

Δx and Δy are illustrated in on the face of HCal in Fig. 4.3.

We use the measurements in the electron arm to select elastic events (or quasi-elastic for deuterium) to make the straight line projection to the H-Arm and the face of HCal. We will go into more detail on this calculation in the following subsections.

Figure 4.4 shows the Δx distribution for hydrogen (LH2) scattering (one proton) and deuterium (LD2) scattering (one proton, one neutron) for a subset of SBS-4, 30% field data. We can see two distinct peaks in the deuterium distribution: the peak around $\Delta x \approx 0$ is made up of neutrons from $d(e, e'n)$ scattering that are not bent by the SBS magnet and thus

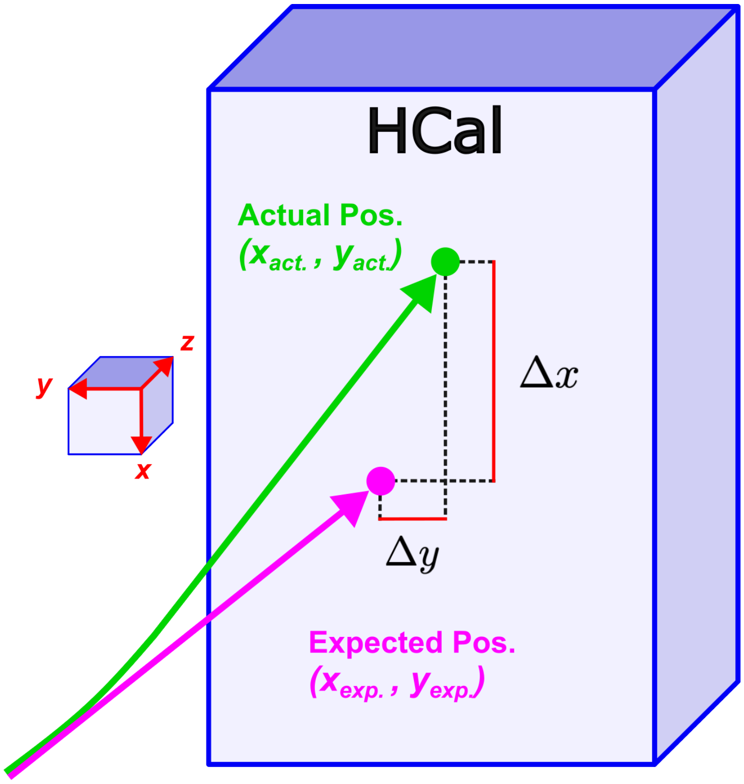

Figure 4.3: Δx and Δy illustrated on the face of HCal. The expected position from the straight line projection (magenta) is calculated from the E-arm measurements. The actual position (green) is where HCal detected a cluster. The difference between these positions is Δx and Δy. The right-handed orthogonal coordinate system is illustrated for convenience, where $z = 0$ is on the face of HCal, $y = 0$ is the center of HCal, and $x = 0$ is at beam height. Diagram is not to scale.

$x_{exp.} \approx x_{actual}$. The peak around $\Delta x \approx 0.75$ in the deuterium distribution is from protons being bent up by the SBS magnet, where the peak is the average deflection of the protons. The deuterium distributions are wide due to Fermi smearing, where the target nucleon is not at rest in the lab frame and has some initial momentum. Nuclear effects, due to the fact that the neutron and proton in the nucleus not free targets but are bound together, also contribute to the width. There are also events from inelastic scattering processes that pass the elastic cuts and contribute to the background. The hydrogen distribution is centered around the average proton deflection as well, but is significantly tighter than the deuterium distribution. This is due to the proton in hydrogen being the only nucleon, and thus it is a free nuclear target and does not feel the binding effects of another nucleon.

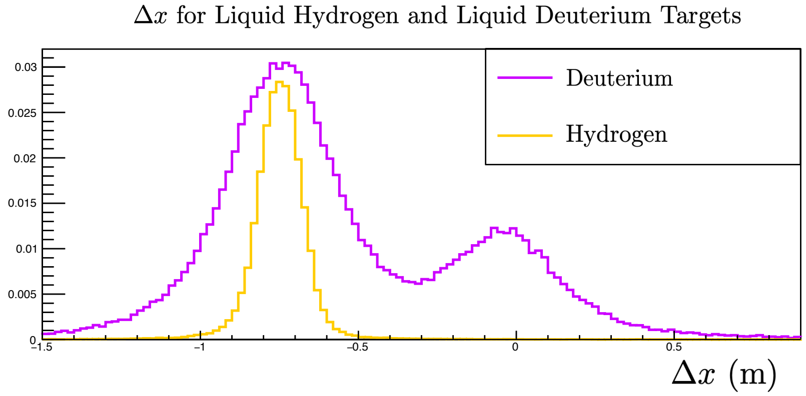

Figure 4.4: Δx for LH2 (orange) and LD2 (violet) experimental data taken at the same kinematics and magnetic field strength: SBS-4, 30% field. The same elastic cuts are applied to each data set. The neutrons in d(e,e'n) scattering are not deflected by the magnetic field, creating a peak around $\Delta x = 0$. Protons are deflected upward by the magnetic filed ($-x$ direction) and create a peak in both the hydrogen and deuterium distributions around $\Delta x = -0.7$. The normalizations of the integrals of these histograms are arbitrary and intended to help demonstrate proton–neutron separation.

4.4.1 q-vector Calculation

The four-vector components of the incident electron k and scattered electron k' in the lab frame can be expressed as

$$
\begin{aligned}
k &= (E_e, \vec{k}) = (E_e, 0, 0, E_e) \\
k' &= (E_{e'}, \vec{k}') = (E_{e'}, E_{e'} \sin\theta_e \cos\phi_e, E_{e'} \sin\theta_e \sin\phi_e, E_{e'} \cos\theta_e)\ .
\end{aligned}
\tag{4.2}
$$

The first component in the four-vector (E) is the time component, which in this case is the energy, and the last three components are the momentum 3-vector in 3D space ($\vec{k}$); E_e is the energy of the beam; $E_{e'}$ is the energy of the scattered electron e'; and θ_e and ϕ_e are the polar and azimuthal angles, respectively.

As outlined in Sec. 1.4, we use the conservation of four-momentum to define the four-momentum transfer q,

$$
q = k - k' = (\nu, \vec{q})\,. \tag{4.3}
$$

We can then express q in terms of the incoming and scattered electron kinematic as

$$
\begin{aligned}
q &= (\nu, \vec{q}) \\
\nu &= E_e - E_{e'} \\
\vec{q} &= \begin{pmatrix} q_x \\ q_y \\ q_z \end{pmatrix} = \begin{pmatrix} -E_{e'} \sin\theta_e \cos\phi_e \\ -E_{e'} \sin\theta_e \sin\phi_e \\ E_e - E_{e'} \cos\theta_e \end{pmatrix}\ .
\end{aligned}
\tag{4.4}
$$

Since the scattered electron is a highly relativistic particle with negligible mass, we can approximate its energy as the magnitude of its three-momentum. So,

$$
E_{e'} = |\vec{k}'|\,. \tag{4.5}
$$

The scattered electron's direction and momentum magnitude can be reconstructed from the tracking variables, which are determined in the data processing software. Using this information, we can express the four-momentum transfer q from Eq. (4.4) in terms of the measured beam energy and the scattered electron's reconstructed momentum:

$$
\begin{aligned}
&q = (\nu, \vec{q}) \\
&\nu = E_e - |\vec{k}'| \\
&\vec{q} = \begin{pmatrix} q_x \\ q_y \\ q_z \end{pmatrix} = \begin{pmatrix} -|\vec{k}'| \sin\theta_e \cos\phi_e \\ -|\vec{k}'| \sin\theta_e \sin\phi_e \\ E_e - |\vec{k}'| \cos\theta_e \end{pmatrix} .
\end{aligned}
\tag{4.6}
$$

With the reconstructed energy and direction of the scattered electron, as well as the known beam energy, we have now determined all the components of the four-momentum transfer vector $q = (\nu, \vec{q})$. Next, we will assume elastic scattering and calculate the expected four-momentum of the scattered nucleon.

4.4.2 Elastic Assumption and Scattered Nucleon Calculation

To calculate the four-vector of the elastically scattered nucleon, we apply conservation of four-momentum. Separating this into energy and momentum components gives

$$
\begin{aligned}
&\vec{k} + \vec{p} = \vec{k}' + \vec{p}_N \\
&E_e + E_{target} = E_{e'} + E_{p_N} \, ,
\end{aligned}
\tag{4.7}
$$

where p is the four-momentum of the target nucleon. Since the target nucleon is initially at rest in the lab frame, $\vec{p} = \vec{0}$ and $E_{target} = M_N$; p_N is the four-momentum of the scattered nucleon; and E_{p_N} is the energy of the scattered nucleon.

Thus we have

$$
\begin{aligned}
&\vec{k} = \vec{k}' + \vec{p}_N \\
&E_e + M_N = E_{e'} + E_{p_N} \\
&\Rightarrow E_{p_N} = M_N + \nu \, ,
\end{aligned}
\tag{4.8}
$$

where $\nu = E_e - E_{e'}$ is the energy transferred from the incident electron to the nucleon. Squaring the four-vector of p_N, using the Minkowski metric, and substituting in Eq. (4.8), we can solve for the magnitude of the three-momentum of the scattered nucleon as

$$
\begin{aligned}
(p_N)^2 &= E_{p_N}^2 - |\vec{p}_N|^2 = M_N^2 && (4.9)\\
|\vec{p}_N| &= \sqrt{E_{p_N}^2 - M_N^2} = \sqrt{\nu^2 + 2M_N\nu}\,. && (4.10)
\end{aligned}
$$

Here, we are using the identity that $(p_N)^2 = M_N^2$ by assuming that the scattered nucleon underwent quasi-elastic scattering.

In elastic scattering, the scattered nucleon and the scattered electron are co-planar, i.e., they lie in the same plane defined by the incoming and outgoing electron momenta. Since the nucleon recoils in the opposite azimuthal direction to the electron in elastic scattering, we define the nucleon azimuthal angle as

$$\phi_N = \phi_e + \pi\,. \tag{4.11}$$

Under the assumption of elastic scattering, the nucleon recoils in the direction of the three-momentum of the momentum transfer vector $\vec{q}$, so we define the nucleon direction to be $\hat{p}_N = \hat{q}$. As we will see in later sections, many inelastic events can be removed by eliminating events that deviate from this assumption in the non-dispersive direction (y). Using this relation to solve for the polar angle of the scattered nucleon, we find

$$
\begin{aligned}
p_{N,z} &= q_z = E_e - |\vec{k}'|\cos\theta_e\\
\cos\theta_N &= \frac{p_{N,z}}{|\vec{p}_N|}\\
\Rightarrow \theta_N &= \cos^{-1}\left(\frac{E_e - |\vec{k}'|\cos\theta_e}{\sqrt{\nu^2 + 2M_N\nu}}\right)\,.
\end{aligned}
\tag{4.12}
$$

With the assumption of elastic scattering, we have all the components to reconstruct the four-momentum of the scattered nucleon p_N along the trajectory of $\hat{q}$. We are now equipped to project the nucleon's path to HCal.

4.4.3 Nucleon Projection onto HCal

Now that we have determined the four-momentum of the scattered nucleon p_N under the elastic hypothesis, we next project its path to the face of HCal. We assume the nucleon travels in a straight line from the interaction vertex in the target along the direction of the momentum transfer $\hat{p}_N = \hat{q}$. Given the known position of HCal in the lab frame, we can calculate the intersection of the $\vec{p}_N$ ray and the HCal detector plane to determine where the nucleon is expected to hit the face of HCal.

To construct the unit vector $\hat{q}$, we normalize the three-vector $\vec{q}$:

$$\hat{q} = \frac{\vec{q}}{|\vec{q}|} \,. \tag{4.13}$$

The nucleon's trajectory under the elastic hypothesis can be expressed as a straight-line projection along $\hat{q}$ from the interaction vertex $\vec{r}_0$. We can define the ray for the nucleon's trajectory as

$$\vec{r}(s) = \vec{r}_0 + s\hat{q} \,, \tag{4.14}$$

where $\vec{r}_0 = (x_0, y_0, z_0)$ is the origin of the ray (interaction vertex); $\hat{q}$ is the direction of the momentum transfer, which is the direction of the ray; and s is a scalar parameter representing the distance traveled along the ray.

Next, we need to write out the equation of the plane of HCal. A plane is defined by

$$(\vec{r} - \vec{r}_{\text{plane}}) \cdot \hat{n} = 0 \,, \tag{4.15}$$

where $\vec{r}_{\text{plane}}$ is a point on the plane, and $\hat{n}$ is a unit normal vector to the plane. $\vec{r} - \vec{r}_{plane}$ is a vector that lies on the plane.

HCal is located beam right, positioned at an angle θ_{HCal} relative to the beamline (the z-axis of the scattering or "hall" frame). While our four-momentum vectors are calculated in this hall coordinate system, the face of HCal lies in a different coordinate system — the HCal coordinate system — which is rotated relative to the hall frame. To compute the expected hit position, we must express the HCal orientation and origin in the hall frame as

$$\hat{\mathcal{O}}_{\text{HCal}} = \begin{pmatrix} \hat{x}_{\text{HCal}} \\ \hat{y}_{\text{HCal}} \\ \hat{z}_{\text{HCal}} \end{pmatrix} . \tag{4.16}$$

To calculate the intersection of the projected nucleon, we will use $\vec{r}_{\text{plane}} = \mathcal{O}_{\text{HCal}}$. We will use $\hat{z}_{\text{HCal}}$, which is perpendicular to the face of HCal, as $\hat{n}$. That is, $\vec{r}_{\text{plane}}$ defines a point on the HCal plane (the HCal origin), and $\hat{n} = \hat{z}_{\text{HCal}}$ is the unit normal vector to that plane, which points from the target toward the center of the detector face. First, we need to express the direction of the origin of HCal in the scattering plane coordinates:

- $\hat{z}_{\text{HCal}}$ points from the target vertex to the center of HCal. This is a clockwise rotation of θ_{HCal} about the y axis in the scattering frame,

$$\hat{z}_{\text{HCal}} = [\sin(-\theta_{HCal}), \quad 0, \quad \cos(-\theta_{HCal})] . \tag{4.17}$$

- $\hat{x}_{\text{HCal}}$ points down towards the ground, which is in the direction of $-\hat{y}$ in the scattering frame,

$$\hat{x}_{\text{HCal}} = [0, \quad -1, \quad 0] . \tag{4.18}$$

- $\hat{y}_{\text{HCal}}$ is the cross product of $\hat{z}_{\text{HCal}}$ and $\hat{x}_{\text{HCal}}$ to complete the right handed system;

$$\hat{y}_{\text{HCal}} = [\hat{z}_{\text{HCal}} \times \hat{x}_{\text{HCal}}]_{\text{unit vector}} . \tag{4.19}$$

The HCal detector is located a known distance from the target along the $\hat{z}_{\text{HCal}}$ direction. To define a point on the HCal plane in the hall coordinate system, we construct the vector from the nominal target center to the center of HCal as

$$\vec{r}_{\text{plane}} = \vec{\mathcal{O}}_{\text{HCal}} = L_{\text{HCal}} \cdot \hat{z}_{\text{HCal}} . \tag{4.20}$$

where L_{HCal} is the distance from the target to the HCal face along $\hat{z}_{\text{HCal}}$. The origin of HCal is located at the same height as the beamline, so no correction is needed in the vertical direction. This ensures the HCal plane is positioned at the correct location in space.

With the HCal origin expressed in the lab frame, and the ray and plane equations defined, we are now ready to compute the scalar parameter s that gives the intersection point of the nucleon's trajectory with the HCal face.

Inserting the ray equation $\vec{r}(s)$ from Eq. (4.14) into the plane equation from Eq. (4.15), we have

$$\begin{aligned} &((\vec{r}_0 + s \cdot \hat{q}) - \vec{r}_{\text{plane}}) \cdot \hat{n} = 0 \\ &\Rightarrow s = \frac{(\vec{r}_{\text{plane}} - \vec{r}_0) \cdot \hat{n}}{\hat{q} \cdot \hat{n}} \, , \end{aligned} \tag{4.21}$$

where $\vec{r}_0$ is the interaction vertex, $\vec{r}_{\text{plane}}$ is the HCal origin in the hall frame, $\hat{n}$ is $\hat{z}_{\text{HCal}}$, and $\hat{q}$ is the unit vector of the direction of the momentum transfer. Therefore

$$s = \frac{(\vec{\mathcal{O}}_{\text{HCal}} - \vec{r}_0) \cdot \hat{z}_{\text{HCal}}}{\hat{q} \cdot \hat{z}_{\text{HCal}}} \, . \tag{4.22}$$

Plugging this value of s back into the ray equation gives the point where the nucleon trajectory intersects the HCal detection plane,

$$\vec{r}_{\text{intersect}} = \vec{r}_0 + s \cdot \hat{q} \, . \tag{4.23}$$

We have now obtained the projected interaction location of the scattered nucleon on the face of HCal, $\vec{r}_{\text{intersect}}$, expressed in the lab frame.

4.4.4 x_{exp}, y_{exp} in HCal Coordinate System

To determine where the scattered nucleon is expected to land on the face of HCal and compare it to the actual location of the cluster, we need to define the intersection point $\vec{r}_{\text{intersect}}$ relative to the HCal coordinate system.

We define the displacement vector $\Delta\vec{r}$ from the HCal origin $\vec{\mathcal{O}}_{\text{HCal}}$ to the projected interaction point $\vec{r}_{\text{intersect}}$ on the face of HCal as

$$\Delta\vec{r} = \vec{r}_{\text{intersect}} - \vec{\mathcal{O}}_{\text{HCal}} \,. \tag{4.24}$$

The expected x and y coordinates in the HCal frame are obtained by projecting $\Delta\vec{r}$ onto the local HCal axes:

$$\begin{aligned} x_{\text{exp}} &= \Delta\vec{r} \cdot \hat{x}_{\text{HCal}} \\ y_{\text{exp}} &= \Delta\vec{r} \cdot \hat{y}_{\text{HCal}} \,. \end{aligned} \tag{4.25}$$

With x_{exp} and y_{exp} defined, we can now compute the variables used in our physics extraction: Δx and Δy, as previously introduced in Eq. (4.1). Repeated here for convenience:

$$\begin{aligned} \Delta x &= x_{\text{act}} - x_{\text{exp}} \\ \Delta y &= y_{\text{act}} - y_{\text{exp}} \,. \end{aligned} \tag{4.26}$$

Here, $(x_{\text{act}}, y_{\text{act}})$ are the weighted center positions of the best cluster in HCal (see Sec. 4.5.2), and $(x_{\text{exp}}, y_{\text{exp}})$ are the expected hit positions based on a straight-line projection of the scattered nucleon, assuming elastic scattering.

Figure 4.5 shows a 2-dimensional histogram of Δx, Δy for SBS-4, 30% field. The proton and neutron spots are indicated by ellipses. The radii of the ellipses are 1–σ of Gaussian fits to the Δx distribution and Δy distribution from simulation, which will be shown in in Fig. 4.21 for SBS-4, 30% field in an upcoming section, and summarized for SBS-4, SBS-8, and SBS-8 in an upcoming section in Tab. 4.2.

4.4.5 HCal z Position Correction

In both data and Monte Carlo simulations, the Δx variable is positively correlated with x_{exp} (also referred to as x_{observed} by other collaborators) when using the distance from the target to the face of HCal. This observed corelation is likely due to the hadronic

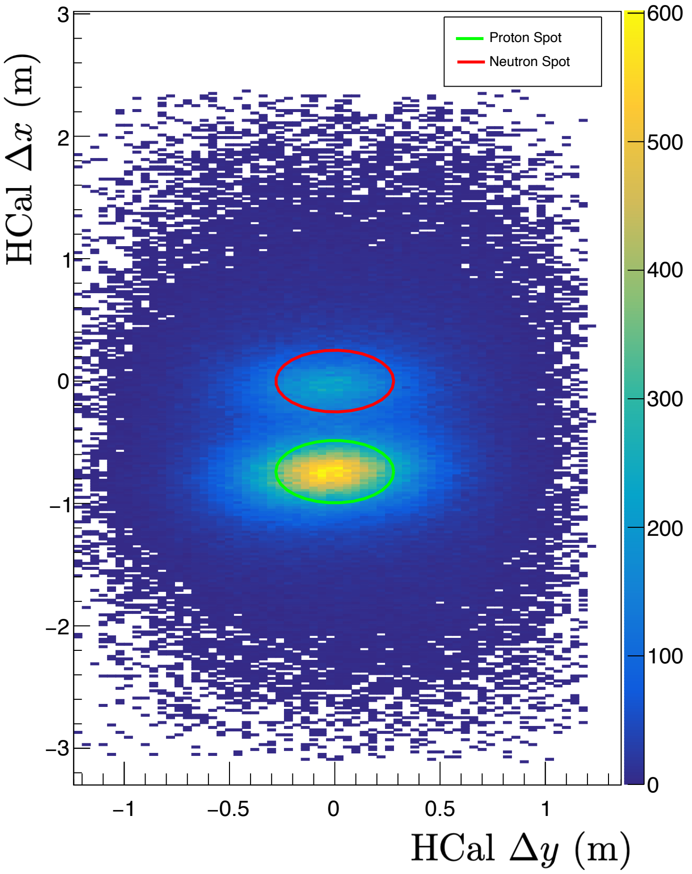

Figure 4.5: Elliptical Spots drawn on Δx, Δy for SBS-4, 30% field data. The dimensions of the ellipses are reflective of 1–σ cuts on the Δx and Δy distributions from simulation for proton (red) and neutron (green).

shower occurring at greater depths into HCal as the nucleon momentum increases. This correlation is corrected by creating by creating an offset for HCal-z for each kinematic when computing the location of the HCal origin in Eq. (4.20) for when calculating x_{expected} and y_{observed}. This correction must be made to eliminate this position dependence of Δx in order to extract G_M^n without any biases.

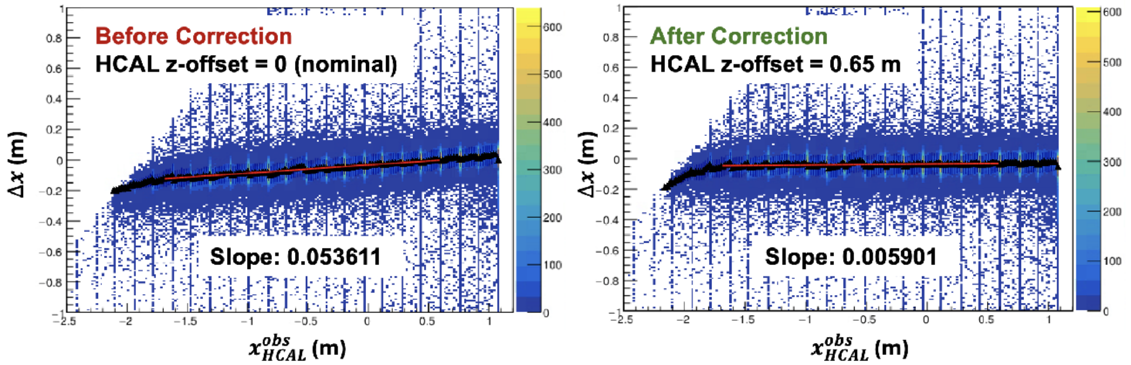

Figure 4.6: HCal-z offset correction. The correlation between Δx and x_{observed} is eliminated by adjusting the HCal-z offset. Elastic $H(e, e'p)$ events from SBS-4, 0% field data ($Q^2 = 3$ GeV^2) were used to create this plot. Figure and analysis done by P. Datta [36].

Table 4.1 shows the HCal-z offsets and effective distances used in this analysis[1]. For this analysis, the same parameters were used in both the data and Monte Carlo. However, the correlations are slightly different between data and Monte Carlo. A future improvement on this work could be a separate characterization and implementation of the slope in Monte Carlo simulation.

4.5 Quasi-Elastic Cuts

The selection of events from $d(e, e'n)$ and $d(e, e'p)$ quasi-elastic scattering in the LD2 target is crucial to this experiment and its physics results. We make cuts to select for "good electrons" on the various detectors in the electron arm. We also make cuts on the

---

[1] Since the completion of the analysis in this work, more precise HCal-z offset corrections have been determined and published in P. Datta's thesis [36].

Table 4.1: HCal-z effective offsets. The HCal distance is measured from the target to the face of HCal. The HCal-z offset are the values used to eliminate the correlation between Δx and x_{observed}.

SBS Config.	Q^2 (GeV^2)	HCal distance (m)	HCal-z offset (m)	HCal effective distance (m)
SBS-4	3.0	11.0	0.65	11.65
SBS-8	4.5	11.0	0.77	11.77
SBS-9	4.5	11.0	0.70	11.70
SBS-14	7.4	14.0	1.13	15.13
SBS-7	9.9	14.0	0.93	14.93
SBS-11	13.6	14.5	1.27	15.77

hadron arm to select for good hadron events. A large source of background are pions that are produced during inelastic events.

4.5.1 Electron Arm Event Selection

To select for "good electrons" in the electron arm, we utilize various kinematic measurements from our detectors, including energy, momentum, trajectory, and particle ID.

4.5.1.1 Invariant Mass Selection

Making a cut on the squared invariant mass (W^2) around the nucleon mass ($M_p^2 \approx M_n^2 \approx 0.98$) eliminates many inelastic events. Note that even for the lowest Q^2 kinematic of $Q^2 = 3.0$ GeV^2, the number of events in the inelastic regime dwarfs the quasi-elastic peak.

One method used to choose the cut boundary is to study the neutron–to–proton (n–p) ratios in data. There is no simulated data involved in this method. This is done by making tight elliptical cuts on the neutron and proton spots in the 2-dimensional $\Delta x, \Delta y$ histogram. An illustration of these elliptical cuts was shown in Fig. 4.5. These cuts give us an idea of the number of neutrons and protons in the data set. This does not take into account the background distribution or the overlap of protons and neutrons, so it can not be used for physics extractions. However, these ratios can give an idea of where good cut regions may be for a given variable.

Figure 4.8 shows 1-dimensional histograms of the W^2 variable without any spot cuts,

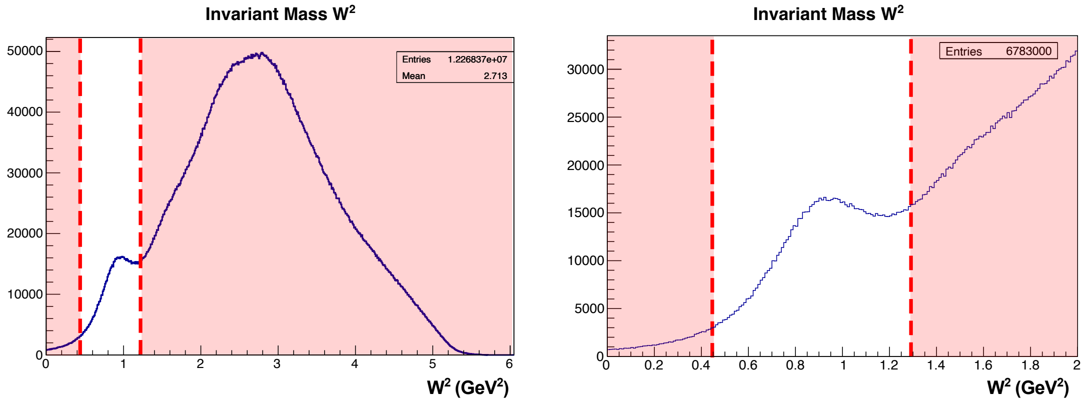

Figure 4.7: Invariant mass squared (W^2) histogram for SBS-4, 30% field setting ($Q^2 = 3.0$ GeV^2). (Left): full W^2 spectrum recorded by the apparatus. (Right): Zoomed in on W^2 around the quasi-elastic peak. The red areas are cut out of the data to remove inelastic background.

with the proton elliptical spot cut, and with the neutron elliptical spot cut. Bin-by-bin, the 1-dimensional neutron spot histogram is divided by the 1-dimensional proton spot histogram. This creates the neutron–to–proton ratio histogram. For W^2, we see a stable region around $W^2 \approx 0.65 - 1.1$ GeV^2. Since we expect W^2 for quasi-elastic events to be around $M_p^2 \approx M_N^2 \approx 0.88$ GeV^2, a symmetrical window or "cut" was chosen for $W^2 = 0.66$ GeV^2 to 1.1 GeV^2. This cut is in the stable region and doesn't cut out too many statistics. The large spread in the quasi-elastic peak is due in part to Fermi smearing (where the nucleons inside the nucleus are not at rest but instead have intrinsic momentum), nuclear effects, and the limited resolution of the electron arm and HCal.

It's important to note that the invariant mass in correlated with Δy. This is demonstrated in the two-dimensional histogram of W^2 vs. Δy shown in Fig. 4.9. This will be important when we look at the systematic uncertainty contributions from W^2 and Δy cuts in Sec. 5.3.1.8 and Sec. 5.3.1.7.

4.5.1.2 Track Quality Selection

To reconstruct a charged particle track in the GEM (Gas Electron Multiplier) system, a minimum of two out of five available GEM planes must register a hit. However, since any

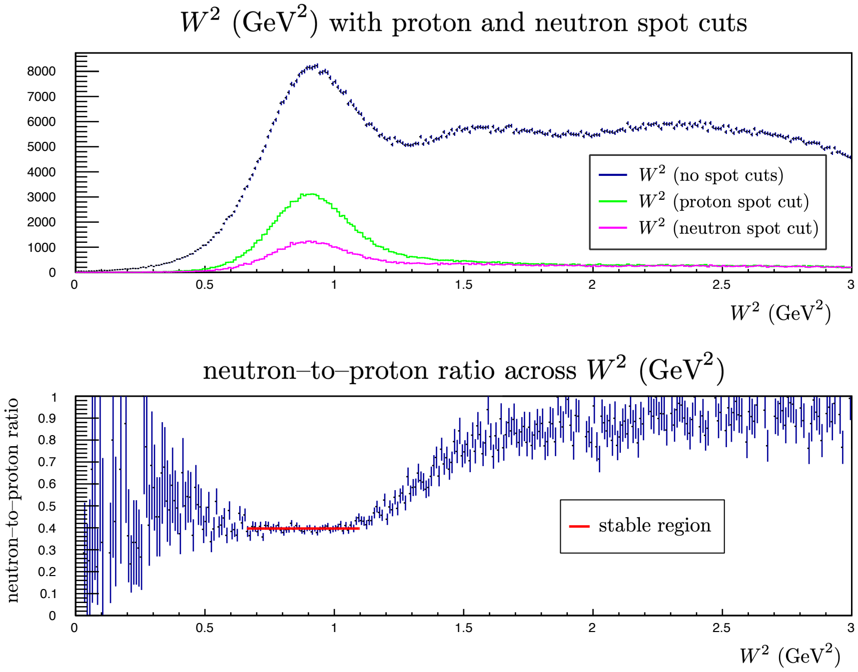

Figure 4.8: W^2 invariant mass spot-cut stability study for SBS-4, 30% field data ($Q^2 = 3.0$ GeV^2). (Top): W^2 is plotted with elliptical cuts on Δx and Δy to isolate the proton (green) and neutron (magenta) spots. (Bottom): The neutron–to–proton ratio is made by dividing bin-by-bin the neutron spot histogram by the proton spot histogram. The red line illustrates the cut region that was chosen for this kinematic.

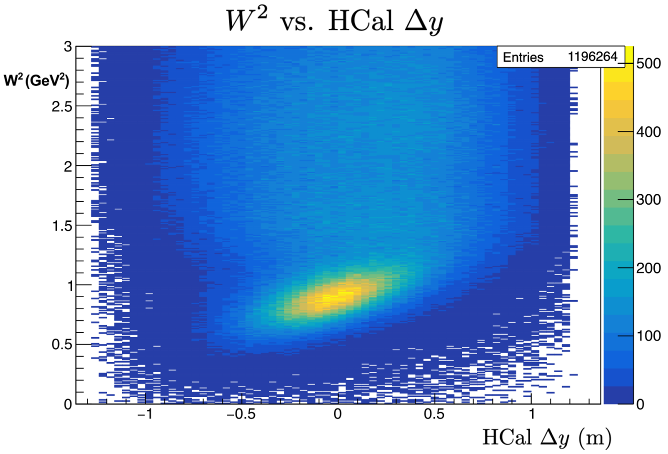

Figure 4.9: Invariant mass W^2 vs. Δy for SBS-4 30% field ($Q^2 = 3.0$ GeV^2). Note that the invariant mass, W^2, and the difference from the straight line projection in the non-dispersive direction, Δy, are correlated.

two points define a line, a fit based on just two hits provides no information about the fit quality. To gain meaningful constraints on the track geometry and to assess the validity of the reconstruction, a stricter requirement is imposed: only tracks with hits in at least three GEM planes are considered. This threshold enables the calculation of fit quality metrics and helps to suppress spurious tracks arising from detector noise or accidental coincidences.

One such metric is the reduced chi-squared value of the linear fit, χ^2/ndf, where "ndf" refers to the number of degrees of freedom in the fit. This quantity serves as a measure of how well the fitted line describes the observed GEM hit positions. A value close to 1 indicates a fit consistent with the expected spatial resolution and detector response. In practice, tracks with $\chi^2/\mathrm{ndf} > 15$ are excluded from further analysis, as they are likely to be poorly reconstructed or not associated with a real charged particle.

Figure 4.10 shows the distribution of χ^2/ndf for SBS-9. While tightening this cut would further reduce contamination from spurious tracks, it would also significantly reduce available statistics—potentially excluding valid events. Thus, the chosen cut represents a balance between track quality and statistical power, and its stability is explored further in Sec. 5.3.1.3 and Sec. 5.3.1.2.

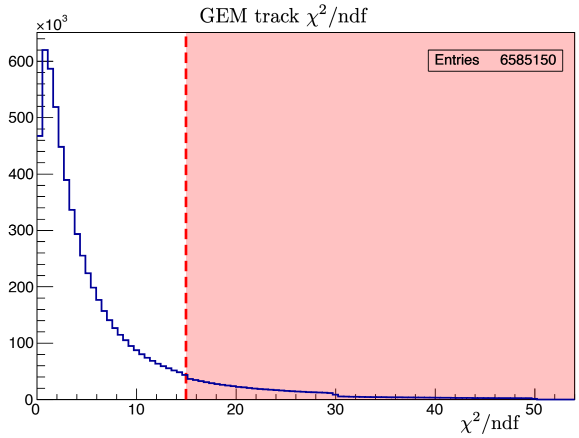

Figure 4.10: GEM track χ^2/ndf for SBS-9. The red area illustrates data points with $\chi^2/\mathrm{ndf} > 15$ are excluded to help eliminate bad tracks.

4.5.1.3 Optics Quality Selection

To check if the track went through a section of the BigBite magnet where the magnetic field is constant and the optics reconstruction is well done, we perform what is colloquially called "optics quality" cuts. To produce the "optics x" and "optics y", we project the track to the entrance of the BigBite magnet using the "ideal coordinate system", denoted $bb.tr.r$. These projections are calculated by

$$\begin{aligned} \text{optics}_x &= bb.tr.r.x - 0.9 * bb.tr.r.th \,, \\ \text{optics}_y &= bb.tr.r.y - 0.9 * bb.tr.r.ph \,, \end{aligned} \tag{4.27}$$

where $r.x$ and $r.y$ are the x and y positions in the coordinate system, and $r.th$ and $r.ph$ are the respective angles to the $r.z$ axis (see Fig 2.4 for reference).

As seen in Fig. 4.11 and Fig. 4.12, it is useful to plot the optics projections against W^2 to look for variations in the distribution, particularly at low-W^2. We have chosen to cut around $|\text{optics}_x| < 0.3$ m and $|\text{optics}_y + 0.005| < 0.1$ m. These cut values are used by the collaboration for GMn and have been vetted by collaborators.

It is also important to note that since these parameters are calculated using the track, they are highly correlated to the projected position of the nucleon on HCal, i.e. to x_{expected} and y_{expected}. This is illustrated in Fig. 4.13. Due to this correlation, we will only add systematic uncertainty from the x_{expected} and y_{expected} variable studies.

4.5.1.4 Track Vertex z at Target

The track vertex z position is a projection of the track back through the magnet and to the target using the optics calibrations. The center of the target is located at $bb.tr.vz = 0$, and the target is 15 cm long. By making a cut around track vertex $bb.tr.vz = 0 \pm 7$cm, we are making sure that the scattered electron originated from the target itself and not the walls of the target. Figure 4.14 shows the track vertex z position with an illustrated cut at ± 0.07 m.

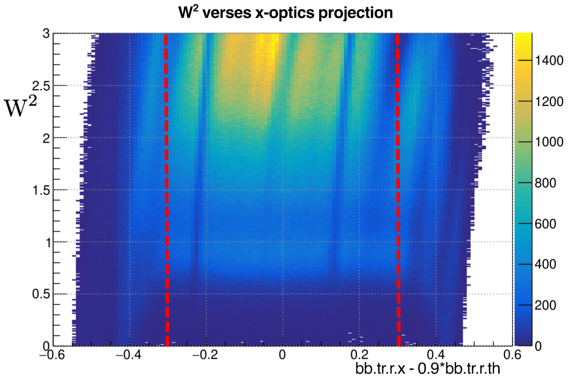

Figure 4.11: W^2 plotted against the x-projection to BigBite Magnet (optics$_x$). Around -0.4 and 0.35, there are slight deviations towards $W^2 = 0$ that are excluded. Events outside the red lines are excluded.

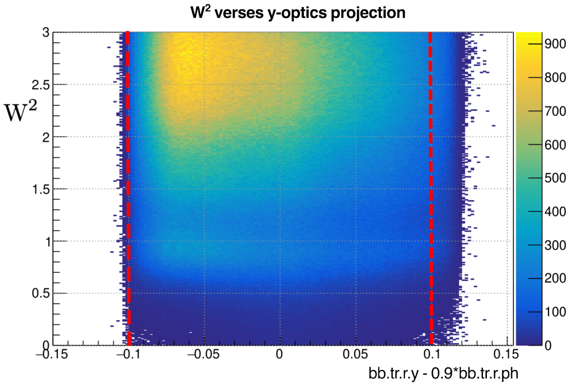

Figure 4.12: W^2 plotted against the y-projection to BigBite Magnet (optics$_y$). Although not as dramatic as the optics$_x$ distribution, we can exclude where the distribution begins to become unstable. Events outside the red lines are excluded.

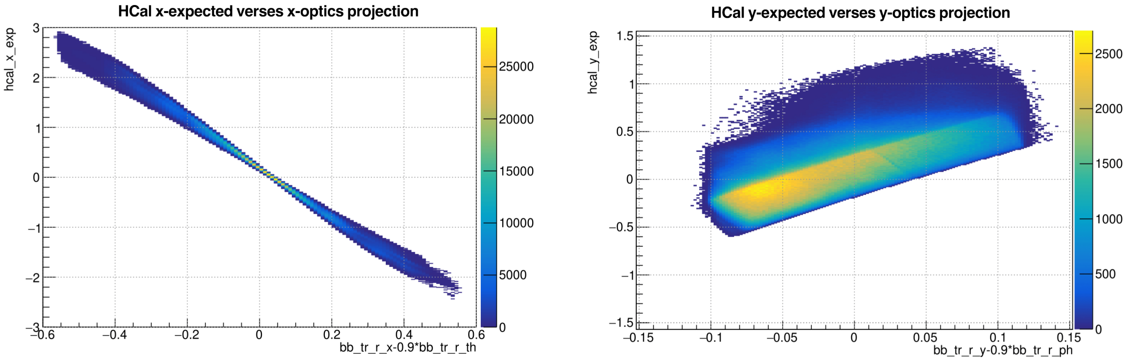

(a) HCal x_{expected} vs BigBite optics$_x$ (b) HCal y_{expected} vs BigBite optics$_y$

Figure 4.13: Comparison of HCal expected positions (x_{expected} and y_{expected}) with the BigBite magnetic optics projections (optics$_x$ and optics$_y$). The optics projections and the expected positions at HCal are highly correlated as they are both derived from the electron track.

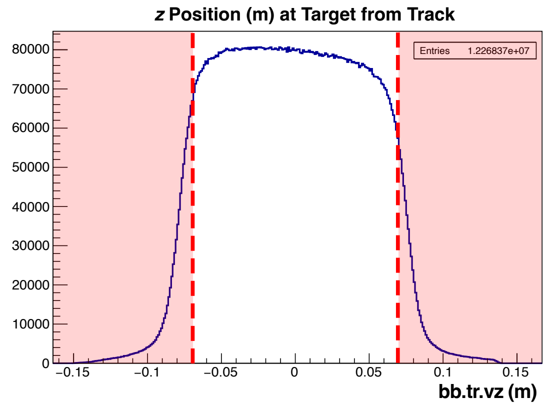

Figure 4.14: Track vertex z at target for SBS-4 30% field ($Q^2 = 3.0$ GeV^2). Events in the red section are cut to eliminate events that may have scattered from the target window, rather than the liquid deuterium.

4.5.1.5 BBCal Energy Selection

As discussed in Sec. 2.5.1, BBCal (Shower and Preshower) measure the energy of a charged particle. Clusters are made using a clustering algorithm, and the energy recorded in all of the blocks in a cluster is reported. More information on clustering can be found in P. Datta's thesis [36]. Pions deposit a small amount of energy in the Preshower and appear as a distinctive narrow signal at low energies in the energy histogram for the Preshower. This allows us to remove a large portion of the background by only accepting events above 0.2 GeV. Figure 4.15 shows the Preshower energy distribution in SBS-4 and where a good electron cut is made to help eliminate the pion peak.

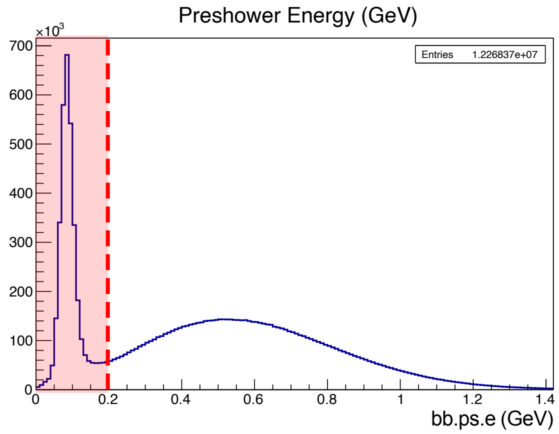

Figure 4.15: Preshower Energy distribution for SBS-4 30% field ($Q^2 = 3.0$ GeV^2). A cut is made to exclude the red area where the Preshower energy is less than 0.2 GeV. The exclusion of low energy signatures helps eliminate pions generated by inelastic events.

4.5.1.6 Total Energy over Momentum

For a relativistic electron, the energy equals its momentum due to it's small mass $E_e \approx P_e$. Therefore, we expect the ratio of $E'_e/P_e = 1$ for good electrons. To calculate the total energy of an event, we add the Shower Energy and the Preshower Energy together. For the momentum, we take the absolute value of the momentum vector that is calculated by GEM tracking and the momentum/optics calibrations. Excluding events that are on the tails of this distribution helps eliminate inelastic background. Figure 4.16 shown this distribution.

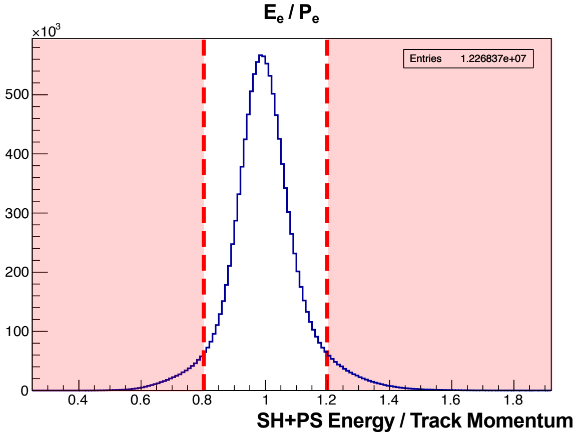

Figure 4.16: Total Energy over momentum for SBS-4, 30% field data ($Q^2 = 3.0$ GeV^2). Events in the red sections are excluded.

However, in the Monte Carlo simulation, there is an error in the shower energy, leading to an error in the total energy. This is fixed in the code now, however, the simulations used in this analysis contain that error. For this analysis, we will be minimally cutting on E/P for the data, and not cutting on E/P for the simulated events. We will discuss this further in Sec. 4.6.2.2 and Sec. 4.6.2.3.

4.5.1.7 GRINCH Selection

The GRINCH Cherenkov detector was only fully operational during SBS-8 and SBS-9 kinematics ($Q^2 = 4.5$ GeV^2). We will discuss GRINCH in detail in Ch. 3.

For GRINCH, the GMn experiment was treated as a commissioning experiment. The Preshower is able to conduct PID quite well for SBS-8 and SBS-9, and GRINCH was mainly needed for the following GEn experiment. The simulations for GRINCH are also in need further adjustment to include in the Data-MC comparison we rely upon for the G_M^n extraction. Therefore, this work does not include cuts on GRINCH for final G_M^n extractions.

4.5.2 Hadron Arm Quasi-Elastic Selection

We also select for good events in the Hadron Arm using several cuts in order to further eliminate background and select quasi-elastic events. In the GMn experiment, the only detector on the Hadron Arm is HCal. Clusters are identified in HCal and the cluster with the highest energy and that is also in coincidence with a good event in the Electron Arm is selected as the best cluster. We then select for events that occur only in the active area of HCal. We calculate the expected position of the nucleon from the electron arm kinematics and then select only the events that pass acceptance-matching cuts and a safety margin cut. Together, the active area cut, the safety margin cut, and the acceptance matching cut are sometimes called a *fiducial cut*.

4.5.2.1 HCal Cluster Selection

After clusters are constructed in HCal and BBCal, a cut is made on the ADC time difference between the clusters. If an electron signal in BBCal and a hadron signal in HCal are caused by the same eN scattering event in the target, their recoded ADC times will be correlated. The timing in HCal has been calibrated so that events from a good electron are centered around a time of 0 ns, regardless of what HCal block they interact with[2]. BBCal timing is calibrated so that the difference between HCal and BBCal ADC time is centered around 0 ns.

First, a cut is made on the HCal ADC time. If it is within ±25 ns of 0, the event is kept. Next, a coincidence cut is made on HCal ADC time minus the BBCal Shower ADC time. If that cut is within ±15 ns of 0 ns, the event is kept. These cuts are about 5 times the sigma of the distributions. This coincidence cut is purposely kept wide to insure good events aren't missed. Figure 4.17 illustrates these cuts on the HCal cluster time histogram and the HCal–Shower coincidence time histogram.

---

[2] This calibration is, of course, much more nuanced than I am describing here. See S. Seeds' thesis for more details [66].

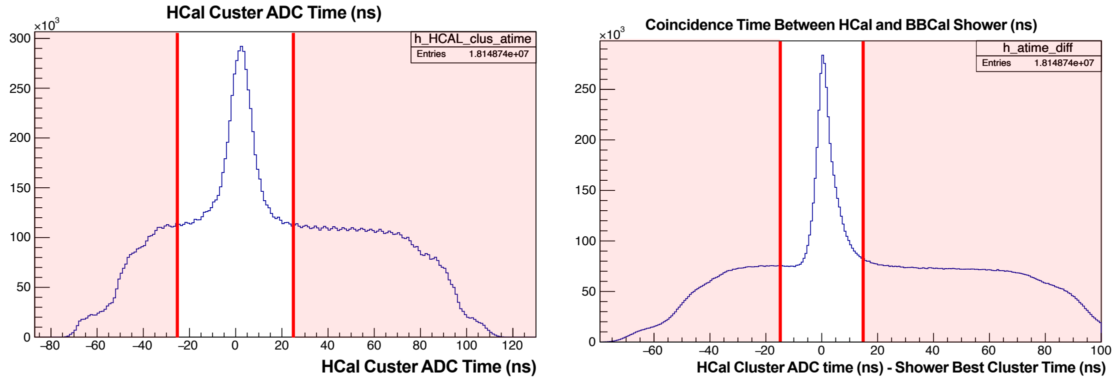

Figure 4.17: Coincidence time between HCal and BBCal Shower. (Left): A cut is made on the HCal Cluster ADC time to exclude the red areas. (Right): A cut is made on the coincidence time between Shower cluster and HCal to exclude the red areas. This helps eliminate out-of-time events that contribute to the background.

Finally, the highest energy cluster is then chosen from the remaining clusters that have passed these time cuts. The distribution of HCal energy can be seen in Fig. 4.18. This surviving cluster with the highest energy within time is our "best cluster". A flag is put up marking that this cluster is in-time (passed_atime_cuts == 1). In events where there are no clusters within the time cuts, the cluster with the largest energy is marked as the "best cluster" and a flag is put up to mark that it is out-of-time (passed_atime _cuts == 0). These out-of-time events will be used to inform the shape of the inelastic background, which will be discussed in Sec. 5.3.2. This first round of coincidence time processing is purposely left wide enough so that it can be further adjusted, but small enough that out-of-time background can be largely eliminated and further reduce the size of the data set.

4.5.2.2 HCal Active Area Cuts

When a high energy hadron is incident on a block in HCal and creates a shower, the secondary particles create signals in the surrounding blocks. This results in a cluster in HCal, with the highest energy typically recorded in the center block. Our goal is to capture and record all of the shower energy and minimize events where the secondaries escape the

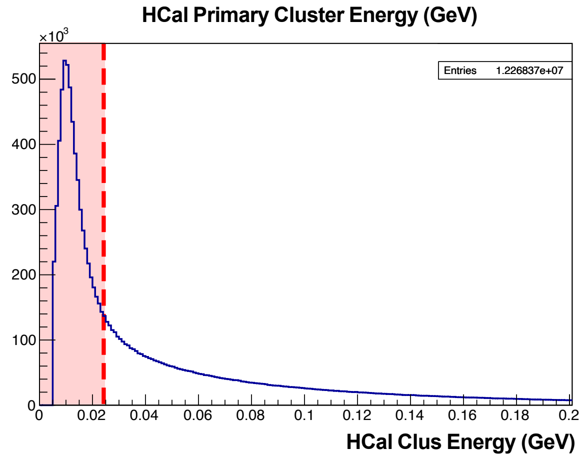

Figure 4.18: HCal energy distribution of the HCal primary cluster. Data points in the red area are excluded when making event selection cuts. The primary cluster is the largest cluster in an event, but does not necessarily have the largest energy sum or pass timing cuts.

sides of HCal, leading to the total energy of the event not being recorded. We do this by making a cut on the "active area" of HCal. This concept is illustrated in Fig. 4.19. We reject any events whose cluster center is located less than one block from the edge of HCal. We also reject events where the expected x position from the straight line projection is less than one block from the edge of HCal. We will go into further detail on the cutting on the expected x and y positions in Sec. 4.5.2.3.

4.5.2.3 HCal Acceptance Matching Cuts

As we've discussed through this work, our final results in this experiment rely heavily on the experimental ratio of protons to neutrons. We need to account for anything that might affect this ratio, such as protons getting bent upward off the face of HCal. Or in other terminology, the *area of acceptance* for a proton event needs to match the area of acceptance of a neutron event. We also want to make sure the event happens in a reliable area of the detector. These cuts together are referred to as a *fiducial cut.*

The core concept of acceptance matching is straightforward: After calculating the straight line projection to the face of HCal from the electron arm event, would the corre-

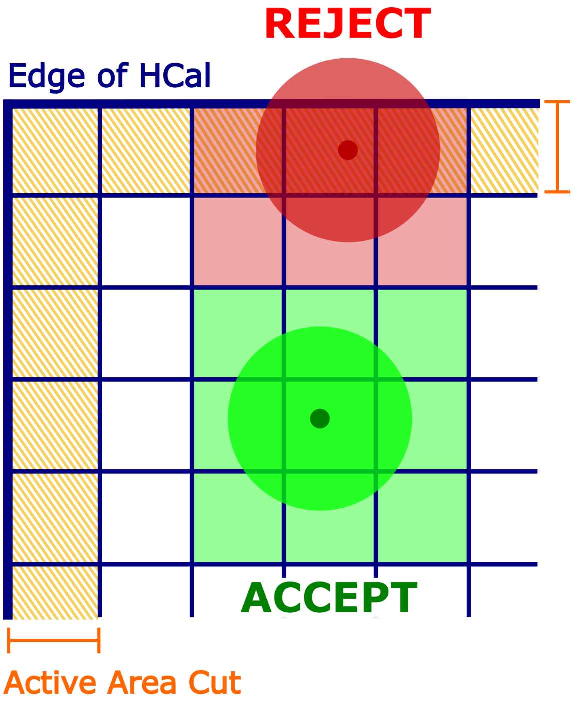

Figure 4.19: Simplified illustration of HCal active area selection. The hadronic shower creates many secondary particles which deposit their energy in the blocks surrounding the block that was struck with the incident particle. The orange fill represents a 1-block active area cut. The small dots represent where an incident particle struck HCal. The larger circles represent the full width of the shower at the time of absorption. And the highlighted blocks represent the HCal blocks that record a signal from the event. In the accepted green event, the signals from the secondary events are recorded by the surrounding blocks, making a cluster. In the rejected red event, secondary particles escape HCal and a portion of the signals are missed. This illustration is not to scale.

sponding scattered nucleon hit the face of HCal if it was either a neutron (no deflection) or a proton (deflected upward)? If either of those answers are "no", we cut that event. Figure 4.20 shows this concept with a simplified illustration. If the proton prediction is outside the boundary of HCal, the event is cut. Furthermore, we will need to take into account the with of the proton and neutron Δx distributions.

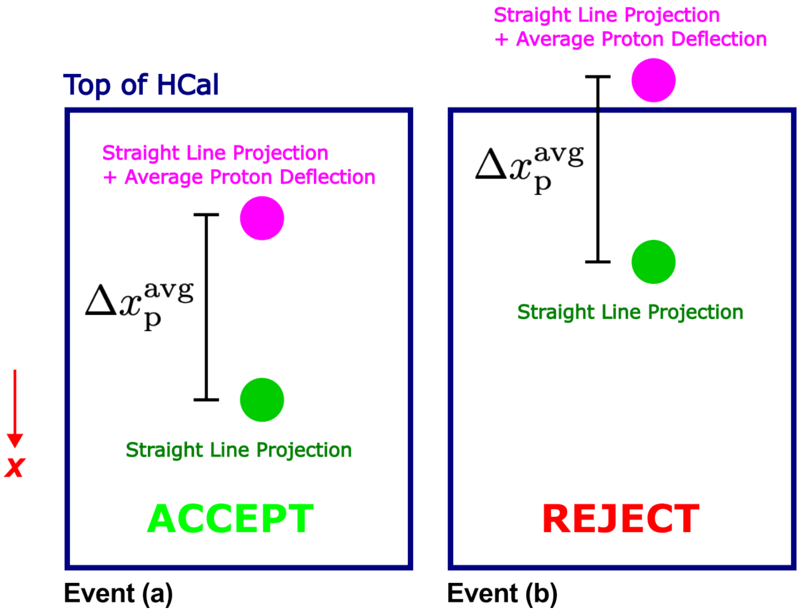

Figure 4.20: Simplified illustration of nucleon acceptance matching in HCal. The green dot represents the straight line projection to the face of HCal that is calculated from the event in the electron arm. We call this the *neutron hypothesis*. The average proton peak location of Δx, $\Delta x_\mathrm{p}^\mathrm{avg}$, is added in the dispersive direction to obtain the magenta *proton hypothesis*. In Event (a), both the proton and neutron hypotheses fall within the HCal boundary, so this event is accepted. In Event (b), the magenta proton hypothesis falls outside the HCal boundary, so this event is rejected. Figure is not to scale.

The implementation of acceptance matching becomes more complex when we take into account how likely an event is to go into the areas of HCal that we want to exclude that are not a part of the active area. This can be done by utilizing the width of the proton and neutron Δx and Δy to determine if the event should be cut or not. We call this the *safety margin* of our fiducial cut.

In a Gaussian distribution, 95.4% of the data lies within 2-sigma around the mean: $\mu \pm 2\sigma$. Approximating the Δx and Δy as Gaussian distributions, we make a Gaussian fit and extract the mean and σ. The values for the average $n-p$ separation and the σ values for the simulated Δx distributions are found in Tab 4.2. Figure 4.21 shows an example of the 1-dimensional Δx and Δy histograms used to extract these parameters.

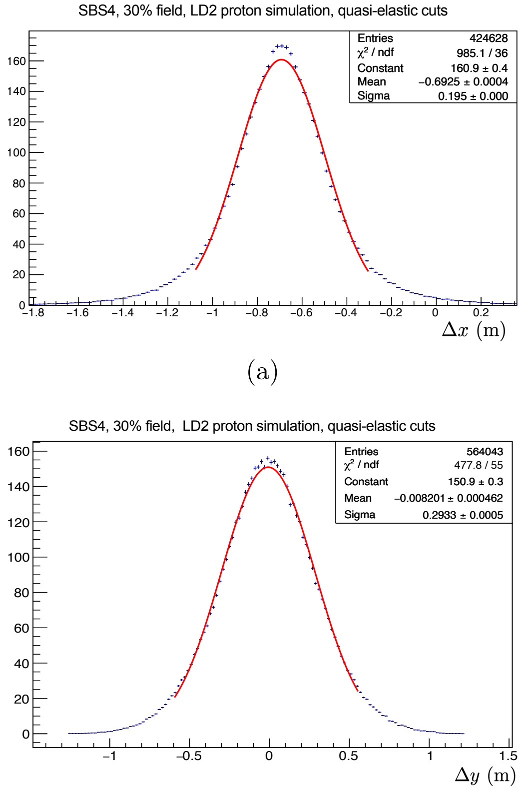

(a)

(b)

Figure 4.21: One-Dimensional Histograms of **(a)** Δx and **(b)** Δy from simulated data. These histograms are fit with a Gaussian distribution. See Appx. C for details of the Gaussian fit function.

Table 4.2 shows the various values needed to calculate an appropriate fiducial cut for each field setting.

Table 4.2: Neutron–proton separation and peak widths.

Measure	SBS-4 30%	SBS-4 50%	SBS-8 50%	SBS-8 70%	SBS-8 100%	SBS-9 70%
Avg. $n-p$ separation (m)	0.74	1.17	0.61	0.88	1.23	0.89
$\sigma^{n}_{\Delta x}$ (m)	0.252	0.21	0.22	0.22	0.22	0.23
$\sigma^{p}_{\Delta x}$ (m)	0.255	0.22	0.23	0.23	0.23	0.227
$\sigma_{\Delta y}$ (m)	0.28	0.29	0.31	0.31	0.31	0.27

In order to account for the variation around the mean of Δx and Δy, we add a safety margin to the active area cut. The choice of the magnitude of the safety margin is informed by the Gaussian statistics; we want to include as much of the distribution as possible, but we don't want to lower the statistics by cutting a large portion of HCal and eliminating too many events. A safety margin cut of between 1-2 sigma is typically acceptable. Different values for the safety margin in Δx and Δy are sometimes appropriate. The optimization of these safety margin cuts will be discussed further in Sec. 5.3.

The active area, the safety margin, and acceptance matching all need to be taken into account together for the final choice of cuts on $x^{\mathrm{exp}}_{\mathrm{HCal}}$ and $y^{\mathrm{exp}}_{\mathrm{HCal}}$. Figure 4.22 focuses on the upper left corner of HCal in order to help illustrate the combined application of active area cuts, the safety margin, and acceptance matching cuts.

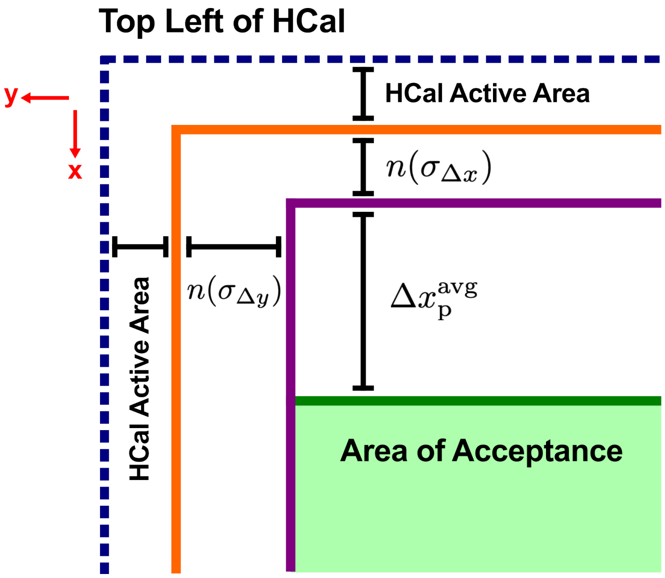

Figure 4.22: Illustration of fiducial cuts on the top left corner of HCal. This figure is zoomed in on the upper left corner of HCal. The cuts for the active area on HCal and acceptance matching for protons and neutrons are illustrated. The "safety margin" buffer, $n(\sigma_{\Delta} x)$ and $n(\sigma_{\Delta} y)$, is applied that is often expressed as a multiple of the width of the proton peak in Δx and Δy as determined in each kinematic and SBS dipole magnetic field setting. Events that are projected to land in the green area are accepted. Figure is not to scale.

Figure 4.23 shows an example of all of the fiducial cuts in $x^{\mathrm{exp}}_{\mathrm{HCal}}$ and $y^{\mathrm{exp}}_{\mathrm{HCal}}$ applied to data in a two-dimensional histogram. The values of $x_{\mathrm{HCal}}^{\mathrm{exp}}$ and $y_{\mathrm{HCal}}^{\mathrm{exp}}$ are for the *neutron hypothesis*, which is calculated from the straight line projection from the scattered electron kinematics, and do not account for the magnetic field. The large envelope of expected positions from the straight line projection is reduced to a much smaller subset of data. When the magnetic field is stronger, creating a larger separation between protons and neutrons, this final area of acceptance is even smaller. A larger n–p separation would make proton–neutron identification more precise, but at the cost of statistics, since many events would be outside the acceptance. Magnetic field values were chosen based on the expected average momentum of the quasi-elastic scattered nucleons, which informs the average proton deflection. Calculations and simulations helped inform magnetic field values that achieved a balance between n–p separation and area of acceptance.

4.6 Analysis Machinery

4.6.1 Strategy

Physics extractions for this experiment rely heavily on the Monte Carlo (MC) physics simulations. Data are compared directly to MC simulation to obtain our results. Therefore, it is vital that the output from the MC and the experimental data be processed using the same analysis tools. Figure 4.24 gives an overview of the analysis process.

The analysis and reconstruction software for SBS is built upon the existing machinery for Hall A, called the Hall A Analyzer. This machinery is based in CERN's ROOT data analysis framework in C++. Additional classes for the SBS detectors were written using the base classes from the Hall A analyzer.

The simulated data are created by first producing events using the SIMC generator. Those events are transported through the experiment geometry which is modeled using G4SBS.

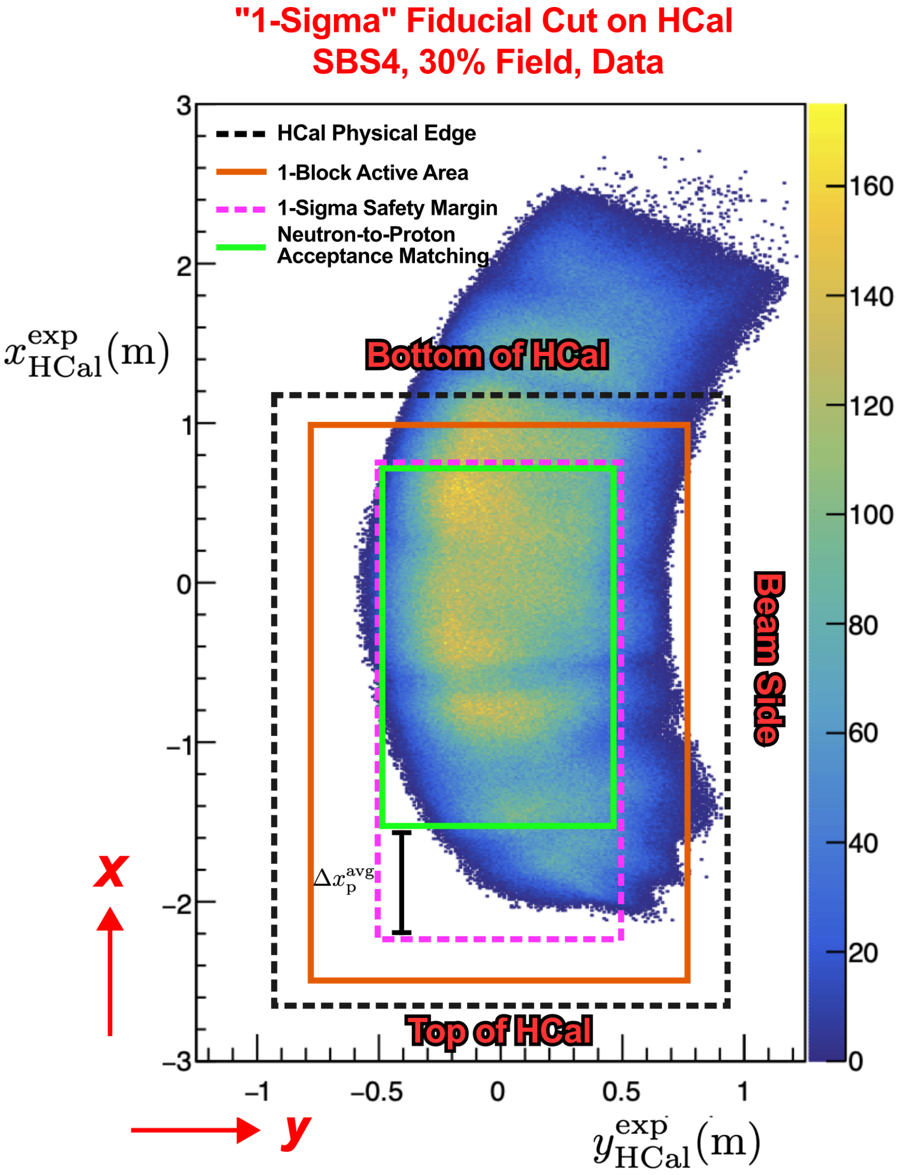

Figure 4.23: HCal fiducial cut illustrated on data. The two-dimensional histogram of $x_{\mathrm{HCal}}^{\mathrm{exp}}$ vs. $y_{\mathrm{HCal}}^{\mathrm{exp}}$ is annotated with the various levels of fiducial cuts. The black box represents the physical location in (x, y) of the edges of HCal. The orange box is a 1-block "active area" cut. The pink box is a 1-sigma "safety margin" cut which takes into account the width of the proton and neutron peaks in Δx. The green box is the acceptance matching cut which takes into account the location of the proton peak in Δx.

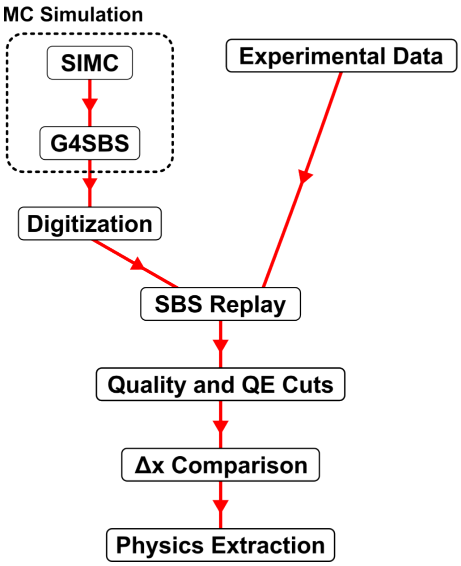

Figure 4.24: Flowchart of GMn analysis. Simulated data and experimental data are processed through the same decoding framework: “SBS Replay”. This allows for experimental data to be directly compared to simulation data.

4.6.2 Monte Carlo

The Monte Carlo simulations used in this experiment use an event generator, SIMC, that then passes the events to a separate particle transport simulation, GEANT4. The output from these simulations is then digitized and compared to real data.

4.6.2.1 SIMC

SIMC is a Monte Carlo event generator created by the Hall C collaboration at Jefferson Lab [67]. It includes several types of nuclear corrections and radiative corrections for the one-photon exchange (Born) cross section. SIMC was adapted by P. Datta and others in the SBS collaboration to interface with the existing G4SBS simulation and include nuclear corrections and radiative corrections in quasi-elastic scattering from deuterium [36]. SIMC calculates “real photon” radiative corrections, also called internal Bremsstrahlung radiation. SIMC also calculates “virtual photon” radiative corrections, including vacuum polarization and electron and nucleon vertex corrections. Two-photon exchange is NOT calculated in SIMC [68]. Figure 4.25 shows Feynman diagrams for these radiative corrections. Two-photon exchange is not simulated in SIMC. It also simulates nuclear effects. This includes nuclear binding, where the protons and neutrons in the nucleus are not free and are bound together [69], and Fermi smearing, where the protons and neutrons inside the nucleus are not at rest and have some initial non-zero four-momentum. The radiative and nuclear corrections "smear" out the distributions of observables. SIMC does not include Final State Interactions (FSI). This is where the struck nucleon can interact with the surrounding nuclear medium in the atom. Since deuterium consists of one proton and one neutron, the effects of FSI are less significant than on heavier nuclei. It is also expected that final state interactions are very similar between protons and neutrons, and these effects will mostly cancel out in the ratio. For future work, these corrections and calculations will be applied separately.

4.6.2.2 Geant4 (G4SBS)

The events created by the SIMC generator are then transported through the detector geometry using G4SBS, which is an application of GEANT4. GEANT4 is a simulation toolkit created by CERN for particle transport and interactions in matter [70]. External bremsstrahlung radiation, where a photon is emitted from interaction between the electron and the magnetic field of atomic nuclei after scattering occurs is one radiative correction modeled by GEANT4. The SBS detectors are created in G4SBS and all of the SBS experiments and experimental configurations can be modeled in G4SBS. Figure 4.26 shows the G4SBS visualization for the GMn experimental setup. Variables such as beam energy, target type and spectrometer angle can be configured and run for a given number of events. However, G4SBS event generation does not contain all of the nuclear and radiative effects for deuterium that we would like to model. Therefore, for direct data-Monte Carlo comparison, we interface with SIMC, which produced the events with the desired corrections at the interaction vertex, and then propagate those events through the detectors using G4SBS.

There are several issues with the geometry in G4SBS that are in progress of being fixed.

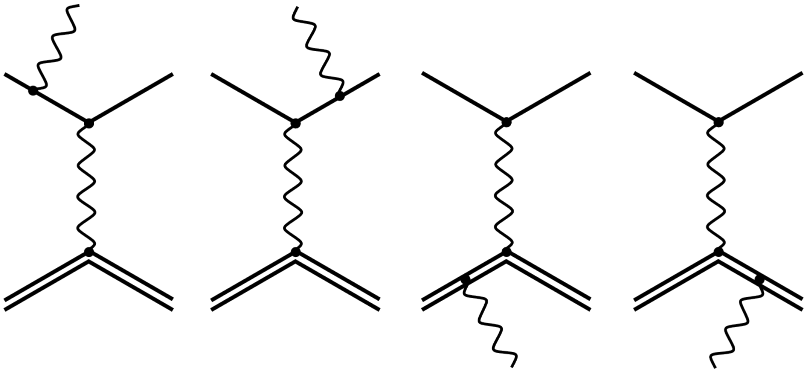

Real Photon Radiative Corrections

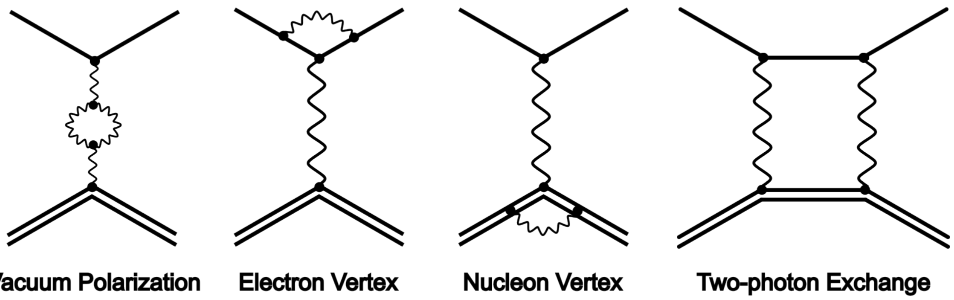

Virtual Photon Radiative Corrections

Figure 4.25: Cartoon of radiative corrections. (Top): "Real Photon" radiative corrections are from Bremsstrahlung radiation emitted by the incident or scattered electron or nucleon. (Bottom): "Virtual Photon" radiative corrections are from a virtual photon being exchanged and no real photon is emitted. These include Vacuum Polarization, Electron or Nuclear Vertex, or Two-photon exchange. Two-photon exchange is not modeled in SIMC.

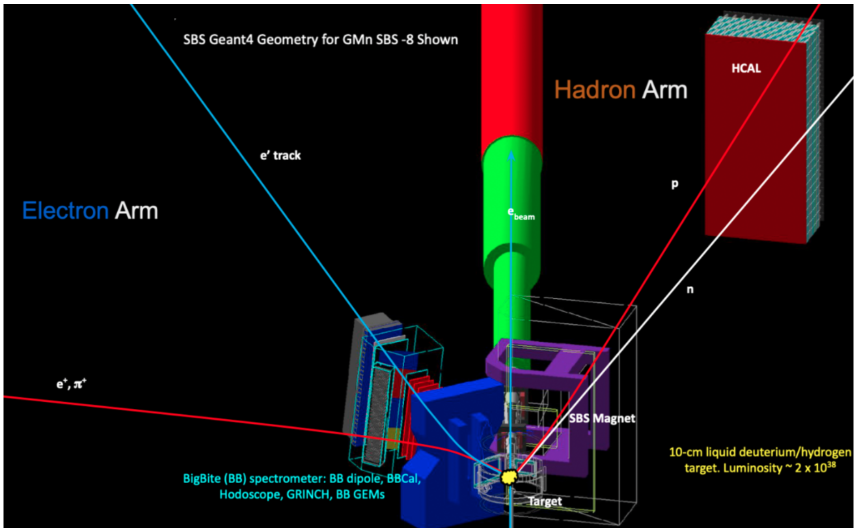

Figure 4.26: eN scattering event illustrated in the G4SBS GEANT4 visualization. The scattered electron, e', is bent up from the BigBite Magnet and is recorded in the BigBite Spectrometer. Positively charged particles that would contribute to background, such as e^+ and π^+, are bent down and away from the BigBite Spectrometer. The scattered proton or neutron is recorded in the hadron arm. Protons are bent towards the top of HCal from the SBS magnet. Figure adapted from S. Seeds.

One issue was that there were non-physical gaps between the blocks in the Shower, which cause the simulated energy distribution to be slightly incorrect. Another issue was that the dimensions of the scattering chamber window were too small [71]. These issues have been fixed and will be implemented in the next large batch of simulations. The simulations used in this work do not have these corrections. A re-run of these extractions could be done in the future with the updated simulation in order to obtain a more accurate extraction of GMn.

4.6.2.3 Digitization

The energy deposits and photoelectrons recorded by the G4SBS simulations must be "digitized" to generate realistic read-out electronic signals. This allows the simulation to be directly compared to experimental data. This process varies between detectors as well as electronics types (ADC and TDC). The energy deposits or photoelectrons, depending on the detector, are first converted into a charge that is used to normalize a pulse shape function. That normalized pulse shape function is then processed through simulated versions of the front-end and read-out electronics [72].

An issue was recently found in the digitization software for the BigBite Shower energy. This caused a tail in the Shower energy distribution on the low energy side. Due to this problem, I will not be cutting on the "E/p" distribution in the simulation, but I will be cutting on "E/p" in the data when making the data-Monte Carlo comparison. This issue has been fixed and will be included in the next "mass replay" of simulation [71]. The extractions in this thesis could be redone with the updated simulations in a straightforward manner in the future.

4.6.2.4 SBS Replay

SBS Replay is a series of scripts and database files that take the raw output from the detectors and process it into meaningful physics quantities such as energy and time [73]. Track reconstruction is also done in this step. Digitized simulation output is also processed by the same SBS Replay software as data. This allows meaningful comparison between simulation and data.

4.6.3 Physics Extraction Software

I have created independent software to analyze data and simulation after they have gone through SBS replay [74]. The series of scripts and classes are applied to both experimental data and Monte Carlo output and eventually produce a value for GMn. The scripts and classes reduce the size of the data, calculate event-by-event quantities including Δx (see Sec. 4.4), fit the Monte Carlo simulations to the data (see Sec. 4.7.1), study the stability of cut choices (see Sec. 5.3), and extract GMn with uncertainties (see Sec. 4.7 and Sec. 5.6). Independent, high-level analysis software and physics extractions allow a double-check between results from various collaborators. Differences can be investigated, and discussions and problem-solving facilitate robust results and a sharing of knowledge.

This software is very flexible with changing variable cuts and changing source files, such as for when updated simulation file are produced in the near future.

4.7 Data–Monte Carlo Comparison

In Eq. (1.17) of Sec. 1.5, we defined the differential cross section $\frac{d\sigma}{d\Omega}$ for *ep* and *en* scattering in the lab frame. To facilitate the Rosenbluth separation technique [6], the literature often introduces a *reduced cross section*, σ_r, defined as

$$\sigma_r = \frac{\varepsilon(1+\tau)}{\tau} \frac{E_e}{E'_e} \frac{\frac{d\sigma}{d\Omega}}{\left(\frac{d\sigma}{d\Omega}\right)_{\text{Mott}}} = G_M^2 + \frac{\varepsilon}{\tau} G_E^2 \,. \tag{4.28}$$

For protons and neutrons, the reduced cross sections become

$$\sigma_p = \left(G_M^p\right)^2 + \frac{\epsilon_p}{\tau_p} \left(G_E^p\right)^2 \,, \tag{4.29}$$

$$\sigma_n = \left(G_M^n\right)^2 + \frac{\epsilon_n}{\tau_n} \left(G_E^n\right)^2 \,. \tag{4.30}$$

In this experiment, we measure *ep* and *en* quasi-elastic scattering from deuterium. Since the proton and neutron are bound in the deuteron rather than free, the measured cross sections must be corrected to account for nuclear and radiative effects, η, as well as nucleon detection efficiencies, ξ[3].

For quasi-elastic scattering from neutrons and protons in deuterium, we write:

$$\left(\frac{d\sigma}{d\Omega}\right)_{d(e,e'n)} = \left(\frac{d\sigma}{d\Omega}\right)_{n(e,e'n)} \eta_n \, \xi_n \,, \tag{4.31}$$

$$\left(\frac{d\sigma}{d\Omega}\right)_{d(e,e'p)} = \left(\frac{d\sigma}{d\Omega}\right)_{p(e,e'p)} \eta_p \, \xi_p \,. \tag{4.32}$$

Our simulation framework (SIMC and G4SBS) calculates the nuclear and radiative corrections and models the interactions of protons and neutrons in HCal that determine

---

[3] We use ξ for detection efficiency to avoid confusion with the virtual photon polarization ε.

their detection efficiencies.

Ideally, if the simulation perfectly reproduced reality, the simulated and measured cross sections would agree. In practice, we observe that the simulated neutron and proton peaks require separate scaling to match the data. We introduce scale factors $[\text{scale factor}]_n$ and $[\text{scale factor}]_p$ such that

$$\left[\frac{\left(\frac{d\sigma}{d\Omega}\right)_{d(e,e'n)}}{\left(\frac{d\sigma}{d\Omega}\right)_{d(e,e'p)}}\right]_{\text{data}} = \frac{[\text{scale factor}]_n}{[\text{scale factor}]_p}\left[\frac{\left(\frac{d\sigma}{d\Omega}\right)_{d(e,e'n)}}{\left(\frac{d\sigma}{d\Omega}\right)_{d(e,e'p)}}\right]_{\text{sim}} = R_{sf}\left[\frac{\left(\frac{d\sigma}{d\Omega}\right)_{d(e,e'n)}}{\left(\frac{d\sigma}{d\Omega}\right)_{d(e,e'p)}}\right]_{\text{sim}}, \tag{4.33}$$

where we define

$$R_{sf} = \frac{[\text{scale factor}]_n}{[\text{scale factor}]_p}. \tag{4.34}$$

Substituting Eqs. (4.31) and (4.32) into Eq. (4.33), we obtain:

$$\frac{\left(\frac{d\sigma}{d\Omega}\right)_{n,\text{data}} \eta_{n,\text{data}}\,\xi_{n,\text{data}}}{\left(\frac{d\sigma}{d\Omega}\right)_{p,\text{data}} \eta_{p,\text{data}}\,\xi_{p,\text{data}}} = R_{sf}\frac{\left(\frac{d\sigma}{d\Omega}\right)_{n,\text{sim}} \eta_{n,\text{sim}}\,\xi_{n,\text{sim}}}{\left(\frac{d\sigma}{d\Omega}\right)_{p,\text{sim}} \eta_{p,\text{sim}}\,\xi_{p,\text{sim}}}. \tag{4.35}$$

For this preliminary analysis, we assume the nuclear and radiative corrections and the detection efficiencies are modeled well in simulation and closely match reality:

$$\frac{\eta_{n,\text{data}}}{\eta_{n,\text{sim}}} = \frac{\eta_{p,\text{data}}}{\eta_{p,\text{sim}}} = \frac{\xi_{n,\text{data}}}{\xi_{n,\text{sim}}} = \frac{\xi_{p,\text{data}}}{\xi_{p,\text{sim}}} = 1\,. \tag{4.36}$$

As HCal calibrations improve and efficiency determinations become more precise, the simulation will be updated accordingly. Ongoing efforts aim to better model the efficiency of individual HCal blocks and to quantify the uncertainty of the assumption in Eq. (4.36). This analysis does not incorporate those uncertainties and thus assumes

$$\frac{\left(\frac{d\sigma}{d\Omega}\right)_{n,\text{data}}}{\left(\frac{d\sigma}{d\Omega}\right)_{p,\text{data}}} = R_{sf}\frac{\left(\frac{d\sigma}{d\Omega}\right)_{n,\text{sim}}}{\left(\frac{d\sigma}{d\Omega}\right)_{p,\text{sim}}}. \tag{4.37}$$

The Monte Carlo simulation uses world-data fits of the nucleon form factors [67] (see Appx. A). If these fits perfectly reflected reality, R_{sf} would equal unity. Since proton form factors are known more precisely than neutron form factors at the relevant Q^2, deviations of R_{sf} from unity likely reflect uncertainties in the neutron cross sections.

We can express the measured ratio of cross sections in terms of reduced cross sections:

$$\left[\frac{\sigma_n}{\sigma_p}\right]_{\text{data}} = R_{sf}\left[\frac{\sigma_n}{\sigma_p}\right]_{\text{sim}} . \tag{4.38}$$

Expanding the reduced cross sections explicitly in terms of the form factors gives:

$$\frac{\left(G_M^n\right)^2 + \frac{\epsilon_n}{\tau_n}\left(G_E^n\right)^2}{\left(G_M^p\right)^2 + \frac{\epsilon_p}{\tau_p}\left(G_E^p\right)^2} = R_{sf}\left[\frac{\sigma_n}{\sigma_p}\right]_{\text{sim}} . \tag{4.39}$$

Finally, solving for G_M^n yields:

$$G_M^n = \sqrt{R_{sf}\left[\frac{\sigma_n}{\sigma_p}\right]_{\text{sim}}\left({G_M^p}^2 + \frac{\epsilon_p}{\tau_p}{G_E^p}^2\right) - \frac{\epsilon_n}{\tau_n}{G_E^n}^2} . \tag{4.40}$$

The ratio $[\sigma_n/\sigma_p]_{\text{sim}}$ is computed directly from the parameterizations of G_M^n, G_E^n, G_M^p, and G_E^p used in the simulation, supplemented by world-data fits to G_M^p, G_E^p, and G_E^n.

4.7.1 Data–Monte Carlo Comparison Fit Function

For this extraction, as explained in Sec. 4.7, we are comparing the data directly to simulation. This is done by fitting the data to a scaled version of the Δx histogram from SIMC and G4SBS for neutrons, and a separate scaled version of the Δx histogram from SIMC and G4SBS for protons, and then adding a background function. We are also allowing the simulation histograms to shift slightly along the x-axis. The mean of the proton simulated histogram is matched to real data by "tuning" an overall field scaling parameter in the simulation code. Several iterations of tuning were done for each kinematic and filed setting, however, it is a challenge to get the peaks to line up, even after several iterations. Writing out this fit function:

$$\begin{aligned} f(\Delta x) = {} & \texttt{[scale factor]}_{\texttt{n}} \times \texttt{hist}_{\texttt{n}}(\Delta x - \texttt{shift}_{\texttt{n}}) \\ & + \texttt{[scale factor]}_{\texttt{p}} \times \texttt{histo}_{\texttt{p}}(\Delta x - \texttt{shift}_{\texttt{p}}) \\ & + \texttt{Background}(\Delta x) \end{aligned} \tag{4.41}$$

We have previously defined the ratio of the scale factors, R_{sf}, in Sec. 4.7. Restating R_{sf} for convince here:

$$R_{sf} = \frac{\texttt{[scale factor]}_{\texttt{n}}}{\texttt{[scale factor]}_{\texttt{p}}} \,. \tag{4.42}$$

Rearranging Eq. (4.41), we can express it in terms of R_{sf} as

$$\begin{aligned} f(\Delta x) = {} & \texttt{[scale factor]}_{\texttt{p}} \times \left\{ \mathrm{hist}_{\mathrm{p}}(\Delta x - \texttt{shift}_{\texttt{p}}) + R_{sf} \times \mathrm{hist}_{\mathrm{n}}(\Delta x - \texttt{shift}_{\texttt{n}}) \right\} \\ & + \texttt{Background}(\Delta x) \,. \end{aligned} \tag{4.43}$$

Using Eq. (4.43), we can make a custom fit function in ROOT that explicitly solves for R_{sf} as a free parameter with uncertainty. The other free parameters are the $\texttt{[scale factor]}_{\texttt{p}}$, the shift of both the SIMC histograms, $\texttt{shift}_{\texttt{p}}$ and $\texttt{shift}_{\texttt{n}}$ and the background fit parameters.

The $\texttt{Interpolate}(x)$ function in ROOT is used to implement the simulation histograms as parameters. It estimates the value of the histogram at a given x by performing a linear interpolation between the two nearest bins. If x is between two bin center, x_i and x_{i+1}, then

$$\texttt{Interpolate}(x) = y_i + (x - x_i) \times \frac{y_{i+1} - y_i}{x_{i+1} - x_i} \,, \tag{4.44}$$

where y_i and y_{i+1} are the bin contents of the left and right bins.

4.8 HCal Nucleon Detection Efficiency

Understanding and modeling the nucleon detection efficiency of HCal is critical to the success of this experiment. We aim to address two key questions: first, *how well does HCal detect protons?* and second, *how does that differ from how well it detects neutrons?*

The final physics extraction relies on the *ratio* of a quantity measured for protons to the corresponding quantity measured for neutrons. Any difference in detection efficiency between protons and neutrons propagates directly into this ratio and therefore must be carefully understood and quantified.

4.8.1 Proton Detection Efficiency: Measurement and Modeling

The first question can be investigated in a straightforward manner[4]; Using the liquid hydrogen target (LH2) as a "proton target", we ask: How often does HCal detect a proton when the electron arm detects a good elastically scattered electron? How does this change across different physical locations on HCal?

We define the HCal detection efficiency for protons or neutrons as the ratio of detected to expected events:

$$\epsilon_{\text{HCal}}^{(p,n)} = \frac{\text{Number of } (p,n) \text{ events detected in HCal}}{\text{Number of } (p,n) \text{ events expected to hit HCal (from electron-arm analysis only)}} . \tag{4.45}$$

To study the efficiency as a function of a kinematic or spatial variable X (e.g., x_{exp}, y_{exp}), we compute the efficiency of bin i in variable X, yielding a histogram of efficiencies:

$$\epsilon_{\text{HCal}}^{(p,n)}(X_i) = \frac{\text{Number of events in bin } i \text{ of } X \text{ with HCal analysis}}{\text{Number of events in bin } i \text{ of } X \text{ from electron-arm analysis only}} . \tag{4.46}$$

---

[4] The larger concept is somewhat straightforward, but as with all experimental physics, the implementation is anything but.

This procedure produces a histogram of $\epsilon_{\text{HCal}}(X_i)$, which represents the efficiency as a function of X. By applying this method in two dimensions over the HCal x-y plane with corrections for deflection of the protons in the magnetic field (δx_{SBS}), which depends on the proton momentum, we construct the efficiency map $\epsilon_{\text{HCal}}(x, y)$. This map is used to correct the MC and assess systematic uncertainties.

The resulting efficiency map for SBS-8, shown in Fig. 4.27 (courtesy of P. Datta [36]), highlights the regions of reduced efficiency that are within the fiducial cuts and are thus of particular concern. We can see distinct drops in efficiency at $x \approx -0.7$ m and $y \approx -1.7$ m, likely due to known hardware issues with those HCal regions.

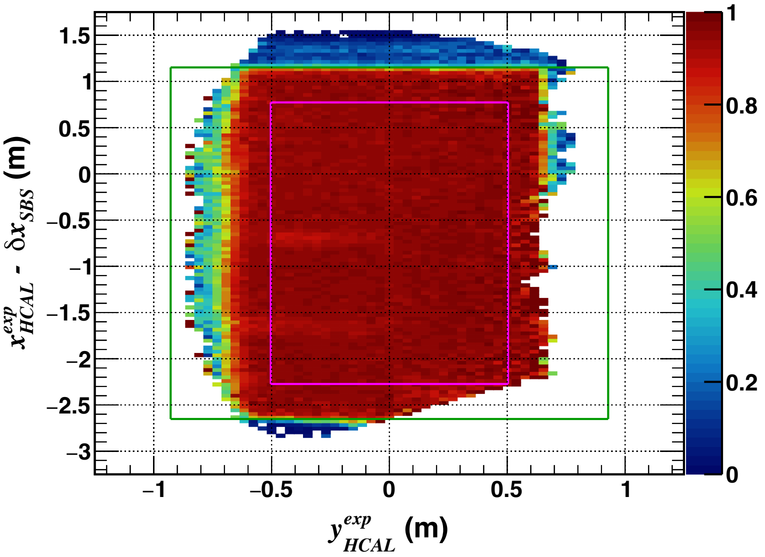

Figure 4.27: HCal proton detection efficiency results from a combined analysis of hydrogen data at multiple field strengths in SBS-8. δx_{SBS} is the calculated deflection of the proton in the magnetic field from its momentum. Green represents the physical boundary of HCal, and magenta represents a possible fiducial cut.

4.8.2 Position-Dependent Efficiency Corrections in MC

To account for the HCal position-dependent inefficiencies and estimate the systematic uncertainty associated with them, we draw on the work of P. Datta [36], who developed and implemented a correction scheme in the Monte Carlo (MC) to account for the observed non-uniformity in the proton detection efficiency across the HCAL acceptance. In his analysis, the detection efficiency was found to vary significantly with position, particularly in the dispersive direction, due to non-uniform response in certain regions of the detector. To model this in MC, Datta constructed a two-dimensional efficiency map, $\epsilon_{\mathrm{HCAL}}^{\mathrm{data}}(x,y)$, using SBS-8 ($Q^2 = 4.5$ GeV^2, $\varepsilon = 0.8$) recorded at multiple SBS magnetic field settings ($0\%, 50\%, 70\%, 100\%$). The efficiency at each position was then normalized to the acceptance-averaged value to produce a relative correction factor:

$$c(x,y) = \frac{\epsilon_{\mathrm{HCAL}}^{\mathrm{data}}(x,y)}{\langle \epsilon_{\mathrm{HCAL}}^{\mathrm{data}}(x,y) \rangle}\,. \tag{4.47}$$

These correction factors were applied to MC events based on their expected impact positions (computed from MC truth information and accounting for the SBS deflection), thereby introducing artificial position-dependent inefficiency in the MC to match the observed data.

The implementation of these corrections in the MC resulted in improved agreement between the data and MC efficiency profiles. Specifically, the characteristic dips in efficiency at $x \approx -1.7$ (m) and $x \approx -0.7$ (m) observed in the data were successfully reproduced in the MC after applying the corrections [36]. Datta quantified the effect of these inefficiencies on physics extractions by comparing results obtained with and without the corrections applied, and he adopted the relative difference as the systematic uncertainty due to position-dependent efficiency. We follow this prescription here, using his reported uncertainties for our own analysis. For further details of the method and validation of the corrections, see [36].

4.8.3 Neutron vs. Proton Efficiency: Challenges and Assumptions

The second question we posed—*how are neutrons and protons affected differently?*—is considerably more difficult to answer, largely because there is no free neutron target.

Experimentally calibrating neutron detectors is therefore challenging.

At Jefferson Lab, pion photoproduction is one technique that can be used to produce neutrons for calibration. In this reaction, a real photon (not a virtual photon) and a proton interact to produce a pion and a neutron: $\gamma p \rightarrow \pi^+ n$. To create this interaction in the lab, the electron beam strikes a copper radiator positioned directly in front of a hydrogen target. Real photons are generated through bremsstrahlung radiation as the electrons interact with the radiator, and these photons can then interact with protons in the hydrogen target[5], producing pions and neutrons [75].

Although neutron detection efficiency measurements using pion photoproduction were originally planned for the GMn experiment [27], logistical and technical constraints ultimately prevented this measurement from being carried out. The plan was to use the Left High Resolution Spectrometer (L-HRS) to detect, or "tag," a pion while checking HCal for a coincident neutron[6]. This method is analogous to how the proton detection efficiency is measured in this experiment using the BigBite spectrometer to detect the electron. However, performing this measurement would have required a special target configuration and moving the BigBite detector stack and magnet with a crane. The Hall A crane was unavailable due to needed repairs, and the combination of limited beam time and reduced personnel during the COVID-19 pandemic made it impractical[7]. After the experiment concluded, an alternative idea—identifying π^+ in the electron arm using an "end point method"—was proposed and is currently under investigation by collaborators [76].

In the absence of direct calibration, this analysis relies on simulation to model the neutron-to-proton detection efficiency ratio—an assumption that must be treated with appropriate caution. Differences in detection efficiency between protons and neutrons are expected to contribute to the systematic uncertainty, though they are not easily quantified.

---

[5] The reaction $\gamma n \rightarrow \pi^- p$ can also be measured using a deuterium target, analogous to how we utilize deuterium in the GMn experiment.

[6] R. Michaels and I (M. Satnik) prepared the L-HRS for several months in anticipation of this measurement. The experience provided valuable insight into the operation and calibration of various detectors and the trigger system.

[7] The L-HRS has since been all but officially decommissioned, and restoring it would require a significant investment of time and resources.

To estimate this uncertainty, we follow Datta's approach and assign a conservative 2% systematic error on R_{sf}, applied uniformly across all kinematics. While this value was not explicitly justified in his thesis, it appears informed by the original GMn proposal [27], which assigned a 2% systematic uncertainty to account for possible efficiency variations in uncalibrated regions of the BigHAND detector. The updated proposal [28], which replaced BigHAND with HCal, anticipated smaller and better-controlled efficiency differences and estimated a systematic uncertainty of approximately 0.5% per kinematic point—assuming calibration measurements were performed. Since those calibrations were ultimately not carried out, we retain the more conservative 2% uncertainty to account for the lack of direct measurement. Future work, incorporating improved simulations and/or calibration data, may enable a more precise determination of this uncertainty.

Despite this limitation, there are good reasons to believe that the simulation reasonably models the relative neutron and proton detection efficiencies. The results for proton detection efficiency obtained from simulation already agree well with experimental data and continue to improve as the simulation is refined. It is worth noting, however, that the simulations used in the present analysis predate some of these recent improvements and likely reflect residual geometric and calibration issues identified as of Spring-2025. Nonetheless, the methods of analysis developed here to extract G_M^n can be readily re-applied with updated simulations as they become available.

In summary, proton detection efficiency is well measured using hydrogen data and modeled in Monte Carlo using the position-dependent map from Datta. Neutron efficiency is assumed to be reasonably modeled by the simulation, with an assigned 2% systematic uncertainty to account for possible differences.

Chapter 5

Results

5.1 Uncertainty Evaluation Strategy

To evaluate the overall uncertainties of our G_M^n extractions, we must evaluate both statistical and systematic uncertainties. Statistical uncertainty is somewhat straightforward: we will utilize the built-in fit uncertainty calculations of ROOT. We will discus statistical uncertainty in Sec. 5.2. Systematic uncertainty is typically more difficult to quantify than systematic uncertainty and will be discussed in Sec. 5.3.

In this work, we will investigate the following systematic uncertainties:

- Variable Cut Choices (Sec. 5.3.1
- Inelastic Background Shape/Background Choice (Sec. 5.3.2)
- HCAL proton detection efficiency non-uniformity
- HCAL neutron-to-proton detection efficiency ratio

For the present analysis, we will lean on others' work for evaluations of these HCal systematics (See Sec. 5.3.4).

5.2 Statistical Uncertainty Evaluation

The statistical uncertainty is a reflection of the amount of data used in an extraction. Assuming Poisson distributions, the more data points used in the final extraction, the smaller the statistical uncertainty. To evaluate the statistical uncertainty of the individual R_{sf} extractions, we will mainly be relying on the reported fit uncertainty in the ROOT fit of simulation to data. The fit in root utilizes chi-squared minimization on a bin-by-bin basis. If the fit perfectly matched the data, i.e. the χ^2/ndf is 1, the uncertainty on R_{sf} extracted by the fit would be a good representation of the statistical uncertainty *on the data*. When using the scaled Δx from $d(e, e'p)$ and $d(e, e'n)$ simulations as a part of the fit, the statistical uncertainty of the simulation is not taken into account. To account for the statistical uncertainty of the simulations, I have enacted the following fit procedure: First, fit the Δx distribution to scaled versions of the Δx distributions from $d(e, e'p)$ and $d(e, e'n)$ simulations. Next, scale up the bin-by-bin uncertainty of each bin in the simulated $d(e, e'p)$ and $d(e, e'n)$ distributions by the scales determined by the fit. Then, add in quadrature the bin-by-bin uncertainty of the real data, scaled $d(e, e'p)$ simulation, and scaled $d(e, e'n)$ simulation, and assign that value as the new bin-by-bin uncertainty of the real data. The error bars will now be bigger. Finally, refit the data with the new larger error bars as before. This will result in fits that have larger errors on R_{sf} and χ^2/ndf closer to 1.

Table 5.1: Statistical uncertainty study. R_{sf} and corresponding errors and χ^2/ndf are compared for various kinematics with and without the MC statistical uncertainty included.

Method	**Fit once (no MC uncert)**				**Bin-by-bin errors added in quad. to data**				
	R_{sf}	R_{sf} err	χ^2/ndf	% err	R_{sf}	R_{sf} err	χ^2/ndf	% err	R_{sf} %change
SBS-4 30%	0.96552	0.006491	2.23	0.67	0.965997	0.007485	1.68	0.77	0.052
SBS-4 50%	1.025847	0.017724	1.498	1.72	1.038236	0.019828	1.546	1.9	1.208
SBS-8 70%	1.086031	0.003659	3.35	0.336	1.083049	0.008228	0.742	0.765	-0.765
SBS-8 50%	1.11401	0.011348	1.611	1.02	1.113612	0.013701	1.138	1.23	-0.036
SBS-8 100%	1.056097	0.009226	1.957	0.87	1.054796	0.012784	1.03	1.07	0.13
SBS-9 70%	1.065389	0.004751	4.19	0.445	1.065761	0.009543	1.17	0.89	0.038

Table 5.1 compares R_{sf} when the Δx histogram is fit once (not taking into account the Monte Carlo statistics) to R_{sf} when the Δx histogram is fit twice using the scaling and quadrature method described above. We see that the error on R_{sf} is larger in the second

method, and the χ^2/ndf is reduced. This suggests that the fit better describes the data, and the poor fit suggested by the large χ^2/ndf values is now numerically represented in the R_{sf} error.

5.3 Systematic Uncertainty Evaluation

This work will focus on two of the source of systematic uncertainty for this experiment: *variable cut choice* and *inelastic background shape*. The systematic uncertainties due to HCal will be cited from other's works.

5.3.1 Cut Variability Studies

The choice of event-by-event cuts on different variable to isolate quasi-elastic scattering events is a source of systematic error. For each variable, we had to make a choice and pick a value for the cut. If we had chosen a slightly different value, how would have that changed our final result?

To conduct this study, all cuts are held constant while only the variable we are studying is changed[1]. The final choice of cuts that apply across all kinematics are found in Tab. 5.2, and the cuts that vary between kinematics are found in Tab. 5.3.

Table 5.2: "Global cuts" used in this analysis across all kinematics. The description of the variable is given along with the SBS-Replay variable name.

Variable	Cut (for all Kinematics)
Preshower Energy	bb.ps.e> 0.2
Num. GEM Tracks	bb.tr.n== 1
Num. GEM Planes Hit	bb.gem.track.nhits>= 3
χ^2/ndf of Track	bb.gem.track.chi2ndf< 15
Track z at Target Vertex	abs(bb.tr.vz)< 0.07
Invariant Mass W^2 Min.	$\mathrm{W}^2 > 0.48$
Invariant Mass W^2 Max.	$\mathrm{W}^2 < 1.28$
Δy	abs(hcal_dy)< 0.5
Optics Check x	abs(bb.tr.r.x-bb.tr.r.th∗0.9) < 0.3
Optics Check y	abs(bb.tr.r.y-0.9*bb.tr.r.ph+0.005)< 0.1
BBCal – HCal Coincidence	abs(hcal_sh_atime_diff)< 10

---

[1] W^2 and Δy studies are the exception to this, as they are highly correlated.

Table 5.3: Kinematic-dependent variable cuts. These cuts are different between each kinematic and are used to isolate quasi-elastic events and reduce proton–neutron biases in HCal.

Cut	SBS-4 30%	SBS-4 50%	SBS-8 50%	SBS-8 70%	SBS-8 100%	SBS-9 70%
x_{exp} (m) min.	-1.3	-0.87	-1.54	-1.27	-0.92	-0.84
x_{exp} (m) max.	0.54	0.54	0.63	0.63	0.63	0.27
y_{exp} (m) min.	-0.35	-0.35	-0.4	-0.4	-0.4	-0.35
y_{exp} (m) max.	0.4	0.4	0.35	0.35	0.35	0.35
abs(e_over_p-0.98) $<$ (Data Only)	0.2	0.2	0.5	0.5	0.5	0.2
hcal energy (GeV) $>$	0.025	0.025	0.04	0.04	0.04	0.04

5.3.1.1 Track Vertex z at Target Stability

Let us take the Track Vertex z that we discussed in Sec. 4.5.1.4 as an example. We chose to only include events where Track Vertex is between (-0.07, 0.07) m. What if we had instead chosen (-0.071, 0.071) m, or (-0.075, 0.07) m, or (-0.07,0.065) m, etc.? All of those seem to be reasonable choices when looking at a histogram of the variable. How do we quantify the uncertainty in our variable selection?

The strategy implemented in this work is to keep one end of the cut boundary the same and change the other cut boundary slightly around the other boundary value. For all variables other than the variable being studied, we will make "ideal cuts" and change only the variable we are studying, one at a time. We will also keep the background shape to be a second order polynomial. These cuts are found in Tab. 5.2 and Tab. 5.3. For the Track Vertex z example, this means evaluating R_{sf} for each cut variation of Track Vertex z cut in the following manor, shown in Tab. 5.4:

These cuts are applied to both data and simulation. Varying the minimum value of the boundary is shown in Fig. 5.1b ("left cut boundary study"), and varying the maximum boundary is shown in Fig. 5.1a ("right cut boundary"). R_{sf} is determined by fitting the background to a 2nd degree polynomial fit for each set of cuts. The extracted R_{sf} values are then plotted against the values of the boundary that was changed. The mean and standard deviation are calculated for the distribution. A linear fit is also applied. The "rise across range" is calculated from the linear fit.

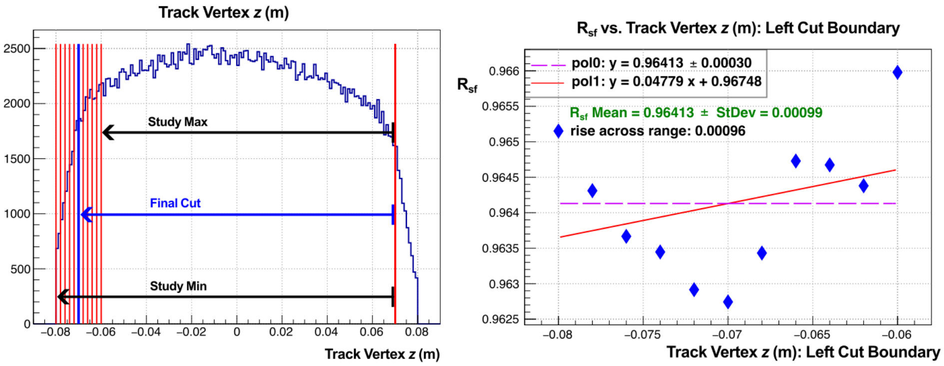

(a) Track Vertex z: left cut boundary study

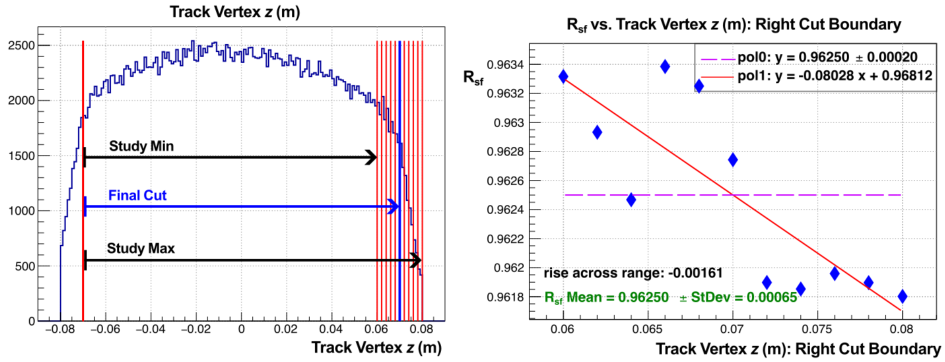

(b) Track Vertex z: right boundary study

Figure 5.1: Target Vertex z Stability Study for SBS-4 30% field ($Q^2 = 3.0$ GeV^2). Subfigure **(a)** shows the left boundary study, where the minimum value of the Track Vertex z is changed to see how R_{sf} changes. Subfigure **(b)** shows the right boundary study, where the maximum value of the Track Vertex z is changed to see how R_{sf} changes. The graphs of R_{sf} vs. the boundary are fitted with constant (pol0), linear (pol1), with the mean and standard deviation are calculated. The "rise across range" is how much the linear fit changes over the range.

Table 5.4: Track vertex z stability ranges. The Left Boundary studies how varying the minimum cut boundary effects R_{sf}, and the Right Boundary studies how the varying the maximum cut boundary effects R_{sf}. (Track z min, Track z max) is the cut applied to Track Vertex z for each extraction. These cuts are applied in Fig. 5.1

Left Boundary Study (min)		Right Boundary Study (max)	
Track z min	Track z max	Track z min	Track z max
-0.08	0.07	-0.07	0.06
-0.078	0.07	-0.07	0.062
-0.076	0.07	-0.07	0.064
-0.074	0.07	-0.07	0.066
-0.072	0.07	-0.07	0.068
-0.07	0.07	-0.07	0.07
-0.068	0.07	-0.07	0.072
-0.066	0.07	-0.07	0.074
-0.064	0.07	-0.07	0.076
-0.062	0.07	-0.07	0.078
-0.06	0.07	-0.07	0.08

If the “rise across range”/2 is greater than the standard deviation, that suggests that there is some correlation between R_{sf} and the cut variable that is more than just random variation. For this study, we will take whatever measure is greater for each boundary, “rise across range”/2 or standard deviation, and add that in quadrature for our systematic contribution.

Note that these subsets of data are highly correlated and dependent on each other, as the subsets will share the majority of the same data points. Therefore, another strategy to evaluate the systematic uncertainty for each variable cut choice is to look at subsections of the data across a given variable and extract R_{sf}. The variation of the value for R_{sf} can shed light on the systematic uncertainty of that variable. This method drastically reduces the statistics in each slice compared to the data set as a whole, and it can be difficult to extract R_{sf} on the slices with lower statistics. This work will not include these type of studies, as I was unable to figure out how to extract useful information with the low statistics.

5.3.1.2 GEM Track χ^2/ndf Stability

As discussed in Sec. 4.2, the tracking algorithm takes the 2-dimensional hits in each GEM module and computes linear fits from combinations of these hits. The χ^2 per number of degrees of freedom is used as a measure of the quality of the fit. Tracks with a larger χ^2/ndf are more likely to not be from real events or poor fits. Figure 5.2 shows how the cut boundary is varied from 10 to 30 and its subsequent effect on R_{sf}. The variation of R_{sf} from this cut is very minimal and could be seen as negligible for this kinematic.

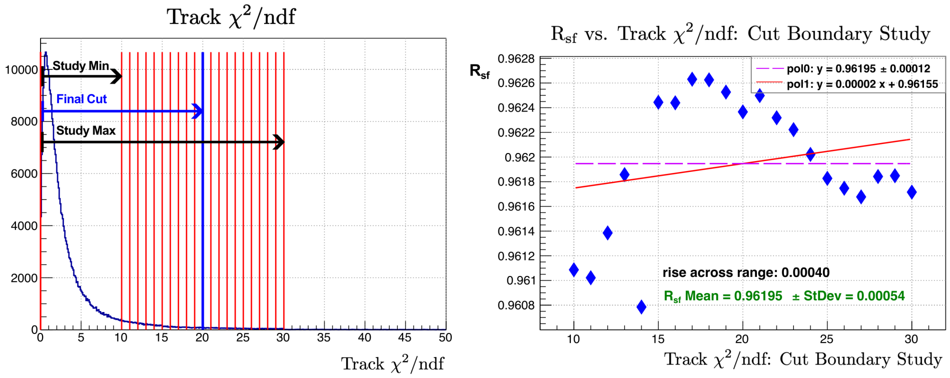

Figure 5.2: Track χ^2/ndf stability study for SBS-4 30% field ($Q^2 = 3.0$ GeV^2). (Left Figure) Visualization of the various slices used to study the stability of the GEM track χ^2/ndf. (Right Figure) R_{sf} vs. the cut boundary. Constant (pol0) and linear (pol1) fits are applied, with the mean and standard deviation are shown. The "rise across range" is how much the linear fit changes over the range.

5.3.1.3 Number of GEM Planes Hit

The cut on the number of GEM modules/planes hit (nhits) is varied to see the cut's effect on R_{sf}. The minimum number of GEM planes hit to produce a track is 2—a line between two points. The data analyzed here already had a cut of nhits>= 3. As the number of modules hit increases, the higher the chance that it is a real track and not random noise. There are a total of five layers of GEM modules. Figure 5.3, demonstrates the change in R_{sf} if the track was required to be nhits>= 3, nhits>= 4, or nhits= 5. The variation of R_{sf} is minimal for this kinematic and will not contribute significantly to the systematic uncertainty,

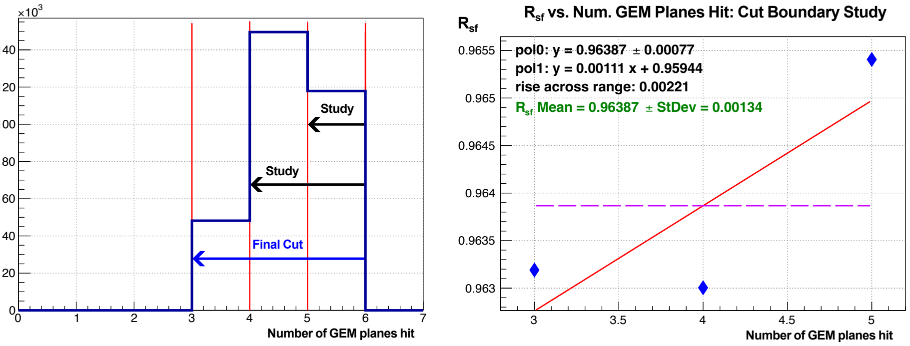

Figure 5.3: Number of GEM planes hit stability study for SBS-4 30% field ($Q^2 = 3.0$ GeV^2). Left Figure: Visualization of the various slices used to study the stability of the number of GEM planes hit (nhits). Right Figure: R_{sf} vs. the cut boundary. Constant (pol0) and linear (pol1) fits are applied, with the mean and standard deviation are shown. The "rise across range" is how much the linear fit changes over the range.

5.3.1.4 HCal Energy Stability

The cut on the energy of the best cluster in HCal is varied to study the cut's effect on R_{sf}. Energies less than the cut are rejected. Figure 5.4 shows the HCal energy cut varied from 0.015 to 0.035 (GeV) for SBS-4 30% field setting ($Q^2 = 3.0$ GeV^2).

We can see a downward trend in the slope of the R_{sf} plot, showing that there is a correlation. However, it is still somewhat insignificant for this kinematic setting, as *rise over range*/2 is less than 0.3% of the mean.

5.3.1.5 Preshower Minimum Energy Stability

To study the systematic uncertainty on the Preshower minimum energy cut, we vary the cut boundary and plot R_{sf} to see how it varies in response. Figure 5.5 shows this study. The standard deviation from the mean of R_{sf} is less than 0.04% of the mean, and thus could be considered negligible for SBS-4 30%.

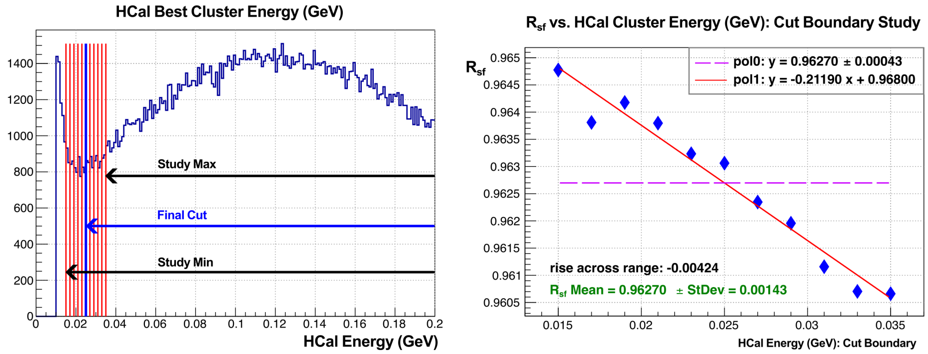

Figure 5.4: HCal cluster energy cut stability study for SBS-4 30% field ($Q^2 = 3.0$ GeV^2). Left Figure: Visualization of the various slices used to study the HCal cluster energy cut. Right Figure: R_{sf} vs. the cut boundary. Constant (pol0) and linear (pol1) fits are applied, with the mean and standard deviation are shown. The "rise across range" is how much the linear fit changes over the range.

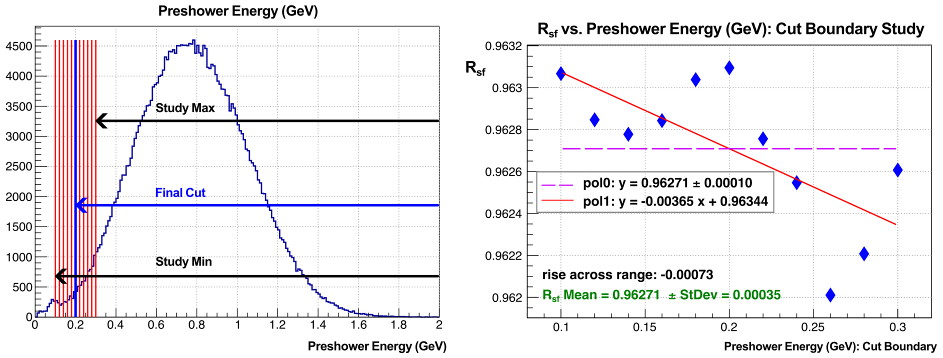

Figure 5.5: Preshower energy stability study for SBS-4 30% field ($Q^2 = 3.0$ GeV^2). Left Figure: Visualization of the various slices used to study the Preshower cluster energy cut. Right Figure: R_{sf} vs. the cut boundary. Constant (pol0) and linear (pol1) fits are applied, with the mean and standard deviation are shown. The "rise across range" is how much the linear fit changes over the range.

5.3.1.6 HCal–Shower Coincidence Time Stability

The coincidence time between the Shower and HCal shows a difference between protons and neutrons. For this analysis, we are going to cut outside to make sure we are not including these biases. Although Fig. 5.6 shows these biases, we see that when we make a wide cut on the coincidence time, the biases result in small variations of R_{sf} in this kinematic of SBS-4, 30% field ($Q^2 = 3.0$ GeV^2). In the right boundary study, the *rise over range*/2 for R_{sf} is less than 0.2% of the mean of R_{sf}.

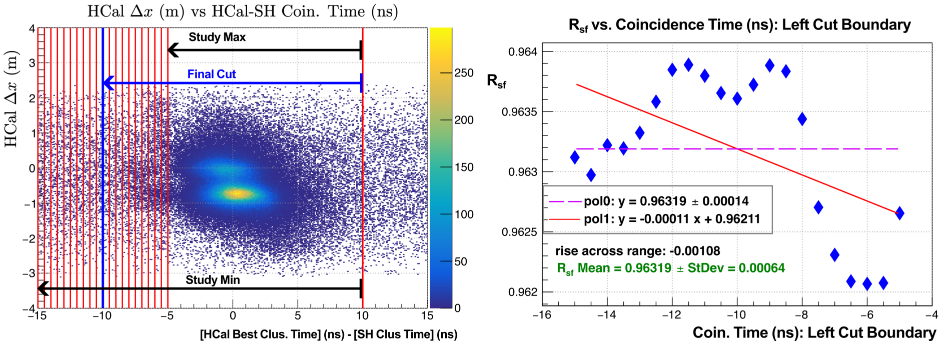

(a) Coincidence time stability study: left boundary

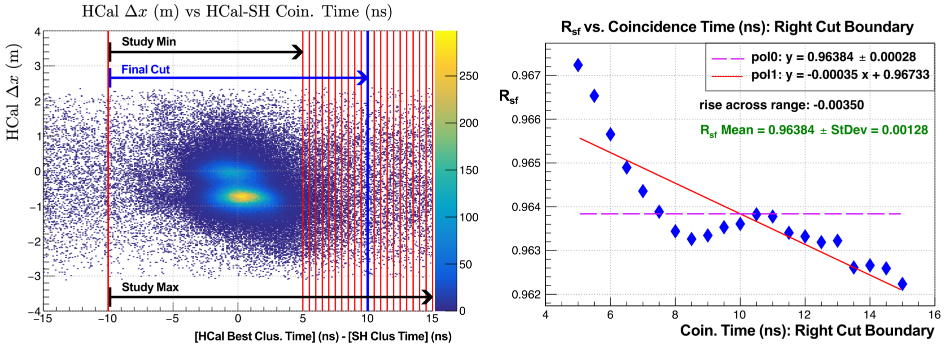

(b) Coincidence time stability study: right boundary

Figure 5.6: Coincidence time stability study for SBS-4 30% field ($Q^2 = 3.0$ GeV^2). Subfigure **(a)** shows the left boundary study, where the minimum value of the coincidence time cut is changed to see how R_{sf} changes. Subfigure **(b)** shows the right boundary study, where the maximum value of the coincidence time cut is changed to see how R_{sf} changes. The graphs of R_{sf} vs. the boundary are fitted with constant (pol0) fits, linear (pol1) fits, with the mean and standard deviation shown. The "rise across range" is how much the linear fit changes over the range.

5.3.1.7 HCal Delta y Stability

The cut on Δy helps eliminate inelastic background. However, this cut does change R_{sf} in a possibly significant way. Δy is correlated to the invariant mass, W^2, thus only the variable with the largest uncertainty will be included. See Fig. 4.9 for this correlation. A further analysis quantifying that correlation and incorporating it into the final uncertainty would be beneficial. The uncertainty from the left and right boundary studies will be added in quadrature. The data in Fig. 5.7 does not contain any cuts on W^2.

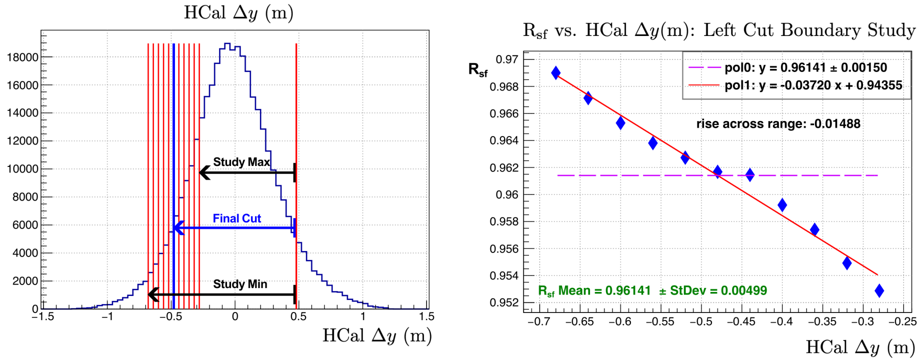

(a) Stability Study of Δy: left boundary

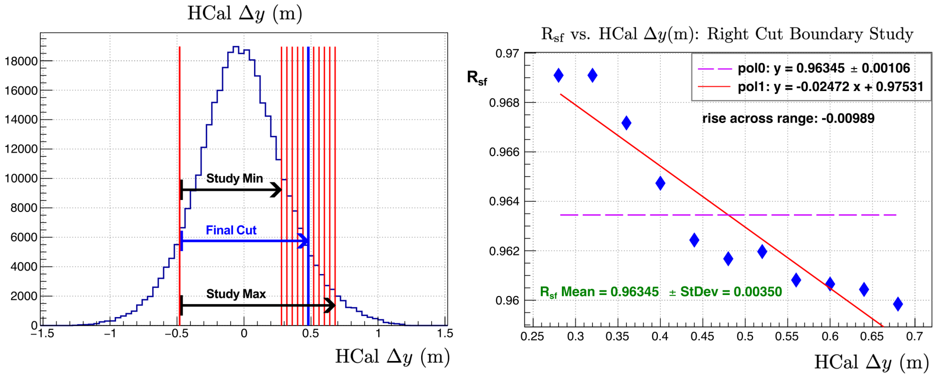

(b) Stability Study of Δy: right boundary

Figure 5.7: Δy stability study for SBS-4 30% field ($Q^2 = 3.0$ GeV^2). Subfigure **(a)** shows the left boundary study, where the minimum value of the Δy cut is changed to see how R_{sf} changes. Subfigure **(b)** shows the right boundary study, where the maximum value of the Δy cut is changed to see how R_{sf} changes. The graphs of R_{sf} vs. the boundary are fitted with constant (pol0) fits, linear (pol1) fits, with the mean and standard deviation shown. The "rise across range" is how much the linear fit changes over the range.

We can see that the Δy uncertainty is much larger than the variables we have studied so far and there is clearly a downward trend. This suggests that events with larger Δy appear more proton-like. Or, it could be that the background in that slice of Δy appears more proton-like. The *rise over range*/2 for the left boundary study in Subfigure **(a)** is $\approx 0.08\%$ of the mean. Although this is still small, it is significantly larger than the other variable cuts we have looked at so far. This study is looking over a large range of Δy cuts. Further investigation into the systematic uncertainty of Δy could be useful. The wide cut study selection is likely over-estimating the uncertainty, and further study of this variable would be useful.

5.3.1.8 Invariant Mass Stability

We can vary the cut boundaries on the invariant mass, W^2, and record how it changes R_{sf} to get a measure of the statistical uncertainty of the invariant mass cut. We will add the uncertainties from the left and right boundaries in quadrature. Since W^2 and Δy are correlated, as previously shown in Fig. 4.9, we will compute the uncertainty from both and take the larger value. The data in the histograms in Fig. 5.8 do not contain any cuts on Δy.

The systematic uncertainty on both W^2 and Δy when measured this way give a significant value for the total uncertainty. Further investigation of these cuts and these systematics could be beneficial. One possibility is that the range studied here is too large. A good future step would be to calculate the correlation factor between these variables and incorporate it into the overall uncertainty calculation.

5.3.1.9 HCal x-expected and y-expected Stability

We make cuts on x-expected (x_{exp}) and y-expected (y_{exp}) to make sure the straight line projection of the scattered nucleon is pointing at the active area of HCal, and that the projection will hit HCal if it is either a proton or a neutron. See Sec. 4.5.2 for more details on calculating x-expected and x-expected.

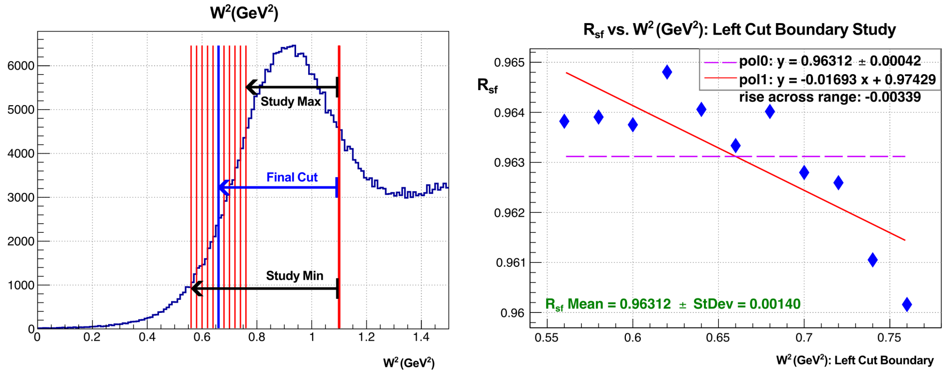

(a) Stability Study of invariant mass, W^2: left boundary

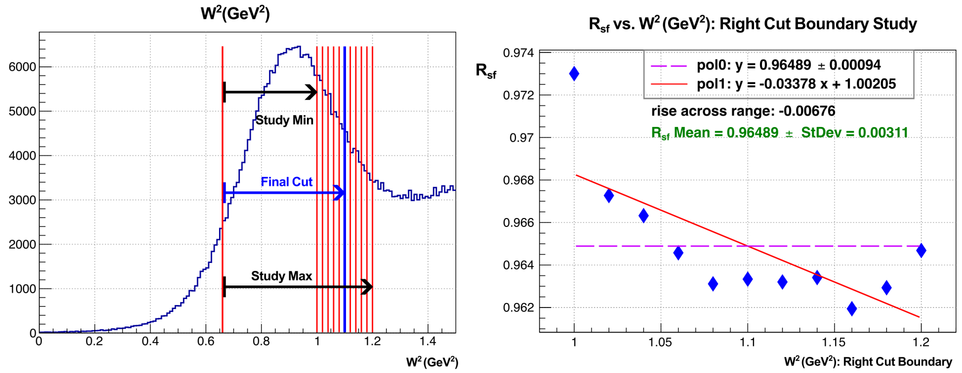

(b) Stability Study of invariant mass, W^2: right boundary

Figure 5.8: Invariant mass (W^2) stability study for SBS-4 30% field ($Q^2 = 3.0$ GeV^2). Subfigure **(a)** shows the left boundary study, where the minimum value of the W^2 cut is changed to see how R_{sf} changes. Subfigure **(b)** shows the right boundary study, where the maximum value of the W^2 cut is changed to see how R_{sf} changes. The graphs of R_{sf} vs. the boundary are fitted with constant (pol0) fits, linear (pol1) fits, with the mean and standard deviation shown. The “rise across range” is how much the linear fit changes over the range.

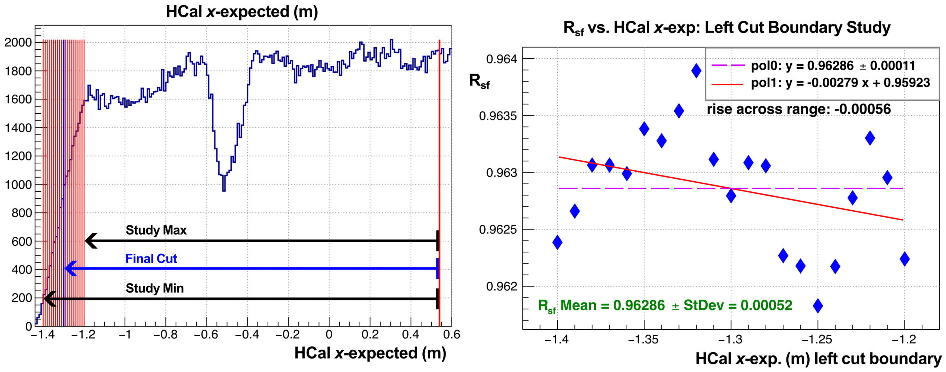

(a) Stability study for x-expected: left boundary

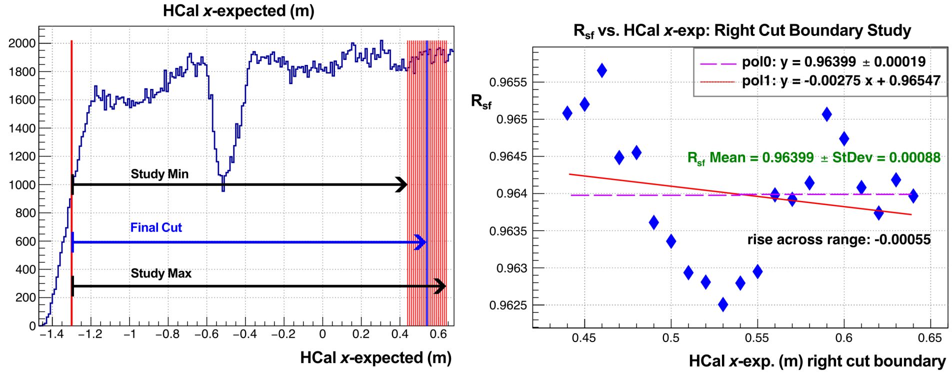

(b) Stability study for x-expected: right boundary

Figure 5.9: x-expected stability study for SBS-4 30% field ($Q^2 = 3.0$ GeV^2). Subfigure **(a)** shows the left boundary study, where the minimum value of the x-expected cut is changed to see how R_{sf} changes. Subfigure **(b)** shows the right boundary study, where the maximum value of the x-expected cut is changed to see how R_{sf} changes. The graphs of R_{sf} vs. the boundary are fitted with constant (pol0) fits, linear (pol1) fits, with the mean and standard deviation shown. The "rise across range" is how much the linear fit changes over the range.

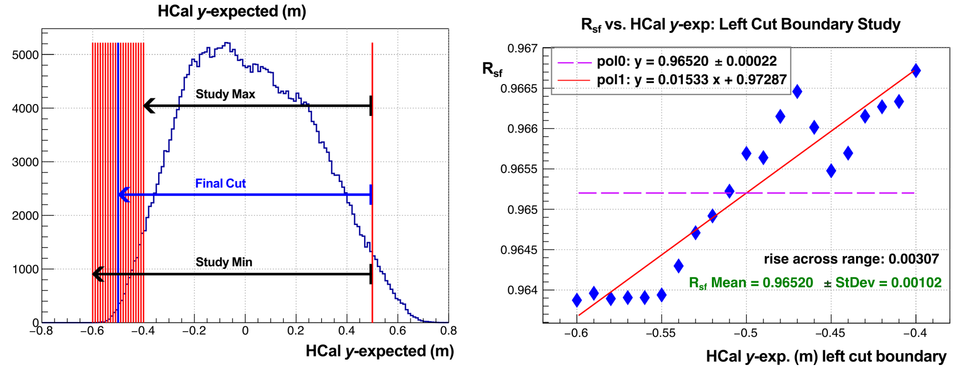

(a) Stability study for y-expected: left boundary

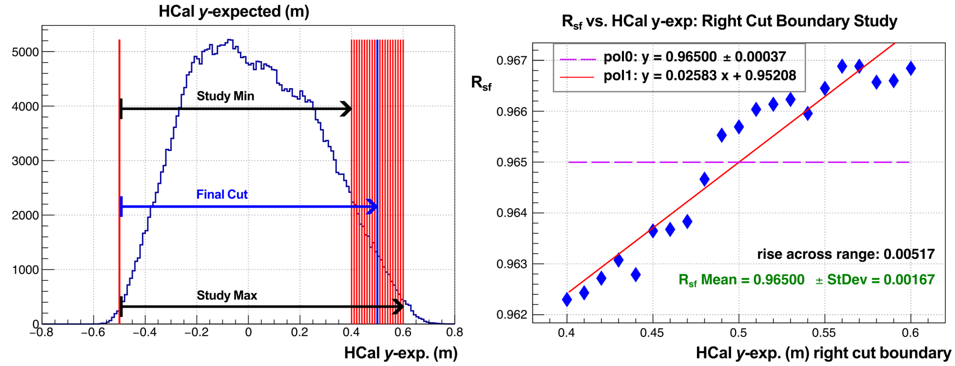

(b) Stability study for y-expected: right boundary

Figure 5.10: y-expected stability study for SBS-4 30% field ($Q^2 = 3.0$ GeV^2). Subfigure **(a)** shows the left boundary study, where the minimum value of the y-expected cut is changed to see how R_{sf} changes. Subfigure **(b)** shows the right boundary study, where the maximum value of the y-expected cut is changed to see how R_{sf} changes. The graphs of R_{sf} vs. the boundary are fitted with constant (pol0) fits, linear (pol1) fits, with the mean and standard deviation shown. The "rise across range" is how much the linear fit changes over the range.

In Fig. 5.9 and Fig. 5.10, we note that the $x-$expected and y-expected boundary selection effects R_{sf}. The relative changes are quite small in comparison with the mean of R_{sf}.

For this work, we will not be explicitly studying the stability of the "optics quality cuts". The projection used for the optics cuts is calculated using the track, and the track is used to calculate x_{exp} and y_{exp}. Thus they are highly correlated and it would be "double counting" to include the uncertainty from both.

5.3.1.10 Cut Stability Study Summary

Table 5.5 shows a summary of the stability studies for SBS-4, SBS-8, and SBS-9 kinematics. The standard deviation from the mean and the "rise over the range"/2 is shown for each variable and boundary studied. The larger of these two values is selected and added in quadrature for each boundary. The numbers in the parenthesis show the minimum and maximum values of the boundary being changed. In SBS-9, the x_{exp}, y_{exp} envelope is very small and is within the calculated values for the active area cuts on the minimum boundary in x_{exp} and the maximum boundary of y_{exp}. The data sets in those cuts are identical, producing the same R_{sf} value and giving a result of 0 and not contributing to the uncertainty.

Table 5.6 shows a breakdown of the uncertainty contributions from each cut variable. These are the squared values which are being added in quadrature. They have been written with scientific notation to help quickly see which variables contribute most to the systematic uncertainty.

We can see that the invariant mass cut, W^2, and the Δy cut, dominate the cut systematic uncertainties. These two variables are correlated, so we are only including the larger of the two in this work. A possible next step could be to quantify the correlation factor by applying a linear fit to the two-dimensional histogram of W^2 vs Δy in Fig. 4.9 for each kinematic. The large values hint that these cuts could be studied further. It could be that this work is doing something that overestimates their systematic contribution, or it

Table 5.5: Stability study details. The boundaries studied and the standard deviation and rise/2 are recorded for each variable at each field setting.

Variable	Boundary	Measure	SBS-4 30%	SBS-4 50%	SBS-8 50%	SBS-8 70%	SBS-8 100%	SBS-9 70%
W^2	left (0.56, 0.76)	stdev	0.0014	0.00327	0.00224	0.00597	0.0089	0.00881
		rise/2	-0.00169	-0.00117	-0.002	-0.00881	-0.01291	-0.0132
	right (1.0, 1.2)	stdev	0.00311	0.00477	0.0044	0.00773	0.01159	0.00447
		rise/2	-0.00338	0.00113	-0.00623	-0.01139	-0.01719	-0.00665
Δy	left (-0.68, -0.28)	stdev	0.00499	0.00611	0.0098	0.00487	0.01045	0.00342
		rise/2	-0.00744	-0.00707	-0.0011	-0.00721	-0.01552	-0.00462
	right (0.28, 0.68)	stdev	0.0035	0.00484	0.001	0.00262	0.00595	0.00224
		rise/2	-0.00494	-0.00231	0.00085	-0.00388	-0.00893	-0.00331
χ^2/ndf	right (10, 30)	stdev	0.00054	0.00236	0.00052	0.00063	0.00085	0.00032
		rise/2	0.0002	-0.00278	-0.00004	0.00088	-0.00085	-0.00016
GEM nhits	left (3, 5)	stdev	0.00134	0.00188	0.00877	0.00405	0.00056	0.0028
		rise/2	0.00111	-0.00022	0.00475	-0.00343	0.00009	0.00273
PS Energy	left (1.0, 0.3)	stdev	0.00035	0.00061	0.00085	0.00089	0.00053	0.00558
		rise/2	-0.00037	0.0002	0.00122	0.00125	-0.00051	0.00716
HCal Energy	left	stdev	0.00143	0.00373	0.0009	0.00024	0.00054	0.00039
		rise/2	-0.00212	-0.00531	0.00087	-0.00012	-0.00034	0.00031
		min	0.015	0.015	0.03	0.03	0.03	0.03
		max	0.035	0.035	0.05	0.05	0.05	0.05
Vertex z	left (-0.08, -0.06)	stdev	0.00099	0.00375	0.00095	0.00073	0.00172	0.00065
		rise/2	0.00048	0.0054	0.00023	0.0005	0.00252	-0.00065
	right (0.06, 0.08)	stdev	0.00065	0.00215	0.00079	0.00064	0.00113	0.00056
		rise/2	-0.0008	-0.00001	-0.00041	-0.00083	-0.00013	-0.00051
x_{exp}	left	stdev	0.00052	0.00437	0.00143	0.00052	0.00163	0
		rise/2	-0.00028	-0.00669	0.00202	-0.00013	-0.00234	0
		min	-1.4	-0.97	-1.64	-1.37	-1.02	-1.4
		max	-1.2	-0.77	-1.44	-1.17	-0.82	-1.2
	right	stdev	0.00088	0.00182	0.00131	0.00244	0.00446	0.0026
		rise/2	-0.00027	0.00122	0.0016	0.0039	0.00672	0.00414
		min	0.44	0.44	0.53	0.53	0.53	0.6
		max	0.64	0.64	0.73	0.73	0.73	0.8
y_{exp}	left (-0.6, -0.4)	stdev	0.00102	0.00097	0.00605	0.00296	0.00088	0.00154
		rise/2	0.00153	0.0009	0.00938	0.0045	0.00008	0.0024
	right (0.4, 0.6)	stdev	0.00167	0.00312	0.00027	0.00085	0.00135	0
		rise/2	0.00258	0.00474	0.00017	0.00128	0.00194	0
Coin. Time	left (-15, -5)	stdev	0.00064	0.00098	0.00193	0.00119	0.00133	0.00092
		rise/2	-0.00054	-0.00093	-0.00234	-0.00143	-0.00144	0.00042
	right (5,15)	stdev	0.00128	0.00335	0.00088	0.00119	0.00162	0.00205
		rise/2	-0.00175	-0.00453	-0.00129	-0.00186	-0.00234	-0.00325

Table 5.6: Cut stability results breakdown. This table shows the squared values from each variable that will be added in quadrature to produce the final uncertainty from the cut choices. The total* includes either W^2 or Δy uncertainty, whichever is higher, but not both. Highlighted in yellow are the contributions that will be treated as uncorrelated when comparing field settings in single kinematic. See Sec. 5.5.

Variable	SBS-4 30%	SBS-4 50%	SBS-8 50%	SBS-8 70%	SBS-8 100%	SBS-9 70%
W^2	1.43×10^{-5}	3.34×10^{-5}	4.38×10^{-5}	2.07×10^{-4}	4.62×10^{-4}	2.18×10^{-4}
Δy	7.98×10^{-5}	7.34×10^{-5}	9.70×10^{-5}	6.70×10^{-5}	3.21×10^{-4}	3.23×10^{-5}
χ^2/ndf	2.92×10^{-7}	7.73×10^{-6}	2.70×10^{-7}	7.74×10^{-7}	7.23×10^{-7}	1.02×10^{-7}
GEM nhits	1.80×10^{-6}	3.53×10^{-6}	7.69×10^{-5}	1.64×10^{-5}	3.14×10^{-7}	7.84×10^{-6}
PS Energy	1.37×10^{-7}	3.72×10^{-7}	1.49×10^{-6}	1.56×10^{-6}	2.81×10^{-7}	5.13×10^{-5}
HCal Energy	4.49×10^{-6}	2.82×10^{-5}	8.10×10^{-7}	5.76×10^{-8}	2.92×10^{-7}	1.52×10^{-7}
Track Vertex z	1.62×10^{-6}	3.38×10^{-5}	1.53×10^{-6}	1.22×10^{-6}	7.63×10^{-6}	7.36×10^{-7}
x_{exp}	1.04×10^{-6}	4.81×10^{-5}	6.64×10^{-6}	1.55×10^{-5}	5.06×10^{-5}	1.71×10^{-5}
y_{exp}	9.00×10^{-6}	2.34×10^{-5}	8.81×10^{-5}	2.19×10^{-5}	4.54×10^{-6}	5.76×10^{-6}
coin. time	3.47×10^{-6}	2.15×10^{-5}	7.14×10^{-6}	5.50×10^{-6}	7.55×10^{-6}	1.14×10^{-5}
total*	1.02×10^{-4}	2.40×10^{-4}	2.80×10^{-4}	2.70×10^{-4}	5.34×10^{-4}	3.13×10^{-4}
$\sqrt{\text{total*}}$	1.01×10^{-2}	1.55×10^{-2}	1.67×10^{-2}	1.64×10^{-2}	2.31×10^{-2}	1.77×10^{-2}
total uncorr.*	1.52×10^{-4}	3.91×10^{-4}	5.65×10^{-4}	4.23×10^{-4}	1.06×10^{-3}	4.01×10^{-4}
$\sqrt{\text{total uncorr.*}}$	1.23×10^{-2}	1.98×10^{-2}	2.38×10^{-2}	2.06×10^{-2}	3.25×10^{-2}	2.00×10^{-2}

could be that they really do contribute that much more to the uncertainty than the other variables. When studying W^2 stability and computing these numbers, I did not include cuts on Δy, and likewise, when studying Δy stability, I did not include cuts on W^2. This likely caused the background to be larger in comparison to other variables being studied, and thus the choice of background fit function (pol2), could have had a larger impact.

5.3.2 Background Shape

The inelastic background is expected to be a large portion of our systematic uncertainty budget. We will try and quantify this by utilizing several different shapes for the background and taking the variation in R_{sf} is a representation of that systematic uncertainty.

We will look at several options for background choice. For several fits, we let ROOT determine the parameters using the built-in fitting methods. This will include polynomial background shapes of various orders and a Gaussian background shape. For several other fits, we fit a Δx distributions from background selections using a sideband method from data. And finally, we will utilize the Geant4 inelastic simulations. We will utilize those fits that have a χ^2/ndf that is less than 5. The variation of Δx between these methods gives us a measure of the systematic uncertainty from the choice of inelastic background shape.

5.3.2.1 Functional Fits

Various orders of simple polynomial fits are used to functionally fit the background. Here, we are exploring polynomials of order 0 (`pol0`, horizontal line), order 1 (`pol1`, linear fit), order 2 (`pol2`, parabolic fit), up to order 4. See Fig. 5.11, Fig. 5.12, and Fig. 5.13. These are functional fits: there is no direct physics motivation for these functions. In Sec. 5.3.2.2, we will explore fit shapes that come from evaluating the data, as well as fit shapes that are from evaluating the inelastic Monte Carlo simulation.

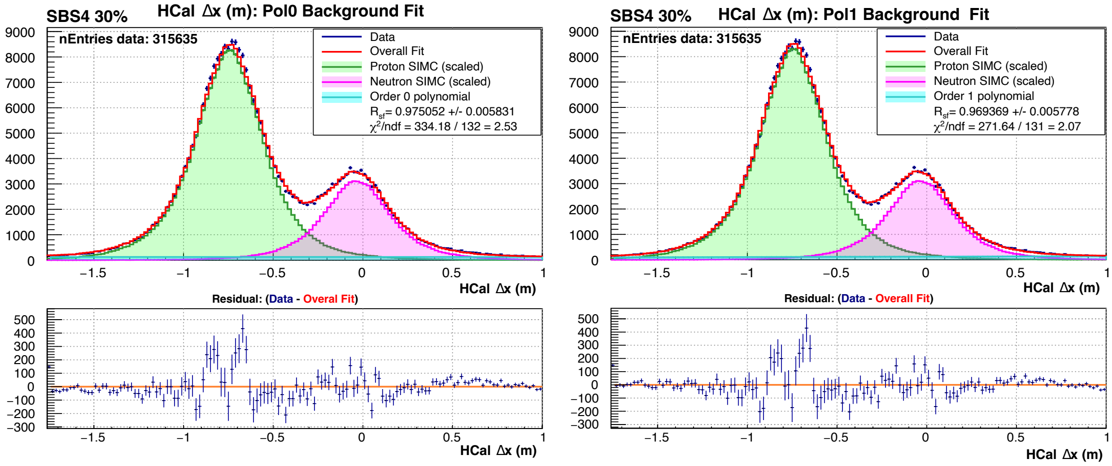

Figure 5.11: Data–MC comparison for Δx for SBS-4 30%. (Left) `pol0` background fit, (Right) `pol1` background fit. The proton and neutron histograms from simulation are scaled to fit the data. The lower histogram is a *residual* histogram where the fit histogram is subtracted from the data histogram, bin-by-bin.

In the $Q^2 = 3.0$ GeV^2 kinematic shown, the small inelastic background does not show a significant difference between the various polynomial fits.

A Gaussian background shape is also used. Figure 5.14 shows the Gaussian background fit for SBS-4 30% field kinematic. We can see that the Gaussian does not fit the data well, in this kinematic. However, it is a much better fit for the other kinematics.

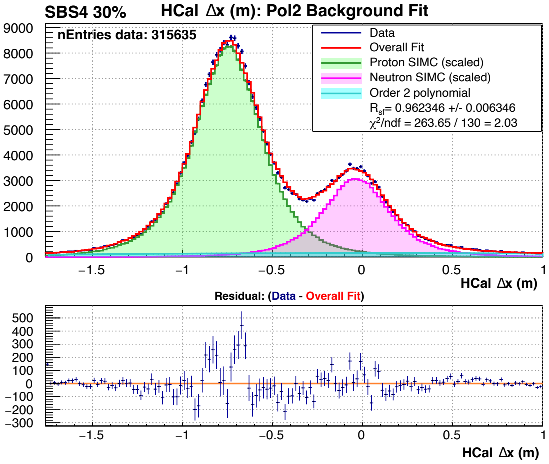

Figure 5.12: Data–MC comparison for Δx for SBS-4 30% ($Q^2 = 3.0$ GeV^2) with `pol2` background fit. The proton and neutron histograms from simulation are scaled to fit the data. The lower histograms are *residual* histograms, where the fit histogram is subtracted from the data histogram, bin-by-bin.

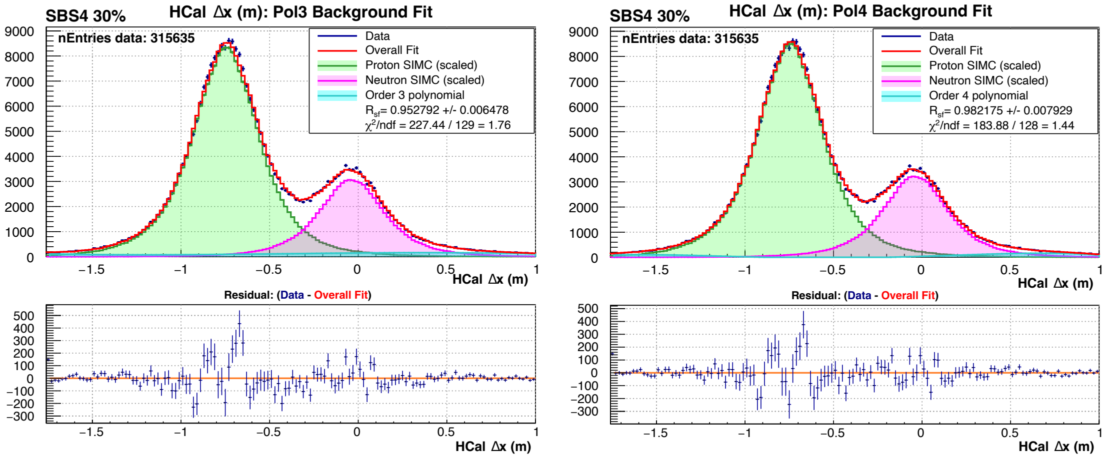

Figure 5.13: Data–MC comparison for Δx for SBS-4 30% ($Q^2 = 3.0$ GeV^2). (left) `pol3` and (right) `pol4` background fits. The proton and neutron histograms from simulation are scaled to fit the data. The `pol4` fit goes to zero at some points and thus is not a good fit for this kinematic, as the background is expected across the entire acceptance. The lower histograms are *residual* histograms: The fit histogram is subtracted from the data histogram, bin-by-bin.

For the final extraction, the `pol2` fit will be used. A parabola helps to protect against overfitting that is likely happening with the `pol4` fit, it does not allow for any bumps and smoothly transitions, and is symmetrical.

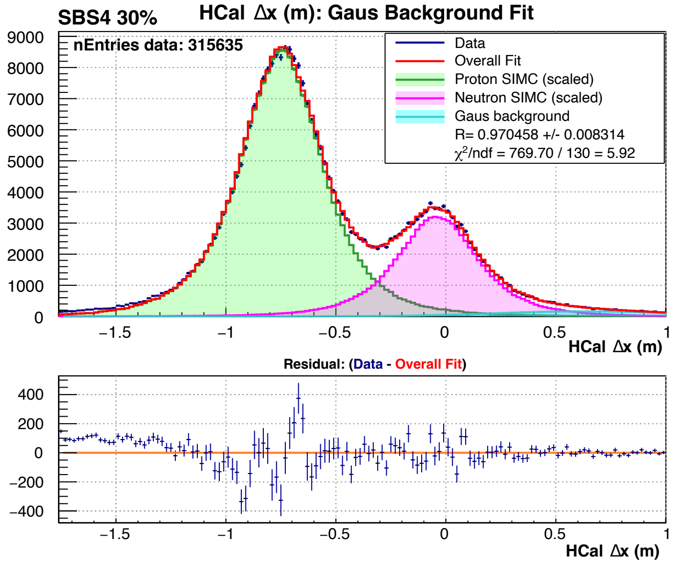

Figure 5.14: Data–MC comparison for SBS-4 30% ($Q^2 = 3.0$ GeV^2), Δx with Gaussian background fit. The proton and neutron histograms from simulation are scaled to fit the data. The lower histogram is a *residual* histogram, where fit histogram is subtracted from the data 'histogram, bin-by-bin. For this kinematic, a Gaussian background does not appear to be a good choice.

5.3.2.2 Background Shape from "Anti-cut" Method

Another way to obtain the shape of the inelastic background is by cutting on a variable to isolate events that are not from quasi-elastic scattering and plotting Δx of those events. In particle physics, this is often called a "sideband cut". In the SBS collaboration, we refer to this as an "anti-cut". This work looks at two anti-cut choices: anti-Δy, shown in Fig. 5.15, and anti-coincidence, shown in Fig. 5.16.

The extremes of Δy contain mainly inelastic events, especially on the beam-side of HCal. This may bias certain types of background events, as a cut on Δy is also a cut on invariant mass, since they are correlated.

The χ^2/ndf of the anti-Δy background suggests that this may not be an ideal choice for a background shape. The number of events used to produce the background shape is quite small, and the shape of Δx has a bias towards the proton peak.

The anti-coincidence cut in Fig. 5.16 looks at events that are out-of-time between HCal

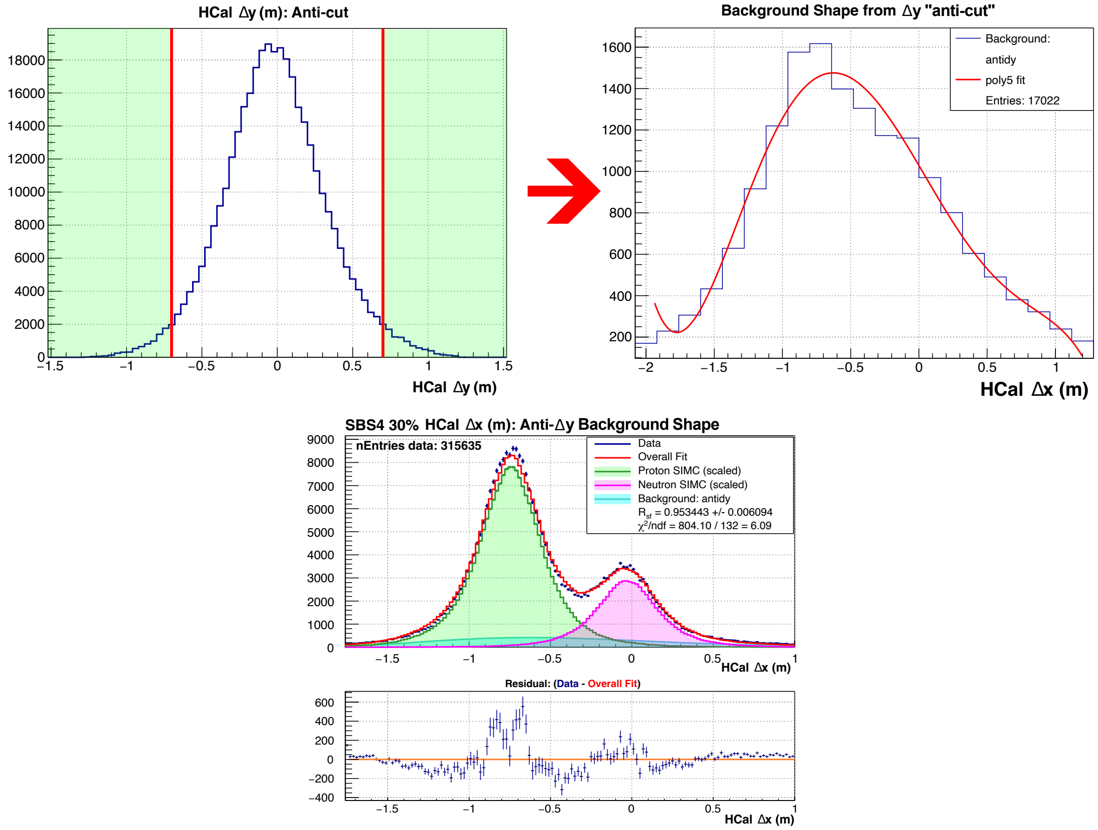

Figure 5.15: Data–MC comparison for Δx with Anti-Δy background fit for SBS-4, 30% field ($Q^2 = 3.0$ GeV^2). (Upper Left): events that are in the green portion of the Δy histogram are used to create a corresponding Δx histogram (upper right). A scaled version of this shape is then used as a background for the Δx histogram (center).

and Shower coincidence. The cut also includes events that are outside the HCal ADC time peak only.

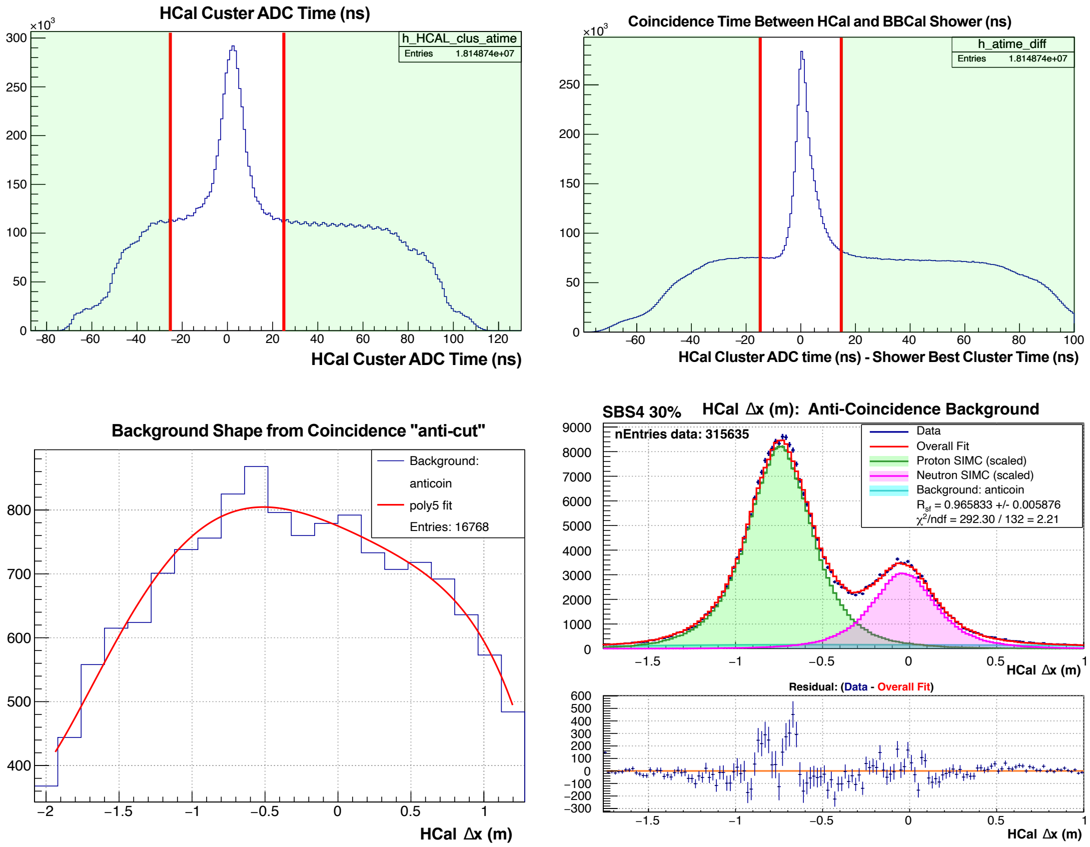

Figure 5.16: Data–MC comparison for Δx with anti-coincidence background fit for SBS-4, 30% field ($Q^2 = 3.0$ GeV^2). (Upper left): Events in the green areas of the HCal Cluster ADC Time histogram, and events in the green areas of the HCal–Shower Coincidence time histogram (upper right) are used to create a corresponding Δx histogram (lower left). A scaled version of this shape is then used as a background for the Δx histogram (lower right).

The anti-coincidence method produces a more reasonable χ^2/ndf than the anti-Δy method and may be a decent choice of background shape.

5.3.2.3 Background from Inelastic MC

We can also take the background shape by running inelastic simulations in G4SBS, applying cuts, and producing the Δx histogram, as seen in Fig. 5.17. This method is mostly limited by statistics—the G4SBS inelastic simulation is costly to run, and the elastic cuts applied greatly reduce the number of events. When more inelastic events are simulated in the future, this could be a very useful tool in determining the background shape.

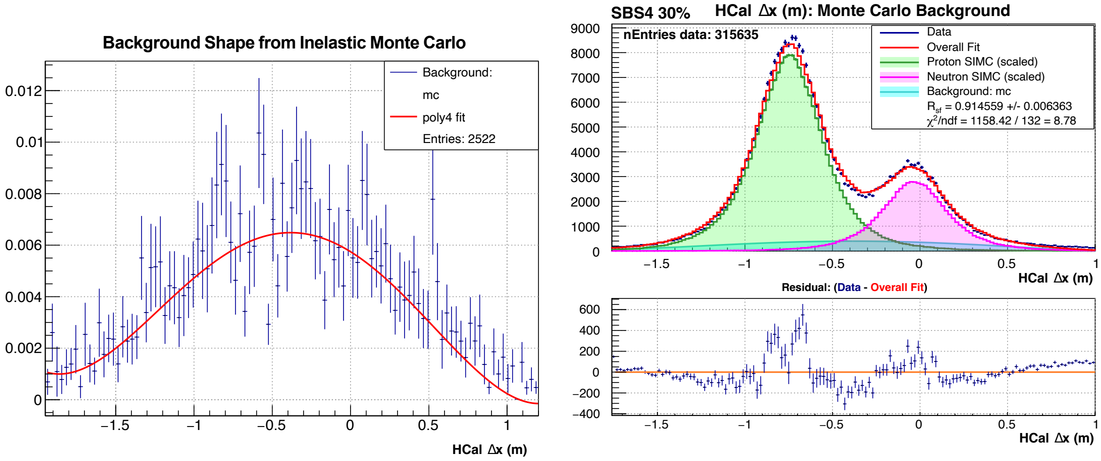

Figure 5.17: Data–MC comparison for Δx with Inelastic Monte Carlo background fit for SBS-4, 30% field ($Q^2 = 3.0$ GeV^2). A scaled version of the shape from the inelastic Monte Carlo is used to create the background for Δx.

The χ^2/ndf for the Monte Carlo background shape is quite large. More work and investigation would need to go into this method before its inclusion into the background systematic uncertainty.

5.3.3 Background Shape Study Summary

Table 5.7 is a summary of the results for the inelastic background shape study over the kinematic regimes. Only fits where the χ^2/ndf < 3 and the background fit did not go to zero were accepted. These are highlighted in yellow. The standard deviation of R_{sf} on the various fits is calculated and reported as the systematic uncertainty due to the unknown shape of the inelastic background.

Table 5.7: Inelastic background shape study results. For each kinematic, various shapes for the inelastic background fit were tried. The resulting value for R_{sf}, the uncertainty on R_{sf} reported by that fit, and the χ^2/ndf are reported. Highlighted: Only fits that have $\chi^2/\text{ndf} < 3.0$ and did not go to zero at any point are included in the uncertainty calculation. (For SBS-4 30%, the `pol4` background shape goes to zero at points.) Inelastic simulations where evaluated for SBS-4 30% field and SBS-8 70% field only.

Fit	Measure	SBS-4 30%	SBS-4 50%	SBS-8 50%	SBS-8 70%	SBS-8 100%	SBS-9 70%
no bg	R_{sf}	1.01063	1.05257	1.22235	1.21362	1.18423	1.18035
	±	0.00562	0.01619	0.00995	0.00569	0.00781	0.00566
	χ^2/ndf	22.06185	2.14667	47.39648	209.50171	61.81486	135.54434
`pol0`	R_{sf}	0.97505	1.01864	1.13249	1.12583	1.09226	1.09208
	±	0.00583	0.01669	0.01029	0.00558	0.00788	0.00562
	χ^2/ndf	2.53165	1.21015	2.16341	7.93588	5.83739	2.14609
`pol1`	R_{sf}	0.96937	1.00895	1.13048	1.12301	1.09029	1.09227
	±	0.00578	0.0169	0.01037	0.00562	0.00806	0.00552
	χ^2/ndf	2.07357	1.16574	2.16295	7.88551	5.86262	2.16113
`pol2`	R_{sf}	0.96235	1.00576	1.09161	1.0806	1.04461	1.07811
	±	0.00635	0.01801	0.01106	0.0057	0.00826	0.00593
	χ^2/ndf	2.02808	1.17231	1.04665	1.2279	1.5357	1.67682
`pol3`	R_{sf}	0.95279	0.98273	1.09162	1.07712	1.04332	1.07123
	±	0.00648	0.02057	0.01106	0.006	0.00948	0.00619
	χ^2/ndf	1.7631	1.14172	1.05461	1.21307	1.5453	1.59556
`pol4`	R_{sf}	0.98218	0.97945	1.09162	1.07686	1.04015	1.07738
	±	0.00793	0.02111	0.01133	0.00621	0.00958	0.00653
	χ^2/ndf	1.43658	1.1465	1.06289	1.22388	1.52923	1.53706
`Gaus`	R_{sf}	0.97046	1.00187	1.08516	1.07595	1.04473	1.07806
	±	0.00831	0.01904	0.0115	0.00581	0.00841	0.00596
	χ^2/ndf	5.9208	1.16974	1.05635	1.32235	1.54796	1.69598
anti-dy	R_{sf}	0.95345	1.0207	1.08981	1.10038	1.09786	1.07059
	±	0.00609	0.01708	0.01094	0.0057	0.00827	0.00572
	χ^2/ndf	6.0917	1.40563	1.97913	4.41332	1.7857	4.57245
anti-coin	R_{sf}	0.96583	1.01949	1.10434	1.10849	1.08089	1.10943
	±	0.00588	0.01687	0.01041	0.00556	0.00801	0.00573
	χ^2/ndf	2.21438	1.22763	1.53382	2.2656	3.21394	2.11383
mc	R_{sf}	0.91456			1.03545		
	±	0.00636			0.00554		
	χ^2/ndf	8.77591			9.23041		

5.3.4 Nucleon Detection Efficiency in HCal

As discussed in Sec. 4.8, we draw on the work of P. Datta to estimate the systematic uncertainties associated with the HCal position-dependent non-uniformity in the proton detection efficiency, as well as the neutron-to-proton detection efficiency ratio.

For the position-dependent non-uniformity, we adopt the relative difference between R_{sf} extracted with and without the HCal efficiency corrections, as determined in Datta's analysis, as the percent uncertainty in the present work. The relative difference is defined as

$$\text{Relative Difference} = \frac{\left(R_{sf\,\text{with corr.}} - R_{sf\,\text{without corr.}}\right)}{R_{sf\,\text{with corr.}}}\,. \tag{5.1}$$

The systematic uncertainty in R_{sf} due to position-dependent inefficiency, denoted as NDE1, is then given by

$$\text{NDE1} = R_{sf} \times (\text{Relative Difference})\,. \tag{5.2}$$

Table 5.8: Relative difference in R_{sf} with and without HCal position-based efficiency corrections in simulation, reproduced from Datta's analysis [36]. These values are used to estimate the systematic uncertainty from HCal position-based efficiency in the present work.

Kinematic	$R_{sf\,\text{with corr.}}$	$R_{sf\ \text{without corr.}}$	Relative Difference
SBS-4 30%	0.9615	0.9624	0.00094
SBS-8 70%	1.105	1.103	0.0018

Datta's study focused on the GMn kinematic points and did not explicitly analyze the SBS-9 kinematic (also at $Q^2 = 4.5$ GeV^2, but low-ε), as it belongs to the nTPE experiment. In the present work, we apply the SBS-8 result from Datta's study to SBS-9. While a direct calculation of the relative difference for SBS-9 would be valuable, the average nucleon momenta for SBS-8 and SBS-9 are the same, supporting the reasonableness of this approximation.

Finally, to account for uncertainty in the neutron-to-proton detection efficiency ratio, we follow Datta's approach and assign a conservative 2% systematic error in R_{sf}, denoted as NDE2, applied uniformly across all kinematics. (Refer to our previous discussion in Sec.4.8.3).

5.4 Data–Monte Carlo Comparison Results

R_{sf} was extracted using Data–Monte Carlo for each field setting for SBS-4 ($Q^2 = 3.0$ GeV^2), SBS-8 and SBS-9 ($Q^2 = 4.5$ GeV^2). The variable cuts found for each of these setting can be found in Tab. 5.2 and Tab. 5.3. For the inelastic background shape, a `pol2`(parabolic) fit was used. This fit was chosen because it typically resulted in $\chi^2/\text{ndf} =< 2$, and it is a simple and smooth function, likely not overfitting the data. A summary of these results can be found in Tab. 5.9 at the end of this section.

We can not straightforwardly combine the results from the different field settings into a final R_{sf} or G_M^n value. Further research would need to untangle what uncertainties would be correlated and uncorrelated between the field settings as well as their correlation factors. For this work, we will report final results for only the magnetic field settings that are the "production" kinematics.

5.4.1 SBS-4

SBS-4 ($Q^2 = 3.0$ GeV^2) was taken at two magnetic field settings: 30% and 50% of the maximum SBS magnetic field strength. The R_{sf} extraction for SBS-4, 30% field data is shown in Fig. 5.18. This overall data set is the "production" kinematic for SBS-4 and will constitute the final report of G_M^n for $Q^2 = 3.0$ GeV^2.

Note the scale on the residual plot in Fig. 5.18 for SBS-4 30% in comparison to the Δx Data–MC plot itself: The very largest bin-by-bin difference between data and MC is ≈ 450 counts, whereas the total number of counts in that bin in the Data–MC comparison is ≈ 8000 counts. The decency of this fit reflects in the fit result of $\chi^2/\text{ndf} \approx 2$.

The R_{sf} extraction for SBS-4 50% field ($Q^2 = 3.0$ GeV^2) is shown in Fig. 5.19. This kinematic was intended for calibrations and not final physics extraction, so it does not

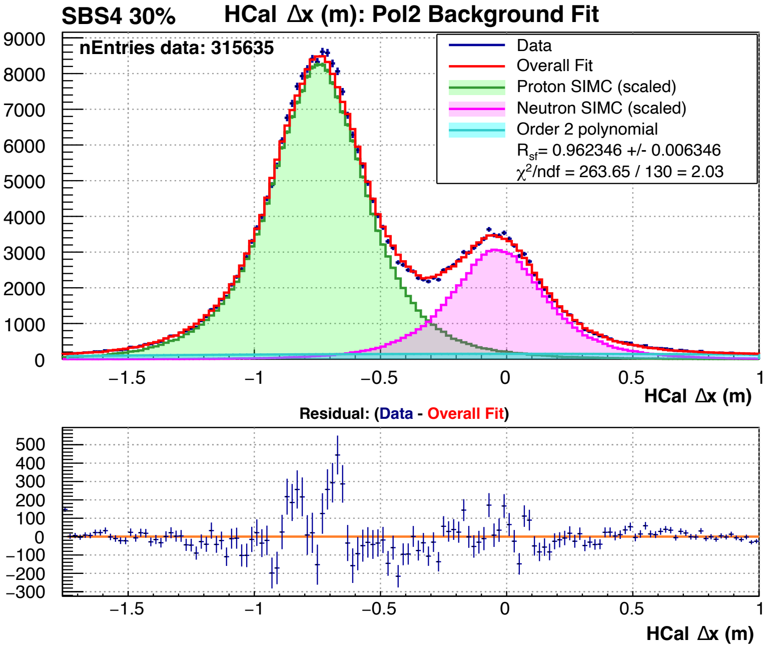

Figure 5.18: (Top): Data–MC comparison for SBS-4 30% field ($Q^2 = 3.0$ GeV^2) using a `pol2` background shape. This is the "production kinematic" for SBS4. The variation from the straight-line projection for the hadron in the vertical direction (Δx) is calculated for both data and Monte Carlo simulations and quasi-elastic cuts are applied to both. The proton simulation (green) histogram and neutron simulation histogram (pink) are scaled to match the data histogram, plus a background.(Bottom): The residual plot for the fit: bin-by-bin subtraction of Data−Overall fit. Horizontal line denotes 0.

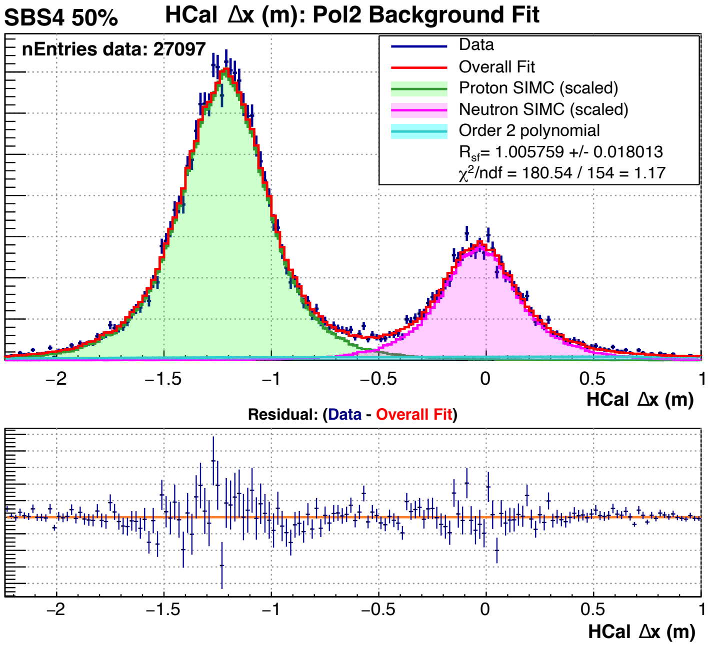

Figure 5.19: (Top): Data–MC comparison for SBS-4 50% field ($Q^2 = 3.0$ GeV^2) using a `pol2` background shape. The variation from the straight-line projection for the hadron in the vertical direction (Δx) is calculated for both data and Monte Carlo simulations and quasi-elastic cuts are applied to both. The proton simulation (green) histogram and neutron simulation histogram (pink) are scaled to match the data histogram, plus a background. (Bottom): The residual plot for the fit: bin-by-bin subtraction of Data−Overall fit. Horizontal line denotes 0.

have nearly as many statistics as the 30% field setting. This is reflected in the statistical uncertainty in R_{sf} which is the uncertainty in the fit that is computed by ROOT. However, we can use this field setting as a double-check on our extraction results. For both field settings, R_{sf} agrees within the fit uncertainty, although this is mostly due to R_{sf} having a large uncertainty in the 50% field setting due to small statistics. We will speak about how these statistical errors propagate through to the final G_M^n extraction in Sec. 5.6.

5.4.2 SBS-8

SBS-8 ($Q^2 = 4.5$ GeV^2) was taken at three magnetic field settings: 50%, 70%, and 100% maximum SBS magnetic field strength. The "production" kinematic for this configuration is SBS-8 70% field. Extractions from this data set, shown in Fig. 5.20 will constitute the final R_{sf} and G_M^n reported for this kinematic.

The fit from SBS-8 70% has a $\chi^2/\text{ndf} \approx 1.2$, suggesting that this is an overall good fit. In Fig. 5.20, we can see that there is a variation in the shape of the proton peak in simulation where there seems to be a small bump at the top of the peak that could be investigated further. This shape could simply be due to needing more statistics in the quasi-elastic simulation. There is also a section of the neutron peak residual that is systematically varying around zero. But even with these variations, in comparison to the overall number of entries in each bin, this is a good fit.

Both SBS-8 50% field and SBS-8 100% field are intended to be used for calibration and cross-checks. They have both have significantly less statistics than SBS-8 70% field, with the data set of 50% field having especially fewer. However, we will see more clearly in Sec. 5.5 that the systematic uncertainties dominate the final result and the statistical uncertainty does not largely contribute to the overall uncertainty in comparison. As we will see in Sec. 5.7, the results of this work show that the G_M^n extractions for SBS-8 are in agreement with each other.

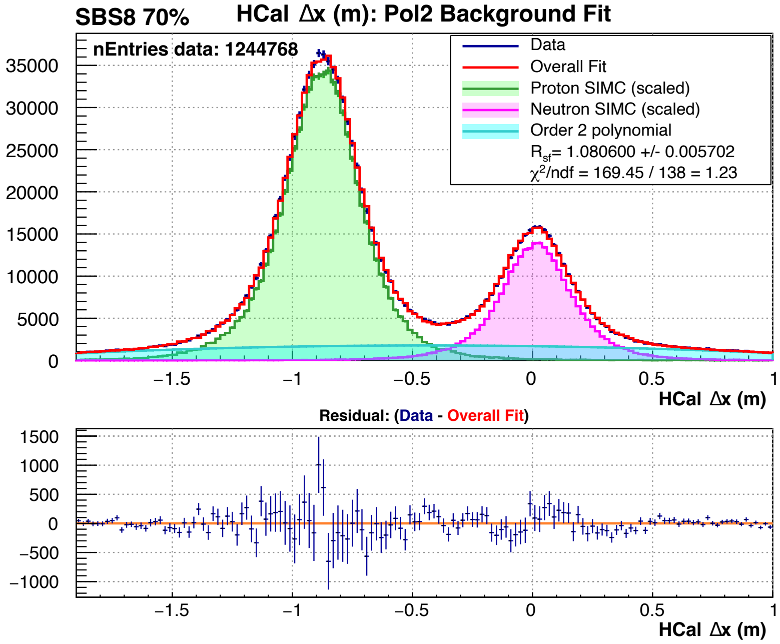

Figure 5.20: (Top): Data–MC comparison for SBS-8 70% field ($Q^2 = 4.5$ GeV^2) using a `pol2` background shape. This is the "production kinematic" for SBS-8. The variation from the straight-line projection for the hadron in the vertical direction (Δx) is calculated for both data and Monte Carlo simulations and quasi-elastic cuts are applied to both. The proton simulation (green) histogram and neutron simulation histogram (pink) are scaled to match the data histogram, plus a background.(Bottom): The residual plot for the fit: bin-by-bin subtraction of Data−Overall fit. Horizontal line denotes 0.

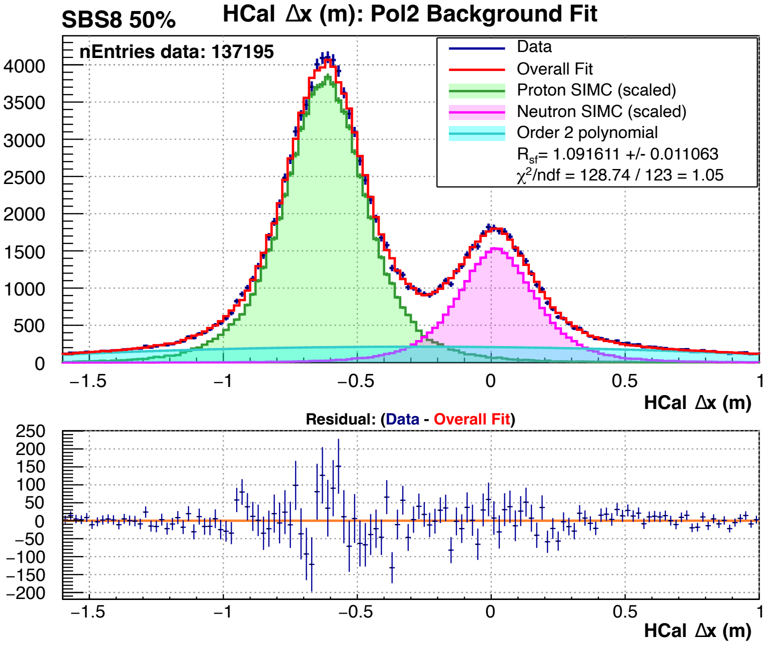

Figure 5.21: (Top): Data–MC comparison for SBS8 50% field ($Q^2 = 4.5\ \text{GeV}^2$) using a `pol2` background shape. The variation from the straight-line projection for the hadron in the vertical direction (Δx) is calculated for both data and Monte Carlo simulations and quasi-elastic cuts are applied to both. The proton simulation (green) histogram and neutron simulation histogram (pink) are scaled to match the data histogram, plus a background. (Bottom): The residual plot for the fit: bin-by-bin subtraction of Data−Overall fit. Horizontal line denotes 0.

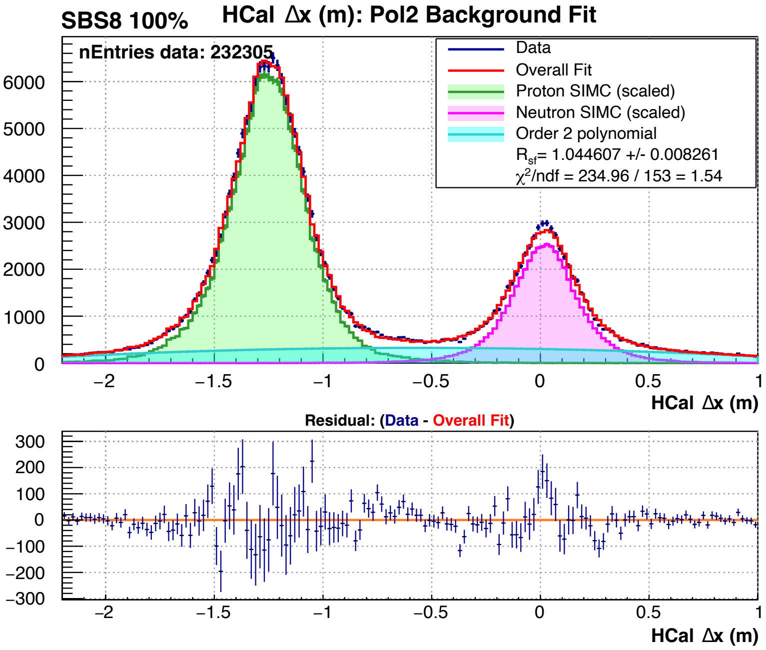

Figure 5.22: (Top): Data–MC comparison for SBS8 100% field ($Q^2 = 4.5$ GeV^2) using a `pol2` background shape. The variation from the straight-line projection for the hadron in the vertical direction (Δx) is calculated for both data and Monte Carlo simulations and quasi-elastic cuts are applied to both. The proton simulation (green) histogram and neutron simulation histogram (pink) are scaled to match the data histogram, plus a background. (Bottom): The residual plot for the fit: bin-by-bin subtraction of Data−Overall fit. Horizontal line denotes 0.

5.4.3 SBS-9

SBS-9 is the low-epsilon point intended to pair with the SBS-8 70% G_M^n measurement to extract a Rosenbluth slope. In this work, we are not extracting a Rosenbluth slope, rather, we will be comparing the final G_M^n extractions as an internal cross-check on the G_M^n extraction techniques[2].

The Data–MC comparison and R_{sf} extraction is found in Fig. 5.23. The $\chi^2/\text{ndf} < 2$, suggesting that the fit is reasonable. The residual plot does show some indication that there is a slight systematic effect around the proton and neutron peaks. This may be eliminated with the addition of more simulated data in the future. However, we note the scale difference and compare the residual plot at its largest near the proton peak, ≈ 800 entries in the bin, to the number of entries in the same place on the extraction plot, ≈ 21000 entries in the bin.

Next, we will summarize our error studies on R_{sf} and then propagate the error through to the final G_M^n result.

5.5 Data–MC Comparison Results and Uncertainties

First, we will review the results for R_{sf} from the Data–MC comparisons, as well as the systematic uncertainty and total uncertainty of R_{sf}. Next, we will investigate the agreement of R_{sf} between magnetic field settings in SBS-4 and SBS-8.

5.5.1 Total Estimated Uncertainty of R_{sf}

A summary of the statistical and systematic uncertainties in R_{sf} is presented in Tab. 5.9. For each field setting, the contributions to the total R_{sf} uncertainty are listed by source. The total systematic uncertainty is computed by adding in quadrature the individual contributions from the inelastic background shape study (Sec. 5.3.2), the cut stability

---

[2] This work evaluates SBS-9 kinematic because GRINCH was operational during this time and the expected electron momentum was below the pion threshold, which was discussed in Ch. 3.

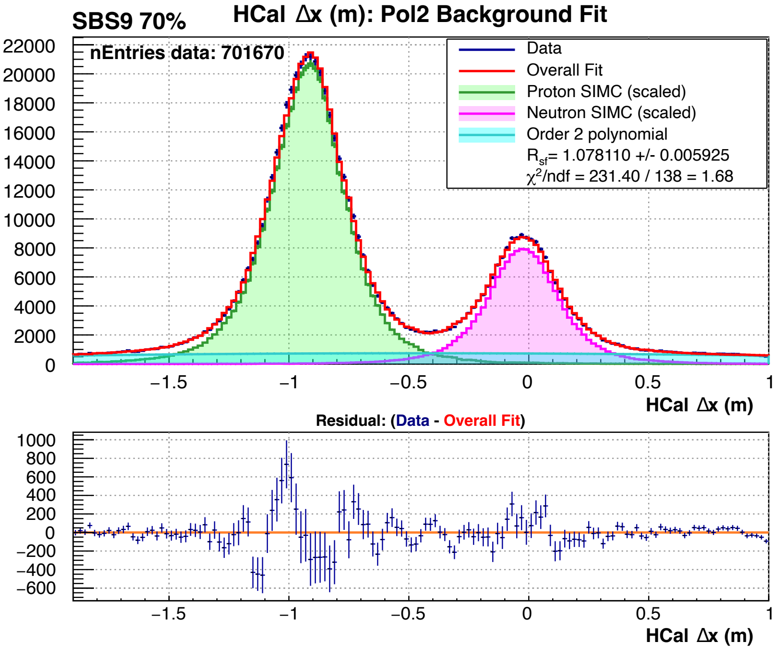

Figure 5.23: (Top): Data–MC comparison for SBS-9 70% field ($Q^2 = 4.5$ GeV^2) using a `pol2` background shape. This is the only magnetic filed taken for SBS-9. The variation from the straight-line projection for the hadron in the vertical direction (Δx) is calculated for both data and Monte Carlo simulations and quasi-elastic cuts are applied to both. The proton simulation (green) histogram and neutron simulation histogram (pink) are scaled to match the data histogram, plus a background. (Bottom): The residual plot for the fit: bin-by-bin subtraction of Data−Overall fit. Horizontal line denotes 0.

study (Sec. 5.3.1), the position-dependent HCal inefficiencies (NDE1), and the neutron-to-proton detection efficiency ratio (NDE2) (Sec. 4.8, Sec. 5.3.4).

The total absolute uncertainty in R_{sf} is then obtained by adding in quadrature the total systematic and statistical uncertainties. The statistical uncertainty is taken from the ROOT fit to the final Δx histograms (see Sec. 5.4).

Table 5.9: Absolute uncertainty estimations of R_{sf} by source for each kinematic. Highlighted in yellow are the "production kinematics", which will be used for the final G_M^n extraction. The total systematic uncertainty is the inelastic background, cut stability, NDE1 (position-dependent HCal inefficiencies), and NDE2 (neutron-proton detection efficiency ratio) systematic uncertainties added in quadrature. The statistical uncertainty is the uncertainty on R_{sf} reported by the ROOT fit in the final Δx histograms from Sec. 5.4. The total uncertainty is the absolute uncertainty of R_{sf}, which is the total systematic uncertainty and the statistical uncertainty added in quadrature. The total percent uncertainty is (total uncertainty/R_{sf}) × 100.

Kinematic	Q^2 (GeV^2)	R_{sf}	$\sigma_{R_{sf}}^{\text{Inel.}}$	$\sigma_{R_{sf}}^{\text{Cuts}}$	$\sigma_{R_{sf}}^{\text{NDE1}}$	$\sigma_{R_{sf}}^{\text{NDE2}}$	$\sigma_{R_{sf}}^{\text{syst. tot.}}$	$\sigma_{R_{sf}}^{\text{stat}}$	$\sigma_{R_{sf}}^{\text{tot.}}$	% uncert.
SBS-4 30%	3	0.962	0.0073	0.01	0.0009	0.019	0.023	0.0064	0.024	2.49%
SBS-4 50%	3	1.006	0.014	0.015	0.0009	0.02	0.029	0.018	0.034	3.38%
SBS-8 50%	4.5	1.092	0.019	0.017	0.002	0.022	0.033	0.011	0.035	3.21%
SBS-8 70%	4.5	1.081	0.013	0.016	0.002	0.022	0.03	0.0057	0.031	2.87%
SBS-8 100%	4.5	1.045	0.023	0.023	0.0019	0.021	0.039	0.0083	0.039	3.37%
SBS-9 70%	4.5	1.078	0.012	0.018	0.002	0.022	0.031	0.0059	0.031	2.88%

We observe that the uncertainties in these results are dominated by systematic contributions. This is particularly evident in the "production kinematics"—SBS-4 30%, SBS-8 70%, and SBS-9 70%—which benefited from substantially higher statistics compared to the calibration field settings (SBS-4 50%, SBS-8 50%, and SBS-8 100%).

Efforts to improve the uncertainty on the neutron-to-proton detection efficiency ratio (NDE2) are ongoing within the collaboration. Future publications from this experiment will likely adopt a less conservative estimate than the 2% uncertainty assigned in this work, informed by more detailed simulation studies.

The cut stability (or cut variability) studies conducted here used intentionally broad ranges of cut values to provide a conservative estimate. In future analyses, narrower and more targeted variations will likely yield a more representative and less conservative estimate of this uncertainty.

The shape of the inelastic background remains a significant contributor to the total R_{sf} uncertainty, as is common in many particle physics experiments. This contribution is expected to become even larger at higher Q^2, where the background increases and the proton and neutron peaks become more difficult to resolve.

5.5.2 Estimated Uncorrelated Uncertainties Between Magnetic Field Settings

Next, we address the question: *"Does R_{sf} agree between the different field settings within a given kinematic?"* Specifically, we test whether R_{sf} extracted at SBS-4 30% agrees with that at SBS-4 50%, and similarly for the SBS-8 settings.

To make this comparison meaningful, it is important to identify and exclude uncertainties that are fully correlated between field settings, since such contributions do not affect differences. We treat the systematic uncertainties as follows:

- NDE2: This uncertainty, assigned as a uniform 2% across all settings, is fully correlated and is therefore excluded from the comparison.
- NDE1: This uncertainty arises from position-dependent HCal inefficiencies. Although partially correlated—since the same HCal is used at all settings—the proton distributions shift between field settings, striking different regions of the calorimeter. We conservatively treat NDE1 as uncorrelated between field settings.
- Inelastic background: Although the same functional form is used for the background fit, the fit ranges and resulting polynomial parameters differ significantly between field settings due to the shifting proton and neutron peaks. This contribution is treated as uncorrelated.
- Cut stability: Uncertainties from cuts on the electron arm are fully correlated between settings, as the electron arm is unaffected by changes to the hadron arm field; these are excluded from the comparison. For cuts on the hadron arm, the proton

impact position shifts between field settings, and we conservatively treat these contributions as uncorrelated.

A summary of the uncorrelated uncertainties included in this comparison is presented in Tab. 5.10. We note that this treatment is likely conservative and may overestimate the uncorrelated uncertainty between field settings.

The individual contributions from the cut stability study are detailed in Tab. 5.6, which lists the uncertainty associated with each variable evaluated. In that table, the variables treated as uncorrelated between field settings—those associated with the HCal—are highlighted in yellow.

Table 5.10: Uncorrelated absolute uncertainty estimations of R_{sf} between field settings in each kinematic by source. The uncorrelated systematic uncertainty is the inelastic background, uncorrelated component of cut stability (see Tab. 5.6), and NDE1 uncertainties added in quadrature. The total absolute uncorrelated uncertainty is the uncorrelated systematic uncertainty and statistical uncertainty added in quadrature. The total percent uncertainty is (total uncertainty/R_{sf}) × 100. SBS-9 has only one field setting and therefore is not included in this table.

Kinematic	Q^2 (GeV^2)	R_{sf}	$\sigma_{R_{sf},\text{ Inel.}}$	$\sigma_{R_{sf}}^{\text{Cuts. uncor.}}$	$\sigma_{R_{sf}}^{\text{NDE1}}$	$\sigma_{R_{sf}}^{\text{syst. uncor.}}$	$\sigma_{R_{sf}}^{\text{stat.}}$	$\sigma_{R_{sf}}^{\text{tot. uncor.}}$	% uncert
SBS-4 30%	3.0	0.962	0.0073	0.0099	0.0009	0.0123	0.0064	0.0139	1.44%
SBS-4 50%	3.0	1.006	0.014	0.014	0.0009	0.0198	0.018	0.0267	2.66%
SBS-8 50%	4.5	1.092	0.019	0.014	0.0020	0.0238	0.011	0.0262	2.40%
SBS-8 70%	4.5	1.081	0.013	0.0158	0.0020	0.0206	0.0057	0.0213	1.97%
SBS-8 100%	4.5	1.045	0.023	0.0229	0.0019	0.0325	0.0083	0.0336	3.21%

Figure 5.24 provides a graphical representation of the statistical and total uncorrelated uncertainties reported in Tab. 5.10.

To quantify the agreement of R_{sf} between the two SBS-4 field settings, we compute the absolute difference:

$$\Delta R_{sf}^{\text{SBS-4}} = \left| R_{sf}^{\text{SBS-4 30\%}} - R_{sf}^{\text{SBS-4 50\%}} \right| . \tag{5.3}$$

The uncertainty on $\Delta R_{sf}^{\text{SBS-4}}$ is given by the quadrature sum of the uncorrelated uncertainties:

$$\sigma^2\left(\Delta R_{sf}^{\text{SBS-4}}\right) = \left(\sigma_{R_{sf,\text{uncorr.}}}^{\text{SBS-4 30\%}}\right)^2 + \left(\sigma_{R_{sf,\text{uncorr.}}}^{\text{SBS-4 50\%}}\right)^2 . \tag{5.4}$$

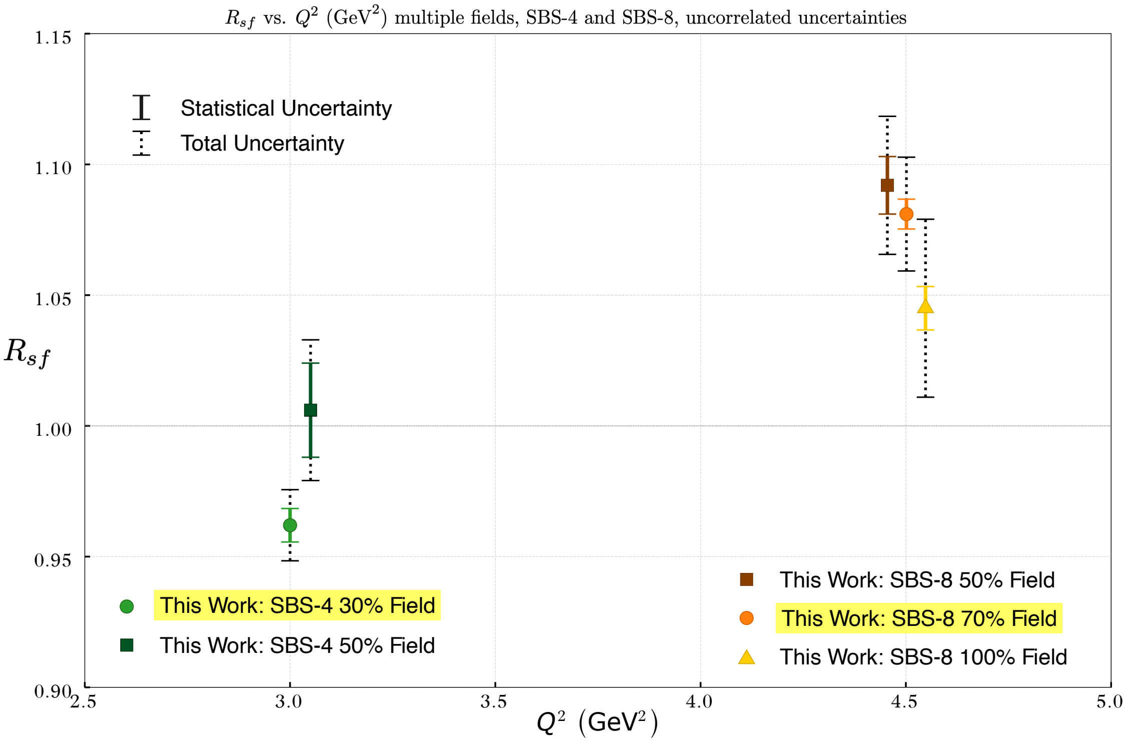

Figure 5.24: Plot of R_{sf} with uncorrelated uncertainties. The statistical uncertainty for each point is shown with solid error bars. The total uncorrelated uncertainty for each point—statistical uncertainty and uncorrelated systematic uncertainties added in quadrature—is shown with dotted error bars. The values used in this plot are found in Tab. 5.10.

We then express the difference in terms of its significance, defined as the number of standard deviations ($N\sigma$) the two measurements differ by:

$$N = \frac{\Delta R_{sf}^{\text{SBS-4}}}{\sqrt{\sigma^2\left(\Delta R_{sf}^{\text{SBS-4}}\right)}} \,, \tag{5.5}$$

where $|N| < 2$ would indicate that values are consistent within 2-σ, etc.

To quantify the agreement of R_{sf} between the three SBS-8 field settings[3], we compute the weighted mean given by

$$\bar{R}_{sf} = \frac{\sum_i R_{sf}^{(i)}/\sigma_i^2}{\sum_i 1/\sigma_i^2} \,, \tag{5.6}$$

where i = 50%, 70%, and 100% field settings for SBS-8, and σ_i is the total uncorrelated uncertainty (rightmost column of Tab 5.10).

The χ^2 of the weighted mean is given by

$$\chi^2 = \sum_{i=1}^{3} \frac{\left(R_{sf}^{(i)} - \bar{R}_{sf}\right)^2}{\sigma_i^2} \,. \tag{5.7}$$

We then compute χ^2/ndf, where the number of degrees of freedom is $3 - 1 = 2$ for SBS-8, to assess whether the measurements are statistically consistent:

- If $\chi^2/\text{ndf} \sim 1$, the measurements are statistically consistent.
- If $\chi^2/\text{ndf} \gg 1$, the measurements are not statistically consistent and may indicate a discrepancy.
- If $\chi^2/\text{ndf} \ll 1$, the scatter among the measurements is smaller than expected given the assigned uncertainties, suggesting that some uncertainties may be correlated or overestimated.

Table 5.11 shows the weighted mean and χ^2/ndf for R_{sf} for the various field settings of SBS-8 and SBS-4, as well as the difference evaluation between the two SBS-4 field settings. These values are calculated using Tab. 5.10.

---

[3] This analysis can also be done for the two field settings in SBS-4

Table 5.11: Comparison of R_{sf} values between the various field settings of SBS-4 and SBS-8. The values to produce this table are found in Tab. 5.10. The weighted mean ($\bar{R}_{sf}$) and χ^2/ndf for are computed for the multiple fields of SBS-8 and SBS-4. For the two field settings of SBS-4, the difference (ΔR_{sf}) the uncertainty of the difference ($\sigma_{(\Delta R_{sf})}$) and the significance of the difference (N) are computed.

Kinematic	R_{sf}	$\bar{R}_{sf}$	χ^2/ndf	ΔR_{sf}	$\sigma_{(\Delta R_{sf})}$	$N = \frac{\Delta R_{sf}}{\sigma_{(\Delta R_{sf})}}$
SBS-4 30%	0.962	0.971	1.42	0.044	0.030	1.46
SBS-4 50%	1.006					
SBS-8 50%	1.092					
SBS-8 70%	1.081	1.078	0.28			
SBS-8 100%	1.045					

As shown in Tab. 5.11, the two field settings of SBS-4 yield $\chi^2/\text{ndf} \approx 1.5$. This suggests that the two R_{sf} measurements are statistically consistent within their assigned uncorrelated uncertainties. The difference between the two measurements corresponds to $|N| \approx 1.5$, meaning they are consistent within approximately 1.5σ, which supports this conclusion. However, these results also leave open the possibility that the uncorrelated uncertainties have been overestimated, as the data lie somewhat closer than expected for truly independent measurements.

For SBS-8, $\chi^2/\text{ndf} \approx 0.3$, significantly below unity. This suggests that the scatter among the three R_{sf} measurements is smaller than expected given the assigned uncertainties, indicating that the uncorrelated uncertainties are possibly too large. As discussed earlier in this section, several conservative assumptions were made when deciding which systematic components to treat as uncorrelated, which likely inflated the total estimated uncorrelated uncertainty at each field setting.

These findings highlight the need for further investigation of which uncertainties should properly be treated as correlated versus uncorrelated in order to make a definitive statement about the consistency of R_{sf} across the field settings in SBS-4 and SBS-8. Importantly, these results also suggest that the total uncertainty in R_{sf} is likely overestimated in this analysis. This is an encouraging outcome, as it implies that the true precision of the GMn experiment at these kinematics may be better than the conservative estimates reported in this work, potentially at the sub-2% level[4].

In the following sections, we extract G_M^n from R_{sf} and propagate the uncertainties for the "production kinematics": SBS-4 30%, SBS-8 70%, and SBS-9 70%. As demonstrated in this section, many of the uncertainties in R_{sf} between field settings are correlated, and our analysis suggests that further work is needed to disentangle the correlated and uncorrelated components. Until this is accomplished, there is no clear method for combining the field settings into a single R_{sf} value with an appropriately quantified uncertainty. Therefore, we will proceed with evaluating only the production kinematics.

5.6 Uncertainty Propagation

To propagate the uncertainty of the expression for G_M^n given in Eq. (4.40), we assume all contributions are uncorrelated. The total uncertainty receives contributions from the statistical and systematic uncertainties in R_{sf}, and from the uncertainties in the fits to world data for G_M^p, G_E^p, and G_E^n.

For a function $f(a, b)$ of uncorrelated variable a with uncertainty σ_a and variable b with uncertainty σ_b, the uncertainty in f is given by

$$\sigma_f^2 = \left(\frac{\partial f}{\partial a}\right)^2 \sigma_a^2 + \left(\frac{\partial f}{\partial b}\right)^2 \sigma_b^2 \,. \tag{5.8}$$

Generalizing to a function of more variables $f(a, b, d, e, \ldots)$, we write:

$$\sigma_f = \sqrt{\left(\frac{\partial f}{\partial a}\right)^2 \sigma_a^2 + \left(\frac{\partial f}{\partial b}\right)^2 \sigma_b^2 + \left(\frac{\partial f}{\partial d}\right)^2 \sigma_d^2 + \left(\frac{\partial f}{\partial e}\right)^2 \sigma_e^2 + \cdots} \,. \tag{5.9}$$

For convenience, we rewrite G_M^n from Eq. (4.40) in a compact form:

$$G_M^n = f = \sqrt{A\, a\big(B\, b^2 + D\, d^2\big) + E\, e^2}\,, \tag{5.10}$$

---

[4] This statement of sub-2% precision comes from the total uncertainty (correlated and uncorrelated) for SBS-4 30% in Tab. 5.9

where the constants and variables are defined as:

$$A = \left[\frac{\sigma_n}{\sigma_p}\right]_{\text{simc}}, \quad a = R_{sf}, \quad B = 1, \quad b = G_M^p, \quad D = \frac{\epsilon_p}{\tau_p}, \quad d = G_E^p, \quad E = -\frac{\epsilon_n}{\tau_n}, \quad e = G_E^n.$$

The partial derivatives of f with respect to a, b, d, and e are:

$$\begin{aligned} \frac{\partial f}{\partial a} &= \frac{A\big(Bb^2 + Dd^2\big)}{2f}, \\ \frac{\partial f}{\partial b} &= \frac{AaBb}{f}, \\ \frac{\partial f}{\partial d} &= \frac{AaDd}{f}, \\ \frac{\partial f}{\partial e} &= \frac{Ee}{f}. \end{aligned} \tag{5.11}$$

Expressed in terms of the original physics variables, these become:

$$\begin{aligned} \frac{\partial G_M^n}{\partial R_{sf}} &= \frac{\left[\frac{\sigma_n}{\sigma_p}\right]_{\text{simc}} \big((G_M^p)^2 + \frac{\epsilon_p}{\tau_p}(G_E^p)^2\big)}{2G_M^n}, \\ \frac{\partial G_M^n}{\partial G_M^p} &= \frac{R_{sf}\left[\frac{\sigma_n}{\sigma_p}\right]_{\text{simc}} G_M^p}{G_M^n}, \\ \frac{\partial G_M^n}{\partial G_E^p} &= \frac{R_{sf}\left[\frac{\sigma_n}{\sigma_p}\right]_{\text{simc}} \frac{\epsilon_p}{\tau_p} G_E^p}{G_M^n}, \\ \frac{\partial G_M^n}{\partial G_E^n} &= -\frac{\frac{\epsilon_n}{\tau_n} G_E^n}{G_M^n}, \end{aligned} \tag{5.12}$$

where G_M^p, G_E^p, G_E^n are calculated from the Ye fit to global data [20]. The parameterization of these fits can be found in Appx. A.

Finally, the total uncertainty in G_M^n is obtained by combining all contributions in quadrature, explicitly accounting for the statistical and each systematic component of R_{sf} and the uncertainties from the world data fits. The systematic uncertainty is

$$\begin{aligned}\sigma_{G_M^n,\mathrm{syst}} = \Bigg[\sum_i \left(\frac{\partial G_M^n}{\partial R_{sf}}\, \delta R_{sf,\mathrm{syst},i} \right)^2 \\ + \left(\frac{\partial G_M^n}{\partial G_M^p}\, \sigma_{G_M^p} \right)^2 + \left(\frac{\partial G_M^n}{\partial G_E^p}\, \sigma_{G_E^p} \right)^2 + \left(\frac{\partial G_M^n}{\partial G_E^n}\, \sigma_{G_E^n} \right)^2 \Bigg]^{1/2} ,\end{aligned} \tag{5.13}$$

where the sum over i runs over the individual systematic components of R_{sf}, and the global-data uncertainties, enter as single terms each. These uncertainties can be calculated using the parameterization found in Appx. A. The statistical contribution is given simply by

$$\sigma_{G_M^n,\mathrm{stat}} = \left| \frac{\partial G_M^n}{\partial R_{sf}} \right| \delta R_{sf,\mathrm{stat}} \, . \tag{5.14}$$

The total uncertainty is then

$$\sigma_{G_M^n,\mathrm{total}} = \sqrt{\sigma^2_{G_M^n,\mathrm{stat}} + \sigma^2_{G_M^n,\mathrm{syst}}} \, . \tag{5.15}$$

Here, $\delta R_{sf,\mathrm{stat}}$ is the statistical uncertainty on R_{sf}, $\delta R_{sf,\mathrm{syst},i}$ are the individual systematic contributions to R_{sf}, and $\sigma_{G_M^p}$, $\sigma_{G_E^p}$, and $\sigma_{G_E^n}$ are the total uncertainties reported from the world data fits. This formulation ensures that all uncorrelated contributions to the uncertainty in G_M^n are accounted for properly, without double-counting or conflation of sources.

It is important to note that the statistical uncertainty on G_M^n arises solely from the statistical uncertainty on R_{sf}, propagated through the appropriate partial derivative. The uncertainties on G_M^p, G_E^p, and G_E^n come from world data fits, which are independent of the counting statistics in this measurement. Therefore, the world data uncertainties contribute only to the systematic uncertainty budget, while the statistical uncertainty budget reflects only the fluctuation of R_{sf} due to the finite number of observed events.

5.7 Results and Comparison to Global Data

5.7.1 G_M^n Extraction Results

To extract G_M^n from R_{sf}, we use Eq. (4.40), propagate the systematic uncertainty using Eq. (5.8), and propagate the statistical uncertainty using Eq. (5.14). The individual contributions to the systematic and statistical uncertainties are displayed in Tab. 5.12, reported as absolute uncertainty and as relative uncertainty with respect to G_M^n. Note that these are measures of G_M^n, not normalized to $G_M^n/(\mu_n G_D)$. The parameters of the Ye fits to the form factors used in these calculations are found in Appx. A. The values and uncertainties of the fits at the Q^2 used in this analysis are found in Tab. A.4.

Table 5.12: Absolute and relative uncertainty contributions to G_M^n. The top panel shows the absolute uncertainties from each source, in units of G_M^n. The bottom panel shows the corresponding relative uncertainties (in %) with respect to G_M^n. The individual contributions correspond to the terms in Eq. (5.12), with $\%\, R_{sf}$, $\%\, G_M^p$, $\%\, G_E^p$, and $\%\, G_E^n$ denoting the percent contributions from the uncertainties on R_{sf}, G_M^p, G_E^p, and G_E^n, respectively. The total systematic uncertainty is computed as the quadrature sum of the individual systematic contributions, and the total uncertainty is the quadrature sum of the statistical and systematic uncertainties. Uncertainties on the Ye fits to the world form factor data are described in Appx. A.

Kinematic	Q^2(GeV^2)	ε	G_M^n	$\left(\frac{\partial G_M^n}{\partial R_{sf}}\sigma_{R_{sf,\text{ syst}}}\right)$	$\left(\frac{\partial G_M^n}{\partial G_M^p}\sigma_{G_M^p}\right)$	$\left(\frac{\partial G_M^n}{\partial G_E^p}\sigma_{G_E^p}\right)$	$\left(\frac{\partial G_M^n}{\partial G_E^n}\sigma_{G_E^n}\right)$	$\sigma_{G_M^n}^{\text{syst.}}$	$\sigma_{G_M^n}^{\text{stat.}}$	$\sigma_{G_M^n}^{tot.}$
SBS-4 30%	3.0	0.72	0.06611	0.000827	0.000470	0.000230	0.000341	0.00104	0.000229	0.00106
SBS-8 70%	4.5	0.80	0.03377	0.000495	0.000372	0.000097	0.000316	0.000702	0.000094	0.000708
SBS-9 70%	4.5	0.51	0.03381	0.000494	0.000369	0.000062	0.000203	0.000652	0.000096	0.000659
Kinematic	Q^2 (GeV^2)	ε	G_M^n	% R_{sf}	% G_M^p	% G_E^p	% G_E^n	% $\sigma_{G_M^n}^{\text{syst.}}$	% $\sigma_{G_M^n}^{\text{stat.}}$	% $\sigma_{G_M^n}^{\text{tot.}}$
SBS-4 30%	3.0	0.72	0.06611	1.25%	0.71%	0.35%	0.52%	1.57%	0.35%	1.61%
SBS-8 70%	4.5	0.80	0.03377	1.46%	1.10%	0.29%	0.94%	2.08%	0.28%	2.10%
SBS-9 70%	4.5	0.51	0.03381	1.46%	1.09%	0.18%	0.60%	1.93%	0.28%	1.95%

Table 5.12 shows that although the largest contribution to the systematic uncertainty comes from R_{sf} (about 1.25–1.5%), the contributions from the global-data fits are of comparable magnitude and therefore not negligible, ranging from roughly 0.3% to 1.1%. This suggests that as the precision of global fits to G_M^p, G_E^p, and G_E^n improves with additional experimental data—such as forthcoming measurements from the SBS program—the uncertainty on these extractions of G_M^n could decrease.[5]

---

[5] However, using improved fits to one form factor to reduce the uncertainty on another could introduce

These results are dominated by systematic uncertainty: the total systematic uncertainty (approximately 1.5–2%) is roughly an order of magnitude larger than the statistical uncertainty (about 0.3%) at each kinematic. This is not unexpected, as scattering experiments such as these typically record millions of events.

5.7.2 $G_M^n/(\mu_n G_D)$ Comparison to Global Fit

To compare our results to global data, we calculate $G_M^n/(\mu_n G_D)$ for each data point, as seen in Tab. 5.13. The expression for the dipole form factor $G_D(Q^2)$ is found in Eq. 1.31.

Table 5.13: Summary of $G_M^n/\mu_n G_D$ measurements, including absolute and percent uncertainties. The total uncertainty is the quadrature sum of statistical and systematic uncertainties.

Kinematic	Q^2 (GeV^2)	ε	$G_M^n/(\mu_n G_D)$	$\pm\sigma^{\text{syst.}}$	$\pm\sigma^{\text{stat.}}$	$\sigma^{\text{tot.}}$	% stat	% syst	% tot
SBS-4 30%	3.0	0.72	0.961	0.015	0.0033	0.015	0.35%	1.57%	1.61%
SBS-8 70%	4.5	0.80	0.952	0.020	0.0026	0.020	0.28%	2.08%	2.10%
SBS-9 70%	4.5	0.51	0.954	0.018	0.0027	0.019	0.28%	1.93%	1.95%

Figures 5.25 and 5.26 plot $G_M^n/(\mu_n G_D)$ for the results of this work as well as the Ye fit and data points from previous experiments used in creating the Ye fit. Figure 5.25 shows the full Q^2 range of the comparison, while Fig. 5.26 focuses on the region around these extractions and shows both the statistical and total uncertainties as separate error bars. The Ye fit is shown as a gray band. The SBS-8 and SBS-9 points are slightly shifted in Q^2 for visualization.

5.7.2.1 Discussion of Two-Photon Exchange Corrections

It is important to note that the Ye fit explicitly applies two-photon exchange (TPE) corrections to the global cross section data, following the SIFF Blunden model [77] along with an additional high-Q^2 phenomenological correction. In contrast, the G_M^n results presented in this work are extracted without applying TPE corrections. Using the results of

---

correlated uncertainties. For example, a more precise G_E^n measurement would lead to a more precise G_M^n, which in turn could feed back into the G_E^n global fit, and so on. This potential recursive effect would need to be accounted for carefully.

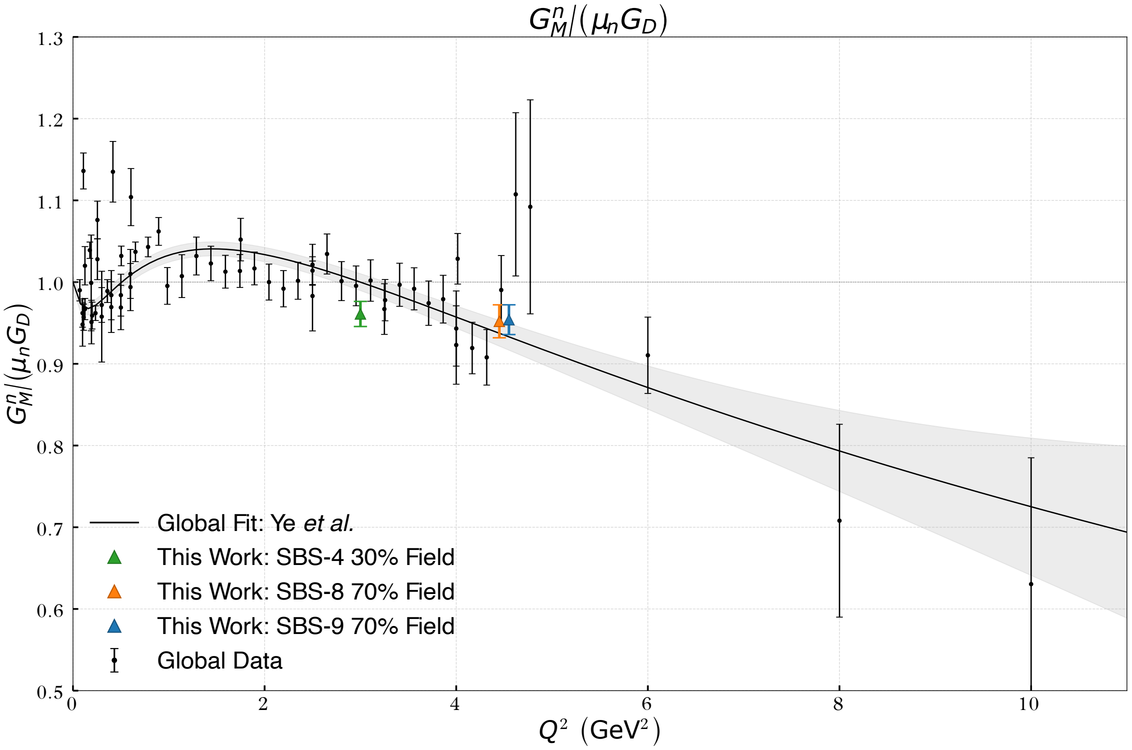

Figure 5.25: $G_M^n/(\mu_n G_D)$ results from this work compared to world data as a function of Q^2. The error bars represent the total uncertainty (statistical and systematic added in quadrature) from Tab. 5.13. The Ye fit to global data [20] is shown in gray; the extractions from this work are **not** included in the fit. The SBS-8 and SBS-9 points are slightly offset in Q^2 for visibility. Note that TPE corrections are not applied to our results.

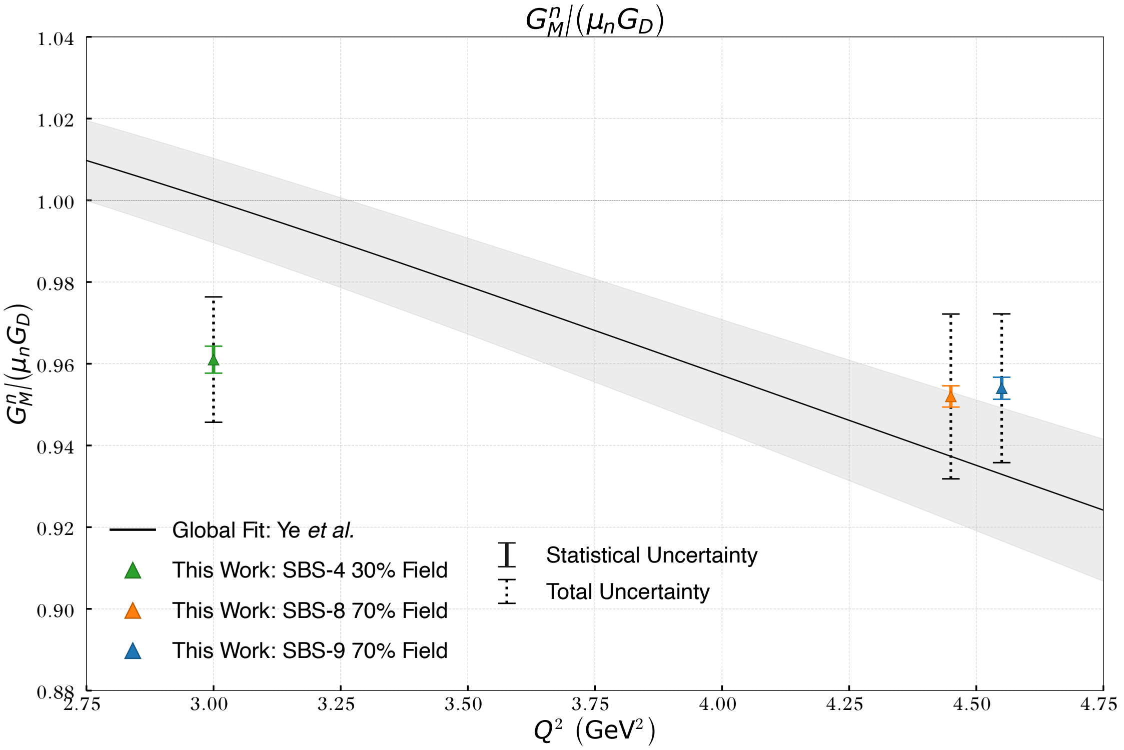

Figure 5.26: Zoomed-in view of $G_M^n/(\mu_n G_D)$ results from this work compared to world data in the Q^2 region of our measurements (see Tab. 5.13). Inner solid error bars show the statistical uncertainty, while outer dotted error bars represent the total uncertainty (statistical and systematic added in quadrature). The Ye fit to global data [20] is shown in gray; the extractions from this work are **not** included in the fit. The SBS-8 and SBS-9 points are slightly offset in Q^2 for visibility. TPE corrections are not applied to our results.

the SIFF Blunden model [77] (particularly Fig. 12), at the kinematics of this experiment ($Q^2 = 3.0$–4.5 GeV^2, $\varepsilon = 0.5$–0.8), the estimated TPE effect is on the order of 0.5–1% at $Q^2 = 3.0$ and up to ∼1–2% at $Q^2 = 4.5$, which is comparable to the quoted total uncertainty (see Tab. 5.13). Correcting for TPE would change the extracted G_M^n by up to ∼1% and could slightly increase the observed discrepancy with the Ye fit at $Q^2 = 3.0$. While this correction does not alter the conclusion of agreement within uncertainties, it is not negligible and should be considered in future analyses.

Collaborators are currently working on implementing TPE corrections into similar G_M^n extractions for future publications. It would be interesting in the future to apply these corrections to the results presented here as well, which could improve the consistency and precision of the comparison to the global fit.

We see that our result for SBS-4 ($Q^2 = 3.0$ GeV^2) is slightly below the fit to global data within uncertainty. However, we see that our results for both SBS-8 and SBS-9 overlap considerably within uncertainty. To numerically compare our results to the Ye fit, we calculate the absolute difference (Δ) and uncertainty between our result and the Ye fit (Tab. 5.14). This follows a similar procedure to how R_{sf} was compared between field settings in Eq. 5.3.

Table 5.14: Comparison of $G_M^n/(\mu_n G_D)$ measurements to the Ye global fit values. The difference Δ is defined as $G_M^n/(\mu_n G_D) - G_M^n/(\mu_n G_D)|_{\mathrm{Ye}}$, with uncertainty propagated in quadrature, and N is the number of sigma.

Kinematic	Q^2 (GeV^2)	$G_M^n/(\mu_n G_D)$	Total Uncert.	$G_M^n/(\mu_n G_D)\vert_{\mathrm{Ye}}$	Ye Uncert.	Δ	Uncert. Δ	$N\sigma$
SBS-4 30%	3.0	0.961	0.015	0.999	0.010	-0.038	0.019	2.04
SBS-8 70%	4.5	0.952	0.020	0.935	0.016	0.017	0.026	0.68
SBS-9 70%	4.5	0.954	0.019	0.935	0.016	0.019	0.025	0.79

The results of SBS-8 and SBS-9 found in Tab. 5.14 both agree with the Ye fit to a high degree within uncertainty: $N\sigma < 1$. The results for SBS-4 agree with the Ye fit to a level of $N\sigma < 2.1$. The $N\sigma$ value of approximately 2.1 at $Q^2 = 3.0$ indicates that our result is within about two standard deviations of the Ye fit, corresponding to a p-value of roughly 0.03 in a Gaussian distribution (i.e., about a 3% probability of observing such a discrepancy by random fluctuation). While this level of discrepancy does not constitute significant evidence for disagreement, it is notable and could in part be exacerbated by fact that our result inherently includes TPE effects, which—if corrected for—would lower G_M^n by an additional ∼1%, slightly increasing the $N\sigma$.

5.7.3 Agreement between SBS-8 and SBS-9

Table 5.15 evaluates the difference between the results of SBS-8 and SBS-9, which are both $Q^2 = 4.5$ GeV^2 with different ε.

Table 5.15: Comparison of $G_M^n/(\mu_n G_D)$ between SBS-8 and SBS-9 field settings at $Q^2 \approx 4.5$ GeV^2. The difference Δ is defined as $G_M^n/(\mu_n G_D)|_{\text{SBS-8}} - G_M^n/(\mu_n G_D)|_{\text{SBS-9}}$, with its uncertainty and corresponding $N\sigma$, computed both with total uncertainties and with statistical uncertainties only.

Kinematic	ε	$G_M^n/(\mu_n G_D)$	Stat. Uncert.	Syst. Uncert.	Total Uncert.	Δ	Uncert. Δ	$N\sigma$	$N\sigma$ (stat only)
SBS-8 70%	0.80	0.952	0.0026	0.020	0.020	0.0017	0.027	0.06	0.46
SBS-9 70%	0.51	0.954	0.0027	0.018	0.019				

Table 5.15 and Fig. 5.26 demonstrate that the SBS-8 and SBS-9 measurements at $Q^2 = 4.5$ agree to a very high degree, with $N\sigma < 0.06$ (total uncertainty) and $N\sigma < 0.5$ (statistical uncertainty only). This level of agreement exceeds what would be expected if all uncertainties were completely uncorrelated, and is consistent with the observation made earlier when comparing R_{sf} between field settings. In that case, the apparent scatter between measurements was also smaller than predicted by the quoted uncertainties. This suggests that the uncorrelated systematic uncertainties between field settings may have been overestimated. Since this analysis intentionally used conservative estimates of systematic uncertainties to ensure robustness, such overestimation is understandable. Nonetheless, these results indicate that a more detailed evaluation of the correlations between systematic contributions could further improve the precision of the combined result.

Chapter 6

Conclusions and Outlook

Summary of the Work

This analysis focused on extracting the neutron magnetic form factor, G_M^n, at $Q^2 = 3.0$ and 4.5 GeV^2 using the Ratio Method. Data were taken from quasi-elastic electron scattering from deuterium in the GMn experiment—part of the Super BigBite Spectrometer (SBS) program in Hall A at Jefferson Lab. Precise measurements of G_M^n are important for understanding how magnetization is distributed inside the neutron and for improving global fits to the nucleon electromagnetic form factors.

Experimental data and Monte Carlo simulations were run through the same reconstruction and analysis chain to ensure a consistent comparison. To extract G_M^n, neutron-to-proton scattering ratios were obtained by directly comparing experimental data to simulated data (Sec. 4.7). Systematic uncertainties related to the inelastic background shape (Sec. 5.3.2) and cut stability (Sec. 5.3.1) were evaluated in this work, while estimates for the nucleon detection efficiency and the neutron-to-proton efficiency ratio were adapted from earlier studies by P. Datta and applied to the present analysis (Sec. 5.3.4).

This work also includes a detailed analysis of the GRINCH heavy gas Cherenkov detector, which is intended for electron identification and pion rejection during SBS experiments. During this experiment, GRINCH achieved an electron detection efficiency of about 97%

and a pion rejection efficiency of roughly 96% (Fig. 3.30), validating its role as a particle identification detector for future SBS experiments. A significant portion of the detector calibration, clustering algorithms, and analysis framework was developed and implemented as part of this work, including during the running of the experiment itself. These efforts are documented in Ch. 3 of this thesis. Altogether, this analysis helps set the stage for future extractions of G_M^n at even higher Q^2, using the full SBS dataset that extends out to 13.5 GeV^2.

Main Findings

This work extracted the neutron magnetic form factor G_M^n at two values of four-momentum transfer: $Q^2 = 3.0$ and 4.5 GeV^2. At $Q^2 = 4.5$, two kinematic points were analyzed—one at high virtual photon polarization ($\varepsilon = 0.80$) and one at lower polarization ($\varepsilon = 0.51$) (Tab. 5.13, Fig 5.25). These points were originally intended for a Rosenbluth separation measurement, which is not pursued in this work. Instead, they were chosen for analysis here because they are the only kinematics in this experiment where GRINCH was operational and stable, allowing for a full evaluation of GRINCH performance in the context of a G_M^n extraction. The $Q^2 = 3.0$ point, while not in the GRINCH dataset, was selected as a useful testbed for validating analysis methods due to its relatively low inelastic background contamination.

Results at both high-ε and low-ε points at $Q^2 = 4.5$ show very good agreement with the global Ye fit [20] as well as with each other, while the $Q^2 = 3.0$ point lies about 2.1 standard deviations (σ) below the fit (Tab 5.14, Fig 5.26). That level of deviation isn't considered significant, but it's enough to raise some curiosity—especially since two-photon exchange (TPE) corrections weren't applied in this analysis.

Overall, the measurements reached a total uncertainty of around 1.5–2.0%, with statistical uncertainties below 0.5%. As expected, systematic effects dominate the total uncertainty. The largest contributions came from the shape of the inelastic background, the choice of analysis cuts, and assumptions about neutron detection efficiency (Tab. 5.12).

The extraction method was tested across multiple hadron arm magnetic field settings for the $Q^2 = 3.0$ point and the $Q^2 = 4.5$, high-ε point. The magnetic field bends charged particles in the hadron arm, enabling proton-neutron separation based on the deflection of the detected nucleon, which is a key input for the extraction of the scattering ratios. The results across different field settings were consistent—in fact, sometimes *more* consistent than expected based on the quoted uncorrelated uncertainties. This may point to an overestimation of those uncertainties in this analysis (Tab 5.15). While this conservative approach was intentional, it likely under represented the true precision of the measurement.

This analysis did not apply two-photon exchange (TPE) corrections. At the kinematics of this experiment, TPE effects are estimated to change G_M^n by roughly 1% (Fig. 12 in Reference [77]), which could slightly increase the tension seen at $Q^2 = 3.0$. Including those corrections in the future would give a more complete comparison with theory and help clarify whether the small discrepancy is meaningful or not.

Critical Evaluation

While the results presented in this analysis are precise and internally consistent, there are several limitations that should be acknowledged. Most notably, the dominant uncertainties are systematic in nature and were treated conservatively throughout the analysis. In particular, a number of assumptions—such as uncorrelated treatment of uncertainties between field settings, and the fixed 2% systematic assigned to the neutron-to-proton detection efficiency ratio—were designed to avoid underestimating the total uncertainty but may overstate it in practice (Sec 4.8.3).

GRINCH, although operational during the $Q^2 = 4.5$ data-taking period and extensively studied in this work, was not used in the final G_M^n extraction due to incomplete simulation modeling. This was a missed opportunity to take advantage of its strong particle identification capabilities, which would have helped suppress pion backgrounds more effectively. That said, GRINCH's ability to reject pions may be limited at low-ε: based on the expected pion momenta and threshold calculations presented in the GRINCH chapter, some pions in the inelastic background are likely above threshold and could produce Cherenkov light. This makes pion rejection more challenging at low-ε than in the high-ε setting. Future analyses with improved simulations may be able to incorporate GRINCH cuts directly into the physics extraction for the $Q^2 = 4.5$ setting where it was operational.

The neutron detection efficiency, unlike the proton case, could not be directly calibrated during the experiment due to hardware limitations and beam time constraints. As a result, we relied on simulation and adopted systematic estimates from prior work. While reasonable, this introduces additional model dependence that would benefit from direct measurement.

Another challenge came from the correlation between key analysis cuts, particularly between W^2 and Δy (Fig. 4.9). In this work, their effects were studied independently, and only the larger of the two uncertainties was included in the final quadrature sum. This was a conservative simplification meant to avoid double-counting correlated effects, but it may still overestimate or underestimate the true impact of these variables. A more targeted approach—such as applying a combined variation or estimating a correlation factor—could give a clearer picture of their actual contribution to the systematic uncertainty.

Finally, two-photon exchange (TPE) corrections were not applied. These effects are expected to shift the extracted G_M^n by around 1% at these kinematics, which is comparable to the total uncertainty and could affect comparisons to global fits. Future work should revisit this extraction with TPE corrections included.

Comparison with Global Fits and Theory

The results presented in this work are compared to the Ye global fit [20], which includes world data up to $Q^2 \sim 10$ GeV^2 and incorporates two-photon exchange (TPE) corrections. As shown in Table 5.14, the measurements at $Q^2 = 4.5$ GeV^2 (SBS-8 and SBS-9) are in excellent agreement with the Ye global fit. The observed differences are less than one standard deviation (σ) when uncertainties are combined in quadrature, indicating no statistically significant deviation. The $Q^2 = 3.0$ GeV^2 point (SBS-4) is approximately 2.0-σ below the fit. This level of disagreement is not statistically significant, but it is interesting—especially since no TPE correction was applied to the result. Including such a correction would likely decrease the measured value of G_M^n slightly, increasing the deviation with respect to the fit.

These extracted G_M^n results are among the most precise measurements of G_M^n in this Q^2 region and help anchor the global fit where the existing data are already relatively dense. At the same time, it's important to acknowledge that these points are still at too low Q^2 to clearly differentiate between competing theoretical models. As seen in global comparisons (e.g., Fig. 1.8), many models—including the Covariant Spectator model, BLFQ, VMD-based fits, and GPD-based approaches—predict similar behavior below $Q^2 \sim 5$ GeV^2, with more noticeable deviations appearing only at higher Q^2 values. Those higher-Q^2 points are where world data are sparse, and where the full GMn dataset from SBS will eventually play a much more decisive role.

In that context, the results presented here serve two key purposes: first, they help refine the normalization and slope of global fits at moderate Q^2; second, they validate the experimental techniques that will be used to push to higher momentum transfers. In particular, the high-ε and low-ε measurements at $Q^2 = 4.5$ GeV^2 demonstrate the robustness of the analysis and show that consistent extractions are possible across different configurations.

Implications and Significance

The results presented in this work show that the Ratio Method, when combined with careful control of systematics and tested across multiple field settings, can reliably extract G_M^n with sub-2% precision at intermediate Q^2. The fact that the measurements came out consistent across different magnet configurations adds confidence to the overall approach and helps set the stage for future extractions at higher Q^2 using the full SBS dataset.

These measurements also contribute to quark flavor decomposition. Assuming isospin symmetry—that is, treating up and down quarks in the proton and neutron as the same except for their electric charge—the Dirac and Pauli form factors, F_1 and F_2, can be used to extract the contributions from up and down quarks individually [15] (1.7.2). To do this cleanly, we need high-precision measurements of all four nucleon form factors. These results for G_M^n help anchor the flavor decomposition at intermediate Q^2, with the idea that future SBS measurements will extend it further. The really interesting behavior—the point where the models start to deviate—doesn't show up until higher Q^2, but that's exactly where the SBS program is heading (Fig. 1.8).

Long term, the full SBS form factor program is expected to push G_M^n measurements up to $Q^2 \sim 12$ GeV^2. Precision data in that region will be important for studying the transition from non-perturbative to perturbative QCD, testing scaling behavior, and probing whether diquark degrees of freedom play a meaningful role in the nucleon's internal structure [17, 18]. The results here provide both a first test and a validation of the tools and analysis methods that will be used to get there.

Beyond this analysis, GRINCH's particle identification performance is especially relevant for the next experiment in the SBS program: GEn-II. In that measurement, where pion rejection is more critical due to increased backgrounds, GRINCH plays a central role. The work presented here—both in calibrating GRINCH and understanding its limitations—directly supports the use of GRINCH in that context. While it wasn't used in the final G_M^n extraction here due to incomplete simulations, the detector's high electron efficiency and pion rejection capabilities make it an essential tool for GEn-II and other future SBS experiments where PID constraints are more severe.

Lessons Learned

This analysis, particularly the work on GRINCH, highlighted several lessons—both technical and structural—that became clear during the experiment.

GRINCH Readiness and Integration

One key takeaway from this work is the value of early integration between detector hardware, simulation tools, and analysis workflows. Prior to the GMn data-taking period, GRINCH lacked updated simulation models compatible with the broader SBS software framework. While clustering was always expected to be part of the analysis, development and integration of these tools were delayed due to limited personnel and competing responsibilities across the collaboration.

Given the high-rate environment, the lack of full ADC coverage, and the relatively small Cherenkov cone radius, clustering was essential for achieving reliable particle identification. During the run, it became clear that the number of tubes fired alone was not sufficient for PID, and clustering provided the needed performance. I developed a standalone clustering algorithm and applied it to the GRINCH output from the standard replay scripts, which—at the time—included only minimal GRINCH variables. This workflow served as the primary method of GRINCH analysis for much of the GMn experiment. Later, the collaboration's software lead adapted the existing clustering tools from HCal and BBCal for GRINCH and integrated them into the standard framework, building on the foundation already established.

This experience demonstrated not only the importance of integrating simulation and analysis earlier in the development cycle, but also the benefits of flexible, modular analysis tools that can evolve as the experiment progresses.

Project Structure and Communication

More broadly, the GRINCH effort during GMn highlighted some of the unique challenges of the user-driven model currently in use in Hall A. With permanent spectrometers decommissioned and new detectors often built by individual groups, institutional knowledge and technical responsibility are sometimes concentrated in just a few people. When personnel transitions happen unexpectedly—as was the case during the GRINCH commissioning—gaps can emerge.

I stepped into a lead analysis and software development role for GRINCH partway through the experiment. This was a valuable learning experience and an opportunity to contribute meaningfully to the detector's commissioning. At the same time, it emphasized how fragile critical systems can become when continuity and collaboration are stretched thin. More structured transition processes, better documentation, and a culture of collaborative problem-solving would strengthen future efforts and help mitigate risks in similar projects.

Analysis-Specific Takeaways

A few key lessons came out of the analysis itself:

- More statistics at different magnetic field settings across the kinematics would have helped improve calibrations and cross-checks—especially for building better efficiency maps.

- Some of the systematic uncertainties, particularly those treated as uncorrelated between field settings, were probably a bit too conservative. It would be good in the future to take a closer look at which uncertainties are really independent and propagate them more realistically.

- We originally planned to calibrate the neutron detection efficiency using pion photoproduction, but hardware issues and beam time limitations meant that didn't happen. It was a good reminder of how important it is to build in some flexibility—especially when you're relying on multi-detector coincidence setups and a tight run plan.

In general, this work was a great example of how complex experimental analysis can be—not just technically, but logistically and collaboratively. These lessons will definitely stick with me and help shape how I approach future projects.

Outlook and Future Work

Several areas remain open for further development and refinement. While this analysis did not apply two-photon exchange (TPE) corrections, they may play a role—particularly at higher Q^2 and low ε. Future extractions of G_M^n using the full SBS dataset could incorporate these corrections for improved precision and to better match global fits.

GRINCH, though not used in the final G_M^n extraction here, is expected to be a key player in upcoming SBS experiments like GEn-II. Integrating the improved GRINCH simulations into the full reconstruction into the replay framework would allow its particle ID capabilities to be fully realized in future analyses. Re-running this G_M^n extraction with updated simulations and incorporating GRINCH PID could help reduce systematic uncertainties from inelastic backgrounds, especially in the low-ε setting.

The uncertainty in G_M^n is still partially limited by the uncertainties in other form factors, especially G_E^p and G_E^n, which propagate through into the G_M^n calculation. As these form factors are better constrained in future experiments, global fits to G_M^n will improve as well. This will be particularly important for extending flavor decomposition studies to higher Q^2, where the up- and down-quark form factors begin to diverge in model predictions.

Finally, as more of the SBS form factor data and analysis comes online—especially at $Q^2 > 6$ GeV^2—we'll begin to enter a kinematic region where theoretical models for nucleon structure start to meaningfully diverge. The combined high-Q^2 results from SBS will not only improve empirical fits, but help test predictions related to diquark correlations, higher-twist effects, and parton dynamics within the nucleon.

There's a lot of exciting physics still to come, and the work presented here helps lay the groundwork for it.

Appendix A

Fits to Global Data

Global measurements of the nucleon form factors G_M^p, G_E^p, G_M^n, and G_E^n are often described using empirical parameterizations as functions of Q^2. Many of these are expressed in terms of the dimensionless variable $\tau = Q^2/(4M_N^2)$ and take the form of polynomial fits with tuned coefficients. These parameterizations are used both to extract quantities like G_M^n from experimental observables, as in this work, and to calculate cross sections in the Monte Carlo simulation during event generation [78].

Two commonly used parameterizations are those from Kelly [79] and Riordan [78], which share a similar functional form:

$$G(Q^2) \propto \frac{\sum_{k=0}^{n_a} a_k \tau^k}{1 + \sum_{k=1}^{n_b} b_k \tau^k},, \tag{A.1}$$

where the coefficients a_k and b_k are specific to each form factor. The simulation package SIMC utilizes Kelly's parameterizations for G_E^p, G_M^p, and G_M^n, and incorporates Riordan's fit for G_E^n. Although the Riordan fits remain unpublished, they are available in the SIMC source code [67]. The numerical values of the coefficients are listed in Tab. A.1.

A more recent parameterization by Ye *et al.* takes a different approach, using a bound polynomial z expansion defined as

$$z = \frac{\sqrt{t_{\text{cut}} + Q^2} - \sqrt{t_{\text{cut}} - t_0}}{\sqrt{t_{\text{cut}} + Q^2} + \sqrt{t_{\text{cut}} - t_0}},, \tag{A.2}$$

Table A.1: Fit parameters for the form factors used in the Kelly, Riordan, and Arrington fits in the form of Eq. A.1.

Fit		a_0	a_1	a_2	a_3	b_1	b_2	b_3	b_4	b_5
Kelly	G_E^p	1.0	-0.24	0.0	0.0	10.98	12.82	0.863	0.0	0.0
Kelly	G_M^p/μ_p	1.0	0.12	0.0	0.0	10.97	18.86	6.55	0.0	0.0
Kelly	G_M^n/μ_n	1.0	2.33	0.0	0.0	14.72	24.2	84.1	0.0	0.0
Riordan	G_E^n	0.0	1.52	2.629	3.055	5.22	0.04	11.438	0.0	0.0
Arrington	G_E^p	1.0	3.439	-1.602	0.068	15.055	48.061	99.304	0.012	8.65
Arrington	G_M^p/μ_p	1.0	-1.465	1.26	0.262	9.627	0.0	0.0	11.179	13.245

and modeling the form factor as a power series in z:

$$G(Q^2) = \sum_{k=0}^{k_{\max}} a_k z^k \, . \tag{A.3}$$

Here, G represents G_E^p, G_M^p/μ_p, G_E^n, or G_M^n/μ_n, with $t_{\text{cut}} = 4m_\pi^2$, where $m_\pi = 0.13957$ GeV is the charged pion mass, and $t_0 = -0.7$ GeV^2. The fit coefficients a_k are given in Tab. A.2.

Table A.2: Fit parameters for the Ye fits to world data for G_E^n, G_E^p and G_M^p/μ_p for Eq. (A.3). These are provided in the supplementary material of the publication [20].

Parameter	G_E^p	G_M^p/μ_p	G_E^n	G_M^n/μ_n
a_0	0.239163298067	0.264142994136	0.048919981379	0.257758326959
a_1	−1.109858574410	−1.095306122120	−0.064525053912	−1.079540642058
a_2	1.444380813060	1.218553781780	−0.240825897382	1.182183812195
a_3	0.479569465603	0.661136493537	0.392108744873	0.711015085833
a_4	−2.286894741870	−1.405678925030	0.300445258602	−1.348080936796
a_5	1.126632984980	−1.356418438880	−0.661888687179	−1.662444025208
a_6	1.250619843540	1.447029155340	−0.175639769687	2.624354426029
a_7	−3.631020471590	4.235669735900	0.624691724461	1.751234494568
a_8	4.082217023790	−5.334045653410	−0.077684299367	−4.922300878888
a_9	0.504097346499	−2.916300520960	−0.236003975259	3.197892727312
a_{10}	−5.085120460510	8.707403067570	0.090401973470	−0.712072389946
a_{11}	3.967742543950	−5.706999943750	0	0
a_{12}	−0.981529071103	1.280814375890	0	0

The associated uncertainties in the Ye *et al.* fits are evaluated using the covariance matrix and are parameterized as a function of $x = \log_{10}(Q^2)$:

$$\delta G(Q^2) = G_D \times 10^{\sum_{k=0}^{14} B_k x^k}, , \tag{A.4}$$

where $G_D = (1 + \frac{Q^2}{0.71})^{-2}$ is the dipole form factor and B_k are coefficients listed in Tab. A.3.

Table A.3: Parameters for the error for world data for G_E^n, G_E^p and G_M^p/μ_p for Eq. (A.4). These are provided in the supplementary material of the publication [20].

Parameter	δG_E^p	$\delta G_M^p/\mu_p$	δG_E^n	$\delta G_M^n/\mu_n$
B_0	-1.97750308×10^0	-1.76549673×10^0	-2.07194073×10^0	-2.06920873×10^0
B_1	$-4.46566998 \times 10^{-1}$	$1.67218457 \times 10^{-1}$	1.13809127×10^0	$6.43156400 \times 10^{-2}$
B_2	$2.94508717 \times 10^{-1}$	-1.20542733×10^0	1.01431277×10^0	$-3.55593786 \times 10^{-1}$
B_3	1.54467525×10^0	$-4.72244127 \times 10^{-1}$	$-3.13301380 \times 10^{-1}$	$4.14897660 \times 10^{-1}$
B_4	$9.05268347 \times 10^{-1}$	1.41548871×10^0	$-2.73293676 \times 10^{-1}$	1.95746824×10^0
B_5	$-6.00008111 \times 10^{-1}$	$6.61320779 \times 10^{-1}$	$2.57350595 \times 10^{-1}$	$2.70525700 \times 10^{-1}$
B_6	-1.10732394×10^0	$-8.16422909 \times 10^{-1}$	$-2.06042113 \times 10^{-1}$	-1.52685784×10^0
B_7	$-9.85982716 \times 10^{-2}$	$-3.73804477 \times 10^{-1}$	$-1.68497332 \times 10^{-1}$	$-4.43527359 \times 10^{-1}$
B_8	$4.63035988 \times 10^{-1}$	$2.62223992 \times 10^{-1}$	$1.37784515 \times 10^{-1}$	$5.16884065 \times 10^{-1}$
B_9	$1.37729116 \times 10^{-1}$	$1.28886639 \times 10^{-1}$	$7.57591964 \times 10^{-2}$	$2.07915837 \times 10^{-1}$
B_{10}	$-7.82991627 \times 10^{-2}$	$-3.90901510 \times 10^{-2}$	$-2.67511301 \times 10^{-2}$	$-7.48665703 \times 10^{-2}$
B_{11}	$-3.63056932 \times 10^{-2}$	$-2.44995181 \times 10^{-2}$	$-1.72573088 \times 10^{-2}$	$-4.25411431 \times 10^{-2}$
B_{12}	$2.64219326 \times 10^{-3}$	$8.34270064 \times 10^{-4}$	$7.03581500 \times 10^{-4}$	$1.54965016 \times 10^{-3}$
B_{13}	$3.13261383 \times 10^{-3}$	$1.88226433 \times 10^{-3}$	$1.47962095 \times 10^{-3}$	$3.25322279 \times 10^{-3}$
B_{14}	$3.89593858 \times 10^{-4}$	$2.43073327 \times 10^{-4}$	$1.97375221 \times 10^{-4}$	$4.20819518 \times 10^{-4}$

This work evaluates G_M^n at $Q^2 = 3.0$ and 4.5 (GeV^2). Table 5.14 computes the values of the form factors and the corresponding uncertainties of the Ye fit using the equations and tables given above for these values of Q^2.

Table A.4: Ye global fit values of form factors at each kinematic. The uncertainties reflect the errors on the fits at the corresponding Q^2.

Q^2 (GeV^2)	$\sigma_{\text{Ye GMn}}$	Ye $G_M^n/(\mu_n G_D)$	$\sigma_{\text{Ye } G_M^n/(\mu_n G_D)}$	Ye G_E^n	$\sigma_{\text{Ye } G_E^n}$	Ye G_M^p	$\sigma_{\text{Ye } G_M^p}$	Ye G_E^p	$\sigma_{\text{Ye } G_E^p}$
3.0	-0.00072	0.999	0.0104	0.0162	0.00167	0.108	0.00076	0.024	0.00201
4.5	-0.00057	0.935	0.016	0.00965	0.00177	0.0547	0.00058	0.00868	0.00154
4.5	-0.00057	0.935	0.016	0.00964	0.00177	0.0547	0.00058	0.00867	0.00154

Appendix B

Tables for GRINCH Analysis

These tables contain additional information and results about the point-by-point GRINCH efficiency analysis.

Definitions of the “tight cuts” and “loose cuts” used in the GRINCH efficiency analysis are found in Tab. B.1.

Table B.1: Cuts for the GRINCH point-by-point efficiency analysis. Leading Edge Calibration utilized the “global cut” only. Highlighted are the cuts used in Fig. 3.30. “bb.tr.n” is the number of good tracks, “e.kine.W2” is the W^2 value calculated by SBS-Replay, “bb.tr.vz” is the z component of where the track orginated from in the target, “bb.ps.e” is the energy recorded in the Preshower, “bb.sh.e” is the energy recorded in the Shower, “bb.tr.p” is the absolute value of the momentum of the particle calculated by the GEM track in SBS-Replay.

global cut	bb.tr.n == 1, e.kine.W2 <= 2, abs(bb.tr.vz <0.07)
loose e- cut	bb.ps.e>0.2, global cut
tight e- cut	bb.ps.e >0.45, bb.ps.e <0.55, bb.sh.e >0.9, bb.sh.e <1.05, abs((bb.ps.e +bb.sh.e) /bb.tr.p) <0.16, global cut
loose pi. cut	bb.ps.e<0.2, global cut
tight pi. cut	bb.ps.e >= 0.08, bb.ps.e <=0.12, bb.sh.e >= 0.1, bb.sh.<= 1.3, ((bb.ps.e + bb.sh.e)/bb.tr.p) <0.5, global cut

Table B.2 shows the results when the “tight” and “loose” electron cuts are applied to the other detectors in the BigBite electron arm.

Table B.2: GRINCH efficiency point-by-point analysis over SBS-9 70%. Highlighted in yellow are the values plotted in the GRINCH efficiency results in Fig. 3.30.

	cut	cluster size	1	2	3	4	5	6	7	8	9	10
Track-Matching	loose cut	e^- detec. eff.	0.96822	0.95474	0.94379	0.92178	0.87804	0.79184	0.6456	0.45745	0.27851	0.14799
		det.	7356649	7254297	7171086	7003822	6671457	6016494	4905367	3475805	2116130	1124415
		exp.	7598152	7598152	7598152	7598152	7598152	7598152	7598152	7598152	7598152	7598152
	tight cut	e^- detec. eff	0.9835	0.9761	0.96703	0.94667	0.90462	0.81957	0.67011	0.47486	0.28785	0.15179
		det.	526192	522233	517381	506491	483992	438488	358524	254058	154005	81213
		exp.	535022	535022	535022	535022	535022	535022	535022	535022	535022	535022
	loose cut	pi rej. eff.	0.59964	0.83562	0.87969	0.89249	0.90106	0.91304	0.9306	0.95167	0.97077	0.98437
		det.	1540072	632333	462810	413579	380611	334514	266983	185897	112427	60134
		exp.	3846761	3846761	3846761	3846761	3846761	3846761	3846761	3846761	3846761	3846761
	tight cut	pi rej. eff.	0.65766	0.91385	0.96112	0.97286	0.97758	0.98109	0.9849	0.98919	0.99287	0.99569
		det.	32067	8070	3642	2542	2100	1771	1414	1013	668	404
		exp.	93670	93670	93670	93670	93670	93670	93670	93670	93670	93670
No Track-Matching	loose cut	e^- detec. eff.	0.99986	0.97887	0.95834	0.93279	0.88781	0.80091	0.65406	0.46527	0.2856	0.15437
		det.	7597109	7437576	7281612	7087496	6745733	6085398	4969615	3535178	2170057	1172933
		exp.	7598152	7598152	7598152	7598152	7598152	7598152	7598152	7598152	7598152	7598152
	tight cut	e^- detec. eff.	0.99989	0.98909	0.97681	0.95524	0.91267	0.82728	0.67751	0.48187	0.29436	0.15772
		det.	534963	529183	522615	511072	488298	442615	362484	257813	157488	84382
		exp.	535022	535022	535022	535022	535022	535022	535022	535022	535022	535022
	loose cut	pi rej. eff.	0.00218	0.41907	0.71691	0.81903	0.85525	0.8791	0.9044	0.93165	0.95577	0.97329
		det.	3838364	2234686	1088995	696132	556818	465072	367739	262934	170153	102753
		exp.	3846761	3846761	3846761	3846761	3846761	3846761	3846761	3846761	3846761	3846761
	tight cut	pi rej. eff.	0.00225	0.45606	0.78328	0.89174	0.9271	0.94386	0.95637	0.96749	0.97673	0.984
		det.	93459	50951	20300	10141	6829	5259	4087	3045	2180	1499
		exp.	93670	93670	93670	93670	93670	93670	93670	93670	93670	93670

Appendix C

Fit Functions

Fit Method in ROOT

ROOT calculates fit results primarily using *chi-squared minimization.* For binned data, the chi-squared function is defined as

$$\chi^2 = \sum_{i=1}^{N_{\text{bins}}} \frac{(y_i - f(x_i; \vec{p}))^2}{\sigma_i^2}\,, \tag{C.1}$$

where y_i is the observed value in bin i, $f(x_i; \vec{p})$ is the fit function evaluated at x_i with parameter vector $\vec{p}$, σ_i is the uncertainty in bin i, and N_{bins} is the number of bins used in the fit.

ROOT minimizes χ^2 using optimization algorithms such as Minuit2's Migrad method. The minimization process adjusts the fit parameters to best match the data, accounting for bin uncertainties.

After minimization, ROOT calculates the covariance matrix, providing parameter uncertainties and correlations. The goodness of fit is typically evaluated by the reduced chi-squared (χ^2/ndf) value, where $\text{ndf} = N_{\text{bins}} - N_{\text{parameters}}$.

Gaussian Fit (Normal Distribution)

A Gaussian (or “normal”) distribution is a type of continuous probability distribution for a real-valued random variable. Many distributions found in nature are Gaussian, making this fit useful for the natural sciences. One possible expression for a Gaussian fit function is

$$f(x) = A \times \exp\left(-\frac{1}{2}\left(\frac{x-\bar{x}}{\sigma}\right)^2\right) , \tag{C.2}$$

where A is the peak amplitude, $\bar{x}$ is the mean (center of the peak), and σ is the width parameter. In this parameterization, σ is related to the standard deviation and serves as a measure of the spread of the Gaussian. In ROOT, the fits are typically labeled p0 (peak amplitude), p1 (mean) and p2 (σ)

Offset Gaussian Fit

When a distribution is expected to contain superposition of Gaussian and a constant (flat) background, an offset Gaussian function is useful. One possible expression of this function is

$$f(x) = A \times \exp\left(-\frac{1}{2}\left(\frac{x-\bar{x}}{\sigma}\right)^2\right) + C\,. \tag{C.3}$$

As with the standard Gaussian fit, A is the peak amplitude, $\bar{x}$ is the mean (center of the peak), σ is the width parameter. C is added as an overall constant.

Polynomial Fit

Polynomial fits are useful for functionally describing a fit that we don’t know the distribution of. Polynomial fits are smooth, making them good candidates to describe the inelastic background. A polynomial fit of order (or degree) N is expresses as

$$f_N(x) = \sum_{n=0}^{N} A_n x^n\,, \tag{C.4}$$

where $A_0, A_1, \ldots, A_N$ are the polynomial coefficients. In ROOT, polynomial fits are typically labeled as pol0 (constant), pol1 (linear), pol2 (quadratic), and so on, where the number corresponds to the polynomial degree N.

References

[1] E. Rutherford, The scattering of α and β particles by matter and the structure of the atom, The London, Edinburgh, and Dublin Philosophical Magazine and Journal of Science **21**, 669 (1911).

[2] J. Chadwick, The existence of a neutron, Proceedings of the Royal Society of London. Series A, Containing Papers of a Mathematical and Physical Character **136**, 692 (1932).

[3] M. Gell-Mann, A Schematic Model of Baryons and Mesons, Phys. Lett. **8**, 214 (1964).

[4] M. Breidenbach, J. I. Friedman, H. W. Kendall, E. D. Bloom, D. H. Coward, H. DeStaebler, J. Drees, L. W. Mo, and R. E. Taylor, Observed behavior of highly inelastic electron-proton scattering, Phys. Rev. Lett. **23**, 935 (1969).

[5] S. Weinberg, The making of the standard model, The European Physical Journal C **34**, 5–13 (2004).

[6] V. Punjabi, C. F. Perdrisat, M. K. Jones, E. J. Brash, and C. E. Carlson, The Structure of the Nucleon: Elastic Electromagnetic Form Factors (2015), arXiv:1503.01452 [nucl-ex] .

[7] F. Wilczek, Origins of mass, Open Physics **10**, 1021 (2012).

[8] Cush, Standard model of elementary particles (wikimedia commons), Image file (2025), [Online; accessed 19-May-2025].

[9] Cush, Standard model deuterium (wikimedia commons), Image file (2024), [Online; accessed 19-May-2025].

[10] D. J. Griffiths, *Introduction to Elementary Particles*, 2nd ed. (Wiley-VCH, Weinheim, Germany, 2008).

[11] F. Halzen and A. D. Martin, *Quarks and Leptons: An Introductory Course in Modern Particle Physics* (John Wiley & Sons, New York, 1984).

[12] R. G. Sachs, Magnetic and electric form factors, in *High-energy physics. Proceedings, 11th International Conference, ICHEP'62, Geneva, Switzerland, Jul 4–11, 1962* (1962) pp. 197–199.

[13] X. Zheng, *Precision Measurement of Neutron Spin Asymmetry* A_1^n *at Large* X_{bj} *Using CEBAF at 5.6 GeV*, Ph.D. thesis, Massachusetts Institute of Technology (2002).

[14] T. W. Donnelly, J. A. Formaggio, B. R. Holstein, R. G. Milner, and B. Surrow, *Foundations of Nuclear and Particle Physics* (Cambridge University Press, 2017).

[15] G. D. Cates, C. W. de Jager, S. Riordan, and B. Wojtsekhowski, Flavor Decomposition of the Elastic Nucleon Electromagnetic Form Factors, Phys. Rev. Lett. **106**, 252003 (2011).

[16] G. Cates, SBS Physics I: Form Factors (2025), hall A Collaboration Meeting.

[17] C. D. Roberts, M. S. Bhagwat, A. Höll, and S. V. Wright, Aspects of hadron physics, The European Physical Journal Special Topics **140**, 53 (2007).

[18] I. C. Cloët, G. Eichmann, B. El-Bennich, T. Klähn, and C. D. Roberts, Survey of nucleon electromagnetic form factors, Few-Body Systems **46**, 1 (2009).

[19] F. Gross *et al.*, 50 Years of Quantum Chromodynamics: Introduction and Review, The European Physical Journal C **83**, 352 (2023).

[20] Z. Ye, J. Arrington, R. J. Hill, and G. Lee, Proton and neutron electromagnetic form factors and uncertainties, Physics Letters B **777**, 8 (2018).

[21] F. Gross, G. Ramalho, and M. T. Peña, Pure s-wave covariant model for the nucleon, Phys. Rev. C **77**, 015202 (2008).

[22] S. Xu, C. Mondal, J. Lan, X. Zhao, Y. Li, and J. P. Vary (BLFQ Collaboration), Nucleon structure from basis light-front quantization, Phys. Rev. D **104**, 094036 (2021).

[23] M. Diehl, T. Feldmann, R. Jakob, and P. Kroll, Generalized parton distributions from nucleon form-factor data, Eur. Phys. J. C **39**, 1 (2005), arXiv:hep-ph/0408173 .

[24] E. L. Lomon, Effect of recent R(p) and R(n) measurements on extended Gari-Krumpelmann model fits to nucleon electromagnetic form-factors, Phys. Rev. C **66**, 045501 (2002), arXiv:nucl-th/0203081 .

[25] J. Segovia, I. C. Cloët, C. D. Roberts, and S. M. Schmidt, Nucleon and Δ elastic and transition form factors, Few-Body Systems **55**, 1185–1222 (2014).

[26] I. C. Cloët and G. A. Miller, Nucleon form factors and spin content in a quark-diquark model with a pion cloud, Phys. Rev. C **86**, 015208 (2012).

[27] B. Wojtsekhowski, D. Hamilton, B. Quinn, *et al.*, Precision Measurement of the Neutron Magnetic Form Factor up to $Q^2 = 18.0(\mathrm{GeV}/c)^2$ by the Ratio Method (E-12-09-019) (2008), experimental proposal.

[28] B. Wojtsekhowski, D. Hamilton, B. Quinn, *et al.*, Update of E12-09-019 to the Jefferson Lab Program Advisory Committee (PAC35): Precision Measurement of the Neutron Magnetic Form Factor up to $Q^2 = 18.0(\mathrm{GeV}/c)^2$ by the Ratio Method (2010), experimental proposal update.

[29] S. Alsalmi, E. Fuchey, B. Wojtsekhowski, *et al.*, Measurement of the Two-Photon Exchange Contribution to the Electron-Neutron Elastic Scattering Cross Section (E12-20-010) (2020), experimental proposal.

[30] R. D. McKeown, The Jefferson Lab 12 GeV Upgrade, Journal of Physics: Conference Series **312**, 032014 (2011).

[31] S. N. Santiesteban, L. Tracy, D. Flay, D. W. Higinbotham, D. Marchand, P. Vernin, and A. Saha, Precise beam energy determination for hall a after the cebaf 12 gev upgrade (2021), arXiv:2110.06281 [physics.acc-ph] .

[32] P. A. Adderley *et al.*, The Continuous Electron Beam Accelerator Facility at 12 GeV, Phys. Rev. Accel. Beams **27**, 084802 (2024).

[33] F. M. Gonzalez (UCNτ Collaboration), Improved Neutron Lifetime Measurement with UCNτ, Phys. Rev. Lett. **127**, 162501 (2021).

[34] Dave Meekins, Pictures of cryo target ladder used during GMn (2024).

[35] Arun Tadepalli, BigBite Calorimeter Status (2021), Hall A/C Collaboration Meeting.

[36] P. Datta, *Precision Measurements of the eutron Magnetic Form Factor to High Momentum Transfer using Durand's Method*, Ph.D. thesis, University of Connecticut (2024).

[37] A. Puckett, SBS Software and Analysis (2022), Hall A Winter Meeting.

[38] F. Hartmann and J. Kaminski, Advances in Tracking Detectors, Annual Review of Nuclear and Particle Science **61**, 197 (2011).

[39] S. Jeffas, *Measurement of the Neutron Electromagnetic Form Facto Ratio at High Momentum Transfer*, Ph.D. thesis, University of Virginia (2024).

[40] F. Sauli, The gas electron multiplier (GEM): Operating principles and applications, Nuclear Instruments and Methods in Physics Research Section A: Accelerators, Spectrometers, Detectors and Associated Equipment **805**, 2 (2016).

[41] S. Bachmann, A. Bressan, B. Ketzer, M. Deutel, L. Ropelewski, F. Sauli, A. Bondar, A. Buzulutskov, L. Shekhtman, A. Sokolov, A. Tatarinov, A. Vasil'ev, S. Kappler, and

E. Schulte, Performance of GEM detectors in high intensity particle beams, Nuclear Instruments and Methods in Physics Research Section A: Accelerators, Spectrometers, Detectors and Associated Equipment **470**, 548 (2001).

[42] F. Sauli, GEM Gas Electron Multiplier Deveopment and Applications (2018), lecture Presentation.

[43] D. Baranov and O. Rogachevsky, Simulation of the GEM Detector for BM@N Experiment, EPJ Web Conf. **138**, 11004 (2017).

[44] J. A. B. III, *Measurements of the Neutron Magnetic Form Factor and the Two-Photon Exchange Contribution to the Electron-Neutron Elastic Scattering Cross Section*, Ph.D. thesis, University of Virginia (2024).

[45] R. Marinaro, *Performance and commissioning of the BigBite Timing Hodoscope for nuceleon form factor measurements at Jefferson Lab*, Ph.D. thesis, University of Glasgow (2023).

[46] R. Montgomery, BigBite Timing Hodoscope Update (2020), presentation, Hall A/C Summer Collaboration Meeting.

[47] W. R. Leo, *Techniques for Nuclear and Particle Physics Experiments* (Springer, 1994) p. 164.

[48] D. Hamilton, R. Montgomery, G. Penman, R. Marinaro, and O. Jones, BigBite Timing Hodoscope Performance Update (2023).

[49] M. Mihovilovič *et al.*, Methods for optical calibration of the bigbite hadron spectrometer, Nuclear Instruments and Methods in Physics Research Section A: Accelerators, Spectrometers, Detectors and Associated Equipment **686**, 20 (2012).

[50] R. Wines, Magnet and Infastructure, DOE Science and Technical Review of the SBS Project.

[51] V. Brio, V. Bellini, C. Petta, L. Re, C. M. Sutera, F. Tortorici, B. Wojtsekhowski, J. C. Cornejo, G. Franklin, and B. Quinn, HCAL-J: Hadron Calorimeter for the Study of Nucleon Form Factors at Jefferson Lab, Radiation Effects and Defects in Solids **173**, 857 (2018).

[52] S. Barcus, GRINCH Mirrors Techncial Report (2014).

[53] I. Adam *et al.*, The dirc particle identification system for the babar experiment, Nuclear Instruments and Methods in Physics Research Section A: Accelerators, Spectrometers, Detectors and Associated Equipment **538**, 281 (2005).

[54] ET Enterprises, Data sheet for 9125b photomulitpler.

[55] P. Bourgeois and J. Va'vra, Corrosion of Glass Windowsn in DIRC PMTs (1999).

[56] D. Hayes, *Studies of Refrigerant Gases for Use in Cherenkov Detectors at Jefferson Lab*, Undergraduate thesis, College of William & Mary (2018).

[57] A. Bideau-Mehu, Y. Guern, R. Abjean, and A. Johannin-Gilles, Interferometric determination of the refractive index of carbon dioxide in the ultraviolet region, Optics Communications **9**, 432 (1973).

[58] P. E. Ciddor, Refractive index of air: new equations for the visible and near infrared, Appl. Opt. **35**, 1566 (1996).

[59] M. N. Polyanskiy, Refractiveindex.info database of optical constants, Scientific Data **11**, 94 (2024).

[60] T. Yi-Ting *et al.*, Ray Optics Simulation (2016).

[61] T. Averett, H. Yao, and B. Wojsekhowski, GRINCH Detector Technical Document v.11 (2012).

[62] R. Montgomery, Nino board studies update (2015), sBS Collaboration Weekly Meeting.

[63] F. Anghinolfi, P. Jarron, A. Martemiyanov, E. Usenko, H. Wenninger, M. Williams, and A. Zichichi, Nino: an ultra-fast and low-power front-end amplifier/discriminator asic designed for the multigap resistive plate chamber, Nuclear Instruments and Methods in Physics Research Section A: Accelerators, Spectrometers, Detectors and Associated Equipment **533**, 183 (2004).

[64] G. Niculescu, GRINCH PMTs HV Groupings (2014).

[65] W. R. Leo, *Techniques for Nuclear and Particle Physics Experiments* (Springer, 1994) p. 326.

[66] S. Seeds, *The Two-Photon Exchange Contribution to Electron-Neutron Elastic Scattering (nTPE) and Extraction of G_M^n at $Q^2 = 4.5\ GeV^2$ in Hall A at Jefferson National Lab*, Ph.D. thesis, University of Connecticut (2024).

[67] M. Jones, P. Datta, *et al.*, SIMC Monte Carlo Simulation, GitHub repository, Accessed: Aug 21, 2024.

[68] R. Ent, B. W. Filippone, N. C. R. Makins, R. G. Milner, T. G. O'Neill, and D. A. Wasson, Radiative corrections for $(e, e^{'}p)$ reactions at gev energies, Phys. Rev. C **64**, 054610 (2001).

[69] R. Machleidt, K. Holinde, and C. Elster, The bonn meson-exchange model for the nucleon—nucleon interaction, Physics Reports **149**, 1 (1987).

[70] J. Allison *et al.*, Recent developments in geant4, Nuclear Instruments and Methods in Physics Research Section A: Accelerators, Spectrometers, Detectors and Associated Equipment **835**, 186 (2016).

[71] E. Fuchey, GMn/nTPE Analysis Update (2025), Hall A Winter Collaboration Meeting.

[72] E. Fuchey, Short Overview of SBS Digitization (2025), Personal Correspondence.

[73] SBS Collaboration, SBS Replay, GitHub repository (2025), accessed: Feb 11, 2025.

[74] M. Satnik, Maria's GMn Analysis GitHub, GitHub repository, Acessed: March 1, 2024.

[75] L. Y. Zhu *et al.* (Jefferson Lab Hall A), Cross-section measurement of charged pion photoproduction from hydrogen and deuterium, Phys. Rev. Lett. **91**, 022003 (2003), arXiv:nucl-ex/0211009 .

[76] A. R. Mudiyanselage, *Measurement of the Neutron Magnetic Form Factor at Large Momentum Transfer Using the Super-Bigbite Apparatus in Jefferson Lab Hall-A*, Ph.D. thesis, University of Virginia (2024).

[77] P. G. Blunden, W. Melnitchouk, and J. A. Tjon, Two-photon exchange in elastic electron-nucleon scattering, Phys. Rev. C **72**, 034612 (2005).

[78] SBS Collaboration, G4SBS Geant4 Simulation, accessed Aug 16, 2024.

[79] J. J. Kelly, Simple parametrization of nucleon form factors, Phys. Rev. C **70**, 068202 (2004).

VITA

Maria Satnik

Maria Satnik (she/they) was born and raised in Altoona, Wisconsin. While attending Altoona High School, Maria took mathematics courses at the University of Wisconsin–Eau Claire. After graduating high school as valedictorian in 2014, they went on to earn a B.S. in Physics from St. Norbert College in 2018, with minors in mathematics and computer science.

During their undergraduate years, Maria participated in SULI research internships at SLAC National Accelerator Laboratory and Jefferson Lab, which sparked her interest in particle and accelerator physics. In the summer of 2018, she began her Ph.D. research under the advisement of Dr. Todd Averett at William & Mary, in the Experimental Nuclear and Hadronic Physics group. Along the way, they earned an M.S. in Physics from William & Mary in 2020.

Maria's research has focused on studying the internal structure of protons and neutrons through electron scattering experiments at Jefferson Lab. In recognition of their excellent work and leadership, she was awarded a Jefferson Science Associates Graduate Fellowship at Jefferson Lab.

Following the completion of their Ph.D., Maria will begin a postdoctoral position at Lawrence Berkeley National Lab in the ATLAS detector group.